

Optical Property Tuning of Sulfur-containing Polymers with Precise Design of Intermolecular Interactions

分子間相互作用の精密設計による含硫黄ポリマーの光学特性制御

February, 2024

Seigo WATANABE

渡辺 清瑚

Optical Property Tuning of Sulfur-containing Polymers with Precise Design of Intermolecular Interactions

分子間相互作用の精密設計による含硫黄ポリマーの光学特性制御

February, 2024

Waseda University Graduate School of Advanced Science and Engineering

Department of Applied Chemistry, Research on Polymer Chemistry

Seigo WATANABE

渡辺 清瑚

Promoter: Prof. Dr. Kenichi Oyaizu
Referees: Prof. Dr. Yoshiyuki Sugahara
Assoc. Prof. Dr. Takeo Suga

Preface

With the recent development of highly efficient optoelectronic devices, high-refractive-index polymers (HRIPs) have become an attractive material owing to their high flexibility, excellent film-formability, and excellent mechanical properties compared to traditional inorganic glasses. In particular, HRIPs can enhance the external quantum efficiencies of various light-emitting materials, including organic light-emitting diodes (OLEDs), light-emitting electrochemical cells (LECs), and charge-coupled devices (CCDs), to maximize the light-extraction efficiencies and miniaturize the coating lenses for encapsulants. The applications of HRIPs vary over wide wavelength regions, from ultraviolet (UV)-visible to near-infrared and infrared light, and an appropriate molecular design in accordance with the intended application is required.

A major approach to achieve HRIPs comparable to high-RI inorganic glasses is to increase the molar refractivity, thereby enhancing their refractive indices (RI). However, this strategy generally involves a trade-off between RI and visible transparency. In particular, excessively high unit polarizability results in severe coloration, which has limited their application to long-wavelength regions (over NIR). Furthermore, HRIPs should also fulfill criteria such as chromatic aberration, birefringence, thermostability, and mechanical properties, besides RI and transparency. Achieving these requirements in a well-balanced manner is necessary for practical applications, although their systematic relationships have not been elucidated in detail.

In this dissertation, ultrahigh-RI and visible-transparent polymers were investigated by combining intermolecular interactions with highly transparent yet polarizable moieties and correlations between the microscopic structures and macroscopic properties were revealed. Chapter 1 provides an overview of HRIPs, including their structure-property relationships. Chapter 2 describes the preparation of high-refractive-index and transparent polymer-inorganic materials using HRIP scaffolds with high reactivity and affinity for inorganic media. Chapters 3 and 4 demonstrate the simultaneous enhancement of the RI and visible-transparency for poly(phenylene sulfide) derivatives via intermolecular hydrogen bonds. Chapter 5 describes HRIPs containing disordered yet multiple hydrogen bonds that exhibit high flexibility, ultrahigh RI, and transparency. Chapter 6 details the facile preparation of telechelic poly(phenylene sulfide)s through an aromatic electrophilic substitution reaction with electron-deficient electrophiles. In Chapter 7, the conclusions of this dissertation and future prospects for the present strategies are summarized.

Seigo Watanabe

Contents

Preface

Chapter 1: General Introduction

- 1.1 Introduction
 - 1.2 Fundamental Properties of High Refractive Index Polymers
 - 1.3 Molecular Design with Polarizable Groups
 - 1.4 Polymer-inorganic Hybrid Materials
 - 1.5 Design for Ultrahigh Refractive Index Polymers
- References

Chapter 2: Synthesis of Methoxy-substituted Poly(phenylene sulfide)s and Their End-modification toward High Refractive Index Polymer-Inorganic Hybrids

- 2.1 Introduction
 - 2.2 Synthesis of Poly(2-methoxy-1,4-phenylenesulfide)
 - 2.3 Optical Properties of Methoxy-substituted Phenylenesulfide Polymers
 - 2.4 End-modification and *in situ* Sol-gel Hybridization with Inorganic Nanoparticles
 - 2.5 Experimental Section
- References

Chapter 3: Ultrahigh Refractive index Poly(phenylene sulfide)s Enabled by Intermolecular Hydrogen Bonds

- 3.1 Introduction
 - 3.2 Synthesis of Hydroxy-Substituted Poly(phenylene sulfide)s
 - 3.3 Optical Properties and Hydrogen Bonding Elucidation
 - 3.4 Dihydroxy-substituted Poly(phenylene sulfide) with Denser Hydrogen Bonds
 - 3.5 Refractive Index Properties for Dihydroxy-containing Poly(phenylene sulfide)s
- References

Chapter 4: Refractive Index Enhancement of Poly(phenylene sulfide)s by Dual Control of Polarizability and Density

- 4.1 Introduction
 - 4.2 Synthesis of Sulfur-rich Aromatic Polymers via Oxidative Polymerization
 - 4.3 Copolymers with Hydroxy- and Methylthio-substituted Poly(phenylene sulfide)s
 - 4.4 Systematic Control of Optical Properties via Hydrogen Bonding and Polarizability
 - 4.5 Experimental Section
- References

Chapter 5: Multi-functional Aromatic Poly(thiourea)s with Ultrahigh Refractive Index and Degradability Based on Polarizable Hydrogen Bonds

- 5.1 Introduction
 - 5.2 Synthesis and Optical Properties of Aromatic Poly(thiourea)s
 - 5.3 Hydrogen Bonding Features in the Bulk States
 - 5.4 Demonstration of Poly(thiourea) thin film as an Amplifying Layer for Light-emitting Electrochemical Cells
 - 5.5 Degradation Studies of Poly(thiourea)s via Dynamic Covalent Chemistry
 - 5.6 Experimental Section
- References

Chapter 6: Synthesis of Telechelic Poly(phenylene sulfide) Derivatives via the Aromatic Electrophilic Substitution with Electron-deficient Electrophiles

- 6.1 Introduction
 - 6.2 One-pot Synthesis of End-functionalized Poly(phenylene sulfide)s
 - 6.3 Telechelic Poly(phenylene sulfide) Synthesis via Post Polymerization Modification
 - 6.4 Cross-coupling Synthesis of Vinyl-terminated Poly(phenylene sulfide)s
 - 6.5 Experimental Section
- References

Chapter 7: Conclusion and Future Prospects

- 7.1 Conclusion
 - 7.2 Future Prospects
- References

List of Publications

List of Presentations

Acknowledgements

Chapter 1

General Introduction

Contents

- 1.1 Introduction
- 1.2 Structure-Property Relationships for High Refractive Index Polymers
- 1.3 Molecular Design with Polarizable Groups
- 1.4 Polymer-inorganic Hybrid Materials
- 1.5 Design for Ultrahigh Refractive Index Polymers

References

1.1 Introduction

With the recent demand for low-cost, bright, and highly efficient light-emitting optical devices, high-refractive-index polymers (HRIPs) has recently been one of the promising materials that help enhancing the light-extraction efficiencies. Other applications of HRIPs vary from organic light-emitting diodes (OLEDs), organic photovoltaics, and solar cells to daily eyeglasses and contact lenses.^[1,2] HRIPs are lightweight, flexible, easily processable, and moldable features, all of which are advantageous from the device application perspectives in contrast to traditional inorganic materials.^[3] However, as major components of polymers (including optical materials) are hydrocarbons with low polarizable structures, they generally show low refractive index (RI) (~ 1.3 - 1.7) far beyond the required criteria (RI ~ 1.7 - 1.8) for optoelectrical applications.^[1,4] The most conventional and frequently used transparent polymers are poly(methyl methacrylate) (PMMA), representing high transparency from the ultraviolet–visible (UV–vis) to near infrared (NIR) regions, but having a low RI of 1.491 (at 587.6 nm).^[5] Other examples are aromatic-based polymers such as polystyrene (PSt) and polycarbonate (PC), having higher RI (\sim approx. 1.6)^[6] as well as thermostability and high mechanical properties, but even higher RI should be needed especially in the field of optoelectrical applications.^[2,7] For breaking through such empirical limit, various HRIP structures were designed and synthesized based on the strategy to make molar refraction (i.e., polarizability) higher according to the Lorentz-Lorenz equation.^[2] However, there still remain many issues to make HRIPs practical materials sufficient towards the device loadings, and many additional functions including optical properties (e.g., transparency, Abbe number, and birefringence) and other fundamental properties (e.g., mechanical and thermal properties) should be optimized according to the intended wavelength range and usable applications. For example, an Abbe number (i.e., RI dispersion or chromatic aberration)^[8] required to be higher or lower depending on the applications.^[9,10] Birefringence should be lower for transparent materials in general,^[11] but strong birefringence are required for exhibiting liquid-crystalline properties in some cases.^[12] Transparency, which is also an important parameter for optical materials, are generally in trade-off with the RI properties that makes it difficult to realize ultrahigh-RI transparent polymers.^[13] In the medical and military fields, HRIPs having well transparency in the mid-wave (MW) to long-wave (LW) infrared (IR) range are strongly required.^[14]

In this chapter, basic strategies for HRIP design were summarized mainly focusing on the multi-scale (hierarchical) structure control: from the first-order (repeating unit) to higher-order structures in the solid, glassy (bulk) states for realizing desirable RI and other properties. Additionally, the fundamental relations among optical properties, such as RI, transparency, and birefringence, are also mentioned in order to simultaneously achieve multifunctional optical properties.

1.2 Structure-Property Relationships for High Refractive Index Polymers

Refractive index of a material can be described by the Lorentz-Lorenz equation (Eq. 1.1), where RI was a function of molar refraction per molecular volume, $[R]/V$.^[2]

$$n = \sqrt{\frac{1 + 2 \frac{[R]}{V_0}}{1 - \frac{[R]}{V_0}}} \dots (1.1)$$

Molar refraction $[R]$ is described as a function of polarizability (α) (Eq. 1.2), using N_A as Avogadro number.^[3]

$$[R] = \frac{4}{3} \pi \alpha N_A \dots (1.2)$$

Eq. 1.2 means that introducing highly polarizable atoms can contribute to high RI of a material. Considering RI of solid materials, V is determined as a summation of the van der Waals volume and the free volume (voids), which can be described as follows:^[15]

$$V = \frac{V_{vdw}}{K_p} \dots (1.3)$$

where V_{vdw} and K_p are the van der Waals volume of the polymer and the packing constant of the material (i.e., occupancy ratio of polymer chains), respectively, and therefore larger packing constant in the bulk state results in a small total volume and high RI. Practically, RI of a polymer can be estimated prior to the synthesis, once $[R]$ and V have been determined. $[R]$ can be estimated by summing atomic/molar refractions of every components, which are precisely calculated by group contribution method or time-dependent density functional theory (TD-DFT) calculations.^[2,16,17] Especially regarding the latter, some suitable calculation conditions (basis and function sets) have been proposed that can generally consider long-range correlations such as Coulomb-attenuating method (CAM) or ω B97XD.^[16] However, V is difficult to precisely estimate only by the computational methods from information of a repeating unit structure, because density of a polymer is determined by many unpredictable factors (e.g., steric effect, intermolecular interactions, processing methods). The most commonly used K_p is 0.681, proposed by Slonimskii *et al.* as experimentally determined empirical value for general amorphous polymers.^[18] However, we should consider that this rule is only applicable to the limited (and selected) structures and impractical for rationally estimating RI for general polymers (e.g. polyimides typically show $K_p \sim 0.6$ ^[19] and therefore inadaptable).^[15]

1.2.1 Relationship between Molar Refractivity

The most facile method to enhance RI is introducing high- $[R]$ components into the repeating unit, which can be easily envisioned by Eq. (1.1). Table 1 shows the reported $[R]$ values for the atoms and substituents that are frequently used in the general polymer design.^[2,4,20,21] For higher $[R]$ values, introducing heavy atoms including heteroatoms (e.g., sulfur, nitrogen, phosphorous), chalcogens, halogens (chlorine, bromine, and iodine), aromatic rings, and metals can contribute to high RI values.^[2] However, excessively high $[R]$ induces strong UV-vis absorption that are inappropriate for the visible-light usage. In detail, such absorption strongly leads to declined transparency as well as low Abbe numbers due to red-shifting of the wavelength range for anomalous dispersion, based on the Kramers–

Kronig relationship.^[13] Therefore, the overall polarizability for the repeating unit should be considered for the visible-usage HRIP designing, although it is unnecessary for NIR or IR applications because UV-vis absorption does not affect the spectrum in the NIR-IR region including RI.

Table 1.1 Summary of $[R]$ values for representative substituents

Atoms/Substituents		$[R]$ (cm ³ mol ⁻¹) (Ref.)
Hydrocarbon	-H	1.100 ([2])
	>C<	2.418 ([2])
	-CH ₂ -	4.711 ([2])
Chalcogenides	-OH	1.525 ([2])
	-O-	1.643 ([2])
	=O	2.211 ([2])
	-S ^{II} -	7.80 ([2])
	-S ^{IV} -	6.98 ([2])
	-S ^{VI} -	5.34 ([2])
	-Se-	11.17 ([20])
	-Te-	13.87 ^{a)}
	Nitrogen	N-N=(C)
-CN		5.415 ([2])
-NC		6.136 ([2])
Halogen	-Cl	5.967 ([2])
	-Br	8.865 ([2])
	-I	13.900 ([2])
Unsaturated bonds	C=C	1.733 ([2])
	C≡C	2.336 ([2])
	-Ph	25.463 ([4])
	Naphthyl	43.000 ([4])

^{a)} Calculated using eq. 2 with $a = 5.5 \text{ \AA}^3$ (for Te).^[21]

1.2.2 Relationship between Molecular Volume

The second solution for RI improvement is to reduce the molecular volume by introducing compact skeletons. To date, such strategy is often adopted for aliphatic HRIPs, such as cycloolefin-containing HRIPs that usually representing high transparency with reasonable RI values.^[22,23] Another solution for decreasing the volume is reducing the porosity *via* intermolecular interactions (e.g., π - π interactions and hydrogen bonds), efficiently contributing to smaller free volume. However, once the excessive amount of intermolecular interaction moieties are introduced, crystallization or insolubilization of the polymers are inevitably occurred because of the strong aggregation ability (i.e.,

intermolecular packing) of the polymer chains, which finally led to turbid films with poor long-term stability. In summary, for obtaining transparent HRIPs, balancing the chain packing features and amorphous properties are essential in order to prepare transparent and high-RI polymer networks with the highest density.

1.2.3 RI Dispersion

The wavelength dependency of RI (i.e., RI dispersion) is also an important parameter for HRIP in order to evaluate the chromatic aberration. Abbe number (ν_D) is the most typical parameter used in the visible light region, which can be described as follows:

$$\nu_D = \frac{n_D - 1}{n_F - n_C} \dots (1.4)$$

where D, F, and C show the sodium D line (589.3 nm), hydrogen F line (486 nm), and hydrogen C line (656 nm), respectively.^[2] Regarding transparent materials, large ν_D means that RI is less dependent with the wavelength change in the visible light region.^[2] Also, the refraction of a material is correlated to the absorption features, and such mutual correlation can be explained by the Kramers-Kronig relationship.^[13] The RI (n) showed anomalous dispersion based on the increment of extinction coefficient (k), and these parameters can be integrated as a complex refractive index.^[3,13] One promising strategy for achieving higher Abbe numbers (i.e., small wavelength dispersion) is to increase the near-UV-visible transparency by reducing the absorption. In general, atomic groups with high $[R]$ inevitably induce the redshift of the near UV-visible absorption, and therefore simultaneous achievement of high RI and high Abbe number (and high visible transparency) in the visible region is difficult. The empirical limit between n_D and ν_D ^[24] was based on such trade-off for these parameters. Moreover, the Abbe number can be described using n_D and the sum of molecular dispersion for each substructure ($[\Delta R]$) as follows, which also can estimate the ν_D values from the molecular structure:^[2]

$$\nu_D = \frac{6n_D}{(n_D^2 + 2)(n_D + 1)} \cdot \frac{[R]}{[\Delta R]} \dots (1.5)$$

According to Eq. 1.5, polymers with small n_D and small $[\Delta R]$ represent high Abbe numbers, which also suggests the empirical n_D - ν_D threshold.

There are other functions regarding RI that explain the wavelength tendencies. As the actual relations of RI and wavelength are difficult to be formulated, some approximated formulas are proposed to explain RI as a function of wavelength λ . In the wavelength range without resonance, the Cauchy equation (Eq. 1.6) is adoptable^[3]:

$$n = C_1 + \frac{C_2}{\lambda^2} + \frac{C_3}{\lambda^4} \dots (1.6)$$

where C_i ($i = 1, 2, 3, \dots$) are constants. In the practical use, the simplified Cauchy's formula (Eq. 7), an approximated formula of the Cauchy equation (Eq. 1.6), is often adopted:^[25]

$$n = n_{\text{inf}} + \frac{D}{\lambda^2} \dots (1.7)$$

where n_{inf} and D means the RI at an infinite wavelength and the wavelength dispersion coefficient, respectively, and therefore HRIPs with small dispersion showed low D values. For all wavelength range including resonance (or absorption effect), the Sellmeier formula (Eq. 1.8) best explains the wavelength tendency of RI as follows:^[3,26]

$$n^2 = 1 + \sum_i \frac{a_i \lambda^2}{\lambda^2 - \lambda_i^2} \dots (1.8)$$

where a_i and λ_i are the resonance strength and the resonance wavelength, respectively. By fitting the RI spectra obtained via spectroscopic ellipsometry, the RI dispersion parameters (mainly wavelength and n) were quantitatively evaluated.

The required Abbe numbers for optical materials range depending on the applications. For example, a small optical lens for optoelectronic devices, such as CCD, is usually the combination of large- and small- n_D polymers which can effectively reduce chromatic aberration.^[10]

1.2.4 Birefringence

Birefringence indicates the optical anisotropy of a material, especially regarding the chain orientation behaviors. Birefringence (Δn) can be qualitatively interpreted as the RI difference between the value in the horizontal (n_{TE}) and in the perpendicular (n_{TM}) directions. Eq. 1.9 shows the definition of Δn :^[2,15]

$$\Delta n = n_{\text{TE}} - n_{\text{TM}} \dots (1.9)$$

The average RI (n_{av}) for all directions is described using n_{TE} and n_{TM} as follows (Eq. 1.10):^[3]

$$n_{\text{av}} = \sqrt{\frac{2n_{\text{TE}}^2 - n_{\text{TM}}^2}{3}} \dots (1.10)$$

Also, birefringence can be subdivided by two categories: orientational birefringence and photoelastic birefringence, which are termed Δn_o and Δn_p in this chapter. Δn_o is described as a product of intrinsic birefringence Δn^0 and the degree of polymer chain orientation f (Eq. 1.11).^[27]

$$\Delta n_o = f \Delta n^0 \dots (1.11)$$

Δn_o is equal to Δn^0 at $f=1$ (i.e. the ideal chain orientation), and Δn^0 is proportional to $\Delta\alpha/V_{\text{vdw}}$, where $\Delta\alpha$ denotes the polarizability anisotropy (Eq. 1.12):^[10]

$$\Delta\alpha = \alpha_{\text{TE}} - \alpha_{\text{TM}} \dots (1.12)$$

For declining the birefringence, the polymer design with a low $\Delta\alpha$ skeleton is effective from the viewpoint of decreasing both intrinsic and orientational birefringence. Photoelastic birefringence Δn_p can be explained as a product of photoelastic coefficient C and external stress $\Delta\sigma$ (Eq. 1.13).^[28]

$$\Delta n_p = C \Delta\sigma \dots (1.13)$$

In order to prepare zero-birefringent polymers, combining structures with positive and negative birefringence, such as copolymerization or polymer-blending techniques, are effective.^[29,30]

1.3 Molecular Design with Polarizable Groups

In this section, general HRIP structures, which have been designed based on the systematic control of the polarizability of the units, have been summarized in each category.

1.3.1 Aliphatic polymers

Aliphatic polymers are frequently used as a HRIP skeleton in the applications especially high transparency with large thickness are required, because of their little absorption features in the near-UV region that are effective for obtaining colorless film with high Abbe numbers. As aliphatic skeletons are less refractive than the aromatic groups for their lack of unsaturated bonds, aliphatic HRIPs generally contain compact skeletons with high- $[R]$ groups (sulfur and cyclic structures).^[2] Ueda *et al.* reported sulfur-containing poly(methacrylate)s bearing alicyclic carbonate groups (**Figure 1.1** (i)).^[31] Depending on the sulfur content of the skeleton, the polymers exhibited higher RI (n_D : 1.59–1.64) while the Abbe numbers were also in a high range of $\nu_D = 40.2$ – 44.5 beyond the empirical threshold of RI and Abbe numbers. No absorption features above 300 nm of the corresponding model compounds of the repeating units were also confirmed by the TD-DFT calculations, which also supports the positive effect of introducing sulfur-rich alicyclic structure in the HRIPs with high Abbe numbers.

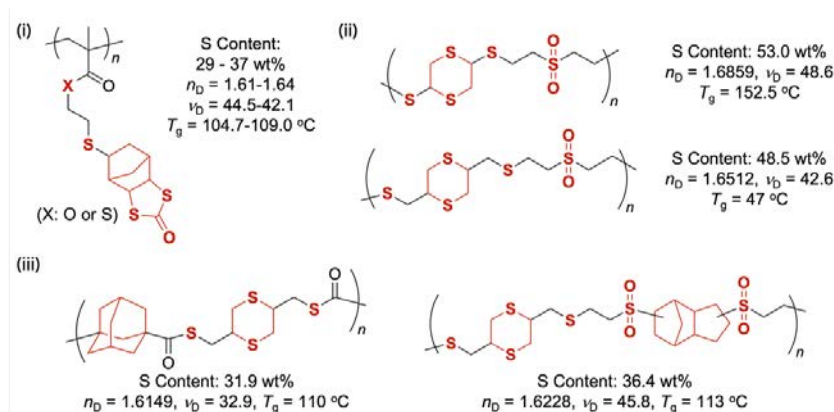


Figure 1.1. Examples of aliphatic HRIPs with sulfur-containing structures: (i) Sulfur-containing poly(methacrylate)s.^[31] (ii) Poly(ether sulfone)s with high Abbe numbers.^[32,33] (iii) Thermostable and sulfur-containing alicyclic HRIPs.^[9,34]

The another solution for increasing the Abbe number is to introduce sulfones with low molecular dispersions ($[\Delta R]_{-S(VI)-} = -0.02$) compared with sulfides and sulfoxides ($[\Delta R]_{-S(II)-} = 0.22$ and $[\Delta R]_{-S(IV)-} = 0.14$) (**Figure 1.1** (ii)).^[2,32] For example, poly(thioether sulfone)s were synthesized from divinyl sulfone and alicyclic dithiols with high RI ($n_D = 1.6461$ – 1.6859) and high Abbe numbers ($\nu_D = 42.6$ – 48.6),^[32,33] although they were less thermostable based on their nonaromatic structures. Bulky polymer skeletons such as adamantyl^[34] and tricyclo[5.2.1.0 2,6]decane^[9] moieties are also effective for yielding thermostable polymers with the similar optical properties ($n_D = 1.6052$ – 1.6278 , $\nu_D = 30.0$ –

48.0) (**Figure 1.1** (iii)). Still, on designing sulfone-containing polymers, S=O groups should not be excessively introduced because the highly polar and bulky structure leads to crystallization and large molecular volume, which might affect on balancing the overall performance (such as RI, Abbe number, transparency).

1.3.2 Cardo-containing polymers

Cardo-containing polymers, especially fluorene-based moieties, represents high refractive index as well as high visible transparency and low birefringence.^[35] For example, 9,9-substituted fluorene, especially 9,9-diaryl fluorene (DAF), is frequently favored because of its suppressed inter/intrachain packing that represents high RI, visible transparency, and small birefringence (**Figure 1.2a**).^[35] Takata *et al.* reported various DAF-containing HRIPs: polycarbonates ($n_D = 1.645\text{--}1.653$),^[36] poly(alkyl aryl ether)s ($n_D = 1.62\text{--}1.66$),^[37] polysiloxanes ($n_D = 1.64\text{--}1.66$),^[38] and poly(arylene thioether)s ($n_D = 1.66\text{--}1.72$),^[39] all of which also showed low birefringence. Higashihara *et al.* synthesized the DAF-based poly(phenylene thioether)s with high RI of $n_{633} = 1.737$ and small birefringence of $\Delta n = 0.0035$.^[40] Further, fluorene-containing polythioethers with ester groups were further low-birefringent owing to the flexibility of the spacers, resulting in $\Delta n = 0.0014$ in minimum with the highest fluorene density, although they were relatively low refractive with RI of $n_{633} = 1.6558\text{--}1.6751$ compared to the common polythioethers.^[10] To the best of my knowledge, there would be the RI threshold for most DAF-based polymers in n_D approx. 1.7, which was based on the bulky structure of the fluorene. As an expanded version, dibenzofluorene with higher aromatic content can enhance RI even higher (**Figure 1.2b**).^[41] Upon incorporating dibenzofluorene in a polycarbonate and polyimide skeleton, RI were increased ($n_D = 1.71$ or 1.67) with higher thermostability ($T_g = 298$ or 308 °C) compared with the DAF-based derivatives ($T_g = 217$ or 293 °C, $n_D = 1.65$ or 1.63), even though such dibenzofluorene-containing polymer did not contain sulfur atoms.^[41]

Another example as an expanded version of DAF is 9,9'-spirobifluorene (SBF), a symmetric fluorene skeleton that represents a perfect C_2 -symmetric structure with the orthogonally arranged aromatic rings, which compensate the axial birefringence while maintaining high RI (**Figure 1.2c**).^[42] Takata *et al.* reported SBF-containing polyesters^[43] with higher RI ($n_D = 1.684$) compared with the DAF-based corresponding polymers ($n_D = 1.658$), and showed low birefringence less than 0.0021. SBF-containing polycarbonates^[42] were also highly refractive ($n_D = 1.62\text{--}1.66$) and had almost zero birefringence ($\sim 10^{-4}$), and had excellent film formability with high flexible and mechanical toughness based on the polycarbonate-containing units.

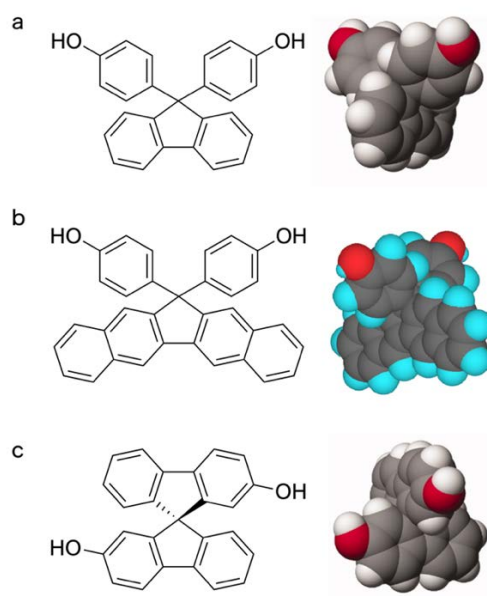


Figure 1.2. Chemical and 3D structures of (a) DAF-diol (reprinted from ref. [42] with permission, Copyright © 2010 Wiley), (b) 9,9-bis(4-hydroxyphenyl)-2,3;6,7-dibenzofluorene (dibenzofluorene-based diol) (reprinted from ref. [41] with permission, Copyright © 2019 Wiley), and (c) SBF-diol (reprinted from ref. [42] with permission, Copyright © 2010 Wiley). In particular, SBF-diol exhibits a completely symmetric structure that enables low birefringence upon the polymerization.

Several reactive SBF monomers were synthesized from the corresponding SBF-diols, which expand the molecular design for fluorene-containing HRIPs. Polycondensation of SBF-dithiols with the difluoro-substituted aromatics yield the SBF-containing poly(arylene thioether)s with high T_g (210–273 °C), high RI ($n_D = 1.6823$ – 1.7342), and small birefringence (0.0003–0.0020).^[44] Oxidation of the sulfides of such polymers gave poly(arylene sulfone)s.^[45] Such poly(arylene sulfone)s are slightly lower refractive but similarly low-birefringent compared with the corresponding polythioethers, while possessing higher T_g (257–370 °C) and higher transparency. Mori *et al.* synthesized high-molecular-weight SBF-based polythioethers through the click Michael addition reaction of DASF with dithiols.^[46] These polymers represented high T_g (90–164 °C), high transparency (above 90 %T), high RI ($n_D = 1.7169$ – 1.6690), and adequate Abbe numbers ($\nu_D = 14$ – 21). Notably, this method can be applied to the UV-induced system suitable for nanoimprint photolithography.

1.3.3 Polyimides with polarizable structures

Polyimide (PI) is a super-engineering plastic with high thermostability, mechanical properties, and solvent resistance, which are favorable properties in the field of optic and electrical fields in which the devices were operated in a harsh conditions (e.g., OLED, CMOS, dielectric materials).^[2,47] PIs are synthesized by the condensation of tetracarboxylic dianhydride and diamine and the heat-imidization to yield the imide-containing structures.^[47] The diamine monomers were easy to commercially obtained and the polymer skeleton design are also highly extensible. High-RI PIs are synthesized by

selecting high- $[R]$ units as monomers.

The RI of high- $[R]$ PI strongly correlates with the sulfur content according to the repeating unit.^[2] Therefore, PIs with phenylenesulfide,^[48,49] thiophene,^[50,51] thianthrene,^[52] or tetrathiaanthracene^[53] were the examples that showed particularly high RI. Although such PI synthesis requires high-temperature reaction conditions, Zhang *et al.* developed the room-temperature synthesis of sulfur-containing PIs using thiol-yne click polymerization. Thanks to the remaining alkenes and high sulfur content, the polymer represented high RI ($n_{633} = 1.7007$) and low birefringence (0.0002).^[54] On the other hand, such PIs generally induce coloration based on the charge-transfer interaction between the dianhydride and high- $[R]$ spacers, which led to low transparency.^[55,56] For preventing such coloration, Ha *et al.* designed PIs bearing side thiophenylene groups that decrease intermolecular interactions, representing low birefringence (0.0007–0.0022) and high RI ($n_{633} = 1.65$ –1.72) (**Figure 1.3 (i)**).^[57] Ueda *et al.* synthesized thianthrene tetraoxide thianthrene-containing PIs that exhibit over 80 %*T* above 450 nm based on the suppression of intermolecular interactions by the bulky S=O moieties (**Figure 1.3 (ii)**).^[58] Ando *et al.* reported PIs with chlorine-substituted high- $[R]$ moieties represented high RI, low birefringence, and improved visible transparency (**Figure 1.3 (iii)**).^[59] However, the inherent excellent thermal and mechanical properties of PIs are derived from such charge transfer interaction, which makes the simultaneous achievement of high RI and suppressed coloration while achieving excellent mechanical/ thermal properties.

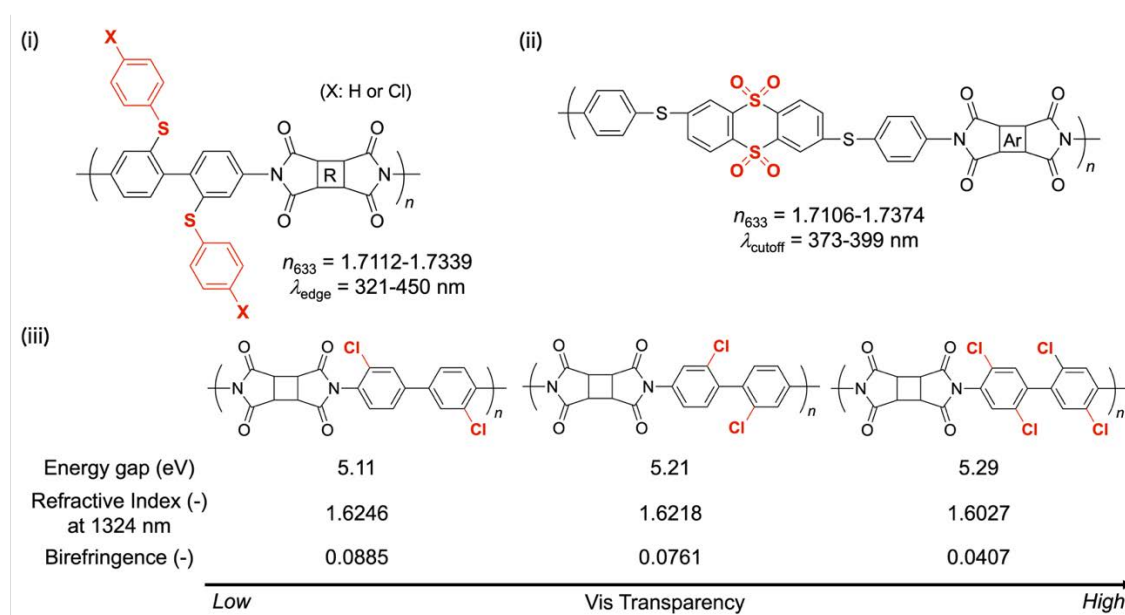


Figure 1.3. Molecular design and properties of colorless PIs (the key structures are highlighted in red): (i) PIs bearing bulky thiophenylene groups.^[57] (ii) Fully oxidized thianthrene-containing PIs, whose sulfone moieties prevent intermolecular interactions.^[58] (iii) Side functionalization of PIs with chlorine atoms, whose energy gap, RI, birefringence, and transparency were cooperatively controlled according to the number and position of the chlorine atoms.^[59]

1.3.4. Network/crosslinking polymers

Thermosetting optical polymers are desired for photopatterning and nanoimprint lithography applications in order to prepare the precise nanopatterns. Network structures including homogeneity and amount of dangling bonds affect the performance of the materials including solvent resistance, photostability, thermostability, and mechanical toughness. A promising route for preparing high-RI network polymers is the thiol-ene reaction, which can be conducted with high selectivity, conversion, and oxygen tolerance. Thiol-ene based network polymers were generally homogeneous and transparent with high sulfur content.^[60]

To date, several groups reported the high-RI thiol-ene networks. Fang *et al.* reported a heat-induced thiol-ene network preparation using aromatic dithiols and multi-functionalized siloxane^[61] or phosphorous^[62] enes. The prepared thermosets showed high T_g (120–155 °C), flexibility, and high transparency with the RI of $n_{546} = 1.63$ –1.72 and Abbe numbers of $\nu_D = 16$ –23. They also reported the thiol-ene system using cyclophosphazene-based ene monomers, yielding network polymers with high RI ($n_{550} = 1.67$ –1.71), thermostability, and high water tolerance with the maintaining optical properties after water immersion.^[63] Moreover, adopting UV-curable systems in the thiol-ene system is an economical strategy in order to obtain high-RI networks, for such system accomplishes the uniform network formation in much shorter time (~ few minutes) comparing with the heat-induced systems (a few hours-days). The most typical structure is a diacrylate resin, and Ueda *et al.* developed the curable polymeric system with thianthrene or phenylenesulfide-containing diacrylates and a photoinitiator, which produced sulfur-containing network polymers with high RI (1.6531–1.6645), high transparency (> 80 %T at 400 nm with 10 mm), and small birefringence (0.0039-0.0069) only after the exposure under UV irradiation for 30 min.^[64] You *et al.* also reported thiophene-based diacrylate sulfur-containing resin. This diacrylate was also mixed with a photoinitiator, and after the UV irradiation for 1 h, a polymer film with RI of 1.6444, low birefringence (0.0043), and moderate visible transparency (80.3 %T at 450 nm) was prepared^[65] based on their large sulfur content over 30 %.

For pursuing higher RI, the monomer should have high RI itself. Endo *et al.* reported the preparation of network polymers from tetrathiaspiro ring-containing dienes and multi-functional thiols, representing excellent RI of $n_D = 1.633$ with $\nu_D = 38.3$.^[66] Bowman *et al.* presented the systematic strategy for preparing photo-synthesized high-RI networks as “thiol-X photopolymerization”. In this system, high-RI multithiol and diallyl ether with low viscosity were polymerized under instant and mild UV irradiation (405 nm, 10 mW cm⁻², 10 seconds).^[67] The obtained polymer networks showed high RI ($n_D = 1.63$ –1.67), high Abbe numbers ($\nu_D = 25$ –32), and low viscosity, which can be applied as aspherical lenses and two-stage materials for fabricating gradient RI structures.^[67] The expanded strategy involving thiol-yne reactions also afford higher RI ($n_D = 1.65$ –1.68) and transparent polymer network, which was based on higher sulfur content compared with the thiol-ene networks because of the twice addition reaction for the thiol-yne system (**Figure 1.4**).^[68] These high-RI thiol-ene/yne networks showed appropriate properties as photo-processable materials including holographic applications.^[69] As another example, Cabrini *et al.* developed an optical resin through the heat-induced

ring-opening polymerization of fluorene-tethered diepisulfide and aromatic dithiols, which showed high RI ($n_{550} = 1.707$) and high degradation temperature (no degradation up to 290 °C). Such thermosetting system can be applied to the fabrication of photonic crystals, patterning, and microlenses.^[70]

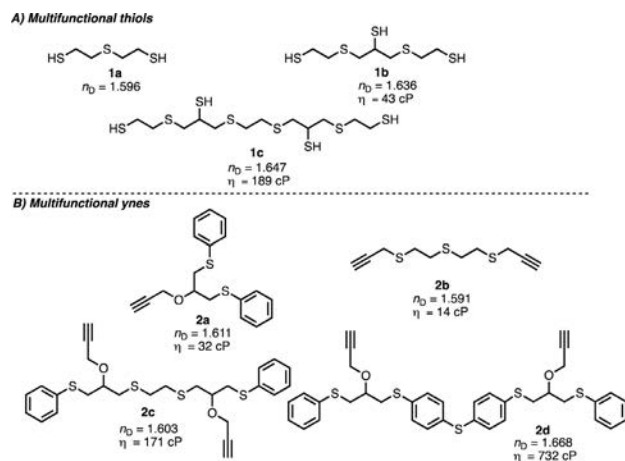
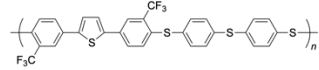
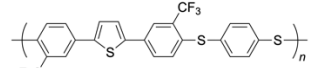
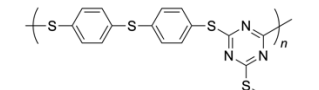
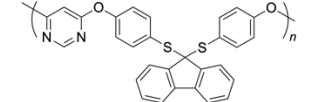
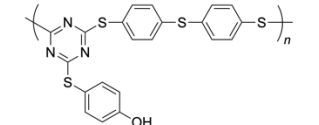
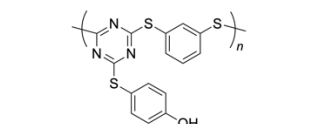
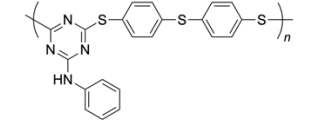
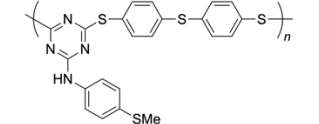


Figure 1.4. Structures of high-RI multi-functional monomers for the photo-induced thiol-yne curing systems yielding HRIP networks with RI of $n_D = 1.65$ -1.68. Reproduced from ref. [68] with permission (Copyright © 2021 American Chemical Society).

1.3.5 Poly(phenylene sulfide)s

Among sulfur-containing polymers, poly(phenylene sulfide) (PPS)-based structure is a first choice on a HRIP design owing to high visible transparency, thermostability, and high aromatic/sulfur content with high polarizability. PPS is a crystalline and insoluble super-engineering plastic which cannot be used for optical applications,^[71–73] which limited its application as a transparent material. However, various examples of the PPS-containing HRIPs have been accomplished by combining with other substructures (i.e, main-chain spacers or side functional groups) in order to induce amorphous properties and high solubility to achieve the use for transparent materials (**Table 1.2**).^[74]

Table 1.2. Structures and optical properties of the selected PPS-based polymers

Structure	Sulfur content (wt%)	RI (Wavelength)	n_D	T_g (°C)	Birefringence (Wavelength)	Ref.
	20.73	1.704 (D line)	7	160	-	86
	18.84	1.710 (D line)	8	175	-	86
	34.3 ^a	1.7492 (633 nm)	-	116	0.0041 (633 nm)	87
	13.0	1.6780 (633 nm)	-	143	0.004 (633 nm)	88
	28.27	1.7530 (633 nm)	15.7	180	0.0080 (633 nm)	89
	27.84	1.7420 (633 nm)	17.7	185	0.0040 (633 nm)	89
	22.98	1.7112 (633 nm)	-	165	0.0018 (633 nm)	90
	27.60	1.7269 (633 nm)	-	175	0.0015 (633 nm)	90

^a Not mentioned in the original literature. Calculated by the author from the repeating structure.

(Continued on the next page)

Table 1.2. Structures and optical properties of the selected PPS-based polymers (continued)

Structure	Sulfur content (wt%)	RI (Wavelength)	n_D	T_g (°C)	Birefringence (Wavelength)	Ref.
	23.5 ^a	1.69 (D line)	18	163	-	91
	23.2 ^a	1.73 (D line)	22	105-132	-	84
	19.1 ^a	1.75 (D line)	15	116	-	98
	41.6 ^a	1.81 (D line)	19	103	-	99
	21.6	1.737 (633 nm)	-	237	0.0035 (633 nm)	50
	21.9 ^a	1.7204 (637 nm)	-	153.05	0.01060 (637 nm)	101
	36.0	1.7516 (633 nm)	-	93.1	0.0051 (633 nm)	102
	38.4	1.7724 (633 nm)	-	185	0.0013 (633 nm)	102
	39.04	1.8020 (633 nm)	-	145	0.0033 (633 nm)	100

^a Not mentioned in the original literature. Calculated by the author from the repeating structure.

PPS-containing HRIPs are generally synthesized via the aromatic nucleophilic substitution (S_NAr) from dihalogenated aromatics and dithiols. Banerjee *et al.* reported a series of sulfur-containing HRIPs from multifluoro-substituted aromatics and dithiols that represented the maximum n_D of 1.717. As such S_NAr -based reaction requires the activation of dihalogenated monomers by electron-deficient moieties, introduction of low-polarizable fluorine and high-temperature conditions are required.^[75,76] Ueda and Higashihara *et al.* reported base-catalyzed polycondensation at low reaction temperature upon utilizing dichlorinated electron-deficient aromatic monomers (e.g., pyrimidine and triazine) to obtain heterocycle-containing PPSs. The polymers represent high molecular weights (M_w over 10^4), visible transparency, and high RI ($n_{633} = 1.7530$ in maximum).^[77-79] By utilizing the side functional group of the heterocyclic PPSs, birefringence was further decreased with the maintained high-RI ($\Delta n = 0.0015$ and $n_{633} = 1.7169$) based on the parallel chain-oriented conformation.^[80]

As side-chain functionalized PPSs, Oyaizu *et al.* have reported amorphous poly(arylene sulfide)s with electron-donating substituents that represented high RI (n_D over 1.7).^[74,81] These PPS derivatives can be accessed only through the oxidative polymerization of diaryl disulfides,^[82-84] which

proceeds in a electrophilic substitution reaction.^[85,86] As PPS derivatives have many reactive groups and showed well solubility, optical properties can be systematically tuned *via* various side-chain functionalization techniques. For example, alkyl- or alkoxy-substituted PPS represented RI of $n_D \sim 1.7$ with visible transparency,^[74,81,87,88] whereas the methylthio-substituted PPS recorded an unprecedentedly high RI of $n_D = 1.81$, which was based on its high sulfur content.^[89] Oxidation of sulfides toward sulfoxides and sulfones in the PPS main chain is effective for enhancing visible transparency by means of removing the lone pairs around the sulfur atoms, while they can maintain high RI in the range of $n_D = 1.66$ - 1.71 .^[81]

Furthermore, thianthrene-containing HRIPs have been reported as more compact sulfur-rich polymers compared with the PPS derivatives. The representable example is poly(thianthrene sulfide)s reported by Ueda *et al.*, showing RI up to $n_{633} = 1.8020$ with small birefringence ($\Delta n = 0.0033$).^[90] Upon the combination with various substructures (e.g., fluorene, biphenyl, and triazine), RI can be controlled more precisely (in the range of 1.7188-1.776 at 633 or 637 nm) in addition to the maintained small birefringence and high transparency.^[40,91,92] Such specific features of thianthrene groups can provide the balanced and better RI properties in the HRIP design.

1.3.6 Nitrogen-based structures

Nitrogen is also a promising candidate that represents high molar refractivity (N (in C–N=C): $4.10 \text{ cm}^3 \text{ mol}^{-1}$).^[2] Nitrogen-containing HRIPs are generally categorized as heterocycle-containing polymers (Note: please refer section 1.3.5 for triazine-containing HRIPs). Tang *et al.* have prepared heterocycle-containing HRIPs using multicomponent polymerizations. For example, three-component polymerization of diyne, disulfonyl azide, and carbodiimide with CuI catalyst obtained the four-membered azetidine ring-containing polymers with high solubility, film-forming ability, high RI of $n_{632.8} = 1.659$ – 1.627 , and various Abbe numbers ($\nu_D = 18.243$ – 34.195).^[93] These azetidine-containing polymers showed unique photophysical properties corresponding to the fused structure, which results in the RI enhancement, fluorescence, and aggregation-induced emission (AIE) features that are applicable for bioimaging applications.^[94] They also reported high nitrogen/oxygen-containing poly(maleimide)s with high RI and various Abbe numbers ($n_{632.8} = 1.614$ – 1.710 , $\nu_D = 6.7$ – 39.8). As polyvinyl-type heterocycle-containing HRIPs, Mori *et al.* reported RAFT-synthesized copolymers with benzothiazole-bearing vinyl sulfide and vinyl naphthalene in which can be tuned thermal properties ($T_g = 75$ – 150 °C), RI ($n_D = 1.7432$ – 1.6672), and Abbe numbers ($n_D = 17$ – 27) according to the copolymerization composition.^[95] As alternative skeletons for polyimides, Aromatic polybenzoxazoles represented higher RI ($n_{637} = 1.7862$) compared with those of the corresponding polyimides as well as good thermal and mechanical properties, which were originated from the compact heterocyclic skeletons.^[96] Nitro-substituents are also effective for enhancing RI, such as thiazole-containing polyamides bearing nitrophenyl side groups with high RI ($n_{632.8} = 1.7660$ in maximum) and low birefringence (≥ 0.0081).^[97]

1.3.7 Miscellaneous

As other high-RI elements, heteroatoms such as phosphorous and bismuth have been recently incorporated into the HRIP backbone achieving high RI,

Phosphorous is another effective element upon the introduction in the HRIPs, such as high polarizability (molar refraction: $4.08 \text{ cm}^3 \text{ mol}^{-1}$)^[98] and flame retardancy.^[99] Phosphine oxide and phosphine sulfide have been frequently used structures in the HRIP design. You *et al.* synthesized phosphine oxide and sulfur-containing polyimides with high RI ($n_{633} = 1.725$) and low birefringence (0.0087) including other excellent thermal and mechanical properties similar to the typical aromatic polyimides.^[100] Hifumi and Tomita reported poly(thiophosphonate)s with variable T_g (117–204 °C) and high RI ($n_D = 1.626$ – 1.687) composed of the bisphenol-A-based main chain and the polarizable P=S groups (**Figure 1.5**).^[101] Notably, such poly(thiophosphonate)s and poly(phosphonate)s were low birefringent compared to the corresponding polycarbonates and bisphenol A-based polymers.^[102,103] Such small birefringence was attributed to the smaller anisotropy of polarizability and more perpendicularly arranged phenylene rings based on the introduction of P=O or P=S moieties.

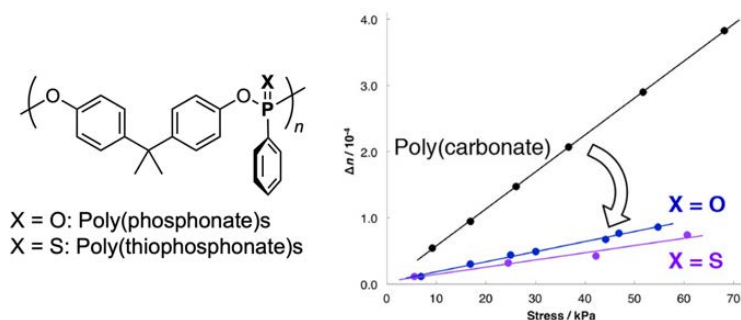


Figure 1.5. Highly refractive and low birefringent poly(phosphonate)s and poly(thiophosphonate)s: (a) Chemical structures^[102] and (b) orientational birefringence compared to those of poly(carbonate)s. Reproduced from ref. [102] with permission (Copyright © 2018 American Chemical Society).

Bismuth has also been reported as a highly refractive element for transparent polymers. Ochiai *et al.* reported bismuth-containing HRIPs using poly(methacrylate)s^[104] and polystyrene-based skeletons,^[105] exhibiting RI of $n_D = 1.51$ – 1.55 and $n_D = 1.71$ – 1.72 , respectively. The representable feature of Bi-containing polymers are their X-ray shielding ability, which can be applied for X-ray shielding glasses.

1.4 Polymer-inorganic Hybrid Materials

1.4.1 Overview of high-RI polymer-inorganic hybridized materials

Hybridization of polymers with inorganic ultrahigh-RI materials is another promising strategy for the RI enhancement. As a inorganic media, metal oxides/sulfides (e.g., TiO_2 , ZrO_2 , and ZnS) are frequently used for their facile preparation and excellent optical properties.^[2,7,106,107] The RI and absorption edge (transparency) of inorganic nanoparticles (NPs) depends on their energy gaps including their crystallinity (**Table 1.3**),^[106] and therefore the appropriate choice of inorganic NP fillers

is important considering the optical properties at the desired wavelength.

Table 1.3 Optical properties of inorganic additives

Inorganic compound	RI (-) (Ref.)	Absorption edge (nm) (Ref.)
TiO ₂ (rutile)	2.70 ([2])	409 ([106])
TiO ₂ (anatase)	2.45 ([2])	390 ([106])
TiO ₂ (sol-gel)	1.983 ([108])	397 ([108])
ZrO ₂	2.10 ([2])	248 ([109])
ZrO ₂ (sol-gel)	1.897 ([108])	230 ([108])
ZnO	1.93 ([110])	388 ([106])
ZnS	2.36 ([2])	- ^{a)}

^{a)} Not reported.

Upon hybridization, dispersing inorganic NPs in a polymer is generally difficult based on their large interfacial energy gaps between each component, leading to the aggregation of the NPs as well as macrophase separation and obtaining turbid films.^[111] Based on the Rayleigh scattering formula (Eq. 1.14), the transparency loss (T) of the bicomponent hybrid film increases as the RI difference of each component (n_p/n_m) and the dispersed radius (r) for the inorganic particles is high.^[7]

$$T = \frac{I}{I_0} = \exp \left\{ - \frac{32\pi^4 \varphi_p x r^3 n_m^4 \left[\left(\frac{n_p}{n_m} \right)^2 - 1 \right]^2}{\lambda^4 \left[\left(\frac{n_p}{n_m} \right)^2 + 2 \right]} \right\} \dots (1.14)$$

where I is the light intensity (subscript 0: the incident light), f is the volume fraction, n is the RI, x is the optical pass length, l is the light wavelength, $[R]$ is the molar refraction, and V is the molar volume. The subscripts p and m denote the particle and matrix, respectively.^[7] The RI of the hybrid material n_{hybrid} can be determined by Eq. 1.15.^[106]

$$n_{\text{hybrid}} = n_p \varphi_p + n_m \varphi_m \dots (1.15)$$

Considering Eq. 1.14 and 1.15, the strategy for preparing a transparent and high-RI polymer–inorganic hybrid film is described as follows: (1) using a higher RI matrix and (2) reducing the inorganic volumetric content, both of which are effective for preventing the scattering effects with the maintained RI and transparency of the film. Therefore, modifying the NP surface with some dispersants is required to achieve high dispersivity and long-time stability of the inorganic NPs inside the polymer matrices.^[112] The determinants of optical properties for polymer–inorganic materials can be categorized into (a) NP dispersivity, (b) RI of the polymer, (c) chemical formula of the NPs, and (d) crystallinity (and degree of sintering) of NPs. Especially (c) and (d) are essential factors because they also affect the RI of the inorganic component itself. Based on these aspects, we categorized the

polymer-inorganic hybridization methods by (1) using surface-modified inorganic nanoparticles and (2) in situ sol-gel hybridization.

1.4.2 Hybridization with surface-modified inorganic nanoparticles

The first solution is a surface-modification technique, in which the crystalline inorganic NP dispersions with high RI are used as inorganic sources. Controlling the chemical properties at the NP surface, the polymers are able to be gradually hybridized while preventing agglomeration. There are two main types according to the composition procedures: (i) polymerization reaction on the NP surface (grafting-from) and (ii) compatible blending of polymers and surface-modified inorganic NPs (grafting-to or just blending).

(1) Surface-initiated polymerization

This method is also known as “grafting-from method”, in which the reactive sites were firstly modified onto the NP surface, and polymerization of the coexisting monomer is directly initiated from the surface to yield polymer-grafted NPs.^[113] Chujo *et al.* reported the preparation of PMMA/ZrO₂ nanocrystal hybrid materials, in which methacrylate-based silane coupling agents were modified onto the ZrO₂ NPs prior to the polymerization. PMMA chains were subjected to prepared via the free-radical polymerization of methyl methacrylate (MMA).^[114] These PMMA/ZrO₂ hybrid films were transparent in the case of MMA-rich polymerization conditions (MMA/NPs = 10/1 (mol/mol) in maximum), and RI was slightly enhanced from 1.48829 (for pristine PMMA) to 1.53407 at 594 nm. In such grafting-from method, the controlled chain length also contribute to the maintained dispersivity of the NPs. Sugahara *et al.* prepared rutile-type TiO₂/PMMA nanohybrid materials by the surface-initiated atom transfer radical polymerization (SI-ATRP), in which the initiator was placed on the NPs using phosphonic acid dispersants.^[115] A long polymerization time (i.e., long grafting length) resulted in the preparation of hybrid films with the few-nanometer dispersion of TiO₂ particles, high transparency of the hybrid film even with 5 mm thickness, and higher RI up to $n_D = 1.566$ with 6.3 vol% TiO₂.

Kawaguchi *et al.* prepared hybrid materials of the modified ZrO₂ NPs with PSt or PMMA via radical polymerization using hexanoic acid and methacrylic acid modifiers, in which the 1-mm thick transparent hybrid films with nanodispersed ZrO₂ were obtained (**Figure 1.6 (i)**).^[109] Based on the large bandgap of ZrO₂ with small absorption edge (248 nm),^[109] the RI of the hybrid films were increased to $n_D = 1.626$ (PMMA, 64.6 wt% ZrO₂) and $n_D = 1.676$ (PSt, 65.1wt% ZrO₂) while little decline in Abbe numbers ($\nu_D \sim 30$ for PSt, $\nu_D \sim 50$ for PMMA hybrids). They expanded this strategy to the direct modification of ZrO₂ NPs by epoxy monomers including the subsequent curing reactions (**Figure 1.6 (i)a**).^[116] These epoxy-modified hybrid films can prevent the decrease in RI thanks to the direct modification of ZrO₂ NPs by epoxy monomers, resulting in even higher RI ($n_{594} = 1.7650$ in maximum), beyond the empirical n_D - ν_D limit (**Figure 1.6 (i)b**).^[116]

(ii) Compatible blending of polymers and surface-modified inorganic NPs

Matyjaszewski *et al.* have reported a hybridization concept using the miscibility between the grafted poly(styrene-*r*-acrylonitrile) (PSAN) ($M_n = 2300$) on ZnO NPs and PMMA matrices.^[117] These PMMA/PSAN-ZnO hybrids showed RI that were well-fitted with the Maxwell–Garnett theory ($RI \geq 1.6$ at 632.8 nm) while the transparency was declined after the NP introduction. Further, Sugahara *et al.* reported the hybrid materials composed of long alkyl-containing rutile-type TiO₂ NPs and cycloolefin copolymers (COP) (**Figure 1.6** (ii)).^[118] Owing to the stable tridentate coordination of the phosphates, these modified NPs were highly dispersed. The hybrid films were visible transparent and showed dramatically increased RI up to 1.83 with 19.1 vol% TiO₂, which was probably the result for highly crystalline rutile-type TiO₂ NPs.

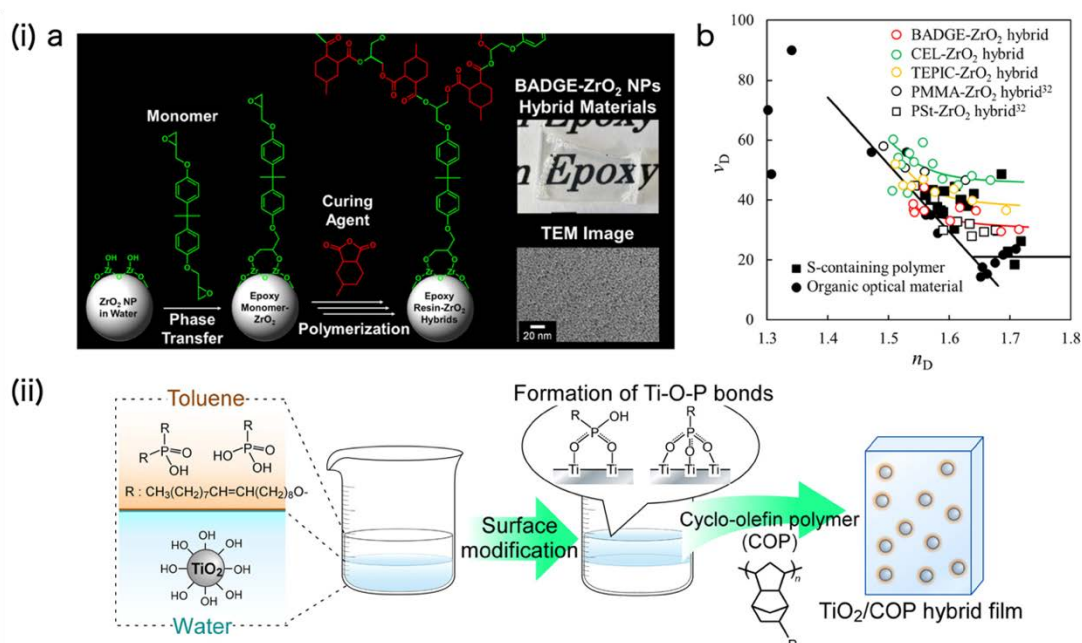


Figure 1.6. Hybridization using surface-modified inorganic NPs: (i) (a) Direct modification of ZrO₂ NPs via epoxy monomers and subsequent polymerization affording transparent and ZrO₂ nanodispersed epoxy-based materials. (b) High n_D and high n_D of the hybrids beyond the empirical limit (BADGE, CEL, and TEPIC are the abbreviations of the epoxy monomers). Those are reproduced from ref. [116] with permission (Copyright © 2018 American Chemical Society). (ii) Surface modification of rutile-type TiO₂ NPs with phosphate modifiers and preparation of its hybrid with COP. Reproduced from ref. [118] with permission (Copyright © 2017 American Chemical Society).

1.4.3 In situ Sol-gel Approach

The second route is the in situ sol–gel process, in which inorganic particles are gradually prepared via the sol–gel reaction of metal alkoxides in the polymer solution (precursor sol) to obtain the polymer–inorganic nanohybrid materials.^[119] The major inorganic source for frequently introduced metal alkoxide is metal butoxide (or its solution),^[2] which was polymerized by acid-catalyzed sol-gel

polycondensation^[120] that prepares small nanoclusters in the early stage of the polymerization. Amide solvents (such as N,N-dimethylacetamide (DMAc)) are often used in order to dissolve and mix both the polymer and inorganic precursors and have a relatively low gelation rate in the sol–gel reaction.^[121] The preparation of high-RI PI/TiO₂ and PI/ZrO₂ hybrids by such process has been reported by Chen and Liou *et al.* By introducing reactive and affinitive sites (such as carboxy^[122,123] and hydroxy^[108,124–126] units) into the PI structures, polymer and inorganic domains were covalently connected via those sites, and the transparent hybrid films with homogeneously dispersed NPs were obtained while representing tunable RI of ca. 1.6–1.9. The advantage of such in situ sol–gel process is that the reactive groups in the polymer chains also serve as surface modifiers for the inorganic domains. Therefore, there is no need for additional modifiers which might decline the RI of the materials though the hybridization. Hence, this strategy would be effective when the polymer matrix inherently shows a high RI. However, thermal sintering processes under severe conditions (up to ca. 350 °C), which would serve as a thermal imidization process for polyimides, are necessary to complete the sol–gel reaction to afford highly nanocrystalline and thermostable hybrid films toward RI enhancement. The hydrothermal method, which achieved lower sol-gel reaction temperature at 110–150 °C, was adopted to solve this issue.^[127–129]

However, the RI of the hybrid films prepared by this in situ sol-gel process generally resulted in lower values compared with the estimated RI according to the additive rules. This was based on the low crystallinity of TiO₂ nanoparticles, which still retain anatase-type crystal structure even after sintering at 350 °C. Furthermore, the bandgap (absorption edge) of TiO₂ is 3.18 eV (390 nm)^[106] and that of the nanodispersed-TiO₂ particles red-shifted upon the hybridization,^[122] and higher reactivity of the anatase-type TiO₂ than the rutyl-type TiO₂ also affected the yellowness of the hybrid materials that affects the coloration of the hybrid films.^[106] On the other hand, ZrO₂-based hybrid materials can further improve RI, Abbe numbers, and transparency. Liou *et al.* prepared the PI-ZrO₂ hybrid materials containing phenolic hydroxy groups via in situ sol–gel process, affording better-balanced optical properties of the hybrid films (RI: $n_{633} = 1.673–1.804$, Abbe numbers: $\nu_D = 20.65–32.18$, transparency: 89–94 %T at 400 nm with 500–600 nm thickness).^[108] The hybrid film with ZrO₂ and polyimidothioethers (PITEs) showed further high Abbe numbers ($\nu_D = 31.73–36.81$) with similar RI values ($n_{633} = 1.701–1.798$) as well as small birefringence (0.0034–0.0087) (Figure 1.7).^[129]

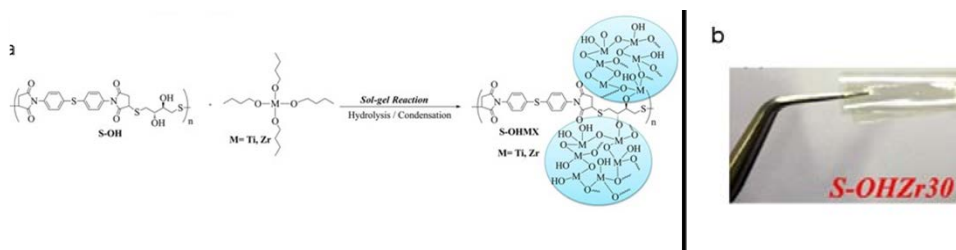


Figure 1.7. Polyimidothioether (PITE)-ZrO₂ hybrids. (a) Synthetic procedures of PITE-ZrO₂ nanohybrids. (b) Photograph of the PITE-ZrO₂ (30wt%) hybrid film. Reproduced from ref. [129] under the Creative Commons CC-BY 4.0 license.

1.5 Design for Ultrahigh Refractive Index Polymers

1.5.1 Inverse vulcanization

Ultrahigh-RI polymers, which generally corresponds to HRIP with RI over 1.8, are more desirable for improving the performances of optical devices with a thin-layer usage, such as the miniaturization and enhancement of light extraction efficiency.^[2] However, based on the small molar refraction of organic materials, achieving ultrahigh RI has been a challenging issue to date.

Char and Pyun *et al.* reported the inverse vulcanization (IV) method, which was the thermal radical-induced reaction of elemental sulfur and multivinylated comonomers (e.g., 1,3-diisopropenylbenzene (DIB)) (**Figure 1.8**).^[130,131] In detail, this system is initiated by the ring-opening of sulfur, and subsequent radical addition with the vinyl comonomers yielding the crosslinking sulfur-rich polymers with ultrahigh RI (in the range of approx. 1.7-2.2 in NIR-IR) and IR transparency.^[14] Therefore, these sulfur-rich polymers can be utilized to not only IR transparent lenses (e.g. sensors) but also the core polymers for NIR-IR optical waveguides representing low transmission loss, as alternatives for previous inorganic-based optical materials.^[14,132]

In addition to the simplicity of the reaction system, the expandable range of monomers is wide (**Table 1.4**). The IV of triisopropenylbenzene (TIB) with sulfur yielded sulfur-rich polymers with higher crosslinking density, T_g also enhanced to more than 50 °C, and ultrahigh RI (up to $n_{633} = 1.83$) was finally accomplished.^[133] As the sulfur-rich polymers with DIB linkages majorly contain linear structures as a major component with few branching structures,^[134] such TIB-containing polymers with branching junctions could contribute to its higher cross-linking density. However, there is a trade-off between the crosslinking density (or T_g) and RI due to the smaller refractivity of the comonomers with tri-reaction points than that of bifunctional counterparts. Such dichotomy has been solved by adopting divinylbenzene (DVB) as an additional comonomer.^[135] In contrast to the DIB linkage, the homopolymerized DVB chains were simultaneously synthesized during the IV process, which finally resulted in high T_g over 80 °C (after thermal annealing). The absence of the methyl group around the vinyl linkage also resulted in higher RI over 1.85 (up to $n_{633} = 1.87$) compared with the RI of the DIB-based structures.

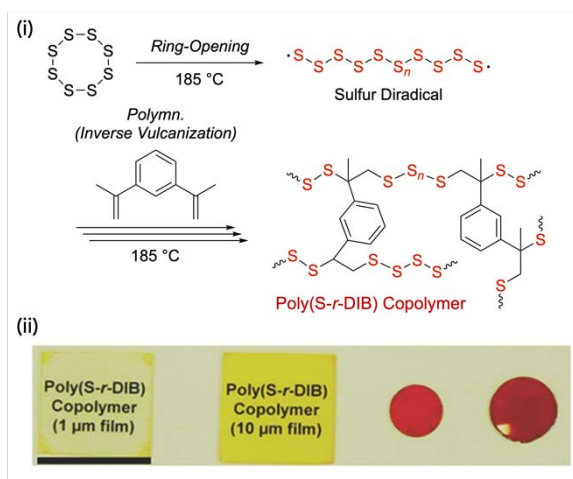


Figure 1.8. Brief outline of inverse vulcanization (IV): (i) Detailed reaction of IV from elemental sulfur and 1,3-diisopropenylbenzene (DIB) to yield the Poly(S-*r*-DIB) copolymer.^[130] (ii) Photographs of Poly(S-*r*-DIB) films (1 μm and 10 μm film on glass, 200 μm film, 2 mm lens). Reprinted from ref. [131] with permission (Copyright © 2014 Wiley).

Table 1.4. Comonomers for IV and the properties of their resulting polymers

Comonomer structure	Sulfur content (wt%)	Color of the film	n_{633} (-)	T_g ($^\circ\text{C}$)	Feature	Ref.
	80-50	Red	1.865-1.765	< 36.5	-Pioneering Work	117, 119
	70-50	Red	1.83-1.75	51.2-116	-High T_g	119
	70-50	Orange	1.87-1.78	25-107	-High T_g -High Sulfur Content	121
	70-50	Yellow	1.83-1.77	100.9 \pm 3.3-104.5 \pm 8.2 ^b	-High T_g -High IR Transparency	122
	80-50	Yellow	1.86777-1.95492 ^a	14.85-100.14	-High T_g -High RI -High IR Transparency	123

^a Value at 637 nm. ^b Measured by dynamic mechanical analysis (DMA).

Furthermore, several attempts have been reported for improving IR transparency of the IV polymers. One example is norbornene-based sulfur-rich polymers,^[136] in which the dimerized norbornene comonomer was adopted as a nonvolatile and nonaromatic skeleton with suitable properties according to the DFT calculation-aided screening, and was conducted to the IV. The resulting polymers were more IR-transparent than the aromatic-based sulfur-rich polymers representing higher RI (1.74–1.83 at 633–1554 nm) based on the absence of unsaturated skeletons. Another representative polymer is the IV polymer using trithiol as comonomers by You *et al.*^[137] In

this system, 1,3,5-benzenetrithiol was adopted as a crosslinker instead of the previous vinyl-based reactants (e.g., DIB or TIB). Finally the obtained polymers represented even higher RI (2.00–1.94 in visible-NIR with 80 wt% sulfur) and higher IR transparency compared with those of DIB/DVB-based IV polymers, which were based on the symmetric crosslinking structure with less numbers of IR vibration patterns.

Despite the superior NIR-IR optical properties of the IV polymers, the long polysulfide chains, which were inevitably contained in the polymerization process, led to the strong UV–vis absorption (and coloration) that hindered their visible-light applications. As a solution for such issues, a vapor-phase sulfur-initiated copolymerization, termed sulfur chemical vapor deposition (sCVD), was developed by Char, Im, and coworkers (**Figure 1.9 (i)**).^[138] The reaction mechanism is similar to the conventional bulk inverse vulcanization including the radical-involved system, whereas sCVD polymers have shorter polysulfide chains compared with the IV polymers using the bulk polymerization technique. This is because of the reaction media in the vapor phase, resulting in the reaction of the evaporated sulfur and the comonomers that could prevent forming long polysulfide chains. Such microstructure resulted in their high visible transparency and ultrahigh RI (~ 1.9) in the thin film states. The comonomer structure in the sCVD system is also widely applicable even with such as the divinyl ether, which was not applicable in the previous IV process due to the lack of miscibility, representing the advantage of the vapor-phase reaction system.^[138]

The sCVD polymers with ether or allyl-based comonomers exhibited high RI up to $n_{632.8} = 1.915$,^[138] whereas the sCVD polymers with DVB comonomers represented the unprecedentedly high RI of $n_{632.8} = 1.9777$ based on the high packing density between polymer chains (**Figure 1.9 (ii)**).^[139] Also, the phenyl-based sCVD polymers were visible transparent, low birefringent ($\Delta n = 0.0010$), and homogenous without any phase separation in spite of their major sulfur content (with over 85 wt%). Although the high sulfur content of the sCVD polymers results in low T_g of 21.1 °C, which was in the same trend as the case of the IV system, their thermostability was improved up to $T_g = 110.0$ °C at 68.45wt% sulfur with the balanced transparency and RI properties.^[140] This sCVD method can stand as an economical production method for ultrahigh-RI, uniform, and transparent thin-layer coatings.

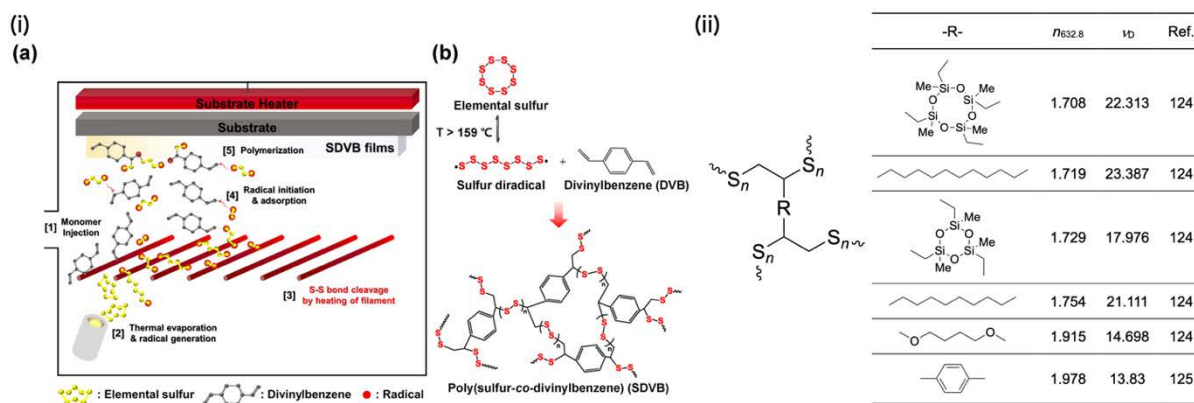


Figure 1.9. Sulfur-containing polymers prepared by sCVD. (i) Outline of sCVD, including the reaction mechanism (ring-opening of elemental sulfur, vaporization of sulfur radicals and monomers (DVB), and vapor-phase polymerization). Reproduced from ref. [140] with permission (Copyright © 2022 American Chemical Society). (ii) RI at 632.8 nm ($n_{632.8}$) and Abbe numbers (n_D) of sCVD polymers.^[138,139]

1.5.2 Thiocarbonyl-containing polymers

Thiocarbonyl-containing polymers also stand as one of the ultrahigh-RI groups because of its high molar refraction based on the presence of C=S group ($[R]_s$ (thiocarbonyl) = 7.97 and $[R]_{cs}$ (xanthate) = 13.07).^[141,142] Especially, trithiocarbonate has the largest molar refraction due to its high sulfur content. Nozaki *et al.* reported the high-RI ($n_D = 1.78$) trithiocarbonate synthesis by the alternating polymerization of propylene sulfide and carbon disulfide (CS₂) with [PPN]Cl and a chromium complex.^[143] Boggioni and Losio adopted a similar system to synthesize cyclohexyl-based poly(trithiocarbonate)s representing higher thermal stability ($T_g = 80$ °C) with similar RI (maximum $n = 1.74$ at 800–1100 nm).^[144] Related to them, Zhang *et al.* reported the copolymers composed of the poly(trithiocarbonate) and poly(monothiocarbonate) skeletons synthesized by CS₂ and phenyl glycidyl ether with Lewis pair catalyst, which led to high RI of 1.73–1.79 at 590 nm.^[145] As a side-chain type trithiocarbonate-containing HRIPs, Endo *et al.* reported the polymethacrylates bearing five-membered cyclic trithiocarbonate side groups, especially showing RI of $n_{632.8} = 1.622$ –1.663 in the case of the copolymers with poly(ethyl acrylate) and poly(acrylonitrile).^[146] Poly(trithiocarbonate)s can also be utilized as multi-functional HRIPs based on the reactivity of trithiocarbonates. Zhao *et al.* reported the recyclable poly(trithiocarbonate)s representing high RI and high Abbe number ($n_D = 1.73$, $\nu_D = 30.6$), which finally led to the recycling system involving the cyclic monomer production through pyrolysis.

As another C=S based HRIPs, poly(thioamide)s can be synthesized via several multicomponent-polymerization routes. Tang *et al.* prepared *p*-xylylene containing poly(thioamide)s from diynes, diamines and elemental sulfur, which showed high RI of 1.8065–1.6693 (at 400–1700 nm).^[147] Huang and Chen *et al.* reported aromatic poly(thioamide)s via the heat-induced direct polymerization of aliphatic diamines and elemental sulfur.^[148] These poly(thioamide)s showed high to ultrahigh RI values of $n_D = 1.58$ –1.87 whereas their Abbe numbers were generally low in the range of $\nu_D = 5.5$ –13.2, which was probably based on the low transparency of the polymers. Recently, Tang *et*

al. reported in preparing aromatic poly(thioamide)s through the three-component polymerization of sulfur, aromatic diamine, and dialdehyde with KOH.^[149] One of these aromatic poly(thioamide) showed ultrahigh RI ($n_{633} = 1.8702$) with large dispersion (RI: 2.034–1.7287 at 400–1700 nm), which was based on the high polarizability of thioamide-based skeleton.

1.5.3 Chalcogenide polymers

Incorporating chalcogenide atoms in the polymer skeleton is another solution to improve the RI. The most representative example is sulfur-containing polymers, which have been systematically summarized in the previous sections. Such wide-spread and large variety of sulfur-containing polymers were based on the readily available monomers and the well-established simple and easy reaction systems (e.g., thiol-based click reactions, nucleophilic additions, etc.).^[150]

On the other hand, selenium and tellurium with larger atomic numbers have higher $[R]$ values, and heavy-chalcogenide-containing polymers are expected to exhibit even ultrahigh RI. Still, they have rarely been used for HRIP substructures due to their high reactivity, toxicity, and low stability,^[151] but an increasing trend for such polymers has been recently arisen.

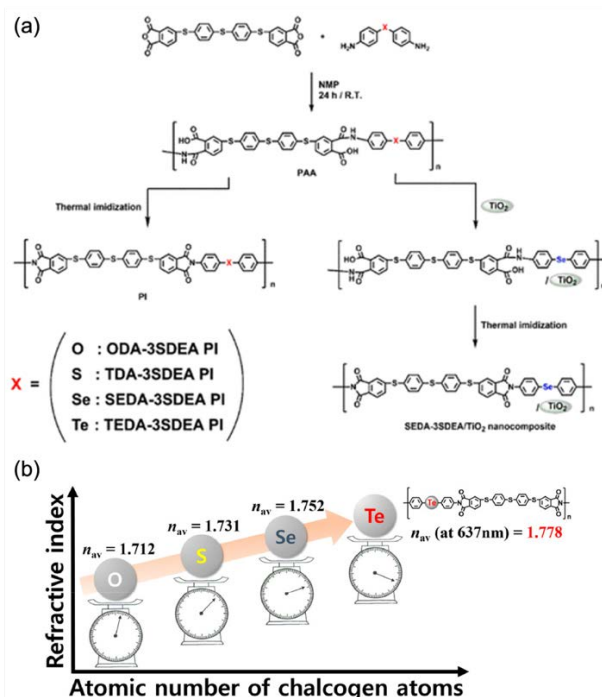


Figure 1.10. Systematic study of chalcogenide introduction:^[21] (a) Synthesis of chalcogenide-containing PIs and nanocomposite of TEDA-3SDEA PI/ TiO_2 . (b) Enhancement of RI for chalcogenide-PIs according to the introduction of heavy atoms. Reproduced from ref. [21] with permission (Copyright © 2019 American Chemical Society).

Selenium-containing HRIPs have frequently been reported as a family of high-RI PI. Especially selenophene, an analog of thiophene, was effective upon incorporating as a substructure of sulfur-containing PI to increase RI up to $n_{633} = 1.7594$, which was slightly higher the corresponding

thiophene-containing PI ($n_{633} = 1.7521$).^[152] Zhu *et al.* replaced oxygen atoms of diphenyl ether-containing PIs with selenium in order to enhance RI based on the increased selenium content, finally achieved the higher RI of $n_D = 1.968$ (Se 18.74%).^[153] Upon introducing trifluoromethyl groups for improving solubility, although the Se and F content were 11.73% and 16.93%, respectively, which were in the direction for decreasing RI, the polymer maintained an ultrahigh RI value ($n_{633} = 1.844$).^[154] Moreover, selenium-containing polymers generally decrease the Abbe numbers,^[155] presumably because of the large UV-vis absorption, the Abbe number of such ultrahigh RI polymer was exceptionally in a high value ($\nu_D = 20$) thanks to the synergy with the transparent properties by the trifluoromethyl groups. Radical copolymerization of chalcogenide-substituted maleimides and styrene derivatives can also access to ultrahigh RI polymers.^[20] Corresponding to the polarizability of side groups changing to oxide, sulfide, and selenide and the counterpart replacing from styrene to (4-phenseleno)styrene, the RI of the copolymers increased finally $n_{633} = 1.869$ with the Abbe number of $\nu_D = 7.4$. These selenide-containing ultrahigh RI polymers can be applied to the redox sensors monitoring by the RI changing, upon the chemical oxidation from selenide to selenoxide or selenone.^[20,154] Elemental selenium is another selenization agent to prepare such chalcogenide HRIPs. Tang *et al.* synthesized poly(oxaselenolane) through the multicomponent polymerization of elemental selenium, diisocyanide, and di(phenyl propargyl alcohol) catalyzed by DBU.^[156] Upon the optimization of the polymer skeleton for RI tuning, the polymer with the maximum selenium content (33.7 wt%) showed the highest RI of $n_{633} = 1.8026$ as well as a high Abbe number of $\nu_D = 17$. Pyun *et al.* adopted selenium-involving reactions to the IV system, in which directly added selenium into the IV reaction system provided the mixed polysulfide and polyselenide network structures, resulting in further enhanced RI over 2.0 at 633–1554 nm wavelength.^[157] Upon combining such sulfur/selenium-rich polymers with the low-refractive cellulose acetate, photonic crystals can also be fabricated.^[158]

In contrast to such reports for selenium-containing HRIPs, tellurium-containing HRIPs, an analogue category of Se-based polymers, have rarely been reported before. Tang *et al.* synthesized a tellurium-containing polymers via the multicomponent polymerization using diphenyl ditelluride as the chalcogen source, in addition to diyne and 4,4'-oxybis(benzenesulfonyl hydrazide) which showed an ultrahigh RI ($n_{550} = 1.8062$).^[159] As such polymer contained tetraphenylethane, an emitter for aggregation induced emission (termed as AIEgen), it exhibited emissive and UV-induced RI-changeable properties that enables the application for optical bioprobes (e.g., cellular imaging).

You *et al.* systematically investigated the optical properties of chalcogenide-containing PIs including their TiO₂ nanocomposites (**Figure 1.10**).^[21] The introduction of heavy chalcogenide (such as Se, Te) led to the higher main chain flexibility as well as decline of T_g , and RI was up to $n_{633} = 1.7783$. The order of dispersion coefficient D (i.e., RI dispersion coefficient) was O > S < Se < Te, which was consistent with the transparency trend for the polymer films. These results indicated that heavy chalcogenides led to the red-shifting of the polymer absorption properties in the near-UV–visible region, and therefore these polymers can be mainly adopted for not visible but NIR applications.

As shown in the above examples, introducing heavy chalcogenides into the polymer skeletons often affects their photophysical properties including RI, transparency, and Abbe number, due to their high polarizability. On utilizing chalcogenide-containing HRIPs as practical applications, we should consider the desired applications and applicable wavelengths which were strongly affected by the RI and absorption features.

1.5.4 Halogen and related element-containing polymers

Halogen atoms (except fluorene) can contribute to larger RI of the polymers based on their high polarizability,^[2] and bromine and iodine are the frequent choice for such strategy. Ober *et al.* reported bromine-containing poly(acrylate)s and poly(methacrylate)s representing high RI ($n_D = 1.62$ – 1.68).^[160] Also, Tang *et al.* reported a facile and precise thiol-yne polymerization of bromoalkynes and aromatic dithiols with a base catalyst.^[161] On using side-substituted phenylene alkynes, the RI systematically increased according to the polarizability order of the substituents: chlorine, methoxy, and bromine, and the bromo-substituted corresponding polymer exhibited the best optical properties with an ultrahigh RI of $n_D = 1.8433$ and a high Abbe number ($\nu_D = 19.5208$).

As other substructures, Iodine-containing polymers also represent ultrahigh RI properties. The first report was by Minns *et al.*, in which halogen-containing carbazole-substituted poly(methacrylate)s including their structure-RI relationship was investigated.^[162] Compared to the RI of Br-containing structures ($n_D = 1.67$ – 1.74), the corresponding iodine-containing polymers showed much higher RI ($n_D = 1.74$ – 1.77). Recently, Kudo *et al.* also reported iodine-containing poly(acrylate)s that exhibited RI of $n_D = 1.815$ – 1.752 ascribed to their high iodine content.^[163] Particularly, the copolymer of 2,4,6-triiodophenyl (TIP) with 20% 2-(2-ethoxyethoxy)ethyl acrylate showed the best-balanced RI properties ($n_D = 1.850$ and $\nu_D = 20.7$) beyond the homopolymers. Moreover, RI of a polymer can be increased by adding iodine-containing low-molecular compounds into the polymers as a filler. Tenhaeff *et al.* demonstrated the RI enhancement strategy through charge transfer complexation through the hybridization of poly(4-vinylpyridine) and halogen molecules (I_2 , IBr , and ICl) (**Figure 1.11**).^[164] Such complex films were prepared in a facile manner, including the film formation via chemical vapor deposition and subsequent complexation through the direct exposure of the thin films to the halogen vapor or solution, which finally resulted in ultrahigh RI (with IBr : n_d (RI at 587.6 nm) = 1.85 and with I_2 : $n_d = 2.08$). However, as the halogen molecule itself was weakly interplayed with the polymers and have sublimability, several of these hybrid films were unstable as well as showing strong coloration, which should be improved in the future.

Although highly polarizable features of the heavy halogens are attractive for RI enhancement, their poor thermal stability (mainly based on the unstable carbon–halogen bonds)^[165] and poor near-UV–visible transparency should be considered for the practical usage of halogen-containing HRIPs.

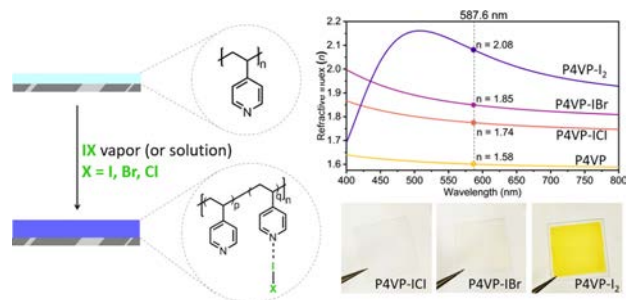


Figure 1.11. Preparation of charge-transfer complex of poly(4-vinylpyridine) (P4VP) and iodine-containing halogen molecules exhibiting ultrahigh RI ranging from $n_d = 1.74$ – 2.08 . Reproduced from ref. [164] under the Creative Commons CC-BY 4.0 license.

1.5.5. Intermolecular interactions

Based on the Lorentz-Lorenz equation, the reduction of free volume is another effective approach for further RI enhancement. To date, several polymers that achieved ultrahigh RI by introducing intermolecular interactions have been reported. Oishi *et al.* reported the high-RI whole-aromatic poly(guanamine)s based on a dense melamine structure.^[166] Based on various intermolecular interactions of guanamine skeletons, including multiple H-bonds and polycyclic aromatic hydrocarbons, poly(guanamine)s can achieve ultrahigh RI up to $n_d = 1.800$ thanks to the reduction of free volume. Moreover, incorporating trichlorotriazine as a comonomer resulted in higher triazine/amine densities which finally represented ultrahigh RI of $n_D = 1.936$ as well as an Abbe number of 9.9 although the polymer skeleton itself has no sulfur.^[167]

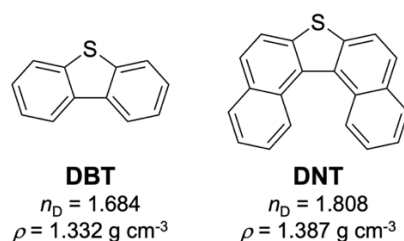


Figure 1.12. Comparison of dibenzothiophene (DBT) and ultrahigh refractive dinaphtho[2,1-*b*:1',2'-*d*]thiophene (DNT).^[168]

Nishikubo *et al.* reported dinaphtho[2,1-*b*:1',2'-*d*]thiophene (DNT) as an ultrahigh-RI molecule ($n_{633} = 1.808$) originated from the dense packing (Figure 1.12).^[168] Dibenzothiophene (DBT), an analogue of DNT, is a flat-shape molecule with a RI of $n_{633} = 1.684$, whereas DNT can form a helix-like herringbone structure ascribed to the stereodynamic features enabling stronger molecular packing and higher density. Also, these high-RI molecules were appropriate for using as a filler with PMMA in order to precisely tune the RI of the hybrid film.

1.5.6 Further strategy toward ultrahigh refractivity

Summarizing the abovementioned examples of the HRIP design, we have one important question: “What is the effective strategy for making polymers with even higher RI, while representing sufficient transparency?” Indeed, this means a challenge toward the empirical limit between RI and transparency of a polymer.

Based on the classical principles including some examples represented in this chapter, one promising strategy to achieve high Abbe numbers and transparency is enhancing the UV–visible transparency according to the Kramers-Kronig relationship, although such way can decrease the RI. On considering the RI in the solid (glassy) states, a free volume (i.e., voids) should be taken into account because the entanglement or penetration of the polymer chains are inevitable and such voids are lower refractive. Considering that the empirical packing constant value for general amorphous polymers ($K_p = 0.681$),^[18] approx. 30 % of the volume fraction are the voids and increasing packing density via intermolecular interactions (i.e., reducing free volume) surely contribute to enhance RI and transparency. However, there are other concerns, especially which is the crystallization or insolubilization induced by the excessive amount of intermolecular interacted functional groups, leading to the formation of ordered microstructures. Therefore, for realizing a colorless HRIP representing ultrahigh RI and a high Abbe number, the important strategy is to incorporate visible-transparent intermolecular interactions with moderately high- $[R]$ (i.e., without affecting the transparent properties) backbones.

In this chapter, overview of the high refractive index polymers, including the detailed structures and their relationships with optical and thermal properties, have been summarized. Upon the rational HRIP design, the most important thing is to consider beforehand the required properties, such as thickness, RI, Abbe number, transparency, thermostability, and flexibility, including the expected applications. Through further molecular design, this strategy could be expanded to developing HRIPs with better and more balanced optical performances.

References

- [1] J.-G. Liu, M. Ueda, *J. Mater. Chem.* **2009**, *19*, 8907.
- [2] T. Higashihara, M. Ueda, *Macromolecules* **2015**, *48*, 1915.
- [3] J. M. Scheiger, P. Theato, in *Sulfur-Containing Polymers*, Wiley, **2021**, pp. 305–338.
- [4] E. K. Macdonald, M. P. Shaver, *Polym. Int.* **2015**, *64*, 6.
- [5] N. Sultanova, S. Kasarova, I. Nikolov, *Acta Phys. Pol. A* **2009**, *116*, 585.
- [6] T. Nakamura, H. Fujii, N. Juni, N. Tsutsumi, *Opt. Rev.* **2006**, *13*, 104.
- [7] C. Lü, B. Yang, *J. Mater. Chem.* **2009**, *19*, 2884.
- [8] Y. Uozu, N. Hirota, K. Horie, *Macromol. Mater. Eng.* **2004**, *289*, 56.
- [9] Y. Suzuki, T. Higashihara, S. Ando, M. Ueda, *Macromolecules* **2012**, *45*, 3402.
- [10] K. Nakabayashi, T. Imai, M.-C. Fu, S. Ando, T. Higashihara, M. Ueda, *Macromolecules* **2016**, *49*, 5849.

- [11] A. Tagaya, H. Ohkita, M. Mukoh, R. Sakaguchi, Y. Koike, *Science* **2003**, *301*, 812.
- [12] Y. Arakawa, S. Nakajima, S. Kang, G.-I. Konishi, J. Watanabe, *J. Mater. Chem.* **2012**, *22*, 14346.
- [13] M. Fox, *Optical Properties of Solids*, OUP Oxford, **2001**.
- [14] T. S. Kleine, R. S. Glass, D. L. Lichtenberger, M. E. Mackay, K. Char, R. A. Norwood, J. Pyun, *ACS Macro Lett.* **2020**, *9*, 245.
- [15] Y. Terui, S. Ando, *J. Polym. Sci. B Polym. Phys.* **2004**, *42*, 2354.
- [16] S. Ando, *Chem. Lett.* **2018**, *47*, 1494.
- [17] C.-J. Yang, S. A. Jenekhe, *Chem. Mater.* **1995**, *7*, 1276.
- [18] G. L. Slonimskii, A. A. Askadskii, A. I. Kitaigorodskii, *Polymer Science U.S.S.R.* **1970**, *12*, 556.
- [19] J.-G. Liu, Y. Nakamura, T. Ogura, Y. Shibasaki, S. Ando, M. Ueda, *Chem. Mater.* **2008**, *20*, 273.
- [20] Q. Li, K. L. Ng, X. Pan, J. Zhu, *Polym. Chem.* **2019**, *10*, 4279.
- [21] H. Kim, B.-C. Ku, M. Goh, H. C. Ko, S. Ando, N.-H. You, *Macromolecules* **2019**, *52*, 827.
- [22] H. Yuan, T. Kida, Y. Ishitobi, R. Tanaka, M. Yamaguchi, Y. Nakayama, T. Shiono, *Macromolecules* **2022**, *55*, 125.
- [23] Y. Zhao, Y. Zhang, L. Cui, Z. Jian, *ACS Macro Lett.* **2023**, *12*, 395.
- [24] H. Dislich, A. Jacobsen, *Angew. Chem. Int. Ed Engl.* **1973**, *12*, 439.
- [25] S. Ando, Y. Watanabe, T. Matsuura, *Jpn. J. Appl. Phys.* **2002**, *41*, 5254.
- [26] D. Y. Smith, M. Inokuti, W. Karstens, *J. Phys. Condens. Matter* **2001**, *13*, 3883.
- [27] A. Tagaya, Y. Koike, *Polym. J.* **2012**, *44*, 306.
- [28] H. Shafiee, A. Tagaya, Y. Koike, *J. Polym. Sci. B Polym. Phys.* **2010**, *48*, 2029.
- [29] A. Tagaya, H. Ohkita, T. Harada, K. Ishibashi, Y. Koike, *Macromolecules* **2006**, *39*, 3019.
- [30] S. Iwasaki, Z. Satoh, H. Shafiee, A. Tagaya, Y. Koike, *Polymer* **2012**, *53*, 3287.
- [31] R. Okutsu, S. Ando, M. Ueda, *Chem. Mater.* **2008**, *20*, 4017.
- [32] R. Okutsu, Y. Suzuki, S. Ando, M. Ueda, *Macromolecules* **2008**, *41*, 6165.
- [33] Y. Suzuki, T. Higashihara, S. Ando, M. Ueda, *Polym. J.* **2009**, *41*, 860.
- [34] N.-H. You, T. Higashihara, S. Yasuo, S. Ando, M. Ueda, *Polym. Chem.* **2010**, *1*, 480.
- [35] Y. Koyama, K. Nakazono, H. Hayashi, T. Tataka, *Chem. Lett.* **2010**, *39*, 2.
- [36] T. Hasegawa, Y. Koyama, R. Seto, T. Kojima, K. Hosokawa, T. Takata, *Macromolecules* **2010**, *43*, 131.
- [37] H. Hayashi, M. Takizawa, T. Arai, K. Ikeda, W. Takarada, T. Kikutani, Y. Koyama, T. Takata, *Polym. J.* **2009**, *41*, 609.
- [38] H. Hayashi, S. Kawasaki, K. Kobori, Y. Koyama, S. Asai, T. Takata, *Polym. J.* **2009**, *41*, 272.
- [39] S. Seesukphronrarak, S. Kawasaki, K. Kobori, T. Takata, *J. Polym. Sci. A Polym. Chem.* **2007**, *45*, 3073.
- [40] Y. Nakagawa, Y. Suzuki, T. Higashihara, S. Ando, M. Ueda, *Polym. Chem.* **2012**, *3*, 2531.
- [41] S. Seesukphronrarak, S. Kawasaki, S. Kuwata, T. Takata, *J. Polym. Sci. A Polym. Chem.* **2019**, *57*,

2602.

- [42] R. Seto, T. Sato, T. Kojima, K. Hosokawa, Y. Koyama, G.-I. Konishi, T. Takata, *J. Polym. Sci. A Polym. Chem.* **2010**, *48*, 3658.
- [43] R. Seto, T. Kojima, K. Hosokawa, Y. Koyama, G.-I. Konishi, T. Takata, *Polymer* **2010**, *51*, 4744.
- [44] H. Okuda, R. Seto, Y. Koyama, T. Takata, *J. Polym. Sci. A Polym. Chem.* **2010**, *48*, 4192.
- [45] H. Okuda, R. Seto, Y. Koyama, T. Takata, *Polym. J.* **2010**, *42*, 795.
- [46] S. Iino, S. Sobu, K. Nakabayashi, S. Samitsu, H. Mori, *Polymer* **2021**, *224*, 123725.
- [47] C.-L. Tsai, H.-J. Yen, G.-S. Liou, *React. Funct. Polym.* **2016**, *108*, 2.
- [48] J.-G. Liu, Y. Nakamura, Y. Shibasaki, S. Ando, M. Ueda, *Polym. J.* **2007**, *39*, 543.
- [49] J.-G. Liu, Y. Nakamura, Y. Shibasaki, S. Ando, M. Ueda, *J. Polym. Sci. A Polym. Chem.* **2007**, *45*, 5606.
- [50] J.-G. Liu, Y. Nakamura, C. A. Terraza, Y. Shibasaki, S. Ando, M. Ueda, *Macromol. Chem. Phys.* **2008**, *209*, 195.
- [51] N. Fukuzaki, T. Higashihara, S. Ando, M. Ueda, *Macromolecules* **2010**, *43*, 1836.
- [52] J.-G. Liu, Y. Nakamura, Y. Shibasaki, S. Ando, M. Ueda, *Macromolecules* **2007**, *40*, 4614.
- [53] N.-H. You, Y. Suzuki, D. Yorifuji, S. Ando, M. Ueda, *Macromolecules* **2008**, *41*, 6361.
- [54] S. Xue, X. Lei, Y. Xiao, G. Xiong, R. Lian, X. Xin, Y. Peng, Q. Zhang, *Macromolecules* **2021**, *54*, 11256.
- [55] S. Ando, T. Matsuura, S. Sasaki, *Polym. J.* **1997**, *29*, 69.
- [56] M. Hasegawa, K. Horie, *Prog. Polym. Sci.* **2001**, *26*, 259.
- [57] P. K. Tapaswi, M.-C. Choi, K.-M. Jeong, S. Ando, C.-S. Ha, *Macromolecules* **2015**, *48*, 3462.
- [58] N.-H. You, Y. Suzuki, T. Higashihara, S. Ando, M. Ueda, *Polymer* **2009**, *50*, 789.
- [59] M.-C. Choi, J. Wakita, C.-S. Ha, S. Ando, *Macromolecules* **2009**, *42*, 5112.
- [60] C. E. Hoyle, C. N. Bowman, *Angew. Chem. Int. Ed Engl.* **2010**, *49*, 1540.
- [61] X. Chen, L. Fang, J. Wang, F. He, X. Chen, Y. Wang, J. Zhou, Y. Tao, J. Sun, Q. Fang, *Macromolecules* **2018**, *51*, 7567.
- [62] L. Fang, J. Sun, X. Chen, Y. Tao, J. Zhou, C. Wang, Q. Fang, *Macromolecules* **2020**, *53*, 125.
- [63] L. Fang, C. Wang, M. Dai, G. Huang, J. Sun, Q. Fang, *Mater. Chem. Front.* **2021**, *5*, 5826.
- [64] N.-H. You, T. Higashihara, S. Ando, M. Ueda, *J. Polym. Sci. A Polym. Chem.* **2010**, *48*, 2604.
- [65] H. Kim, H. Yeo, M. Goh, B.-C. Ku, J. R. Hahn, N.-H. You, *Eur. Polym. J.* **2016**, *75*, 303.
- [66] N. Aoyagi, T. Endo, *J. Polym. Sci. A Polym. Chem.* **2019**, *57*, 1160.
- [67] M. D. Alim, S. Mavila, D. B. Miller, S. Huang, M. Podgórski, L. M. Cox, A. C. Sullivan, R. R. McLeod, C. N. Bowman, *ACS Materials Lett.* **2019**, *1*, 582.
- [68] S. Mavila, J. Sinha, Y. Hu, M. Podgórski, P. K. Shah, C. N. Bowman, *ACS Appl. Mater. Interfaces* **2021**, *13*, 15647.
- [69] Y. Hu, B. A. Kowalski, S. Mavila, M. Podgórski, J. Sinha, A. C. Sullivan, R. R. McLeod, C. N.

- Bowman, *ACS Appl. Mater. Interfaces* **2020**, *12*, 44103.
- [70] Y. Tang, C. Pina-Hernandez, Q. Niu, J. Nie, S. Cabrini, *J. Mater. Chem. C* **2018**, *6*, 8823.
- [71] F. Aida, K. Oyaizu, *Chem. Lett.* **2016**, *45*, 102.
- [72] F. Aida, N. Takasu, Y. Takatori, H. Nishide, K. Oyaizu, *Bull. Chem. Soc. Jpn.* **2017**, *90*, 843.
- [73] P. Zuo, A. Tcharkhtchi, M. Shirinbayan, J. Fitoussi, F. Bakir, *Macromol. Mater. Eng.* **2019**, *304*, 1800686.
- [74] S. Watanabe, K. Oyaizu, *BCSJ* **2020**, *93*, 1287.
- [75] K. Mazumder, H. Komber, E. Bittrich, K. Uhlig, B. Voit, S. Banerjee, *Macromolecules* **2022**, *55*, 9766.
- [76] K. Mazumder, H. Komber, E. Bittrich, B. Voit, S. Banerjee, *Macromolecules* **2022**, *55*, 1015.
- [77] N.-H. You, T. Higashihara, Y. Oishi, S. Ando, M. Ueda, *Macromolecules* **2010**, *43*, 4613.
- [78] K. Nakabayashi, T. Imai, M.-C. Fu, S. Ando, T. Higashihara, M. Ueda, *J. Mater. Chem. C* **2015**, *3*, 7081.
- [79] M.-C. Fu, Y. Murakami, M. Ueda, S. Ando, T. Higashihara, *J. Polym. Sci. A Polym. Chem.* **2018**, *56*, 724.
- [80] M.-C. Fu, M. Ueda, S. Ando, T. Higashihara, *ACS Omega* **2020**, *5*, 5134.
- [81] S. Watanabe, T. Takayama, H. Nishio, K. Matsushima, Y. Tanaka, S. Saito, Y. Sun, K. Oyaizu, *Polym. Chem.* **2022**, *13*, 1705.
- [82] K. Yamamoto, E. Tsuchida, H. Nishide, M. Jikei, K. Oyaizu, *Macromolecules* **1993**, *26*, 3432.
- [83] E. Tsuchida, K. Oyaizu, *BCSJ* **2003**, *76*, 15.
- [84] S. Watanabe, S. Saito, M. Hirai, K. Oyaizu, *Polym. J.* **2022**, *54*, 1.
- [85] J. W. Cleary, in *Advances in Polymer Synthesis* (Eds.: B. M. Culbertson, J. E. McGrath), Springer US, Boston, MA, **1985**, pp. 173–185.
- [86] L. Rebenfeld, G. P. Desio, J. C. Wu, *J. Appl. Polym. Sci.* **1991**, *42*, 801.
- [87] S. Watanabe, K. Oyaizu, *ACS Appl. Polym. Mater.* **2021**, *3*, 4495.
- [88] S. Watanabe, H. Nishio, T. Takayama, K. Oyaizu, *ACS Appl. Polym. Mater.* **2023**, *5*, 2307.
- [89] S. Watanabe, T. Takayama, K. Oyaizu, *ACS Polym Au* **2022**, *2*, 458.
- [90] Y. Suzuki, K. Murakami, S. Ando, T. Higashihara, M. Ueda, *J. Mater. Chem.* **2011**, *21*, 15727.
- [91] N. Oh, K.-H. Nam, M. Goh, B.-C. Ku, J. G. Kim, N.-H. You, *Polymer* **2019**, *165*, 191.
- [92] Y. Nakagawa, Y. Suzuki, T. Higashihara, S. Ando, M. Ueda, *Macromolecules* **2011**, *44*, 9180.
- [93] T. Han, H. Deng, Z. Qiu, Z. Zhao, H. Zhang, H. Zou, N. L. C. Leung, G. Shan, M. R. J. Elsegood, J. W. Y. Lam, B. Z. Tang, *J. Am. Chem. Soc.* **2018**, *140*, 5588.
- [94] D. Fan, D. Wang, T. Han, B. Z. Tang, *ACS Appl. Polym. Mater.* **2022**, *4*, 3120.
- [95] Y. Sato, S. Sobu, K. Nakabayashi, S. Samitsu, H. Mori, *ACS Appl. Polym. Mater.* **2020**, *2*, 3205.
- [96] H. Kim, H. Yeo, H. C. Ko, N.-H. You, *ACS Appl. Polym. Mater.* **2021**, *3*, 4932.
- [97] A. Javadi, A. Shockravi, M. Koohgard, A. Malek, F. A. Shourkaei, S. Ando, *Eur. Polym. J.* **2015**,

66, 328.

- [98] T. Fushimi, H. R. Allcock, *Dalton Trans.* **2009**, 2477.
- [99] S. Huo, P. Song, B. Yu, S. Ran, V. S. Chevali, L. Liu, Z. Fang, H. Wang, *Prog. Polym. Sci.* **2021**, *114*, 101366.
- [100] H. Kim, B.-C. Ku, M. Goh, H. Yeo, H. C. Ko, N.-H. You, *Polymer* **2018**, *136*, 143.
- [101] R. Hifumi, I. Tomita, *Polym. J.* **2018**, *50*, 467.
- [102] R. Hifumi, I. Tomita, *Macromolecules* **2018**, *51*, 5594.
- [103] R. Hifumi, I. Tomita, *Polym. J.* **2019**, *51*, 905.
- [104] B. Ochiai, K. Kikuta, Y. Matsumura, H. Horikoshi, K. Furukawa, M. Miyamoto, Y. Nishimura, *ACS Appl. Polym. Mater.* **2021**, *3*, 4419.
- [105] Y. Matsumura, H. Horikoshi, K. Furukawa, M. Miyamoto, Y. Nishimura, B. Ochiai, *ACS Macro Lett.* **2022**, *11*, 723.
- [106] H. Althues, J. Henle, S. Kaskel, *Chem. Soc. Rev.* **2007**, *36*, 1454.
- [107] J. Loste, J.-M. Lopez-Cuesta, L. Billon, H. Garay, M. Save, *Prog. Polym. Sci.* **2019**, *89*, 133.
- [108] C.-L. Tsai, G.-S. Liou, *Chem. Commun.* **2015**, *51*, 13523.
- [109] K. Enomoto, Y. Ichijo, M. Nakano, M. Kikuchi, A. Narumi, S. Horiuchi, S. Kawaguchi, *Macromolecules* **2017**, *50*, 9713.
- [110] A. Suzuki, S. Ando, *J. Photopolym. Sci. Technol.* **2010**, *23*, 521.
- [111] J. Xu, Y. Zhang, W. Zhu, Y. Cui, *Macromolecules* **2018**, *51*, 2672.
- [112] C.-H. Hung, W.-T. Whang, *J. Mater. Chem.* **2005**, *15*, 267.
- [113] M. M. Demir, K. Koynov, Ü. Akbey, C. Bubeck, I. Park, I. Lieberwirth, G. Wegner, *Macromolecules* **2007**, *40*, 1089.
- [114] T. Otsuka, Y. Chujo, *Polym. J.* **2010**, *42*, 58.
- [115] S. Maeda, M. Fujita, N. Idota, K. Matsukawa, Y. Sugahara, *ACS Appl. Mater. Interfaces* **2016**, *8*, 34762.
- [116] K. Enomoto, M. Kikuchi, A. Narumi, S. Kawaguchi, *ACS Appl. Mater. Interfaces* **2018**, *10*, 13985.
- [117] Z. Wang, Z. Lu, C. Mahoney, J. Yan, R. Ferebee, D. Luo, K. Matyjaszewski, M. R. Bockstaller, *ACS Appl. Mater. Interfaces* **2017**, *9*, 7515.
- [118] S. Takahashi, S. Hotta, A. Watanabe, N. Idota, K. Matsukawa, Y. Sugahara, *ACS Appl. Mater. Interfaces* **2017**, *9*, 1907.
- [119] P.-C. Chiang, W.-T. Whang, *Polymer* **2003**, *44*, 2249.
- [120] S. Pandey, S. B. Mishra, *J. Sol-Gel Sci. Technol.* **2011**, *59*, 73.
- [121] J. B. Chan, J. Jonas, *J. Non-Cryst. Solids* **1990**, *126*, 79.
- [122] H.-W. Su, W.-C. Chen, *J. Mater. Chem.* **2008**, *18*, 1139.
- [123] T.-T. Huang, C.-L. Tsai, S. Tateyama, T. Kaneko, G.-S. Liou, *Nanoscale* **2016**, *8*, 12793.
- [124] G.-S. Liou, P.-H. Lin, H.-J. Yen, Y.-Y. Yu, W.-C. Chen, *J. Polym. Sci. A Polym. Chem.* **2010**, *48*,

1433.

- [125]H.-J. Yen, G.-S. Liou, *J. Mater. Chem.* **2010**, *20*, 4080.
- [126]S.-W. Cheng, T.-T. Huang, C.-L. Tsai, G.-S. Liou, *J. Mater. Chem. C* **2017**, *5*, 8444.
- [127]H.-W. Su, W.-C. Chen, *Macromol. Chem. Phys.* **2008**, *209*, 1778.
- [128]C.-L. Tsai, H.-J. Yen, W.-C. Chen, G.-S. Liou, *J. Mater. Chem.* **2012**, *22*, 17236.
- [129]T.-T. Huang, S.-W. Cheng, C.-L. Tsai, G.-S. Liou, *Sci. Rep.* **2017**, *7*, 7978.
- [130]W. J. Chung, J. J. Griebel, E. T. Kim, H. Yoon, A. G. Simmonds, H. J. Ji, P. T. Dirlam, R. S. Glass, J. J. Wie, N. A. Nguyen, B. W. Guralnick, J. Park, A. Somogyi, P. Theato, M. E. Mackay, Y.-E. Sung, K. Char, J. Pyun, *Nat. Chem.* **2013**, *5*, 518.
- [131]J. J. Griebel, S. Namnabat, E. T. Kim, R. Himmelhuber, D. H. Moronta, W. J. Chung, A. G. Simmonds, K.-J. Kim, J. van der Laan, N. A. Nguyen, E. L. Dereniak, M. E. Mackay, K. Char, R. S. Glass, R. A. Norwood, J. Pyun, *Adv. Mater.* **2014**, *26*, 3014.
- [132]A. Nishant, K.-J. Kim, S. A. Showghi, R. Himmelhuber, T. S. Kleine, T. Lee, J. Pyun, R. A. Norwood, *Adv. Opt. Mater.* **2022**, *10*, 2200176.
- [133]T. S. Kleine, N. A. Nguyen, L. E. Anderson, S. Namnabat, E. A. LaVilla, S. A. Showghi, P. T. Dirlam, C. B. Arrington, M. S. Manchester, J. Schwiegerling, R. S. Glass, K. Char, R. A. Norwood, M. E. Mackay, J. Pyun, *ACS Macro Lett.* **2016**, *5*, 1152.
- [134]J. Bao, K. P. Martin, E. Cho, K.-S. Kang, R. S. Glass, V. Coropceanu, J.-L. Bredas, W. O. Parker Jr, J. T. Njardarson, J. Pyun, *J. Am. Chem. Soc.* **2023**, *145*, 12386.
- [135]S. Park, D. Lee, H. Cho, J. Lim, K. Char, *ACS Macro Lett.* **2019**, *8*, 1670.
- [136]T. S. Kleine, T. Lee, K. J. Carothers, M. O. Hamilton, L. E. Anderson, L. Ruiz Diaz, N. P. Lyons, K. R. Coasey, W. O. Parker Jr, L. Borghi, M. E. Mackay, K. Char, R. S. Glass, D. L. Lichtenberger, R. A. Norwood, J. Pyun, *Angew. Chem. Int. Ed Engl.* **2019**, *58*, 17656.
- [137]M. Lee, Y. Oh, J. Yu, S. G. Jang, H. Yeo, J.-J. Park, N.-H. You, *Nat. Commun.* **2023**, *14*, 2866.
- [138]D. H. Kim, W. Jang, K. Choi, J. S. Choi, J. Pyun, J. Lim, K. Char, S. G. Im, *Sci Adv* **2020**, *6*, eabb5320.
- [139]W. Jang, K. Choi, J. S. Choi, D. H. Kim, K. Char, J. Lim, S. G. Im, *ACS Appl. Mater. Interfaces* **2021**, *13*, 61629.
- [140]K. Choi, W. Jang, W. Lee, J. S. Choi, M. Kang, J. Kim, K. Char, J. Lim, S. G. Im, *Macromolecules* **2022**, *55*, 7222.
- [141]T.-J. Yue, L.-Y. Wang, W.-M. Ren, *Polym. Chem.* **2021**, *12*, 6650.
- [142]W. Cao, F. Dai, R. Hu, B. Z. Tang, *J. Am. Chem. Soc.* **2020**, *142*, 978.
- [143]K. Nakano, G. Tatsumi, K. Nozaki, *J. Am. Chem. Soc.* **2007**, *129*, 15116.
- [144]S. Silvano, C. F. Carrozza, A. R. de Angelis, I. Tritto, L. Boggioni, S. Losio, *Macromolecules* **2020**, *53*, 8837.
- [145]J.-L. Yang, L.-F. Hu, X.-H. Cao, Y. Wang, X.-H. Zhang, *Chin. J. Chem.* **2020**, *38*, 269.

- [146]M. Nishi, M. Komeda, N. Aoyagi, Y. Yoshida, T. Endo, *J. Polym. Sci.* **2020**, *58*, 2126.
- [147]W. Li, X. Wu, Z. Zhao, A. Qin, R. Hu, B. Z. Tang, *Macromolecules* **2015**, *48*, 7747.
- [148]Z. Sun, H. Huang, L. Li, L. Liu, Y. Chen, *Macromolecules* **2017**, *50*, 8505.
- [149]Y. Hu, L. Zhang, Z. Wang, R. Hu, B. Z. Tang, *Polym. Chem.* **2023**, *14*, 2617.
- [150]H. Mutlu, E. B. Ceper, X. Li, J. Yang, W. Dong, M. M. Ozmen, P. Theato, *Macromol. Rapid Commun.* **2019**, *40*, e1800650.
- [151]Q. Li, Y. Zhang, Z. Chen, X. Pan, Z. Zhang, J. Zhu, X. Zhu, *Org. Chem. Front.* **2020**, *7*, 2815.
- [152]N.-H. You, N. Fukuzaki, Y. Suzuki, Y. Nakamura, T. Higashihara, S. Ando, M. Ueda, *J. Polym. Sci. A Polym. Chem.* **2009**, *47*, 4428.
- [153]Q. Li, J. Zhang, X. Pan, Z. Zhang, J. Zhu, X. Zhu, *Polymers* **2018**, *10*, DOI 10.3390/polym10040417.
- [154]Q. Li, S. Liu, M. Xu, X. Pan, N. Li, J. Zhu, X. Zhu, *Eur. Polym. J.* **2020**, *122*, 109358.
- [155]H. Jiang, X. Pan, N. Li, Z. Zhang, J. Zhu, X. Zhu, *React. Funct. Polym.* **2017**, *111*, 1.
- [156]X. Wu, J. He, R. Hu, B. Z. Tang, *J. Am. Chem. Soc.* **2021**, *143*, 15723.
- [157]L. E. Anderson, T. S. Kleine, Y. Zhang, D. D. Phan, S. Namnabat, E. A. LaVilla, K. M. Konopka, L. Ruiz Diaz, M. S. Manchester, J. Schwiegerling, R. S. Glass, M. E. Mackay, K. Char, R. A. Norwood, J. Pyun, *ACS Macro Lett.* **2017**, *6*, 500.
- [158]T. S. Kleine, L. R. Diaz, K. M. Konopka, L. E. Anderson, N. G. Pavlopolous, N. P. Lyons, E. T. Kim, Y. Kim, R. S. Glass, K. Char, R. A. Norwood, J. Pyun, *ACS Macro Lett.* **2018**, *7*, 875.
- [159]Q. Gao, L.-H. Xiong, T. Han, Z. Qiu, X. He, H. H. Y. Sung, R. T. K. Kwok, I. D. Williams, J. W. Y. Lam, B. Z. Tang, *J. Am. Chem. Soc.* **2019**, *141*, 14712.
- [160]L. L. Beecroft, C. K. Ober, *J. Macromol. Sci. Part A Pure Appl. Chem.* **1997**, *34*, 573.
- [161]J. Zhang, T. Bai, W. Liu, M. Li, Q. Zang, C. Ye, J. Z. Sun, Y. Shi, J. Ling, A. Qin, B. Z. Tang, *Nat. Commun.* **2023**, *14*, 3524.
- [162]R. A. Minns, R. A. Gaudiana, *J. Macromol. Sci. Part A Pure Appl. Chem.* **1992**, *29*, 19.
- [163]H. Maekawa, H. Amano, I. Nishina, H. Kudo, *ChemistrySelect* **2022**, *7*, e20220154.
- [164]N. Huo, W. E. Tenhaeff, *Macromolecules* **2023**, *56*, 2113.
- [165]N. Furusho, T. Komatsu, T. Nakagawa, *BCSJ* **1974**, *47*, 1573.
- [166]T. Kotaki, N. Nishimura, M. Ozawa, A. Fujimori, H. Muraoka, S. Ogawa, T. Korenaga, E. Suzuki, Y. Oishi, Y. Shibasaki, *Polym. Chem.* **2016**, *7*, 1297.
- [167]N. Nishimura, Y. Shibasaki, M. Ozawa, Y. Oishi, *J. Photopolym. Sci. Technol.* **2012**, *25*, 355.
- [168]Y. Nambu, Y. Yoshitake, S. Yanagi, K. Mineyama, K. Tsurui, S. Kuwata, T. Takata, T. Nishikubo, K. Ishikawa, *J. Mater. Chem. C* **2022**, *10*, 726.

Figures, tables, and texts are partially adapted from S. Watanabe, K. Oyaizu, *Bull. Chem. Soc. Jpn.* **2023**, *96*, 1108-1128. (Copyright © 2023 The Chemical Society of Japan).

Chapter 2:

Synthesis of Methoxy-substituted Poly(phenylene sulfide)s and Their End-modification toward High Refractive Index Polymer-Inorganic Hybrids

Contents

- 2.1 Introduction
 - 2.2 Synthesis of Poly(2-methoxy-1,4-phenylenesulfide)
 - 2.3 Optical Properties of Methoxy-substituted Phenylenesulfide Polymers
 - 2.4 End-modification of Poly(2-methoxy-1,4-phenylenesulfide) and Their Hybridization with Inorganic Nanoparticles
 - 2.5 Experimental Section
- References

2.1 Introduction

Poly(1,4-phenylenesulfide) (PPS) is one of the industrially-used engineering plastics that possess excellent mechanical, thermal and dielectric properties for electronics and automobile applications.^[1] PPS is industrially produced via the polycondensation of *p*-dichlorobenzene and sodium sulfide (Na₂S) in *N*-methylpyrrolidone (NMP) at high temperature and pressure,^[2] although there remain environmental issues such as the use of poisonous NMP, high halogen content due to the by-produced sodium chloride leading to poor insulation properties.^[3] Upon recent environmental issues, PPS production processes involving low halogen content of less than 900 ppm has been strongly required in industrial and practical levels.^[4]

In response to such request, many attempts have been reported for realizing environmentally friendly PPS synthesis. For example, INITZ co. ltd developed the chlorine-free PPS production process through the direct polycondensation of *p*-diiodobenzene and sulfur.^[5] Tsuchida and Oyaizu *et al.* have reported the oxidative polymerization of diphenyl disulfide, which proceeds in mild reaction conditions (e.g. at room temperature and in an air atmosphere) and by-produces only water.^[6-12] In this polymerization, diphenyl disulfide (DPS) is firstly oxidized by vanadyl binuclear catalyst under strong acid conditions, allowing the electron transfer reactions from DPS to oxygen, and the subsequently formed bis(phenylthio)phenyl sulfonium cation reacted with another DPS (or oligomer) via Friedel-Crafts type electrophilic substitution to give rise to the polymerization.^[13-16] Oxidative polymerization of DPS also undergoes with another strong oxidants such as 2,3-dichloro-5,6-dicyano-1,4-benzoquinone (DDQ).^[17] As the oxidative polymerization proceeded even under bulk conditions or with non-halogenated solvents, PPS produced by the oxidative polymerization shows high purity, low halogen content and excellent environmental compatibility.^[3] Furthermore, this oxidative polymerization can be expanded to producing PPS derivatives having electron-donating substituents owing to the acceleration effect of the electrophilic reactions.^[18,19] Except for 2,5-dimethyl substituted PPS,^[20] most of the PPS derivatives are amorphous, well-soluble, thermostable with higher T_g than PPS, all of which were ascribed to the steric effect of side groups.^[21]

These amorphous PPS derivatives can be applied to high-refractive-index polymers (HRIPs) based on their highly polarizable aromatic and sulfur contents.^[22] Among HRIP structures, sulfur-containing aromatics, such as phenylene sulfide and thianthrene, are one of the promising candidates of HRIPs especially for their high thermostability and well visible transparency.^[23-27] Most of such PPS-based HRIPs are required the short phenylene sulfide repeating structure and the combination with other bulky substituents presumably for maintaining amorphous properties that are necessary for transparent optical materials. In contrast, PPS derivatives have more compact skeleton composed of the phenylene sulfide moiety with small side groups notwithstanding its amorphous nature and therefore can maintain high refractive indices ($n_D \sim 1.7$ or higher).

For achieving further high refractive index (RI), one of the efficient methods is the hybridization with high-RI inorganic nanoparticles (NPs).^[28] Among various inorganics, titanium

dioxide (TiO₂) and zirconium dioxide (ZrO₂) are commonly used for their high RI ($n_D = 2.45$ for anatase TiO₂, $n_D = 2.70$ for rutile TiO₂, and $n_D = 2.10$ for ZrO₂) as well as absorption edge in small wavelength (ranging in 230-409 nm).^[29-31]

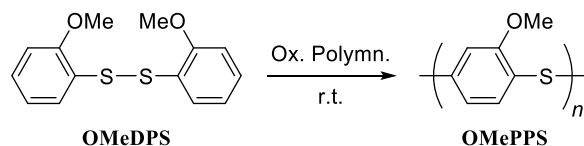
The most efficient hybrid method is dispersing inorganic NPs into the polymers because nanocrystalline inorganic NPs with high stability and RI can be directly used.^[32,33] For preventing aggregation of the NPs, surface of the NPs should be well-modified with the additives, such as silane coupling agents and organic acids. Kawaguchi *et al.* reported novel surface treatment method of ZrO₂ nanoparticles using hydrophobic surface modifier and solvent exchange from water to organic solvents, which can be applied to the preparation of transparent hybrid materials of ZrO₂ with polystyrene, poly(methylmethacrylate) and epoxy resins.^[31,33] However, as the polymer matrix does not have high affinity with the hybridized inorganic domains, large amount of modifiers are necessary to achieve single-dispersion of NPs into the polymer matrix. As lowering amount of modifiers and enhancing dispersivity of the NPs are in trade-off, the actual RI of the modified NPs generally resulted lower than those of the pristine inorganic materials. Another hybridization method is *in-situ* sol-gel route, by which inorganic nanoparticles are directly synthesized in a polymer solution through the sol-gel polycondensation of the corresponding metal alkoxide monomers.^[34] Although the inorganic domains showed low crystallinity as well as low RI (1.897 and 1.983 for ZrO₂ and TiO₂) in this route, no additives were needed once some reactive scaffolds, such as hydrophilic (hydroxyl or carboxyl) groups or silane coupling agents as a side/end groups, are introduced in the polymer for achieving well dispersion of the inorganic NPs.^[35-37] Furthermore, amount of the inorganic domains should be decreased in industrial aspects because it might cause crucial decline of transparency, moldability and flexibility due to the aggregation of inorganic nanoparticles in macroscopic/long time scale. Previously hybrid materials^[38-41] required high content of TiO₂ or ZrO₂ for achieving ultrahigh RI of $n_D \sim 1.8$ due to the low RI of the polymer. Once the RI of the polymer matrix has been enhanced, fewer amount of inorganic NPs should be required to realize the transparent nanohybrid materials with such ultrahigh RI.

In this chapter, methoxy-substituted PPS (**OMePPS**) was designed as a new PPS derivative representing high affinity with inorganic NPs. **OMePPS** showed amorphous properties, thermostability, and excellent optical properties. Including the end-functionalized **OMePPS** with hydrophilic terminal groups (i.e., catechol and carboxyl groups), the nanohybridization of the **OMePPS** family with TiO₂ or ZrO₂ were demonstrated via *in situ* sol-gel route, which enabled the RI enhancement of **OMePPS** from $n_D = 1.73$ up to 1.82 while preventing macroscopic aggregation of the NPs or severe coloration of the hybrid thin films.

2.2 Synthesis of Poly(2-methoxy-1,4-phenylenesulfide)

Oxidative polymerization of bis(2-methoxyphenyl) disulfide (**OMeDPS**) proceeded with the VO(acac)₂-oxygen or DDQ under TFA as an acid catalyst (**Scheme 2.1**, **Table 2.1**). Cyclic voltammetry revealed that **OMeDPS** was oxidized irreversibly at $E_{ox} = 1.58$ V vs. Ag/AgCl, which was close to the

E_{ox} of diphenyl disulfide (1.65 V) and bis(3,5-dimethylphenyl) disulfide (1.4 V) (**Figure 2.1**),^[6] suggesting the feasibility of the oxidative polymerization.



Scheme 2.1. Oxidative polymerization of **OMeDPS** in strong acid condition.

Table 2.1 Oxidative polymerization of **OMeDPS**^{a)}

Run	Solvent	DN ^{b)} (-)	Oxidant	[OMe DPS] (M)	Time (h)	Yield (%)	$M_n^c)$ ($\times 10^3$)	$M_w^c)$ ($\times 10^3$)	$M_w / M_n^c)$ (-)	$T_g^d)$ ($^{\circ}\text{C}$)
1			O ₂ with VO(acac) ₂	0.1	20	65	1.5	2.1	1.4	125
2	CH ₂ Cl ₂	0	DDQ	1	20	79	1.4	2.7	1.9	105
3			DDQ	2	20	84	2.0	3.9	2.0	115
4			DDQ	3	20	73	2.5	5.0	2.0	121
5	(CHCl ₂) ₂	0	DDQ	3	20	86	1.7	2.8	1.6	106
6	(CH ₂ Cl) ₂	0	DDQ	3	20	82	2.3	4.9	2.1	126
7	Chloroform	4	DDQ	3	40 ^{e)}	79	2.9	6.0	2.1	125
8	Toluene	0.1	DDQ	3	20	81	2.6	4.4	1.7	123
9	Nitrobenzene	4.4	DDQ	3	20	75	1.8	3.1	1.7	132

^{a)} Temp. = r.t. ^{b)} Donor number of solvent, according to the previous report.^[42,43] ^{c)} Determined by SEC in chloroform. ^{d)} Determined by DSC. ^{e)} The reaction solution remained partially green at 20 h and therefore the polymerization was continued for another 20 h.

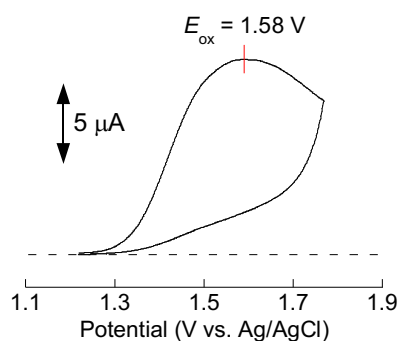


Figure 2.1. Cyclic voltammogram of 10 mM **OMeDPS** dissolved in dichloromethane containing 0.1 M TBABF₄ (Scan rate: 10 mV/s).

Molecular weight of **OMePPS** was the highest ($M_w = 6.0 \times 10^3$) with chloroform as the solvent (Run 5

in **Table 2.1**) because of its polar structure, high solubility, and suitable donor number ($DN = 4$) that contributes to the acceleration of the polymerization by the solvent effect and avoiding deactivation of the sulfonium cation owing to its cationic-like polymerization mechanism.^[41] The polar structure of **OMeDPS** seemed to be also effective for the progress of the polymerization.

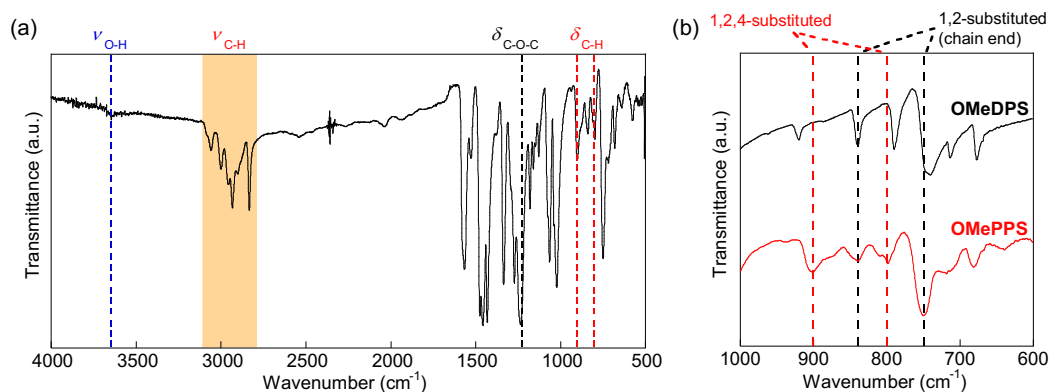


Figure 2.2. (a) Entire IR spectrum of **OMePPS** (expanded in the aromatic region). (b) Expanded IR spectrum of **OMeDPS** and **OMePPS**. The C-H out-of-plane absorptions at 800 and 900 cm^{-1} were characterized as the interchain aromatic protons.

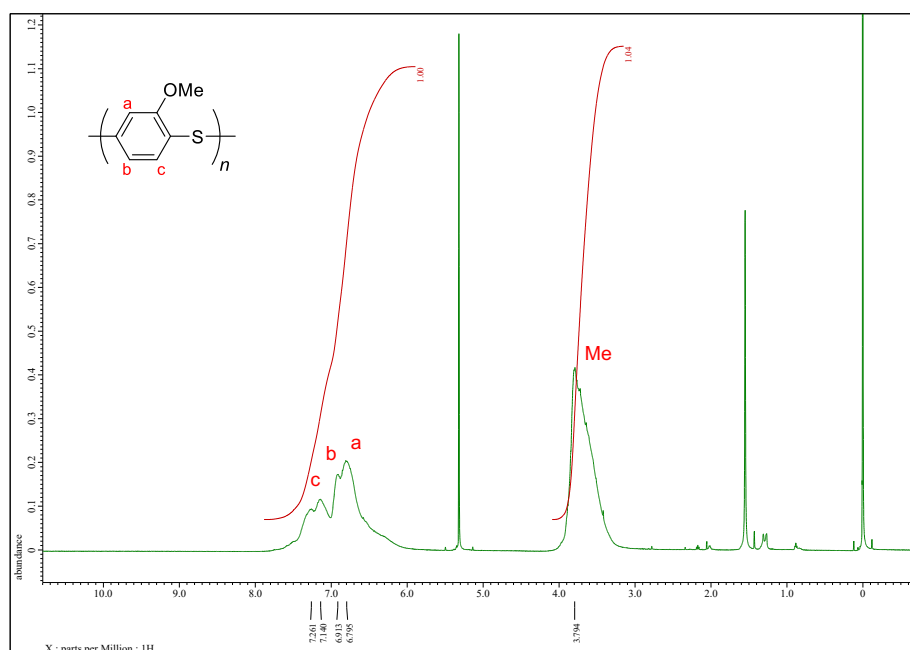


Figure 2.3. ^1H NMR spectrum of **OMePPS** in dichloromethane- d_2 .

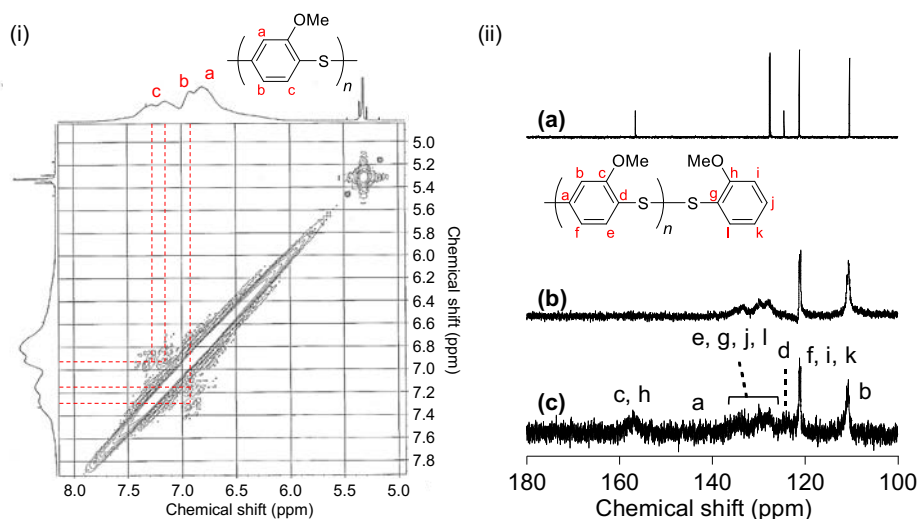


Figure 2.4. (i) ^1H - ^1H COSY spectrum (600 MHz) of **OMePPS** in dichloromethane- d_2 (expanded in the aromatic region). The correlation signals of protons “b” and “c” suggested that they are in *o*- positions. (ii) Expanded ^{13}C NMR spectra (125 MHz) of the aromatic carbons of (a) **OMeDPS**, (b) **OMePPS** (DEPT135) and (c) **OMePPS** in chloroform- d .

Structure of the resultant **OMePPS** was determined by spectroscopic analyses. First, linear 1,2,4-phenylene of **OMePPS** was identified from the IR spectrum bands at 800 and 900 cm^{-1} attributed to the aromatic C-H out-of-plane vibration of adjacent and isolated C-H bonds, respectively (**Figure 2.2a**). Other absorption peaks of the polymer at 750 and 840 cm^{-1} were the C-H out-of-plane vibration of the C-H bonds of the end aromatic rings (*o*-substituted phenylene), which were also identical in the IR spectrum of **OMeDPS** (**Figure 2.2b**). In the ^1H NMR spectrum, multimodal peaks (at 7.26, 7.14, 6.91, 6.80 ppm) in the aromatic region and a single broad peak (at 3.79 ppm) of the methoxy protons were observed with the peak integral ratio of 1:1, indicating that the polymer contained no branched (i.e., multi-substituted) structure (**Figure 2.3**). Focusing on peaks of aromatic carbons, in ^1H - ^1H COSY spectrum correlation signals between proton nuclei were observed only at three peaks at 7.26, 7.14 and 6.91 ppm, thus these aromatic protons were in *o*-position. As no correlation with other protons were observed at the peak in the upfield (6.80 ppm), this peak can be assigned as an isolated proton (**Figure 2.4a**). These results explain that the polymer had a 2-methoxy-1,4-phenylene repeating unit, because if phenylene sulfide unit was substituted in other positions (*o*- or *m*- positions of sulfide), the peak of the isolated aromatic proton should appear in the downfield. ^{13}C and ^{13}C DEPT NMR spectra also supported the existence of three aromatic C-H and three quaternary carbons, and those peaks except for 4-position were also observed at almost the same chemical shifts in the spectrum of **OMeDPS** (**Figure 2.4b**). Summarizing the above spectroscopic results, the polymer can be assigned as poly(2-methoxy-1,4-phenylenesulfide) (**OMePPS**).

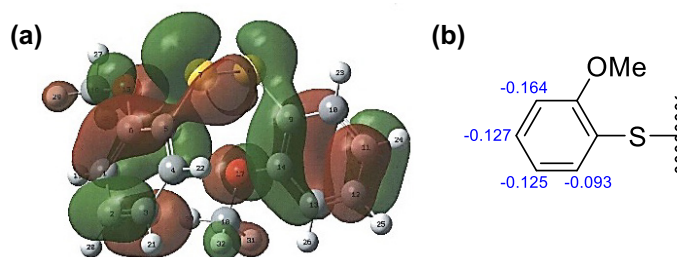


Figure 2.5. DFT calculation results of the monomer at wB97XD/6-31G(d,p) level of theory. (a) HOMO shape of **OMeDPS**. (b) Mulliken charges of aromatic carbons of **OMeDPS**.

We also examine the polymerization mechanism from mechanistic perspectives by density functional theory (DFT) calculations in order to confirm the regioselectivity. As oxidative polymerization proceeds via the Friedel-Crafts reaction, whose selectivity is dominated by electrophilic attack between the highest occupied molecular orbital (HOMO) of the disulfide monomer or the oligomer and the lowest unoccupied molecular orbital (LUMO) of the sulfonium cation, the HOMO distribution and the charge distribution for the **DPS** monomer suggest the reactive position of the aromatic carbons.^[3,44] The structure optimization was conducted for **OMeDPS** at the ω B97XD/6-31G(d,p) level of theory (**Figure 2.5**). HOMO of the monomer localized in 4- and 5-positions of the disulfide, indicating carbon atoms in these positions can be electrophilically attacked by the sulfonium cation. Slightly larger Mulliken charge on the aromatic ring at 4-position than at 5-position gave rise to the selective substitution at the 4-position, which also suggested the results of the spectroscopic analyses.

2.3 Optical Properties of Methoxy-substituted Phenylenesulfide Polymers

2.3.1 Crystalline and Thermal Properties

OMePPS represented amorphous features, confirmed from the absence of crystalline peaks in the XRD profile and single glass transition in the range of $T_g = 105\text{--}132\text{ }^\circ\text{C}$ from the DSC thermograms (**Figure 2.6a**). TGA trace showed excellent thermal stability with high thermal decomposition temperature ($T_{d5} = 329\text{ }^\circ\text{C}$) (**Figure 2.6b**). In contrast to the alkyl-substituted PPSs, which were soluble in such as chloroform, dichloromethane, tetrahydrofuran (THF) and NMP, **OMePPS** was soluble in not only these solvents but also polar amide solvents such as *N,N*-dimethylformamide (DMF) and *N,N*-dimethylacetamide (DMAc) ascribed to the polarizability of its side methoxy group.

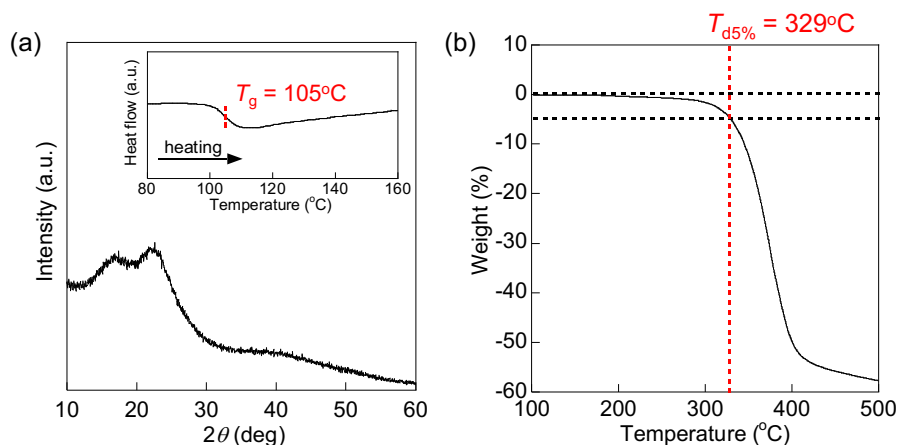


Figure 2.6. Crystalline and thermal properties of **OMePPS**. (a) X-ray diffraction (XRD) profile (powder, $\text{CuK}\alpha$) (Inset: DSC curve of **OMePPS** (Run 2 in **Table 2.1**), scan rate: $20\text{ }^\circ\text{C min}^{-1}$). (b) TGA trace (scan rate: $10\text{ }^\circ\text{C min}^{-1}$).

2.3.2 Optical Properties

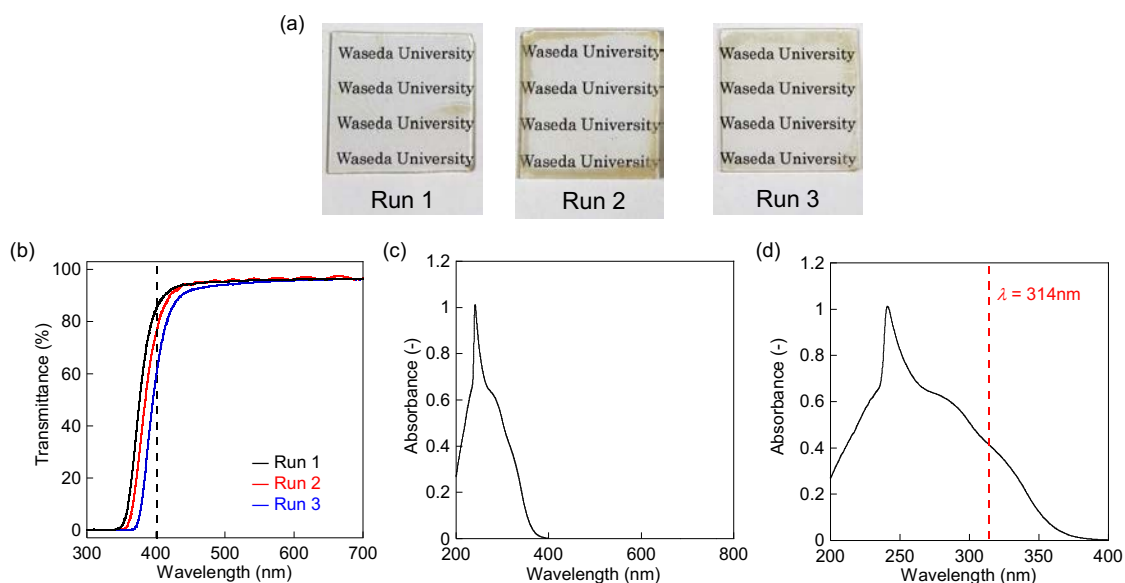


Figure 2.7. Absorption properties of **OMePPS**. (a) **OMePPS** thin films with varied thickness (thickness: $4.7\text{ }\mu\text{m}$, $7.0\text{ }\mu\text{m}$, $12.8\text{ }\mu\text{m}$ for Run 1, 2, and 3, respectively). (b) UV-vis spectra of the **OMePPS** films. (c, d) UV-vis absorbance spectra of **OMePPS** (0.1mM solution in chloroform): (c) entire, (d) expanded wavelength region.

Based on the amorphous property of **OMePPS**, its transparent and homogeneous thin film was prepared via dropcasting its solution in DMAc at $50\text{ }^\circ\text{C}$ onto the glass substrate in vacuo to investigate the optical properties (**Figure 2.7a**). **Figure 2.7b** shows excellent visible transparency with $76\%T$ for $7.0\text{ }\mu\text{m}$ thickness, which can be normalized as $96\%T$ with a $1\text{ }\mu\text{m}$ thick-film.

Figure 2.7c and 2.7d shows UV-vis absorbance spectrum of **OMePPS** solution in chloroform, and the wide absorption was observed in the range of 300–390 nm ascribed to the the shoulder peak at 314 nm, estimated as the HOMO-LUMO transition of **OMePPS**. The presence of methoxy group having lone pairs, which was directly substituted to the aromatic ring, presumably contributed to the lengthening of conjugation length. Absorptivity of **OMePPS** in the film state was calculated as $1.7 \times 10^2 \text{ cm}^{-1}$ from **Figure 7b**, which was smaller than that of thianthrene-based PPS^[45] (calculated as $7.6 \times 10^2 \text{ cm}^{-1}$). For improving transparency, a polymer skeleton with shorter conjugation length (i.e. larger HOMO-LUMO bandgap) should be required by controlling orbitals around the sulfide atoms by chemical oxidation.^[46] RI of **OMePPS** was determined as $n_D = 1.73$ by spectroscopic ellipsometry, higher than the calculated value from the Lorentz-Lorenz equation ($n_{D, \text{calc}} = 1.68$) (note that the spectrum was shown in the latter section 2.4.2). In the **OMePPS** film, high refractive units were arranged in high density induced by strong interactions among the polymer chains notwithstanding its amorphous nature. These interactions were probably attributed to the intermolecular interactions between main chain aromatics or side methoxy groups. The Abbe number of **OMePPS** were high ($\nu_D = 22$) compared to the empirical n_D - ν_D trade-off^[47] owing to the small dispersion of ether ($[\Delta R]_{-O} = 0.012$) than alkyl carbons ($[\Delta R]_{>C} = 0.025$, $[\Delta R]_{-CH_2} = 0.072$) or hydrogen ($[\Delta R]_H = 0.023$).^[28] Considering few polymers with both high n_D (>1.70) and ν_D (>20) were reported,^[48] **OMePPS** showed the balanced optical properties achieving both high RI and Abbe number simultaneously.

2.3.3 Nanohybridization of Methoxy-substituted PPS with TiO₂

Next, hybrid film of **OMePPS** with TiO₂ was subsequently prepared. Upon the hybridization, the *in-situ* sol-gel route was adopted for its facile preparation method, irrelevance of adding dispersant except for the polymer itself.^[39] Following the previous report,^[45] DMAc was used as a cosolvent for the polymer and TiO₂ precursors for obtaining transparent hybrid films. The hybrid film with 10 wt% of TiO₂ was transparent, and its TEM image revealed well dispersity of TiO₂ particles in the size range of 20-100 nm (**Figure 2.8a, 2.8b**). On using poly(2,6-dimethyl-1,4-phenylenesulfide) (**PMPS**) as an alternative polymer matrix, the hybrid film was inhomogeneous and opaque accompanying the unsuccessful dispersion of TiO₂ into the polymer matrix (**Figure 2.8c**). Therefore, a key for such well affinity of **OMePPS** with TiO₂ is the oxygen atom of methoxy side group, which is more polar and represents higher solubility than the alkyl substituents to obtain the transparent films. Absorptivity of **OMePPS**/TiO₂ (= 90/10 (w/w)) was calculated as $7.6 \times 10^2 \text{ cm}^{-1}$ (i.e., 84 %*T* with a normalized thickness of 1 μm), similar to that of thianthrene-based PPS^[45] (**Table 2.2**). RI was enhanced up to $n_D = 1.76$ upon the hybridization with TiO₂ (**Figure 2.8d**), representing effect of the TiO₂ loading.

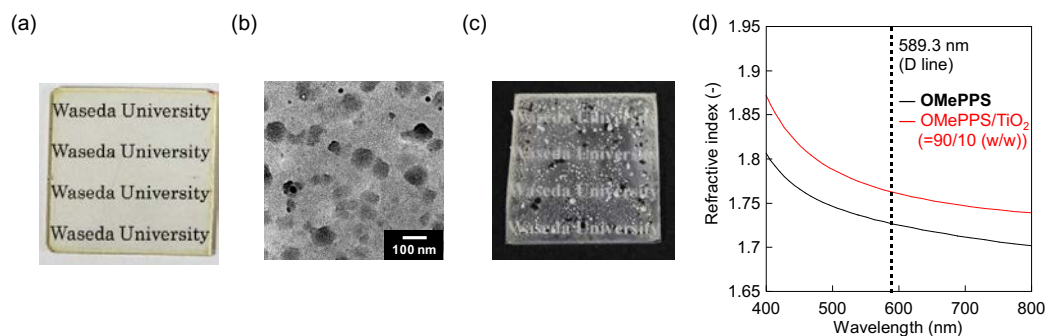


Figure 2.8. In situ sol-gel hybridization. (a) Photograph of **OMePPS**/ TiO_2 (=90/10 (w/w)) thin film. (b) TEM image of the hybrid film. (c) Photograph of **PMPS**/ TiO_2 (=90/10 (w/w)) thin film, whose preparation procedure was according to the previous report^[45] by replacing the solvent as THF (cosolvent for the polymer and the inorganic precursors). (d) Refractive indices of **OMePPS** and **OMePPS**/ TiO_2 (=90/10 (w/w)) hybrid film.

Table 2.2 Absorptivity of **OMePPS** and **OMePPS**/ TiO_2 hybrid film

Sample	$\%T^{\text{a}}$ at 400 nm	Abs. ^{a)} at 400 nm (-)	Absorptivity ^{b)} at 400 nm ($\times 10^2 \text{ cm}^{-1}$)
OMePPS	96	0.017 ^{c)}	1.7
OMePPS / TiO_2	84	0.075 ^{e)}	7.5
Thianthrene-based PPS	84 ^{d)}	0.076 ^{e)}	7.6

^{a)} Determined by UV-vis spectroscopy. Thickness of the film was normalized to 1 μm . ^{b)} Calculated by following equation: Absorptivity = Abs. / thickness. ^{c)} Calculated from **Figure 2.7**. ^{d)} Value from Ref. ^[45]. ^{e)} Calculated from the Lambert-Beer's Law approximating that no Fresnel reflection has been observed between the glass/film interface.

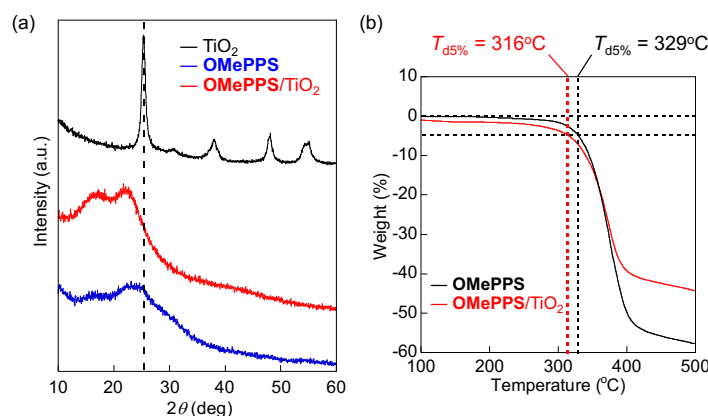


Figure 2.9. Crystalline and thermal properties upon hybridization. (a) XRD profiles of **OMePPS**, **OMePPS**/ TiO_2 (=90/10 (w/w)) hybrid, and TiO_2 prepared by sol-gel reaction according to the previous report.^[49] (b) TGA traces of **OMePPS** and **OMePPS**/ TiO_2 (=90/10 (w/w)) hybrid under nitrogen.

XRD profile of the hybrid film showed a new broad peak near $2\theta = 25.4$ deg (**Figure 2.9a**), which can be assigned as the diffraction at the (101) plane of anatase-type TiO_2 .^[49] The hybrid film showed slightly lower decomposition temperature ($T_{d5} = 316$ °C) than **OMePPS** ($T_{d5} = 329$ °C) that would be ascribed to the low processing temperature of the sol-gel reaction (**Figure 2.9b**). Also, Liou *et al.* reported the hydrothermal in situ sol-gel hybridization of polyimidethioether and TiO_2 or ZrO_2 that requires heat treatment at lower temperature (100 °C in maximum) in water atmosphere^[34], which also be suitable for low-temperature preparation of the polymer- TiO_2 (or ZrO_2) hybrid films.

2.4 End-modification of Poly(2-methoxy-1,4-phenylenesulfide) and Their Hybridization with Inorganic Nanoparticles

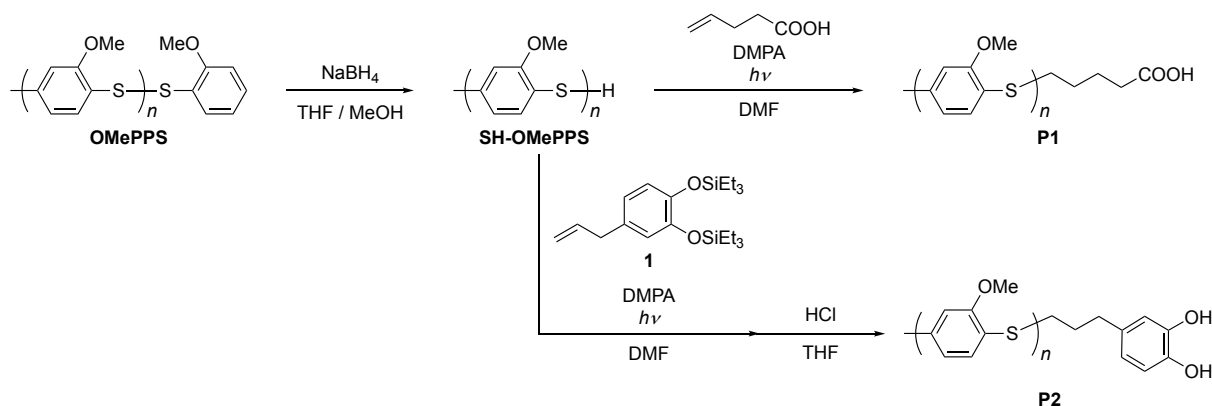
2.4.1 Post-polymerization Modification of Methoxy-substituted PPS

Based on the results for **OMePPS**/ TiO_2 hybrid films, further improvement for inorganic dispersibility (i.e., further homogeneity and smaller size of the inorganic nanoparticles) was conducted through introducing hydrophilic moiety at the terminus of the **OMePPS** chain. According to the Rayleigh scattering formula,^[29] hybrid materials based on dispersed inorganic NPs with a small size and a small difference in the refractive index between the components exhibit low scattering intensity. Therefore, particle size less than 40 nm should be ideally required for avoiding the optical loss from the light scattering to maintain sufficient film transparency,^[37,50,51] and polymers capable of dispersing larger amount of inorganic nanoparticles in even smaller size should be required.

One promising approach for preparing highly transparent hybrid materials with polymers and inorganic nanoparticles is to introduce substituents capable of coordination or forming covalent bonds with inorganic NPs, such as carboxyl and hydroxyl groups.^[37,50,51] Moreover, the author focused on the terminal functionalization as a suitable hybridization solution based on their minimum modification sites that can maintain excellent thermal/optical properties of polymers in contrast to the side-chain modification strategy. For example, Cheng *et al.* reported polyimide- TiO_2 nanohybrid materials with high TiO_2 content simply by introducing carbonyl groups to both terminal of the polymer.^[52] Upon introducing adequate amount of suitable dispersible groups into the polymer, the polymer show higher affinity with the inorganic NPs to afford highly transparent and more refractive films. From this perspective, PPS derivatives obtained by oxidative polymerization can be subjected to the further post-polymerization modification through reducing the disulfide bond in the **OMePPS** chain and the subsequent thiol-involved click reaction to afford end-functionalized PPS with high selectivity and functional group tolerance.^[44,53]

This section focused on the catechol (1,2-dihydroxybenzene) terminal group, which is known as a partial structure of 3,4-dihydroxy-L-phenylalanine (L-Dopa) that compose mussel adhesive proteins. Catechol unit displays unique redox properties and strong adhesiveness with various substrates owing to the bidentate coordination ability, dimerizing behavior, and hydrogen bonding (H-bonding).^[54-56] To date, various bio-inspired catechol-containing adhesive polymers have been reported,^[57,58] in addition

to multifunctional polymers combining adhesiveness and other properties such as thermal stability,^[59] water repellency,^[60] and amphiphilicity.^[61] Catechol groups can also form complexes with inorganic metal oxide particles, and several catechol-intervened organic-inorganic hybrid materials have also been reported.^[62,63] Anticipating that the dispersivity of the inorganic nanoparticles of PPS derivatives could be enhanced by simply introducing a small amount of catechol groups, catechol end-terminated derivatives were synthesized without any deterioration of the characteristic polymer properties derived from the phenylenesulfide chain (e.g. thermal stability, solubility, and refractive index) while representing even higher inorganic NP dispersivity.



Scheme 2.2. End-modification of **OMePPS** using the disulfide end.

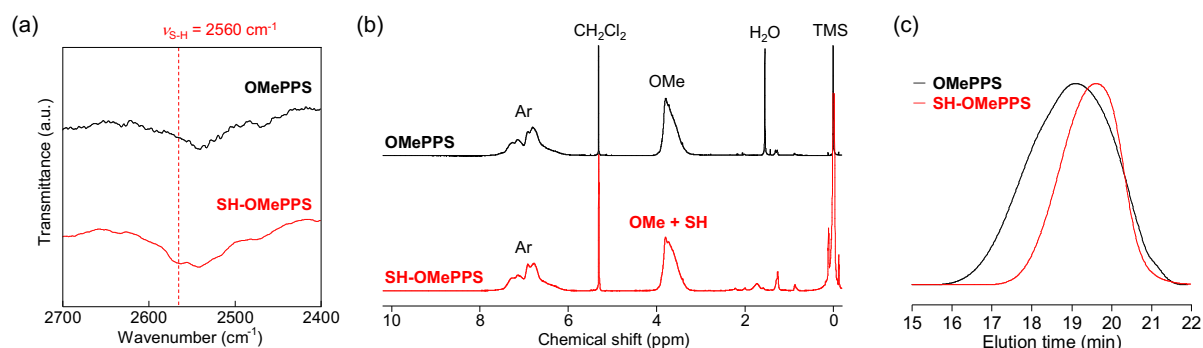


Figure 2.10. Disulfide reduction of **OMePPS**. (a) Expanded IR spectra of **OMePPS** and **SH-OMePPS** (2700-2400 cm^{-1}). (b) ^1H NMR spectra of **OMePPS** and **SH-OMePPS**. Introduction ratio of the end thiol group was calculated by comparing integral ratio of the peaks corresponding to the aromatic protons and the peaks in 3-4 ppm. (c) SEC chromatograms of **OMePPS** and **SH-OMePPS** (Eluent: chloroform).

The post-polymerization modification of **OMePPS** was conducted as follows: (1) disulfide reduction of **OMePPS** and (2) subsequent thiol-ene reaction and deprotection reaction (if necessary). In the first step, disulfide bond of **OMePPS** was selectively reduced with sodium borohydride (NaBH_4) in THF/methanol mixture to afford thiol-terminated **OMePPS** (**SH-OMePPS**) (Scheme 2.2). The reaction

proceeded successfully, which was confirmed by the absorption band of the S-H vibration ($\nu_{\text{S-H}}$: 2560 cm^{-1}) for **SH-OMePPS** (**Figure 2.10a**). Molecular weight of **SH-OMePPS** was determined as $M_n = 2.3 \times 10^3$ from the ^1H NMR spectrum by comparing integral values for the aromatic, methoxy and thiol protons (**Figure 2.10b**). The M_n values of **OMePPS** and **SH-OMePPS** were estimated as 3.4×10^3 and 2.7×10^3 respectively from the SEC elution curves, where the latter value was mostly in agreement with that obtained from the ^1H NMR spectrum, while the M_w value was noticeably decreased from 7.2×10^3 to 4.2×10^3 upon reduction (**Figure 2.10c**), indicating that the disulfide bond in the high molecular-weight component of **OMePPS** was not always at the end of the polymer chain. This was because of the stepwise behavior of oxidative polymerization of methoxy-substituted DPS (**OMeDPS**) with DDQ, which was supported by the polydispersity index (PDI) of the obtained product ($M_w/M_n = 2.2$). In summary, thiol-terminated **OMePPS** was quantitatively obtained without any side reactions.

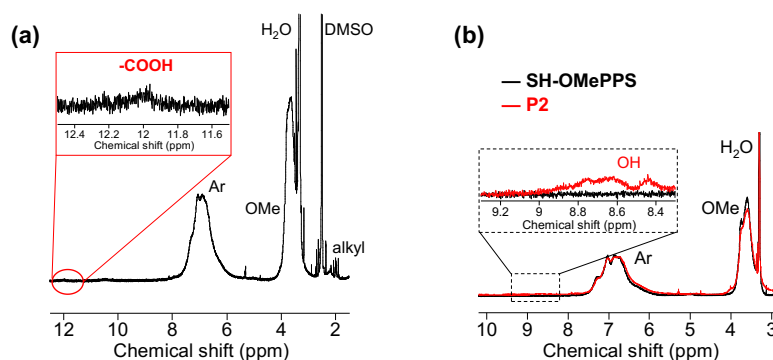


Figure 2.11. ^1H NMR spectra of (a) **P1** and (b) **P2** in $\text{DMSO-}d_6$. End functionality of the polymer was determined by comparing the integral values of the signals for the aromatic protons and terminal (carboxyl or catechol group) protons.

Table 2.3 Thiol-ene End Functionalization of **SH-OMePPS**

Sample	Yield ^{a)} (%)	End Functionality (%)	M_n ^{b)} ($\times 10^3$)	M_w ^{b)} ($\times 10^3$)	M_w/M_n ^{b)} (-)	T_g ^{c)} ($^{\circ}\text{C}$)	n_D ^{d)} (-)	ν_D ^{d)} (-)
SH-OMePPS	-	-	2.8	4.2	1.5	128	1.73	22
P1	78	93	2.8	5.6	2.0	128	1.72	21
P2	80	68	2.9	6.1	2.1	136	1.73	20

^{a)} Yield for **SH-OMePPS**. ^{b)} Determined by SEC in chloroform. ^{c)} Determined by DSC. ^{d)} Determined by spectroscopic ellipsometry.

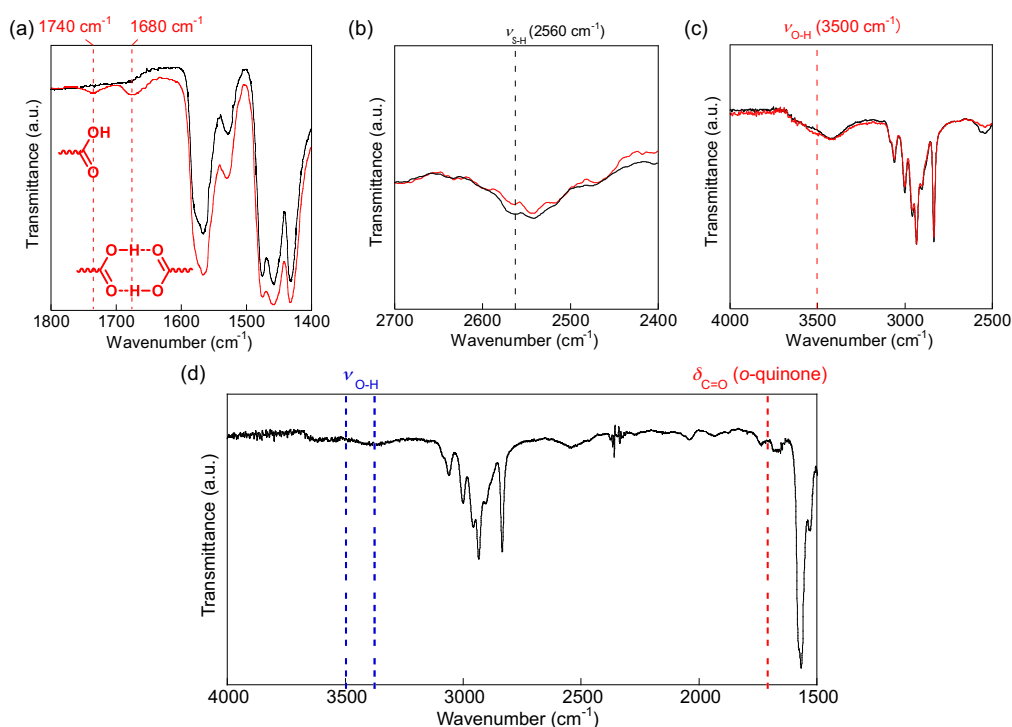


Figure 2.12. IR spectra of (a) **SH-OMePPS** (black) and **P1** (red), (b) (c) **SH-OMePPS** (black) and **P2** (red). For each spectrum, the specific bands for the terminal structures were detected. (d) Overall IR spectrum of **P2**. The absence of $\nu_{C=O}$ band for *o*-quinone (1710 cm^{-1}) indicates that the catechol moiety of **P2** was not oxidized.

Next, End-functionalized **OMePPS** with carboxylic acid (**P1**) or catechol (**P2**) have been synthesized via the radical-type photoinduced thiol-ene reactions between the end thiol group of **SH-OMePPS** and the corresponding vinyl compounds (4-pentenoic acid or silyl-protected catechol ene **1**).

The carboxyl moiety was quantitatively introduced without protection, whereas the catechol group was protected because of its radical inhibition properties. Regarding the introduction of catechol terminus, thiol-ene reaction of **SH-OMePPS** with **1** and subsequent mild deprotection with hydrochloric acid was conducted to afford catechol-terminated **OMePPS** (**P2**).^[64,65] Peaks corresponding to the carboxylic acid and catechol units were observed in the ¹H NMR spectra after the functionalization (**Figure 2.11a, 2.11b**). The end functionality with the catechol unit was slightly lower than that with the carboxyl unit presumably because of the low reactivity of **1** and **SH-OMePPS**, as **1** was soluble in DMF but slight light scattering could be observed, suggesting the formation of colloidal particles of the polymer (**Table 2.3**). M_n values of the polymers increased after the thiol-ene reaction in proportion to the molecular weights of the end groups, whereas the M_w increased much more significantly (**Table 2.3**). This result indicates that the end carboxyl or catechol groups associated in diluted low-polarity solution and the polymers partially existed in a dimeric state. The IR spectra of the end-functionalized polymers also indicated the success of the thiol-ene reactions from the absence of the peaks corresponding to the S-H vibration mode (**Figure 2.12**). **P1** existed in both monomeric and dimeric states (i.e., the end

carboxyl groups partially associated in the bulk state), as confirmed by two IR absorption peaks at 1740 and 1680 cm^{-1} (**Figure 2.12a**). In the case of **P2**, the appearance of a new shoulder peak at 3500 cm^{-1} corresponding to the O-H vibration of the catechol moiety indicated the association of two catechol groups via hydrogen bonding (**Figure 2.12b**). The *o*-quinone structure (1710 cm^{-1}), corresponding to the oxidated state of the catechol unit, was not observed in the IR spectrum of **P2** (**Figure 2.12c**).^[66]

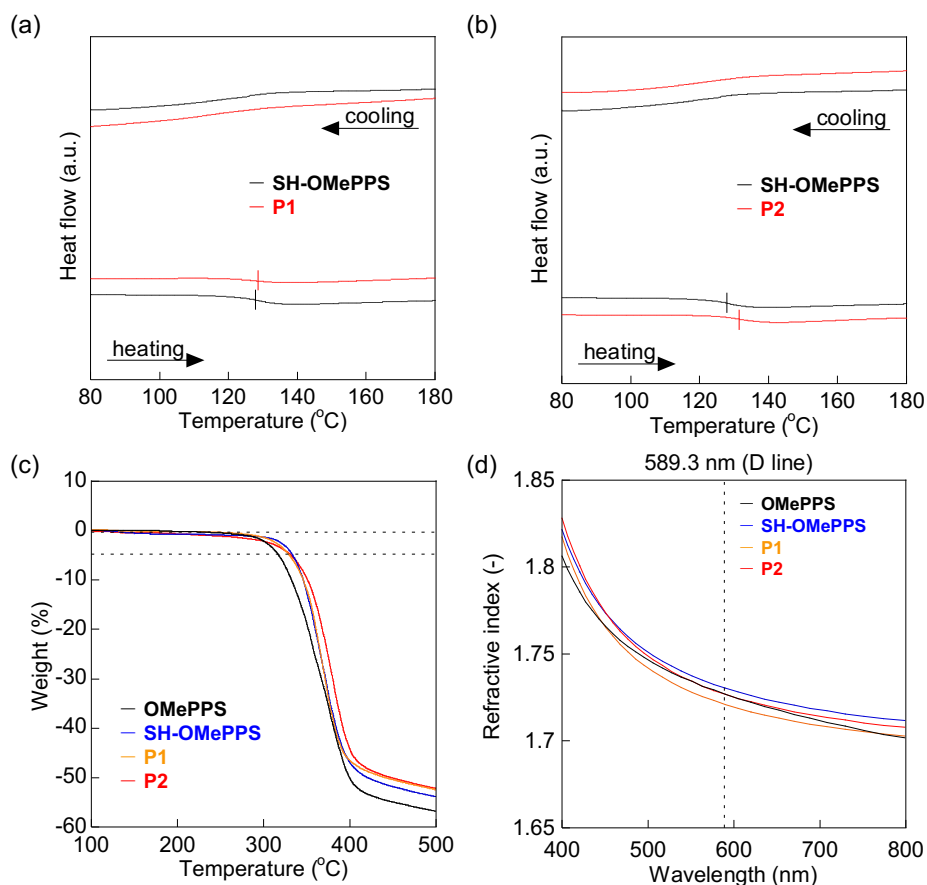


Figure 2.13. Thermal and optical properties of the end-functionalized **OMePPS**. (a) DSC thermograms of **SH-OMePPS** and **P1**. (b) DSC thermograms of **SH-OMePPS** and **P2**. (c) TGA traces. (d) Refractive indices.

Thermal and optical properties before and after the end-functionalization were subsequently compared. T_g of the functionalized polymer was similar to that of **SH-OMePPS** in the case of **P1**, whereas it slightly increased in the case of **P2**. The introduced hydrogen bonding moieties at the terminus strengthened the chain packing after the end-functionalization (**Figure 2.13a**, **2.13b**). The thermal decomposition temperatures (T_{d5}) of **SH-OMePPS**, **P1**, and **P2** were higher than that of **OMePPS** prior to disulfide reduction (**Figure 2.13c**). As PPS derivatives synthesized via oxidative polymerization undergo thermal decomposition below 250 $^{\circ}\text{C}$ due to the disulfide bond cleavage,^[67] the reduction of disulfide including the subsequent thiol-ene reaction effectively enhanced thermal stabilities. Solubility of the polymers remained unchanged before and after the end-functionalization,

and thin films of the functionalized polymers could also be fabricated via wet-processing (dropcasting or spin coating). Both RI and Abbe number remained similar, particularly with the RI values exceeding 1.7 (**Figure 2.13d**). These results demonstrate that various substituents can be quantitatively introduced at the end of the polymer chain, without affecting any deterioration in thermal and optical properties.

2.4.2 In Situ Hybridization of the End-functionalized Derivatives

Table 2.4. Hybridization of End-Functionalized **OMePPS** with TiO_2 and ZrO_2

Run	Polymer	Additive	Inorganic content				$T_g^{d)}$ (°C)	Thick- ness ^{e)} (mm)	$\%T^f)$		
			Theo (wt%)	Exp ^{b)} (wt%)	Theo ^{c)} (vol%)	Exp ^{b)c)} (vol%)			at 400 nm	$n_D^g)$ (-)	$\nu_D^g)$ (-)
Initial		-	-	-	-	-	128	4.4	92	1.72	21
1		TiO_2	10	12	4	5	125	5.5	80	1.77	18
2	P1	TiO_2	30	28	14	13	136	4.7	86	1.80	19
3		ZrO_2	10	14	3	4	135	4.4	91	1.75	19
4 ^{a)}		ZrO_2	30	-	10	-	-	-	-	-	-
Initial		-	-	-	-	-	136	3.6	90	1.73	20
5		TiO_2	10	9	4	4	134	5.3	52	1.78	15
6	P2	TiO_2	30	24	14	10	149	4.2	58	1.84	7
7		ZrO_2	10	11	3	4	138	4.7	82	1.78	17
8		ZrO_2	30	29	10	10	143	6.5	81	1.82	18

^{a)} Hybrid film was not be obtained due to the gelation of the hybrid precursor solution. ^{b)} Determined by TGA in air atmosphere. ^{c)} Calculated values assuming that the inorganic domains was fully converted during the in situ sol-gel process. ^{d)} Determined by DSC. ^{e)} Determined by stylus profiler. ^{f)} Determined by UV-vis spectroscopy. Thickness of the film was normalized to 1 μm . ^{g)} Determined by spectroscopic ellipsometry.



Figure 2.14. (a) Thin films of **OMePPS** with 20 wt% TiO_2 , **P1** and its hybrid films (Runs 1-3 in Table 2.4), and **P2** and its hybrid films (Runs 5-8 on glass substrates. (b) Precursor solution for **P1** with (a) 10 wt% ZrO_2 hybrid (Run 3 in Table 4) and (b) 30 wt% ZrO_2 hybrid (Run 4 in Table 4) after stirring at r.t.

The hybrid films of **P1** or **P2** with TiO₂ or ZrO₂ NPs were prepared via *in situ* sol-gel route with the similar procedure as the case for section 2.3.3 (Table 4). The obtained hybrid films were visually transparent even at 30 wt% inorganic content, whereas hybrid films of the non-functionalized **OMePPS** with TiO₂ became opaque even with only 20 wt% of TiO₂ loadings (**Figure 2.14a**). **P1** and **P2** showed more hydrophobicity than non-functionalized **OMePPS** that can effectively enhance the inorganic NP dispersivity of the polymers achieving nanodispersion of large amount of the inorganic NPs. In the case of hybridization with 30 wt% ZrO₂, the precursor solution with **P1** was transparent but that with **P2** underwent gelation and became cloudy (**Figure 2.14b**), indicating that the catechol group afforded greater dispersivity as well as larger binding strength with the TiO₂ NPs than the carboxyl group.^[67] Such difference was attributed to better stability of catechol moieties with TiO₂ that can prevent agglomeration of the NPs in the precursor and during the film fabrication steps.^[67]

The IR spectra of the hybrid films confirmed the sol-gel hybridization progress based on the absorptions originating from the inorganic NPs ($\nu_{\text{Ti-O-Ti}}$ or $\nu_{\text{Zr-O-Zr}} = 650 \text{ cm}^{-1}$) (**Figure 2.15**). The contents of the inorganic NPs were experimentally determined from the TGA traces in air, which were almost identical to the calculated values (**Figure 2.16**). DSC measurements were conducted to further investigate the compatibility of **P1** or **P2** and inorganic NPs in the hybrid films (**Figure 2.17**). Similar or higher T_g values were observed upon the hybridization, indicating that the interactions between polymer-inorganic domains were enhanced through the partial immobilization of the polymers onto the NP surface, suppressing the decrease in T_g .

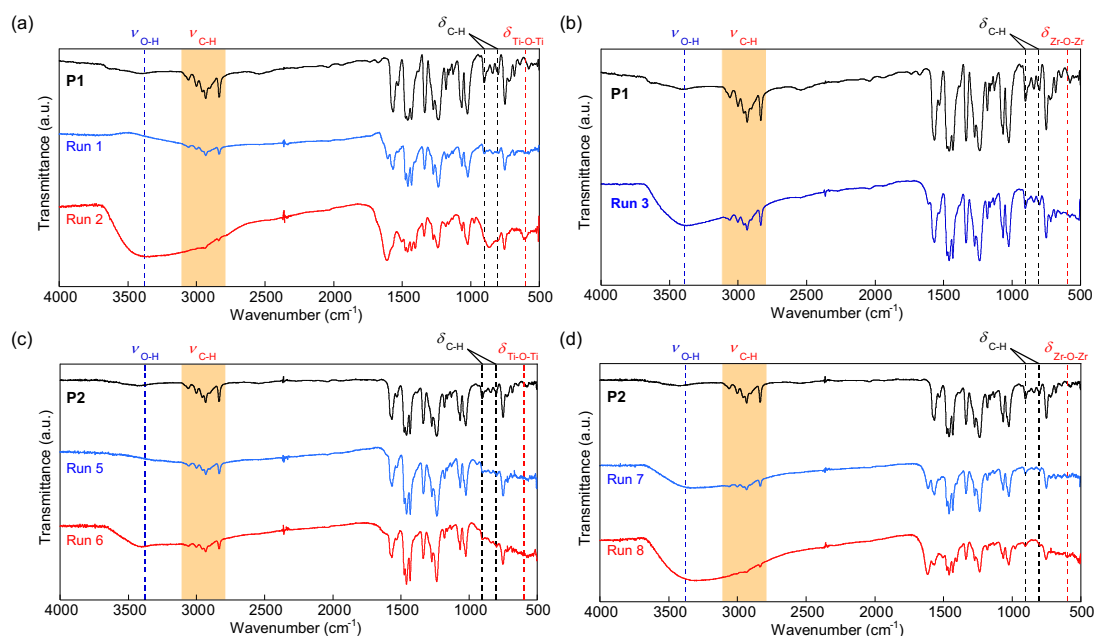


Figure 2.15. IR spectra of end-functionalized polymers their hybrid films. (a) **P1**, Run 1, and Run 2. (b) **P1** and Run 3. (c) **P2**, Run 5, and Run 6. (d) **P2**, Run 7, and Run 8.

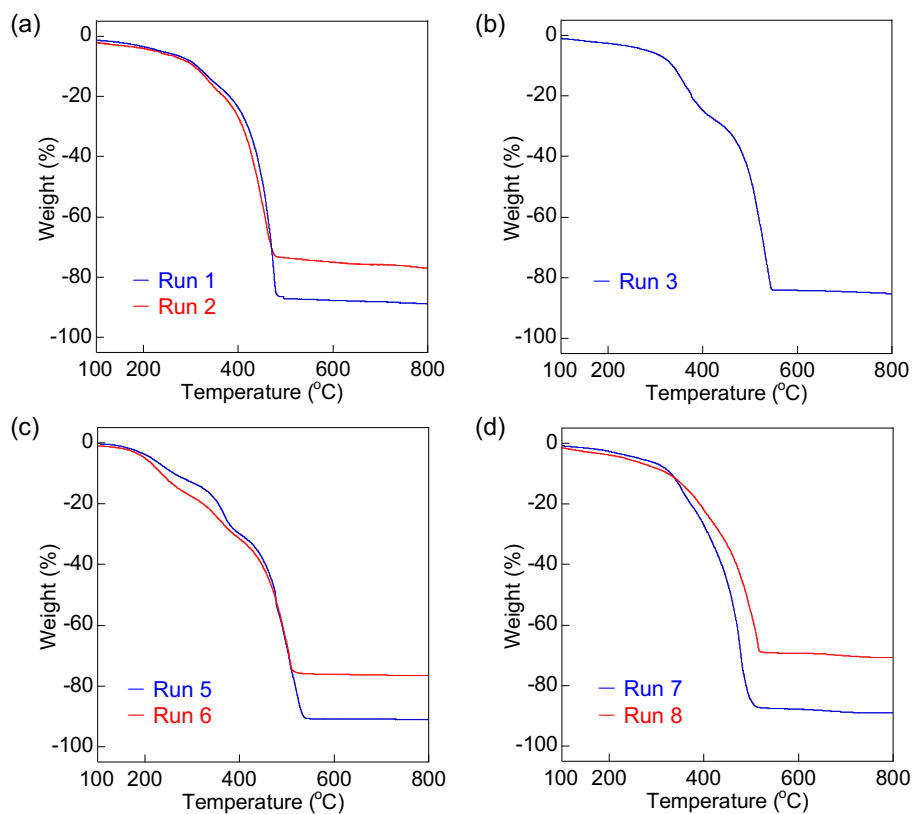


Figure 2.16. TGA traces of the hybrid films in air atmosphere: (a) Run 1 and Run 2. (b) Run 3. (c) Run 5 and Run 6. (d) Run 7 and Run 8.

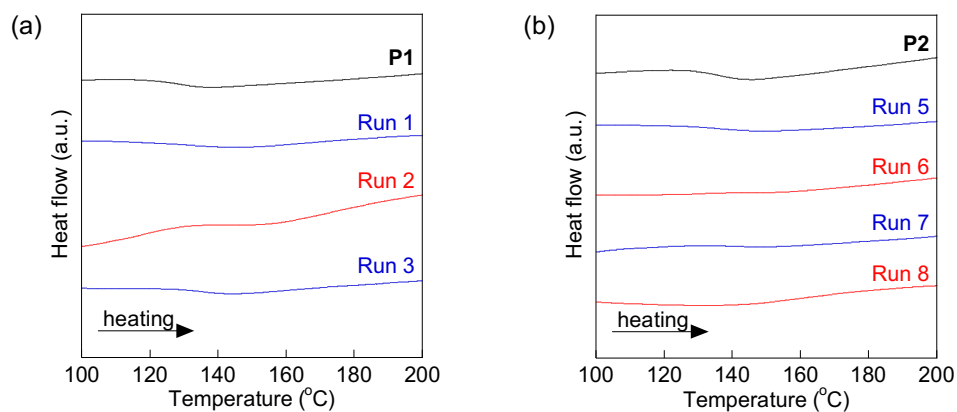


Figure 2.17. DSC curves of (a) P1 and Runs 1-3, (b) P2 and Runs 5-8 (scan rate: $20\text{ }^{\circ}\text{C min}^{-1}$).

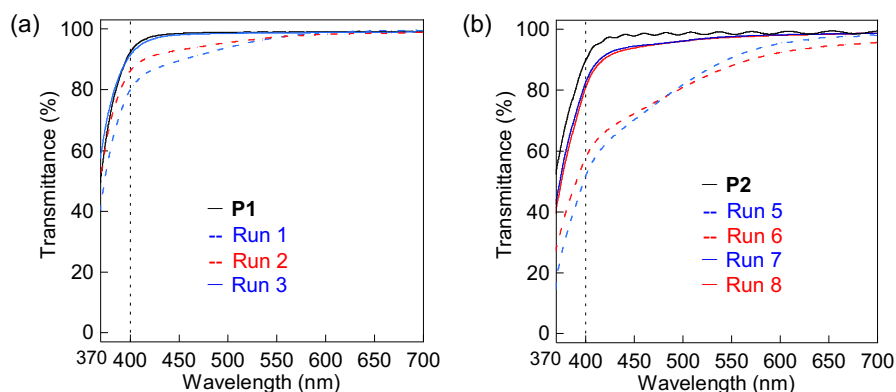


Figure 2.18. Normalized UV-vis spectra of **P1**, **P2** and their hybrid films with TiO₂ or ZrO₂: (a) **P1** and Runs 1-3, (b) **P2** and Runs 5-8. Thickness of the films were normalized to 1 μm.

Figure 2.18 shows the UV-vis transmittance spectra of **P1**, **P2** and hybrid thin films with a normalized thickness of 1 μm. The hybrid films with TiO₂ exhibited low transparency and appeared reddish, owing to the coordination of the catechol onto the surface of the TiO₂ NPs that lowered the bandgap. Although the UV-vis spectrum of catechol itself contained no significant absorption bands in the >300 nm region, peaks corresponding to the interaction between catechol and TiO₂ were observed at 390 nm (shoulder) and 600 nm (edge) according to the previous report.^[69] Considering that the bandgap of anatase-type TiO₂ is 3.2 eV (optical wavelength of 388 nm), the former shoulder peak was ascribed to the absorption of TiO₂ that was red-shifted upon the coordination with catechol moieties.^[68] The latter edge was not observed for pure TiO₂,^[69] which also suggested the remarkable coloration of the hybrid films attributed to this absorption that were ascribed to the new charge transfer interactions between the interface upon complexation. Furthermore, the hybrid films of **P1** displayed higher transparency compared with those of **P2**. As carboxyl group coordinates TiO₂ in a bidentate manner with a concomitant redshift in the absorbance of TiO₂, but other specific absorption bands in the visible region (> 400 nm) have not been reported.^[40] Therefore, carboxyl groups are more effective than catechol group for attaining good transparency, despite its lower binding ability to the inorganic nanoparticles. On using ZrO₂ as a hybridized counterpart for **P1** and **P2**, transparency of the hybrid films were improved, and especially, **P2**/ZrO₂ hybrid film displayed similar transparency to the **P1**/TiO₂ films (see Runs 1, 2, 7, and 8 in **Table 4** and **Figure 2.18**).

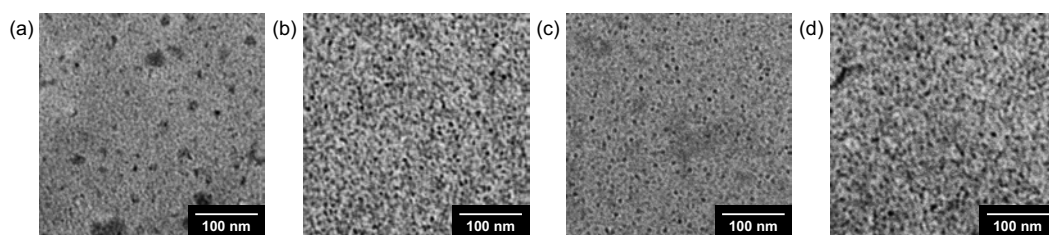


Figure 2.19. TEM images of hybrid films with 10 wt% TiO₂ or ZrO₂: (a) Run 1, (b) Run 3, (c) Run 5, and (d) Run 7 in **Table 2.4**.

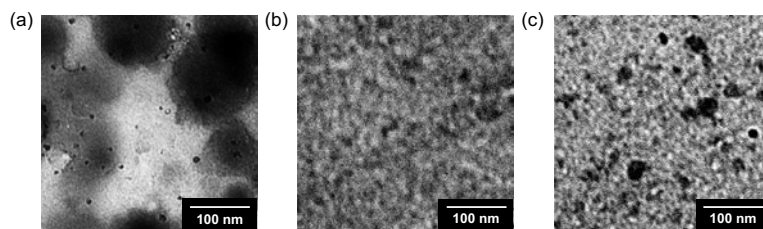


Figure 2.20. TEM images of the hybrid films with 30 wt% TiO_2 or ZrO_2 : (a) Run 2, (b) Run 6, and (c) Run 8 in Table 2.4.

Dispersivity of the inorganic NPs were investigated from the TEM images (Figure 2.19 and 2.20). For run 8 in Table 4 ($\text{P2}/30\text{wt}\%$ ZrO_2), dispersed ZrO_2 NPs with the size of > 30 nm were observed with slight inhomogeneity, suggesting the partial aggregation of the NPs within the range that did not affect the film transparency (Figure 20c). In contrast, aggregation of TiO_2 with particle sizes of > 100 nm was observed for Run 2 ($\text{P1}/30\text{wt}\%$ TiO_2) that also held the poor dispersivity of the inorganic NPs of **P1** (Figure 2.20a). Summarizing such results, aggregation of the NPs were not fully prevented and was observed due to the several factors: (1) lack of terminal reactive groups contributable to poor dispersivity. (2) excess number of inorganic NPs unable to be fully modified by the catechol terminus. Moreover, as number of the terminal groups were limited based on the polymer chain length, effect of molecular weight on the dispersivity should be taken into account for further discussions (i.e. small molecular weight leads to high catechol concentration).

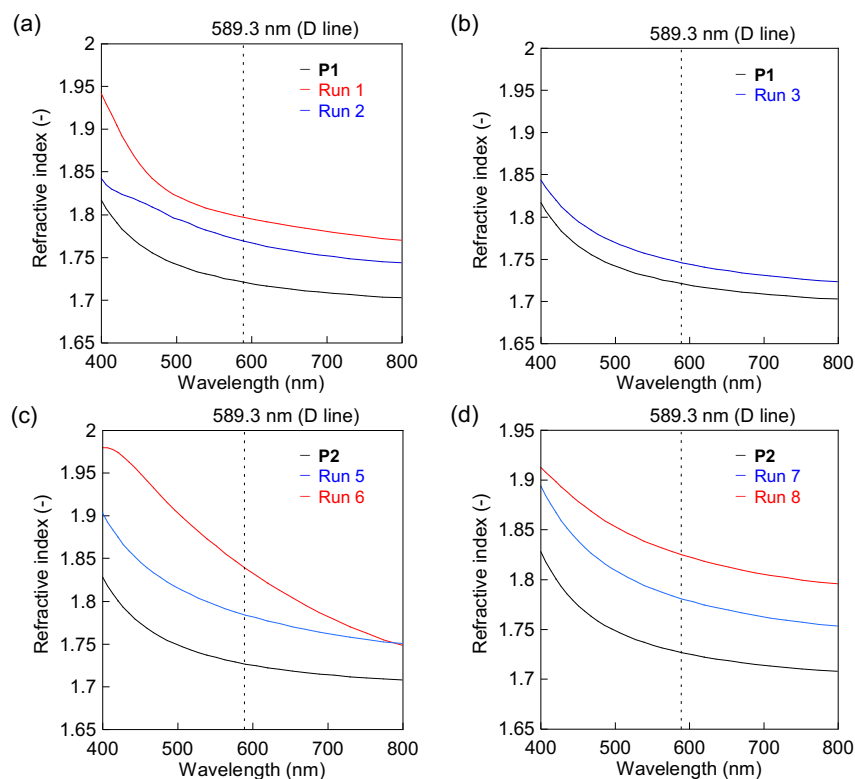


Figure 2.21 RI of **P1**, **P2**, and their hybrid films: (a) **P1** and **P1**/ TiO_2 (Runs 1 and 2), (b) **P1** and **P1**/ ZrO_2 (Run 3), (c) **P2** and **P2**/ TiO_2 (Runs 5 and 6), and (d) **P2** and **P2**/ ZrO_2 (Runs 7 and 8).

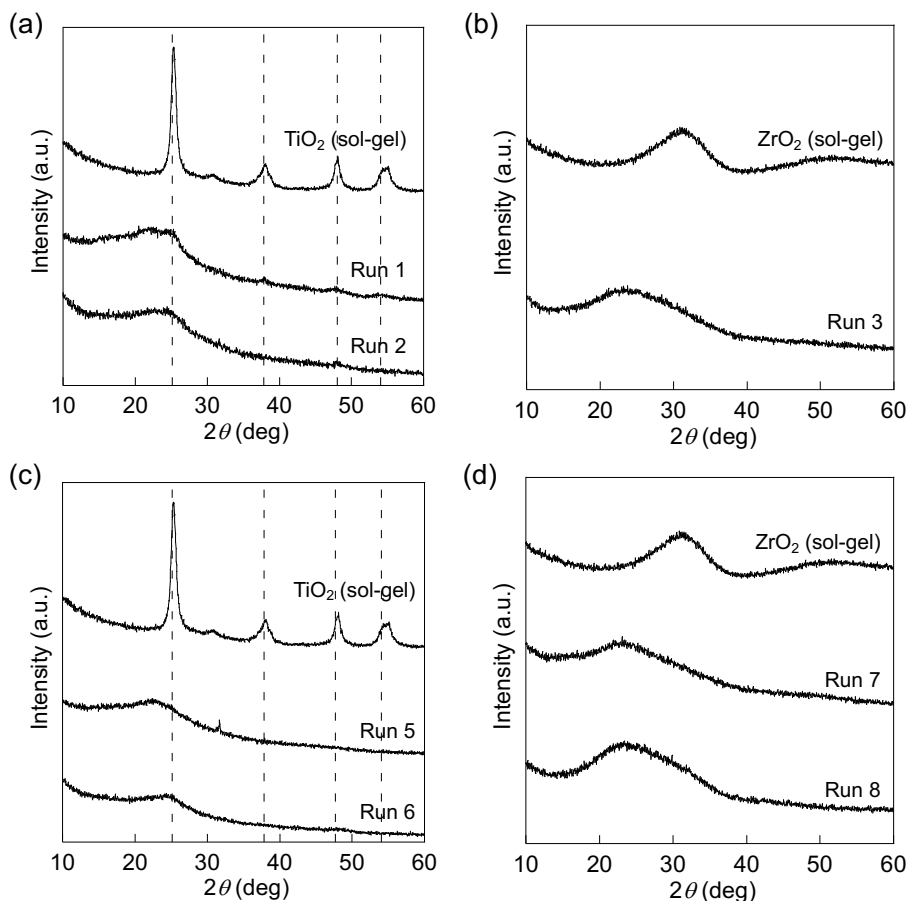


Figure 2.22. X-ray diffraction patterns of TiO₂, ZrO₂, and their hybrid films with **P1** or **P2**: (a) TiO₂ and **P1**/TiO₂ (Runs 1 and 2), (b) ZrO₂ and **P1**/ZrO₂ (Run 3), (c) TiO₂ and **P2**/TiO₂ (Runs 5 and 6), and (d) ZrO₂ and **P2**/ZrO₂ (Runs 7 and 8).

Figure 2.21 shows the RI spectra for the hybrid films. Despite the slightly lower RI of ZrO₂ than TiO₂, hybridization with ZrO₂ is more effective than with TiO₂ for simultaneously achieving various excellent optical properties, such as high Abbe numbers and high visible transparency while maintaining moderately high RI values. In the case of TiO₂ addition, the RI reached to a maximum value of $n_D = 1.84$ (Run 2 in Table 2) but the Abbe number was low ($\nu_D = 7$), whereas the hybrid films with ZrO₂ displayed both high RI ($n_D = 1.82$) and high Abbe numbers ($\nu_D = 19$). These results were attributable to the small bandgap of TiO₂ with a long optical wavelength (380–400 nm) and redshift of the absorption bands in the case of nanodispersed inorganic nanoparticles, as mentioned in the previous section. XRD profiles were also measured for evaluating the crystallinity of the inorganic domains, including crystallinities for the polymer scaffolds (**Figure 2.22**). Hybrid films with TiO₂ showed slight diffraction peaks for the anatase-type TiO₂ nanocrystals, although the films with ZrO₂ remained amorphous because of high crystallization temperature (approx. 450–500 °C).^[31,70] For pursuing even higher RI, enhancing crystallinity of the inorganic NPs should be necessary by using surface-modified

nanocrystal dispersions.^[33] However, the deterioration of RI due to the excessive amount of dispersing agent might be concerned upon blending within the NP size of few-nm, which can be speculated from relatively lower RI of previously reported polymer-inorganic nanocrystal hybrid films than the pristine inorganic nanocrystals (e.g., $n_{594} \sim 1.7650$ even after 75 wt% ZrO₂ loadings into the epoxy resin).^[40] For such reasons, the author conclude that *in situ* sol-gel route is more effective method for enhancing RI with a small amount of the inorganic additive.

Although pristine TiO₂ tends to afford a higher RI than pristine ZrO₂, RI of the hybrid films with **P1/P2** were relatively similar because of the low processing temperature (below 200 °C) of the *in situ* sol-gel route, resulting in low crystallinity and RI of the NPs (estimated as RI ~ 2.0 according to the previous report^[40,41,52,71]), compared with anatase-type TiO₂ (RI > 2.5) (vide supra). So far, incorporation of a large amount of inorganic nanoparticles to the polymer matrices is expected to be necessary for achieving RI over 1.8, because of the low RI of the general polymers (up to $n_D = 1.657$).^[72] On the other hand, this study provides a new concept that the use of HRIPs such as **P1** or **P2** ($n_D > 1.72$) as the polymer matrix is further effective for achieving ultrahigh-RI hybrid materials ($n_D \sim 1.8$) with a smaller inorganic loading (up to 30 wt%) while maintaining high film transparency and long-term stability.

In conclusion, methoxy-substituted PPS (**OMePPS**) and its end-functionalized polymers with catechol and carboxylic acid moieties were synthesized and their nanohybridization properties with TiO₂ and ZrO₂ NPs were investigated in detail. Oxidative polymerization of **OMeDPS** gave linear **OMePPS** ($M_w = 6.0 \times 10^3$) with amorphous properties and excellent thermal stability ($T_g = 105\text{--}132$ °C, $T_{d5} = 329$ °C), high visible transparency, high RI ($n_D = 1.73$), and well TiO₂ dispersivity (20-100 nm). End-functionalized **OMePPS** were synthesized via disulfide reduction and thiol-ene reaction of **OMePPS**, which displayed not only high RI beyond 1.7 but better dispersivity of TiO₂ and ZrO₂ NPs with sizes of few-30 nm. In particular, the hybrid film of catechol-terminated **OMePPS** and 30 wt% ZrO₂ represented the best optical properties of high RI ($n_D = 1.82$ and $v_D = 19$) and well visible-transparency owing to the excellent NP dispersivity based on the catechol unit. For maintaining high transparency even for thicker films, it might be necessary to modulate the energy bandgap of the polymer-inorganic interface to prevent redshift of the absorption peak upon hybridization, which would be overcome by using silane-coupling agents^[39] or surface modification of the inorganic NPs by highly polarizable modifiers such as sulfur-containing agents. Also, other hybridization strategies including direct surface modification by surfactants and using side-functionalized PPS derivatives (e.g. catechol/carboxy-substituted PPS) as matrices would be effective for achieving better nano-compatible high-RI hybrid materials.

2.5 Experimental Section

2.5.1 Materials, measurements, and procedures for sections 2.2 and 2.3

Materials. 2-Methoxybenzenethiol, iodine, vanadyl acetylacetonate (VO(acac)₂), 2,3-dichloro-5,6-dicyano-1,4-benzoquinone (DDQ), trifluoromethanesulfonic acid (TfOH), trifluoroacetic anhydride, trifluoroacetic acid (TFA), tetramethylammonium tetrafluoroborate (TBABF₄) and tetrabutyl

orthotitanate (Ti(OBu)₄) were purchased at Tokyo Chemical Industry Co. Chloroform, methanol, dichloromethane, sodium thiosulfate, sodium sulfate, hydrochloric acid, sodium hydroxide and sodium chloride were purchased by Kanto Chemical Co. Ethanol was purchased by Junsei Chemicals Co. 1-Butanol was purchased by FUJIFILM Wako Pure Chemical Co. All materials were used without purification.

Synthesis of bis(2-methoxyphenyl) disulfide. Bis(2-methoxyphenyl) disulfide (**OMeDPS**) was prepared by oxidation of corresponding thiol with iodine as an oxidant. 2-methoxybenzenethiol (10 g, 72 mmol) was dissolved in chloroform (150 mL), and iodine (9.1 g, 35.7 mmol) in methanol (75 mL) was poured dropwise. The solution was stirred at room temperature for 1 hour, and the reaction was quenched by adding 10 wt% sodium thiosulfate aqueous until the color of the solution was completely changed from brown to light yellow. The solvent was removed, and the residue was extracted by chloroform/3 wt% hydrochloric acid, 5 wt% sodium hydroxide aqueous and 5 wt% brine. The extraction was dehydrated by sodium sulfate and purified by recrystallization with chloroform/methanol = 1/7 (v/v) solution. The product was obtained as a pale yellow needle-like crystal. Yield: 98 %. FAB-MS (*m/z*): M⁺ 278.4. Found 277.8. ¹H-NMR (chloroform-*d*, 500 MHz, ppm, TMS): δ 7.53 (dd, *J* = 7.4, 1.7 Hz, 2H, Ph), 7.18 (td, *J* = 7.4, 1.7 Hz, 2H, Ph), 6.91(td, *J* = 7.4, 1.1 Hz, 2H, Ph), 6.85 (dd, *J* = 7.9, 1.1 Hz, 2H, Ph), 3.90 (s, 6H, Me). ¹³C-NMR (chloroform-*d*, 125 MHz, ppm, TMS): δ 156.6, 127.7, 127.6, 124.6, 121.3, 110.5, 55.9. Melting point (DSC): 121 °C.

Oxidative polymerization. The procedure for run 7 in **Table 1** has been described here as an example. 2,3-dichloro-5,6-dicyano-1,4-benzoquinone (DDQ) (3.41 g, 15 mmol) was dispersed in chloroform (5 mL), and trifluoroacetic acid (383 μL, 5 mmol) and **OMeDPS** (4.17 g, 15 mmol) were added. The solution was stirred at room temperature for 40 hours and was diluted by chloroform (55 mL) and the precipitate of by-produced 2,3-dichloro-5,6-dicyano-1,4-hydroquinone (DDH) was collected by filtration. The filtrate was precipitated in ethanol/hydrochloric acid mixture (= 95/5 (v/v)) (600 mL). The precipitate was collected by filtration, was washed by ethanol, methanol, 3 wt% potassium hydroxide aqueous and water. The precipitate was dissolved in chloroform and reprecipitated in 10-fold excess methanol/hydrochloric acid mixture (= 95/5 (v/v)), was collected, was washed in the same procedure and dried under vacuum condition both at room temperature and at 80 °C to give **OMePPS** as a white powder (79% yield).

Film fabrication of OMePPS. To a vial was dissolved **OMePPS** (30 mg) in *N,N*-dimethylacetamide (DMAc) (2 mL) and was filtered through 0.2 μm PTFE filter. The solution (400 μL) was dropped on a glass substrate, was kept at 50 °C for 12 hours for fabrication of the film. The film was dried overnight in vacuo at room temperature. The thin film of **OMePPS** thin film with a thickness of 7.0 μm was prepared.

Hybridization of OMePPS with TiO₂ via *in-situ* sol-gel route. The following procedure was based on the previous report.^[55,64] To a vial, was dissolved **OMePPS** (Run 2 in **Table 1**, 102 mg) in DMAc (1.5 mL), was added hydrochloric acid (25 μ L) dropwise, and was stirred for 30 min. Ti(OBu)₄ (48.3 μ L) was dissolved in 1-butanol (100 μ L) under argon atmosphere readily. Ti(OBu)₄ was added dropwise in the polymer solution above, and was vigorously stirred for 30 minutes. After the reaction, the solution was filtered through 0.2 μ m PTFE filter and obtained as the precursor for **OMePPS**/TiO₂ hybrid film. The precursor solution was diluted by DMAc as the concentration of 15 mg/mL, and the diluted solution (400 μ L) was dropped on a glass substrate, was kept at 60 °C for 4 hours and at 150 °C for 3 hours under vacuum condition for fabrication of the film. The film was then cooled to room temperature and dried *in vacuo*. The hybrid film with a thickness of 5.2 μ m was obtained.

Methods. ¹H, ¹³C and ¹³C DEPT NMR spectra were measured by JEOL ECX-500 spectrometer, and 2D NMR (¹H-¹H COSY, HMQC, HMBC and NOESY) spectra were measured by Bruker AVANCE III 600 spectrometer. Tetramethylsilane (TMS) was used as the internal standard for the NMR measurements. FAB-MS spectrum was measured by JMS-GCMATE II. Molecular weights of the polymer were determined by size exclusion chromatography (SEC) using TOSOH HLC 8220 instrument with chloroform as an eluent. Cyclic voltammetry was carried out using ALS electrochemical analyzer (Model 760EW) with a three-electrode system (the Pt working electrode, the Pt wire counter electrode, and the Ag/AgCl reference electrode), in which the potential was corrected by ferrocene/ferrocenium redox couple. Infrared (IR) spectra were measured by Jasco FT/IR 6100 spectrometer with KBr pellets. UV-vis spectra were measured by JASCO V-550. Wide-angle X-ray diffraction (XRD) profiles were measured by Rigaku RINT-Ultima III. Dynamic scanning calorimetry (DSC) was conducted by TA Instruments Q200 or Perkin Elmer DSC8500, scanning from 50 °C to 250 °C at a rate of 20 °C/min. TGA analyses were conducted by Rigaku TG8120 using α -alumina as a standard at a heating rate of 10 °C/min with nitrogen or air flow. Refractive indices and thickness of thin films were measured by Horiba UVISEL ERAGMS iHR320 and KLA tencor P-6, respectively. TEM image of the hybrid film was obtained by JEOL TEM100.

2.5.2 Materials, measurements, and procedures for section 2.4

Materials. Sodium borohydride, tetrahydrofuran (dehydrated), methanol (dehydrated), N,N-dimethylacetamide (dehydrated), N,N-dimethylformamide (dehydrated), toluene (dehydrated) and hydrochloric acid, hexane, ethyl acetate and sodium sulfate were purchased from Kanto Chemical Co. 4-Pentenoic acid, 2,2-Dimethoxy-2-phenylacetophenone (DMPA), eugenol, triethylsilane, tris(pentafluorophenyl)borane, tetrabutyl orthotitanate, zirconium(IV) tetrabutoxide (ca. 80% in 1-butanol) were purchased from Tokyo Chemical Industry Co. 1-Butanol (dehydrated) was purchased by FUJIFILM Wako Pure Chemical Co. All reagents and solvents were used without further purification.

Ene **1** was prepared following previous report.^[73]

Disulfide reduction of OMePPS. To a 200 mL three necked flask, **OMePPS** ($M_n = 3.4 \times 10^3$) (2 g) was dissolved in THF (72 mL), was added sodium borohydride (2 g) and methanol (8 mL, dropwise), heated at 70 °C and stirred for 15 hours. After cooling at room temperature, the reaction solution was precipitated in methanol with 5 vol% hydrochloric acid mixture (1500 mL in total). The precipitate was collected, washed with methanol and water and dried under vacuo to give thiol-end **OMePPS** (**SH-OMePPS**) as a white powder (1.53 g, 76 % yield).

Synthesis of end-terminated OMePPS via thiol-ene reaction. Carboxyl- (**P1**) or catechol- (**P2**) functionalized **OMePPS** were synthesized via thiol-ene reaction of **SH-OMePPS** and 4-pentenoic acid or silyl-protected ene **1**, with further deprotection of silyl groups only in the case of **P2**. Here, synthesis of **P2** is described as an example. To a 5 mL flask, **SH-OMePPS** ($M_n = 2.7 \times 10^3$) (450 mg, 0.17 mmol of -SH), **1** (630 mg, 1.7 mmol) and DMPA (43 mg, 0.17 mmol) were added and dissolved in DMF (2 mL), was degassed through five times freeze-pump thaw cycles, and was stirred at room temperature under UV irradiation (Intensity: 60 mW cm⁻², $h\nu = 365$ nm) for 4 hours. Solvents were removed by rotary evaporation and residue was dissolved in tetrahydrofuran (10 mL). Subsequent deprotection of silyl groups was conducted by addition of hydrochloric acid (6 mL, dropwise) and stirring for 3 hours at room temperature. The solution was precipitated in methanol with hydrochloric acid (5 wt%) mixture (300 mL), and the precipitate was collected, washed with methanol and water and dried under vacuo to give catechol-functionalized **OMePPS** (**P2**) as a white powder (370 mg, 83 % yield).

Fabrication of the hybrid films. Hybridization of the polymer with inorganic nanoparticles were performed by *in situ* sol-gel hybridization following the previous report.^[74] Here Preparation procedure of Run 7 in Table 2 was described. To a vial was dissolved **P2** (102 mg) in DMAc (1.5 mL), was added hydrochloric acid (25 μ L), and was stirred for 30 minutes at room temperature. Zr(OBu)₄ (80 wt% solution in 1-butanol) (60.4 μ L) was dissolved in 1-butanol (100 μ L) under argon atmosphere (inside the glovebox) readily, which was further added into the polymer solution and stirred for another 30 minutes to give the precursor hybrid solution. The solution was filtrated, was diluted with DMAc in 30 mg/mL concentration, was casted onto a glass substrate, and was kept in vacuo at 60 °C for 2 hours, 150 °C for 2 hours, 180 °C for 30 minutes and 200 °C for 30 minutes to evaporate the solvent and proceed the sol-gel polycondensation. Heat-treated hybrid film was cooled to room temperature and dried in vacuo for an overnight.

Estimation of the polymer density.^[75,76] Density of the polymer (d_{polymer}) is determined by following equations, using the value of experimental refractive index in **Table 4**. The value 138.2 shown in eq. (2.1) is the molecular weight corresponding to the repeating unit of **OMePPS**. Eq. (2) was derived

by rearranging Lorentz-Lorenz equation and the definition of packing coefficient K_p :

$$d_{\text{polymer}} = 138.2 \frac{K_p}{V_{\text{vdw}}} \quad \dots (2.1)$$

$$\frac{K_p}{V_{\text{vdw}}} = \frac{n^2 - 1}{n^2 + 2} \cdot \frac{1}{[R]} \quad \dots (2.2)$$

where d shows density, V_{vdw} shows Van der Waals volume, n shows refractive index, and $[R]$ shows Molar reflection of the repeating unit. For example, n_D of **P1** was 1.72 from Table 1, and V_{vdw} and $[R]$ were calculated as 97.0 cm³ and 38.3 respectively from the reported values.^[75,76] Using these values, d_{polymer} was finally estimated as 1.42.

Prediction of Refractive Index of the hybrid films by Maxwell-Garnett Model

Refractive index of the composite materials can be estimated by applying Maxwell-Garnett model, assuming that the nanoparticles are homogeneously dispersed in the matrix and they formed a core-shell structure.^[3,4] For simplifying the model in the present case, dispersed TiO₂ or ZrO₂ nanoparticles (core) were assumed to be surrounded by the polymer matrix (shell) (**P1** or **P2**). Refractive index of the hybrid film (n_{hybrid}) can be described as follows:

$$n_{\text{hybrid}}^2 = n_{\text{polymer}}^2 \left(1 + \frac{3\phi x}{1 - \phi x} \right) \quad \dots (2.3)$$

$$x = \frac{n_{\text{inorganic}}^2 - n_{\text{polymer}}^2}{n_{\text{inorganic}}^2 + 2n_{\text{polymer}}^2} \quad \dots (2.4)$$

$$\phi = \frac{V_{\text{inorganic}}}{V_{\text{inorganic}} + V_{\text{polymer}}} = \frac{\frac{y}{d_{\text{inorganic}}}}{\frac{y}{d_{\text{inorganic}}} + \frac{1-y}{d_{\text{polymer}}}} \quad \dots (2.5)$$

Where suffix: hybrid, polymer, and inorganic represents hybrid film, **P1** or **P2**, and TiO₂ or ZrO₂, respectively, and n , V , y , d , and ϕ denotes refractive index, volume, inorganic content (wt%), density, and relative inorganic volume, respectively. In this study, $n_{\text{inorganic}}$ ($n_{\text{TiO}_2} = 1.983$, $n_{\text{ZrO}_2} = 1.897$) was adopted from the previous report,⁵ and $d_{\text{inorganic}}$ ($d_{\text{TiO}_2(\text{anatase})} = 3.84$ (assuming the fully converted crystalline structure of TiO₂ prepared by sol-gel route was anatase-type), $d_{\text{ZrO}_2} = 5.56$ (density of monoclinic ZrO₂ was adopted in this case, although ZrO₂ was not crystallized in the range of processed temperature in *in situ* sol-gel reaction of Zr(OBu)₄) values were referenced from the literature.¹¹

References

- [1] P. Zuo, A. Tcharkhtchi, M. Shirinbayan, J. Fitoussi, F. Bakir, *Macromol. Mater. Eng.* **2019**, 304, 1800686.
- [2] J. T. Edmonds Jr, H. W. Hill Jr, *U.S. Patent*, **1967**.
- [3] F. Aida, N. Takasu, Y. Takatori, H. Nishide, K. Oyaizu, *Bull. Chem. Soc. Jpn.* **2017**, 90, 843.
- [4] K. Kang, J. Park, S. Hyung, J. Y. Oh, *U.S. Patent 9,000,104 B2*, **2014**.

- [5] S.-G. Kim, J.-B. Lim, I.-H. Cha, (12) *United States Patent*, **2016**.
- [6] K. Yamamoto, E. Tsuchida, H. Nishide, M. Jikei, K. Oyaizu, *Macromolecules* **1993**, *26*, 3432.
- [7] K. Yamamoto, M. Jikei, K. Oyaizu, F. Suzuki, H. Nishide, E. Tsuchida, *BCSJ* **1994**, *67*, 251.
- [8] K. Oyaizu, Y. Kumaki, K. Saito, E. Tsuchida, *Macromolecules* **2000**, *33*, 5766.
- [9] K. Miyatake, K. Oyaizu, Y. Nishimura, E. Tsuchida, *Macromolecules* **2001**, *34*, 1172.
- [10] K. Oyaizu, T. Mikami, F. Mitsunashi, E. Tsuchida, *Macromolecules* **2002**, *35*, 67.
- [11] K. Oyaizu, T. Mikami, E. Tsuchida, *Macromolecules* **2004**, *37*, 2325.
- [12] K. Oyaizu, T. Iwasaki, Y. Tsukahara, E. Tsuchida, *Macromolecules* **2004**, *37*, 1257.
- [13] K. Oyaizu, K. Yamamoto, K. Yoneda, E. Tsuchida, *Inorg. Chem.* **1996**, *35*, 6634.
- [14] K. Yamamoto, K. Oyaizu, E. Tsuchida, *J. Am. Chem. Soc.* **1996**, *118*, 12665.
- [15] E. Tsuchida, K. Oyaizu, E. L. Dewi, T. Imai, F. C. Anson, *Inorg. Chem.* **1999**, *38*, 3704.
- [16] F. Aida, Y. Takatori, D. Kiyokawa, K. Nagamatsu, K. Oyaizu, H. Nishide, *Polym. Chem.* **2016**, *7*, 2087.
- [17] F. Aida, S. Yamaguchi, Y. Takatori, K. Nagamatsu, D. Kiyokawa, K. Oyaizu, H. Nishide, *Macromol. Chem. Phys.* **2015**, *216*, 1850.
- [18] K. Yamamoto, M. Jikei, J. Katoh, H. Nishide, E. Tsuchida, *Macromolecules* **1992**, *25*, 2698.
- [19] E. Tsuchida, K. Oyaizu, *BCSJ* **2003**, *76*, 15.
- [20] S. Watanabe, S. Saito, M. Hirai, K. Oyaizu, *Polym. J.* **2022**, *54*, 1.
- [21] K. Miyatake, M. Jikei, K. Yamamoto, E. Tsuchida, *Macromol. Chem. Phys.* **1996**, *197*, 595.
- [22] F. Aida, K. Oyaizu, *Chem. Lett.* **2016**, *45*, 102.
- [23] Y. Nakagawa, T. Ogura, T. Higashihara, M. Ueda, *Chem. Lett.* **2010**, *39*, 392.
- [24] Y. Nakagawa, Y. Suzuki, T. Higashihara, S. Ando, M. Ueda, *Polym. Chem.* **2012**, *3*, 2531.
- [25] M.-C. Fu, Y. Murakami, M. Ueda, S. Ando, T. Higashihara, *J. Polym. Sci. A Polym. Chem.* **2018**, *56*, 724.
- [26] M.-C. Fu, M. Ueda, S. Ando, T. Higashihara, *ACS Omega* **2020**, *5*, 5134.
- [27] Y. Zhou, Z. Zhu, K. Zhang, B. Yang, *Macromol. Rapid Commun.* **2023**, e2300411.
- [28] T. Higashihara, M. Ueda, *Macromolecules* **2015**, *48*, 1915.
- [29] H. Althues, J. Henle, S. Kaskel, *Chem. Soc. Rev.* **2007**, *36*, 1454.
- [30] C.-L. Tsai, G.-S. Liou, *Chem. Commun.* **2015**, *51*, 13523.
- [31] K. Enomoto, Y. Ichijo, M. Nakano, M. Kikuchi, A. Narumi, S. Horiuchi, S. Kawaguchi, *Macromolecules* **2017**, *50*, 9713.
- [32] S. Takahashi, S. Hotta, A. Watanabe, N. Idota, K. Matsukawa, Y. Sugahara, *ACS Appl. Mater. Interfaces* **2017**, *9*, 1907.
- [33] K. Enomoto, M. Kikuchi, A. Narumi, S. Kawaguchi, *ACS Appl. Mater. Interfaces* **2018**, *10*, 13985.
- [34] C. Lü, B. Yang, *J. Mater. Chem.* **2009**, *19*, 2884.
- [35] L.-H. Lee, W.-C. Chen, *Chem. Mater.* **2001**, *13*, 1137.
- [36] H.-W. Su, W.-C. Chen, *J. Mater. Chem.* **2008**, *18*, 1139.

- [37] G.-S. Liou, P.-H. Lin, H.-J. Yen, Y.-Y. Yu, W.-C. Chen, *J. Polym. Sci. A Polym. Chem.* **2010**, *48*, 1433.
- [38] J. G. Liu, Y. Nakamura, T. Ogura, Y. Shibasaki, S. Ando, M. Ueda, *Chem. Mater.* **2008**, *20*, 273.
- [39] G. S. Liou, P. H. Lin, H. J. Yen, Y. Y. Yu, T. W. Tsai, W. C. Chen, *J. Mater. Chem.* **2010**, *20*, 531.
- [40] C.-L. Tsai, G.-S. Liou, *Chem. Commun.* **2015**, *51*, 13523.
- [41] T.-T. Huang, S.-W. Cheng, C.-L. Tsai, G.-S. Liou, *Sci. Rep.* **2017**, *7*, 7978.
- [42] F. Cataldo, *Eur. Chem. Bull.* **2015**, *4*, 92.
- [43] M. Jikei, J. Katoh, N. Sato, K. Yamamoto, H. Nishide, E. Tsuchida, *Bull. Chem. Soc. Jpn.* **1992**, *65*, 2029.
- [44] F. Aida, Y. Takatori, D. Kiyokawa, K. Nagamatsu, H. Nishide, K. Oyaizu, *Chem. Lett.* **2015**, *44*, 767.
- [45] Y. Suzuki, K. Murakami, S. Ando, T. Higashihara, M. Ueda, *J. Mater. Chem.* **2011**, *21*, 15727.
- [46] S. Watanabe, T. Takayama, H. Nishio, K. Matsushima, Y. Tanaka, S. Saito, Y. Sun, K. Oyaizu, *Polym. Chem.* **2022**, *13*, 1705.
- [47] H. Dislich, A. Jacobsen, *Angew. Chem. Int. Ed Engl.* **1973**, *12*, 439.
- [48] J. G. Liu, M. Ueda, *Journal of Materials Chemistry* **2009**, *19*, 8907.
- [49] H.-J. Yen, C.-L. Tsai, P.-H. Wang, J.-J. Lin, G.-S. Liou, *RSC Adv.* **2013**, *3*, 17048.
- [50] C.-L. Tsai, H.-J. Yen, W.-C. Chen, G.-S. Liou, *J. Mater. Chem.* **2012**, *22*, 17236.
- [51] T.-T. Huang, C.-L. Tsai, S. Tateyama, T. Kaneko, G.-S. Liou, *Nanoscale* **2016**, *8*, 12793.
- [52] H. W. Su, W. C. Chen, *J. Mater. Chem.* **2008**, *18*, 1139.
- [53] E. Tsuchida, K. Yamamoto, K. Oyaizu, F. Suzuki, A. S. Hay, Z. Y. Wang, *Macromolecules* **1995**, *28*, 409.
- [54] H. Lee, B. P. Lee, P. B. Messersmith, *Nature* **2007**, *448*, 338.
- [55] J. Heo, T. Kang, S. G. Jang, D. S. Hwang, J. M. Spruell, K. L. Killups, J. H. Waite, C. J. Hawker, *J. Am. Chem. Soc.* **2012**, *134*, 20139.
- [56] J. Sedó, J. Saiz-Poseu, F. Busqué, D. Ruiz-Molina, *Adv. Mater.* **2013**, *25*, 653.
- [57] H. Xu, J. Nishida, W. Ma, H. Wu, M. Kobayashi, H. Otsuka, A. Takahara, *ACS Macro Lett.* **2012**, *1*, 457.
- [58] M. A. North, C. A. Del Grosso, J. J. Wilker, *ACS Appl. Mater. Interfaces* **2017**, *9*, 7866.
- [59] B. J. Sparks, E. F. T. Hoff, L. P. Hayes, D. L. Patton, *Chem. Mater.* **2012**, *24*, 3633.
- [60] K. Nishimori, M. Tenjimbayashi, M. Naito, M. Ouchi, *ACS Appl. Polym. Mater.* **2020**, *2*, 4604.
- [61] D. W. R. Balkenende, S. M. Winkler, Y. Li, P. B. Messersmith, *ACS Macro Lett.* **2020**, *9*, 1439.
- [62] Q. Zhang, G. Nurumbetov, A. Simula, C. Zhu, M. Li, P. Wilson, K. Kempe, B. Yang, L. Tao, D. M. Haddleton, *Polym. Chem.* **2016**, *7*, 7002.
- [63] P. Karthik, R. Vinoth, P. Selvam, E. Balaraman, M. Navaneethan, Y. Hayakawa, B. Neppolian, *J. Mater. Chem. A* **2017**, *5*, 384.
- [64] H. Takeshima, K. Satoh, M. Kamigaito, *Macromolecules* **2017**, *50*, 4206.

- [65] H. Takeshima, K. Satoh, M. Kamigaito, *J. Polym. Sci.* **2020**, 58, 91.
- [66] K. Zhan, C. Kim, K. Sung, H. Ejima, N. Yoshie, *Biomacromolecules* **2017**, 18, 2959.
- [67] L. Zeininger, L. Portilla, M. Halik, A. Hirsch, *Chem. Eur. J.* **2016**, 22, 13506.
- [68] R. Sánchez-de-Armas, M. A. San-Miguel, J. Oviedo, A. Márquez, J. F. Sanz, *Phys. Chem. Chem. Phys.* **2011**, 13, 1506.
- [69] N. Nakayama, T. Hayashi, *Colloids Surf. A Physicochem. Eng. Asp.* **2008**, 317, 543.
- [70] T. Otsuka, Y. Chujo, *Polym. J.* **2010**, 42, 58.
- [71] T.-T. Huang, C.-L. Tsai, S. Tateyama, T. Kaneko, G.-S. Liou, *Nanoscale* **2016**, 8, 12793.
- [72] S. Kango, S. Kalia, A. Celli, J. Njuguna, Y. Habibi, R. Kumar, *Prog. Polym. Sci.* **2013**, 38, 1232.
- [73] S. Watanabe, K. Oyaizu, *Bull. Chem. Soc. Jpn.* **2020**, 93, 1287.
- [74] Y. Terui, S. Ando, *J. Polym. Sci. B Polym. Phys.* **2004**, 42, 2354.
- [75] R. J. Gehr, R. W. Boyd, *Chem. Mater.* **1996**, 8, 1807.
- [76] Z. Wang, Z. Lu, C. Mahoney, J. Yan, R. Ferebee, D. Luo, K. Matyjaszewski, M. R. Bockstaller, *ACS Appl. Mater. Interfaces* **2017**, 9, 7515.

Figures, tables, and texts are partially adapted from S. Watanabe, K. Oyaizu, *Bull. Chem. Soc. Jpn.* **2020**, 93, 1287-1292 (Reproduced with permission, Copyright © 2020 The Chemical Society of Japan); S. Watanabe, K. Oyaizu, *ACS Appl. Polym. Mater.* **2021**, 3, 4495-4503 (Reproduced with permission, Copyright © 2021 American Chemical Society).

Chapter 3:

Ultrahigh Refractive index Poly(phenylene sulfide)s Enabled by Intermolecular Hydrogen Bonds

Contents

- 3.1 Introduction
 - 3.2 Synthesis of Hydroxy-Substituted Poly(phenylene sulfide)
 - 3.3 Optical Properties and Hydrogen Bonding Elucidation
 - 3.4 Dihydroxy-substituted Poly(phenylene sulfide) with Denser Hydrogen Bonds
 - 3.5 Refractive Index Properties for Dihydroxy-containing Poly(phenylene sulfide)s
 - 3.6 Experimental Section
- References

3.1 Introduction

Over the past several years, transparent optical materials with a high refractive index (RI, n) have been sought after for their promising properties suitable for optoelectronics and photonic technologies,^[1,2] in which polymers with high RI (≥ 1.7) and good transparency, so-called high refractive index polymers (HRIPs), are especially required.^[1] The general design for HRIPs is arranging functional groups with high molar refraction ($[R]$) and low molecular volume (V , the sum of van der Waals volume V_{vdw} and free volume) in the highest density possible according to the Lorentz-Lorenz equation (Eq. (3.1)),^[3,4] as mentioned in the chapter 1. Substituents with especially high $[R]$ values (i.e. high polarizability per unit V_{vdw}), such as nitrogen, phosphorous, sulfur, and aromatic structures, have been frequently incorporated in the structure of HRIPs with a large content.^[1,3,5-7]

$$n = \sqrt{\frac{1 + 2[R]/V}{1 - [R]/V}} \quad \dots (3.1)$$

One large HRIP category is sulfur-containing polymers, because sulfur is an abundant source, shows relatively high $[R]$ values among general structural components, and there are well-established synthetic routes for sulfur-containing polymers.^[8,9] For example, sulfur-containing polyimides exhibited high RI ($n \sim 1.7$) alongside excellent mechanical properties, despite their poor transparency owing to the coloration by the charge-transfer complexation.^[10,11] Recently, spirobifluorenes^[12,13] and triazines bearing aromatic rings^[14,15] were reported as substructures for low birefringent and high transparent polymers with RI of 1.6-1.7 upon combining high- $[R]$ structures (e.g., phenylenesulfide or thianthrene). Poly(phenylene sulfide) (PPS) derivatives^[16-19] are in another HRIP category, affording amorphous polymers with balanced thermal and optical properties (high glass-transition temperature ($T_g > 100$ °C), good solubility, high transparency, and high RI of ~ 1.7).^[19,20] In addition, Pyun and co-workers reported a wide variety of sulfur-rich polymers synthesized via the inverse vulcanization, displaying ultrahigh RI over 1.8 from the near-infrared (NIR) (> 600 nm) to the infrared (IR) regions.^[21,22] Upon the partial replacement of sulfur by selenium, the obtained inverse-vulcanized polymer showed even higher RI (~ 2.1) owing to the higher $[R]$ of Se (11.17) compared with that of S (7.69).^[23,24] These ultrahigh-RI polymers are useful for the sensing applications that require high IR transparency.^[25] Another RI enhancing technique is the nanohybridization of polymer with high-RI inorganic nanoparticles, among which ZrO_2 is the effective choice for their high RI and visible transparency.^[26]

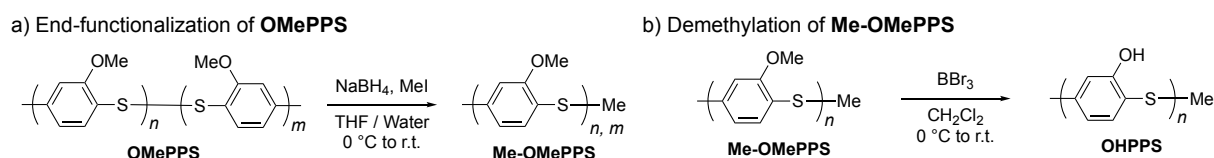
On the other hand, decreasing free volume of polymers in the solid state through inducing polymer chain packing by intermolecular interactions is another approach for the RI enhancement, because polymer chains inevitably produce voids that increase free volume in the bulk states. Several attempts to enhance the RI of HRIPs through intermolecular hydrogen bonds (H-bonds) were reported so far,^[27] but the polymer skeleton inevitably tends to become bulky in order to maintain an amorphous nature and high solubility, resulting in only limited enhancement through the introduction of H-bonds. Also, no systematic investigation of the RI enhancement upon H-bond introduction has been reported

before.

Herein, we report a new type of HRIP bearing functional groups capable of intermolecular H-bonds with the high- $[R]$ PPS main chain, which represented ultrahigh RI over 1.8. Intermolecular H-bonds as well as the moderate rotational barrier of the rigid PPS backbone achieved the strong side-chain interactions and the suppression of the π - π interactions between the main chains. Consequently, hydroxy-substituted PPS exhibited high $[R]/V$ with an amorphous nature, leading to the superior optical properties to previous HRIPs.

3.2 Synthesis of Hydroxy-Substituted Poly(phenylene sulfide)

First, we designed the simplest hydroxy-bearing PPS skeleton: poly(2-hydroxy-1,4-phenylenesulfide) (**OHPPS**). **OHPPS** was synthesized from the corresponding methoxy-substituted PPS by demethylating the side groups (**Scheme 3.1**).



Scheme 3.1. Synthesis of **OHPPS**: (a) end-functionalization of **OMePPS**. (b) Demethylation of **Me-OMePPS** to afford **OHPPS**.

3.2.1. Synthesis of Methyl-terminated **OMePPS**

As PPS derivatives including **OMePPS** have one disulfide bond per one chain,^[20] which was based on its Friedel-Crafts type reaction system,^[28] there is a concern that direct demethylation of **OMePPS** results in the depolymerization or the side reactions triggered by the disulfide cleavage by the strong Lewis acid (e.g., HBr, BBr_3)^[29] to generate thiol-derived reactive species.^[20,30]

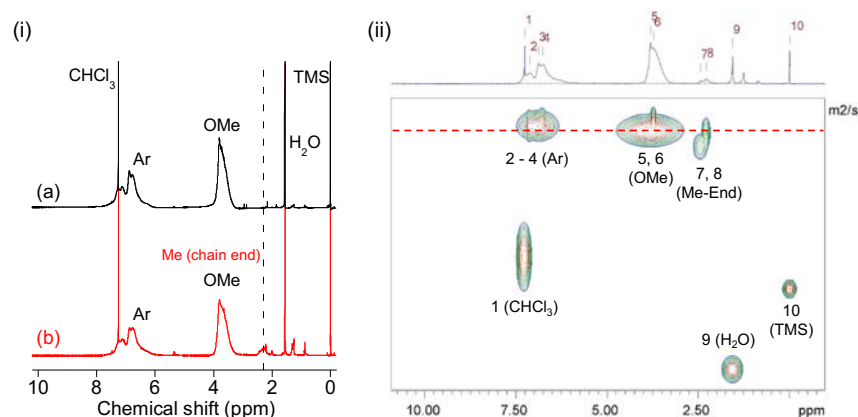


Figure 3.1. End-functionalization of **OMePPS** by methyl groups. (i) ^1H NMR spectra of (a) **OMePPS** and (b) **Me-OMePPS** in chloroform-*d*. (ii) ^1H DOSY-NMR spectra of **Me-OMePPS** in chloroform-*d*.

Therefore, **OMePPS** was subjected to the end-functionalization prior to the demethylation, via

the one-pot end modification via the reductive cleavage of the disulfide bond and the subsequent nucleophilic substitution (**Scheme 3.1a**). Methyl-terminated **OMePPS (Me-OMePPS)** was obtained in high yield with an end-functionality of $f = 0.94$ (**Figure 3.1a**). The progress of the end-functionalization was monitored by DOSY spectroscopy, where the same diffusion coefficient was observed for all the peaks from **Me-OMePPS (Figure 3.1b)**. The number-average molecular weight (M_n) was not substantially decreased after the end-functionalization (from 2.5×10^3 to 2.1×10^3), although the weight-average molecular weight (M_w) was much reduced (from 5.3×10^3 to 3.8×10^3) (see section 3.6 for the details). These results indicated the various distribution of the disulfide bonds in the **OMePPS** chain, which were mostly distributed at the terminal for the low-molecular-weight compounds but were moved toward the chain center according to the polymerization progress. Moreover, M_n of these PPS derivatives were too low ($\sim 2 \times 10^3$) to use as free-standing optical elements, because of the living-like oxidative polymerization mechanism with a low reaction rate^[28] that might precipitate the products in the middle-latter stage of the polymerization.

3.2.2. Demethylation of Me-OMePPS

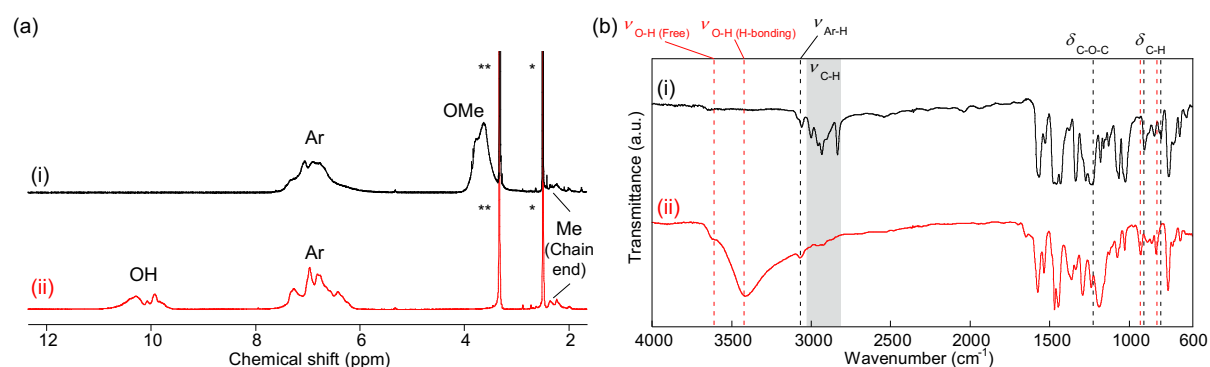


Figure 3.2. (a) ^1H NMR spectra of (i) **Me-OMePPS** and (ii) **OHPPS** in $\text{DMSO}-d_6$ (* and ** correspond to the signals of DMSO and H_2O , respectively). (b) IR spectra of (i) **Me-OMePPS** and (ii) **OHPPS**.

Table 3.1 Properties of PPS derivatives before and after demethylation

Polymer	M_n^{a} ($\times 10^3$)	T_g^{b} ($^{\circ}\text{C}$)	$\%T^{\text{c}}$ at 400 nm	n_D^{d} (-)	n_F^{d} (-)	n_C^{d} (-)	ν_D^{d} (-)	$\Delta n^{\text{d(e)}}$ (-)	Density ^{f)} (g cm^{-3})
Me-OMePPS	2.1	119	93	1.73	1.75	1.72	22	0.001	1.47
OHPPS	2.0	125	97	1.80	1.83	1.79	20	0.003	1.50

^{a)} Determined by ^1H NMR. ^{b)} Determined by DSC. ^{c)} Determined by UV-vis spectroscopy (thickness: normalized to 1 μm .) ^{d)} Determined by spectroscopic ellipsometry. ^{e)} Birefringence at 633 nm. The determination procedure was described in ^{f)} Determined by densimeter (pycnometer).

OHPPS was prepared via the demethylation of the side groups for **Me-OMePPS** (**Scheme**

3.1b, Table 3.1). Figure 3.2a showed the ^1H NMR spectra before and after the reaction with the complete conversion of methoxy groups to hydroxy groups, which was confirmed by the absence of the signals for methoxy groups and the presence of the signals for hydroxy protons after the demethylation. The M_n values from the NMR integrals of the main-chain and terminal signals were almost identical upon the demethylation (from 2.1×10^3 to 2.0×10^3), indicating the precise depolymerization without any side reactions (Table 3.1). Figure 3.2b showed the IR spectra, indicating the presence of the hydroxy groups after the demethylation from the broad absorption of the $\nu_{\text{O-H}}$ vibrations with H-bonds (3410 cm^{-1}) while a slight absorption of hydroxy groups in the free state (i.e. not involving the intermolecular H-bonds) were observed at 3610 cm^{-1} . Additionally, ether ($\delta_{\text{C-O-C}} = 1240 \text{ cm}^{-1}$) was not detected and the peak intensity for the methyl C-H ($\nu_{\text{C-H}} = 3030\text{-}2790 \text{ cm}^{-1}$) was considerably decreased after the demethylation, which were all consistent with the ^1H NMR analysis.

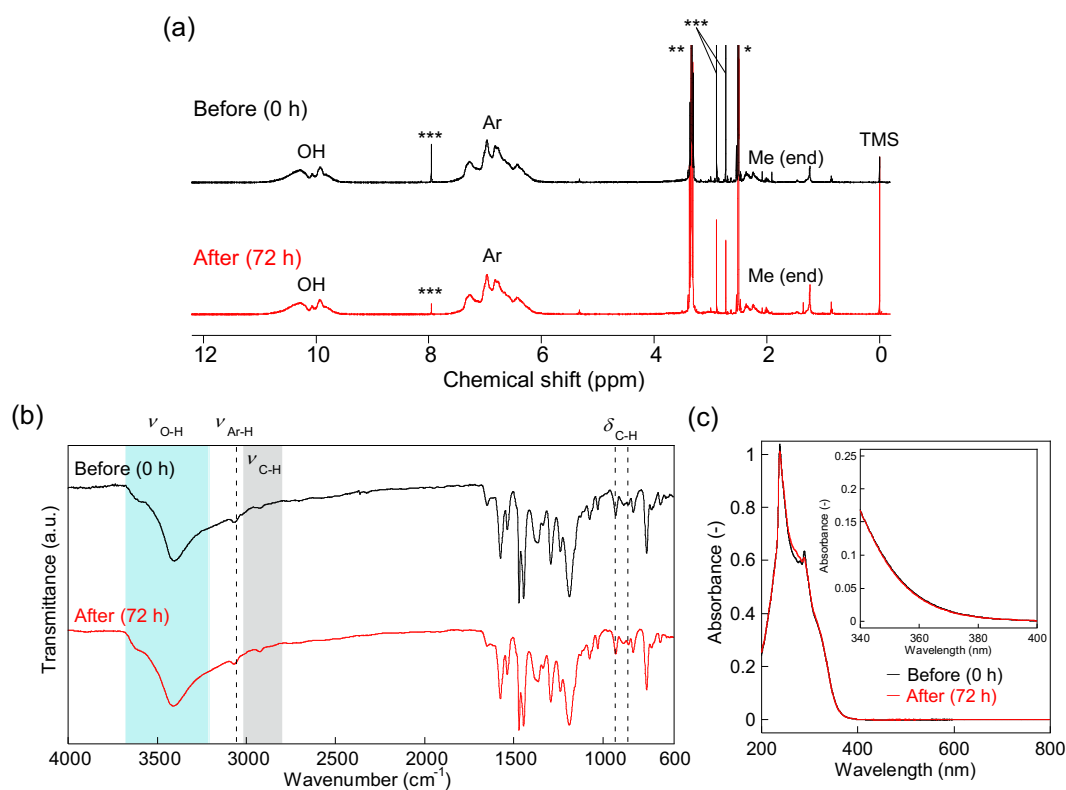


Figure 3.3. Oxidation stability test of OHPPS. (a) ^1H NMR spectra of OHPPS (in $\text{DMSO-}d_6$) before and after oxygen bubbling treatment in DMF at 80°C for 72 hours. (* and ** correspond to the signals of DMSO and H_2O , respectively). (b) IR spectra of OHPPS before and after the bubbling. (c) UV-vis spectra of the OHPPS solution (0.1 mM solution in THF) before and after the bubbling.

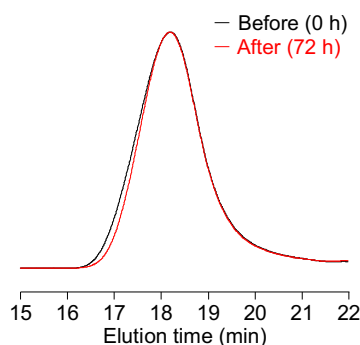


Figure 3.4. SEC charts of **OHPPS** in DMF (containing 0.1 M LiCl) before and after the bubbling.

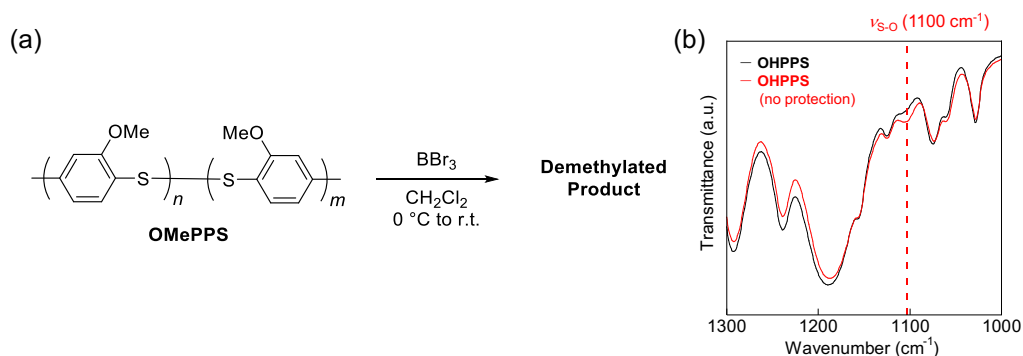


Figure 3.5. Demethylation of **OMePPS** containing interchain disulfide. (a) Scheme. (b) IR spectra of the demethylated **OHPPS** (with or without protection).

We further examined the stability of **OHPPS** toward various external conditions. After bubbling the oxygen in the **OHPPS** solution under heating, ^1H NMR, IR, and UV-vis measurements showed no spectral change as shown in **Figure 3.3**. Molecular weight were almost the same upon the oxygen bubbling, indicating its well oxidation stability (**Figure 3.4**). Demethylation of the **OMePPS** derivative without end functionalization (i.e., containing a disulfide bond in the chain) was further conducted to evaluate the end-functionalization effect (**Figure 3.5a**), and the product was obtained as a whitish orange powder in lower yield of 50 %. The IR spectrum of the product indicated the presence of a slight absorption of S-O ($\nu_{\text{S-O}} = 1110 \text{ cm}^{-1}$) (**Figure 3.5b**), which might be the result for the interchain disulfide cleavage and suggested the depolymerization or side reactions between thiol-derived species and side hydroxy groups.

3.3 Optical Properties and Hydrogen Bonding Elucidation

3.3.1 Thermal and Optical Properties

Effects of the introduction of hydrogen bonds to the polymer chain on several properties were investigated by examining crystalline and thermal properties. **Figure 3.6a** showed the powder XRD profiles with broad halos, in which no crystalline peaks were detected for both **Me-OMePPS** and **OHPPS**. These results revealed the amorphous properties of **OHPPS** even in the presence of H-bonding

networks. The diffraction angle of the halo peak, corresponding to the average π - π spacing value (d), was smaller for **OHPPS** than in the case of **Me-OMePPS**, indicating the slight increase of the minimum d value (from 3.89 Å to 4.23 Å) upon the demethylation. The DSC thermograms shown in Figure 3.6b represented the increment of T_g to 125 °C without no crystalline features for **OHPPS**. Such results were attributed to the strengthened intermolecular H-bonds upon the demethylation, while suppressing the π - π interactions between the phenylene skeletons based on limited main-chain conformations of the rigid PPS backbones.

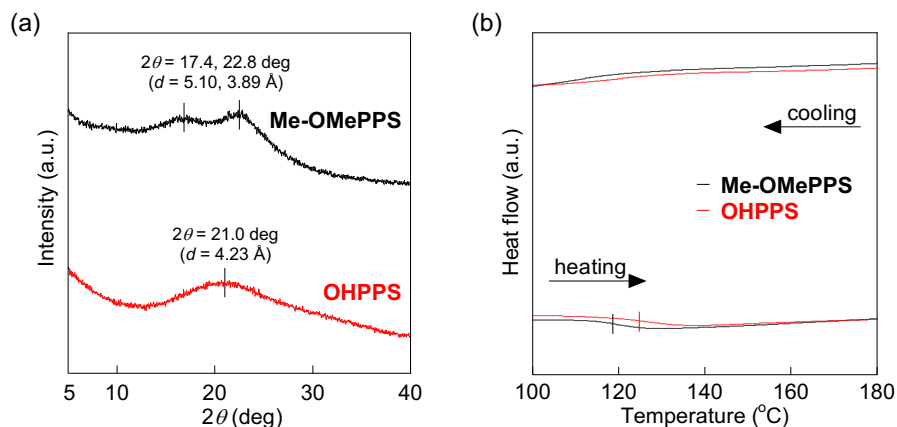


Figure 3.6. Properties of **Me-OMePPS** and **OHPPS**. (a) XRD profiles. (b) DSC thermograms (scan rate: 20 °C min⁻¹).

Taking advantage of the above amorphous and soluble features, **OHPPS** showed excellent features for the application of transparent optical materials such as functional coatings. Thin polymer films were successfully prepared on the substrates via wet-processing (dropcasting or spincoating) of the solutions.

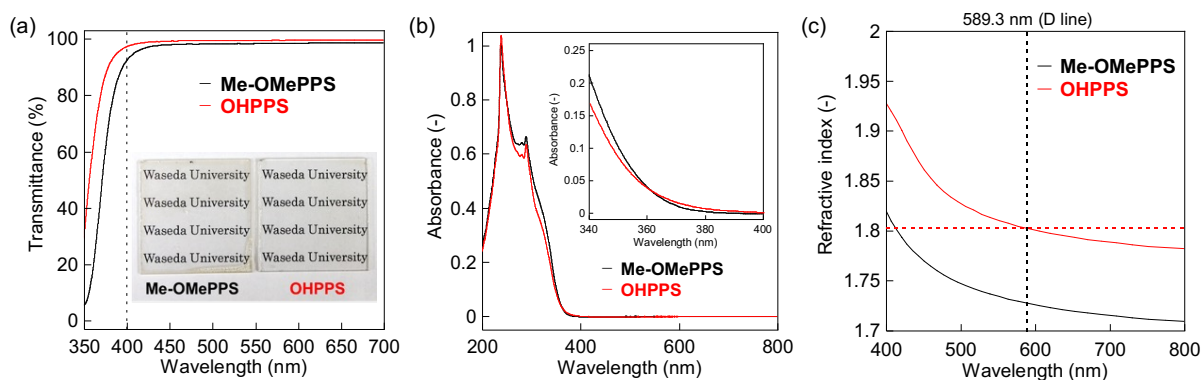


Figure 3.7. Optical properties of **Me-OMePPS** and **OHPPS**. (a) UV-vis spectra of the polymer thin films (thickness: normalized to 1 μm) (inset: thin films of **Me-OMePPS** (2.8 μm) and **OHPPS** (4.5 μm)). (b) UV-vis spectra of the polymer solutions (0.1 mM in THF) (Inset: expanded spectra). (c) RI before and after the demethylation.

OHPPS was more transparent (97 %*T* at 400 nm) without any coloration than **Me-OMePPS** (93 %*T*) with a normalized thickness of 1 μm (**Figure 3.7a**), which was adequate properties for the CMOS applications that requires film thickness of 1-2 μm.^[31] In the solution state, **OHPPS** exhibited lower transparency at 400 nm in THF than **Me-OMePPS** (**Figure 3.7b**). Such slight difference of the absorption properties indicated the presence of conformational changes of the polymer chains from solution to the bulk (solid) states for **Me-OMePPS** and **OHPPS**. **Figure 3.7c** showed significantly increased RI of **OHPPS** up to $n_D = 1.80$ compared to the RI of **Me-OMePPS** ($n_D = 1.73$). Also, Abbe number, which is expressed the wavelength dispersion of RI as the following Eq. (3.2):

$$\nu_D = \frac{n_D - 1}{n_F - n_C} \quad \dots (3.2)$$

where D, F, and C shows 589.3 nm, 486.1 nm, and 656.3 nm respectively, was determined as $\nu_D = 20$ for **OHPPS**, which was beyond the typical trade-off between n_D and ν_D . Such transparency and RI properties of **OHPPS** are superior to those for the previously reported HRIPs: Although some high-RI polyimides showed similar Abbe numbers ($\nu_D \sim 20$ -30) as well as high vis-transparency via suppressing charge-transfer interactions,^[32,33] although their RI remained lower values of below 1.8. Birefringence (Δn) of the polymers were also determined by adopting the anisotropic uniaxial layer fitting model to the obtained ellipsometry results. The Δn of **OHPPS** remained in a small value of 0.003 at 633 nm while was slightly larger than that of **Me-OMePPS**, which would be attributed to the directivity of the H-bonding, the rigid PPS backbone, and amorphous features rendering the isotropic H-bond polymer networks. The author concludes that **OHPPS** achieved such unprecedented properties based on their H-bond-assisted RI enhancement system.

3.3.2 Detailed Investigations of Hydrogen Bonding Features

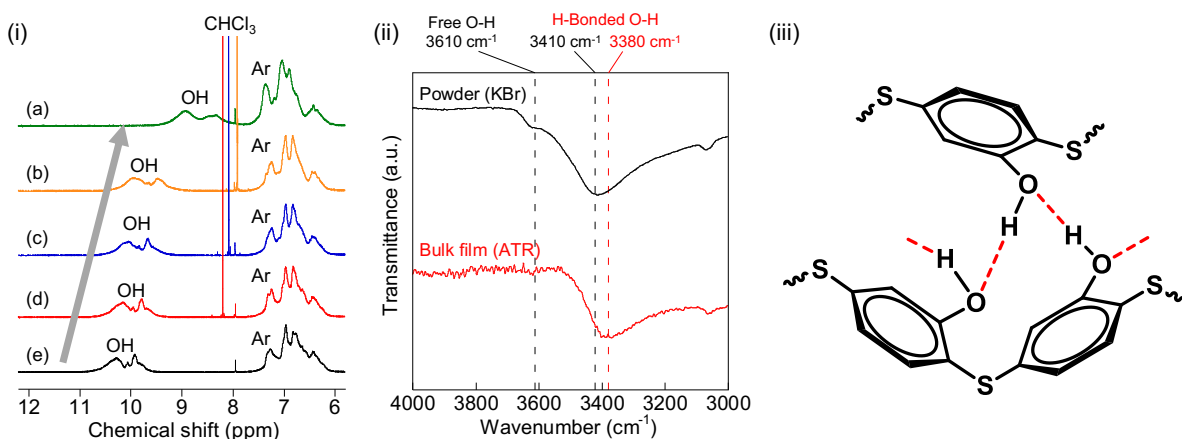


Figure 3.8. Elucidating H-bonds of **OHPPS**. (a) ¹H NMR spectra of **OHPPS** in variable solvents: (a) acetone-*d*₆, (ii) DMSO-*d*₆/chloroform-*d* (= 1/2, v/v), (iii) DMSO-*d*₆/chloroform-*d* (= 1/1, v/v), (iv) DMSO-*d*₆/chloroform-*d* (= 2/1, v/v), and (v) DMSO-*d*₆ (concentration: 10 mg mL⁻¹). (b) IR spectra of **OHPPS** in the powder (black line, KBr pellet) and in the film state (red line, ATR-IR). (c) Representation of the intermolecular H-bonds between the hydroxy groups of **OHPPS** in the solid states.

For elucidating the underlying mechanism for the optical properties of **OHPPS**, intermolecular interactions have been comprehensively examined. First, ^1H NMR measurements were conducted with various solvents (**Figure 3.8a**). The signals for hydroxy groups shifted to the upfield as the solvent polarity was decreased, because of the changing behavior of hydroxy groups as H-bonding sites in the solution. The IR spectra of **OHPPS** revealed redshift of the $\nu_{\text{O-H}}$ peaks from 3410 to 3380 cm^{-1} upon the film formation, and the free O-H vibration peak has been disappeared simultaneously (**Figure 3.8b**). Such trend was ascribed to more widespread H-bond networks in the bulk state compared to the case for the film state. Higher density of **OHPPS** (1.50 g cm^{-3}) than **Me-OMePPS** (1.47 g cm^{-3}) also held the enhancement of H-bonding networks upon the demethylation. In summary, presence of the dense polymer network for **OHPPS** in the bulk state has been revealed according to the strong intermolecular interactions between the hydroxy units, as well as the weakened p-p interactions and rigid zig-zag skeleton of the PPS backbone^[34] leading to suppressing excessive interactions (**Figure 3.8c**). Such bulk structures resulted in high solubility, transparency, and amorphous properties of the bulk **OHPPS**.

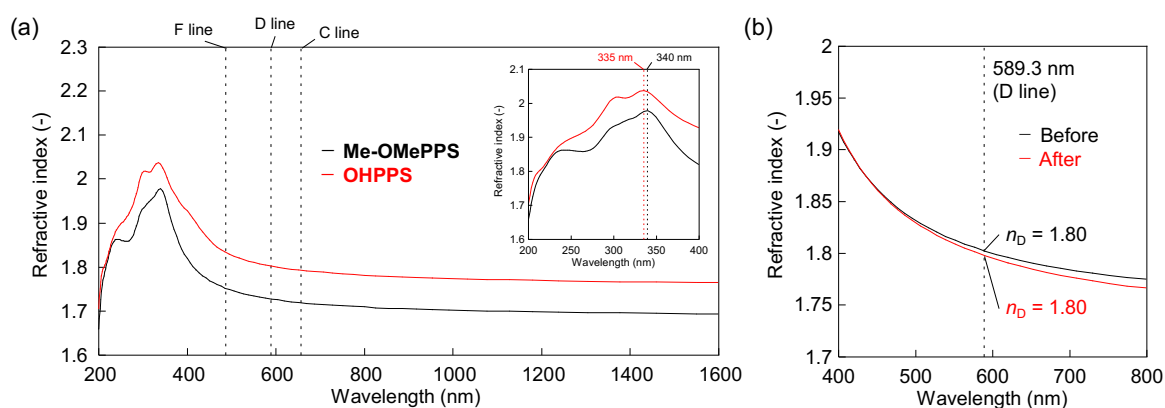
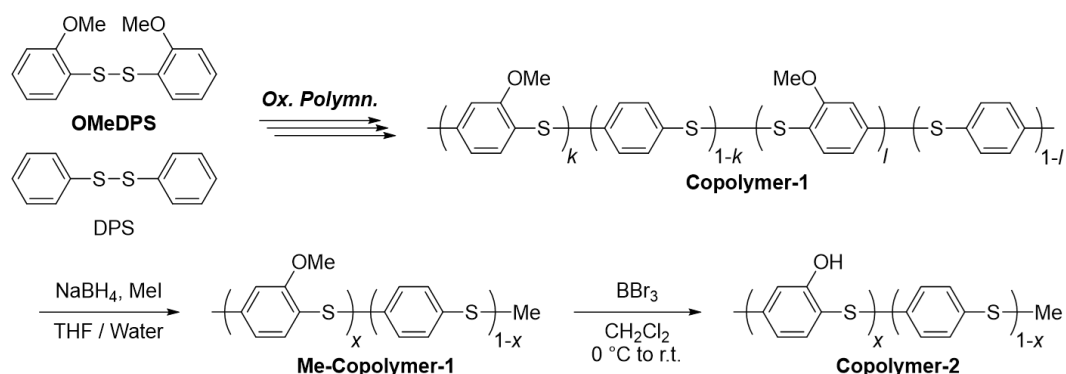


Figure 3.9. Detailed optical properties. (a) RI of **Me-OMePPS** and **OHPPS** (200-1600 nm) (inset: expanded spectra in the near-UV region). (b) RI of **OHPPS** under humidity test: before and after the replacement under the condition with a humidity of 85 ± 3 %RH, at room temperature.

3.3.3 Comparison with Hydroxy-/Non-substituted Poly(phenylene sulfide) Copolymers

Therefore, the author conclude that the simultaneous enhancement of RI (up to the ultrahigh RI region) and high Abbe number for **OHPPS** was realized according to three reasons: (1) high- $[R]$, low- V PPS backbone, (2) small dispersion of hydroxy group ($[\Delta R]_{\text{OH}} = 0.006$) compared with other substituents (0.072 for CH_2 and 0.012 for ether),^[1] and (3) anomalous dispersion in the smaller wavelength (**Figure 3.9a** inset), which resulted in small dispersion of RI. Such properties of **OHPPS** were almost maintained even after the replacement under humid conditions, which resulted in the slightly decreased (less than 0.01) RI of $n_D = 1.80$ after 1 day (**Figure 3.9b**) presumably owing to the rigid and hydrophobic PPS backbone.



Scheme 3.2. Synthesis of OHPPS-PPS copolymers (Copolymer-2).

In order to understand the roles of H-bonds for enhancing RI, the copolymers composed of OHPPS and non-substituted PPS (Copolymer-2) were synthesized and their RI properties were revealed. Two copolymers with different unit ratios ($x = 0.58$ and 0.37) were obtained via the oxidative polymerization, end-methylation, and demethylation of the methoxy groups, which were the similar procedure as the case of OHPPS synthesis (Scheme 3.2).

Table 3.2 Synthesis of OMePPS/OHPPS-PPS copolymers

Run	Polymer	Yield (%)	x^i (-)	M_n^j ($\times 10^3$)	M_n^j ($\times 10^3$)	M_w^j ($\times 10^3$)	M_w/M_n^j ($\times 10^3$)	T_g^k ($^\circ\text{C}$)
1	Copolymer-1		0.55	-	2.2	4.2	2.0	104
2	Copolymer-1		0.37	-	1.8	2.9	1.6	89
1 ^{a)}	Me-Copolymer-1	72 ^{e)}	0.61	1.9	2.0	3.2	1.6	114
2 ^{b)}	Me-Copolymer-1	68 ^{f)}	0.40	1.5	1.5	2.2	1.4	86
3 ^{c)}	Copolymer-2	94 ^{g)}	0.58	1.7	-	-	-	110
4 ^{d)}	Copolymer-2	65 ^{h)}	0.37	1.5	-	-	-	77

Feed polymer: ^{a)} Run 1, ^{b)} Run 2, ^{c)} Run 1', and ^{d)} Run 2'. Yield for ^{e)} Run 1, ^{f)} Run 2, ^{g)} Run 1', and ^{h)} Run 2'. ⁱ⁾ Determined by $^1\text{H NMR}$. ^{j)} Determined by SEC in chloroform. ^{k)} Determined by DSC.

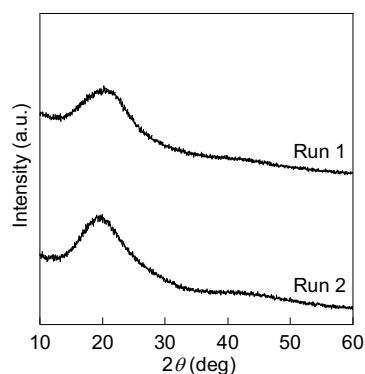


Figure 3.10. XRD profiles of Copolymer-1.

Oxidative polymerization of diphenyl disulfide (DPS) and **OMeDPS** yielded **Copolymer-1** with lower molecular weight than those of **OMePPS** due to the higher solvent-resistance of non-substituted PPS skeleton (**Table 3.2**).^[19] Therefore, molecular weights of **Copolymer-1** were in lower values especially in the PPS-rich conditions. Also, the DPS-favored copolymerization kinetics (the details were described in chapter 4) also resulted in the gradient-like random and nonlocalized sequence for **Copolymer-1**, which also led to their amorphous properties in the XRD profiles (**Figure 3.10**) and good solubility.

The end-methylated copolymers (**Me-Copolymer-1**) were obtained with higher x values (i.e., methoxy-substituted unit-rich products) according to the ¹H NMR spectra, also suggesting the larger distribution of non-substituted PPS unit at the terminus (**Figure 3.11a, 3.11b**). Also, the demethylation of **Me-Copolymer-1** successfully afforded **Copolymer-2** with fully introduced hydroxy groups (**Figure 3.11c, 3.11d**).

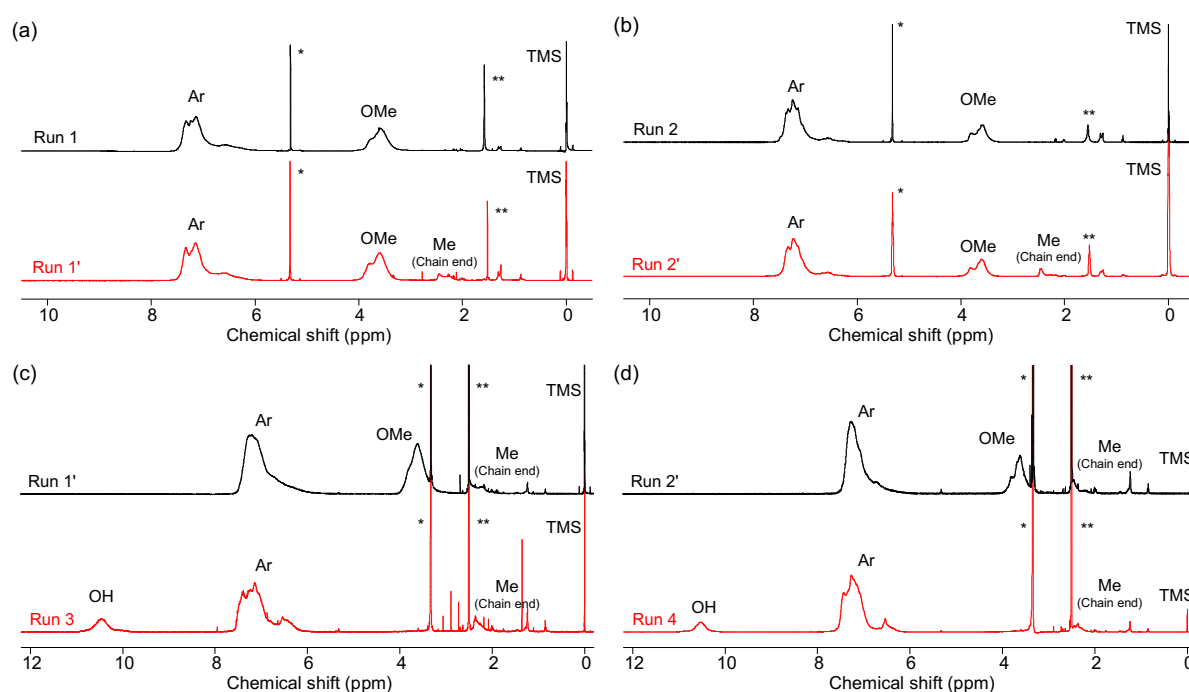


Figure 3.11 ¹H NMR spectra of **Copolymer-1**, **Me-Copolymer-1**, and **Copolymer-2**: (a) Run 1 and 1' in dichloromethane- d_2 , (b) Run 2 and 2' in dichloromethane- d_2 , (c) Run 1' and Run 3 in DMSO- d_6 , and (d) Run 2' and Run 4 in DMSO- d_6 . (for **Figures 3.11a** and **3.11b**, * and ** indicate signals for dichloromethane and water, respectively, and for **Figures 3.11c** and **3.11d**, * and ** indicate signals for water and DMSO, respectively).

DSC, UV-vis, and spectroscopic ellipsometry were conducted to understand the structure-property relationships for **Copolymer-2**. Larger amount of H-bonds generally results in higher T_g and RI owing to the decline of free volume by the H-bonding effect. Compared with **OHPPS**, the T_g of **Copolymer-2** from the DSC thermograms were lower than the corresponding **Me-Copolymer-1** (**Figure 3.12**), which

can be explained by the more random and sparser H-bonding sequence in contrast to the case of **OHPPS**. Smaller amount of the hydroxy groups for **Copolymer-2** resulted in weaker H-bonding in a macroscopic scale and higher effect of small rotation barrier than enhanced intermolecular H-bonds.

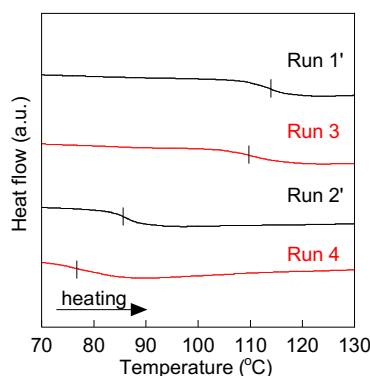


Figure 3.12. DSC thermograms of **Me-Copolymer-1** and **Copolymer-2**.

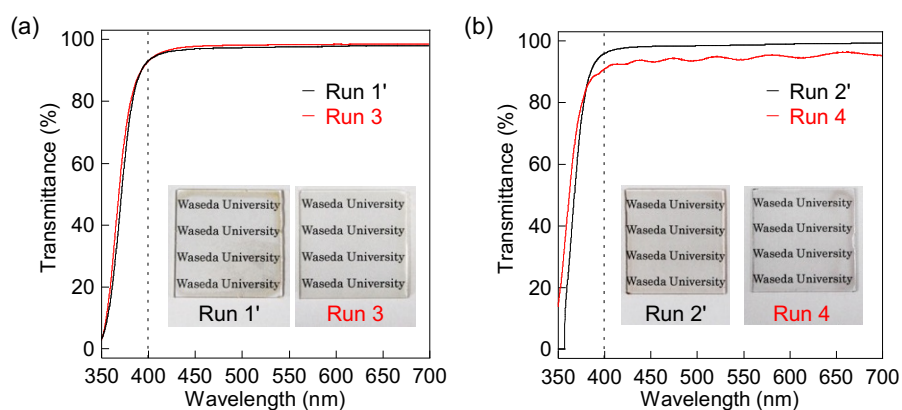


Figure 3.13. Normalized UV-vis spectra of thin films of **Me-Copolymer-1** and **Copolymer-2**: (a) Run 1 and 3, (b) Run 2 and 4 (Thickness of the film was normalized to 1 μm) (inset: photographs of the films).

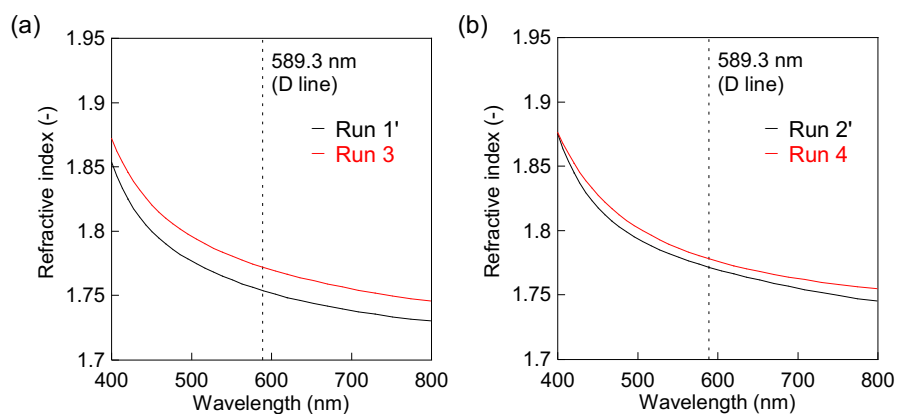


Figure 3.14. Refractive indices of the copolymers before and after the demethylation: (a) Run 1' and 3, (b) Run 2' and 4.

Table 3.3 Synthesis of hydroxy-substituted copolymers

Run	Polymer	x^e (-)	T_g^f (°C)	$\%T^g$ at 400 nm	n_D^h (-)	v_D^h (-)	Δn^{hi} (-)
1'	Me-Copolymer-1	0.61	114	93	1.75	20	0.001
2'	Me-Copolymer-1	0.40	86	96	1.77	21	0.001
3 ^{a)}	Copolymer-2	0.58	110	93	1.77	19	0.001
4 ^{b)}	Copolymer-2	0.37	77	91	1.78	20	0.002

^{a)} Feed polymer: Run 1'. ^{b)} Feed polymer: Run 2'. Yield for ^{c)} Run 1' and ^{d)} Run 2'. ^{e)} Determined by ¹H NMR.

^{f)} Determined by DSC. ^{g)} Determined by UV-vis (normalized thickness of 1 μm). ^{h)} Determined by spectroscopic ellipsometry. ⁱ⁾ Birefringence at 633 nm.

Regarding their optical properties, **Copolymer-2** showed lower film transparency than **OHPPS** (**Figure 3.13**). RI of **Copolymer-2** ($n_D = 1.77$ (Run 3) and 1.78 (Run 4)) were in higher than the values for the corresponding precursor (**Me-Copolymer-1**) ($n_D = 1.77$ (Run 2) in maximum) but lower than the RI of **OHPPS** ($n_D = 1.80$) (**Figure 3.14**). In the RI changing behavior of **Copolymer-2** depending on the x value, RI was in minimum at Run 3 ($x = 0.58$) and slightly increased at Run 4 ($x = 0.37$) (**Table 3.3**). In the **Copolymer-2** system, the contribution of the H-bonds was smaller as x decreased, but RI was increased in the small- x region based on the more compact (i.e., small V_{vdw}) non-substituted PPS skeleton. Small n_D difference upon the demethylation (less than 0.02) suggested that larger H-bonds should be necessary for simultaneously enhancing RI and the film transparency. **Copolymer-2** showed larger birefringence than the corresponding **Me-Copolymer-1**, which was in the same trend as the case of the demethylation of **Me-OMePPS** (Table 3.3).

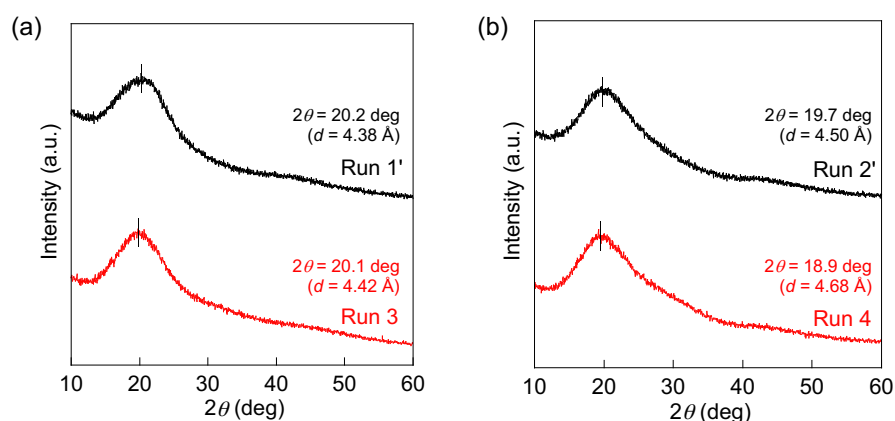


Figure 3.15. XRD profiles of **Me-Copolymer-1** and **Copolymer-2** including their average p-p spacing (determined from the diffraction angle of the halo peaktop): (a) Run 1 and 3, (b) Run 2 and 4.

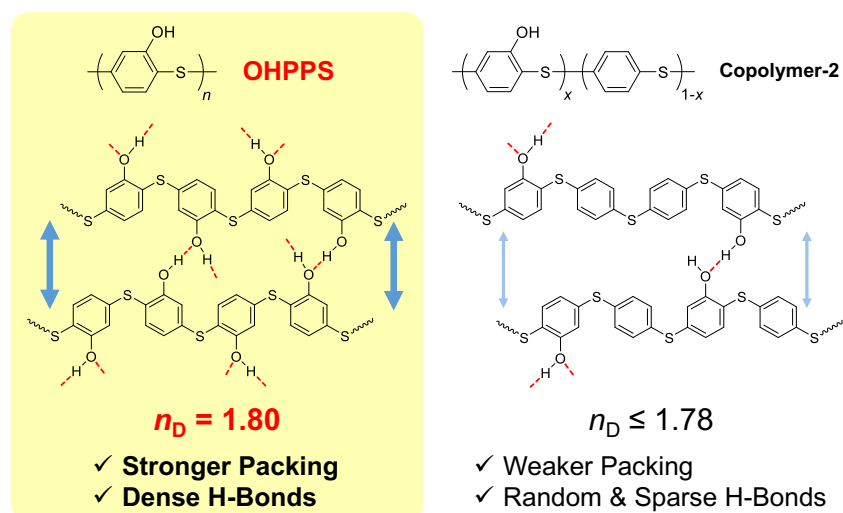


Figure 3.16. Schematic comparison of the chain packing of **OHPPS** and **Copolymer-2** (assuming the same amount of **OMePPS** unit and PPS unit was introduced). The width and the color intensity of the arrows described the strength of intermolecular H-bonds between the chains.

Finally, the structure-property relationships for the single H-bonded poly(phenylene sulfide)s was studied, especially by focusing on the H-bonding densities. From the XRD profiles of the copolymer system, the π - π spacing was slightly decreased for the positive effect of intermolecular H-bonds (**Figure 3.15**). However, considering that the diffraction patterns for **Copolymer-2** and **Me-Copolymer-1** were mostly the same patterns, comparing with the different profiles for **OHPPS** and **Me-OMePPS** with one or two halos depending on the structures (**Figure 3.6a**), the overall high-order structure was not drastically changed upon the demethylation in the case of the copolymer system. Therefore, the author concludes that the homopolymer **OHPPS** represented denser H-bonding networks than **Copolymer-2** with sparsely distributed H-bonds, leading to the significant increase of RI and transparency for **OHPPS** (**Figure 3.16**).

3.4 Dihydroxy-substituted Poly(phenylene sulfide) with Denser Hydrogen Bonds

Expanding the H-bond driven RI enhancing strategy for transparent polymers, which was demonstrated in the section 3.3, the author focused on the multiple H-bonding system: dihydroxy-substituted PPS (**DOHPPS**) (**Figure 3.17**). Taking account of the steric effect of side groups and densely incorporated H-bonding sites, higher RI represented by further reinforced H-bonds can be realized while maintaining amorphous nature of the PPS derivatives. **DOHPPS** was synthesized with two steps: (1) synthesis of the precursor, dimethoxy-substituted PPS (**DOMePPS**) via oxidative polymerization, (2) demethylating the side methoxy groups.

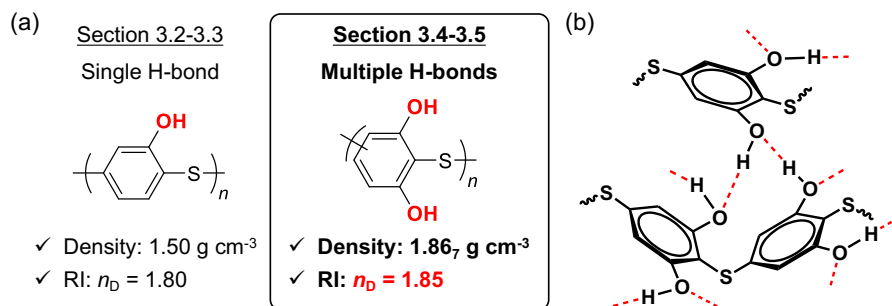
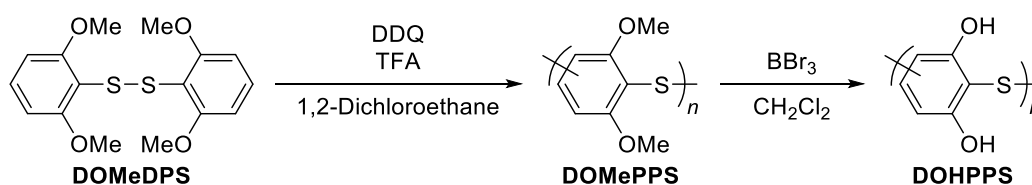


Figure 3.17. Outline of section 3.4-3.5. (a) OHPPS (section 3.2-3.3) and DOHPPS (this section and section 3.5) representing further ultrahigh RI. (b) Schematic representation for supramolecular H-bond crosslinking of DOHPPS (here, all sulfide bonds were assumed as *p*-linkages in this figure).

3.4.1 Synthesis of Dimethoxy-substituted PPS by Oxidative Polymerization



Scheme 3.3. Route for the OHPPS synthesis: oxidative polymerization and demethylation.

First, the precursor polymer, **DOMEPPS** was synthesized via the oxidative polymerization of bis(2,6-dimethylphenyl) disulfide (**DOMEPPS**) (**Scheme 3.3**). The polymerization was rapidly proceeded based on its lower oxidation potential of **DOMEPPS** (1.33 V vs. Ag/AgNO₃) than previously reported DPS monomers (approx. 1.4-1.6 V).^[17,19,35]

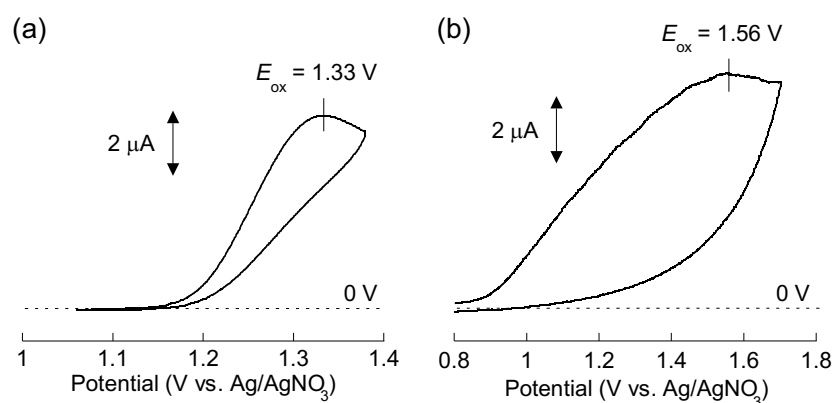
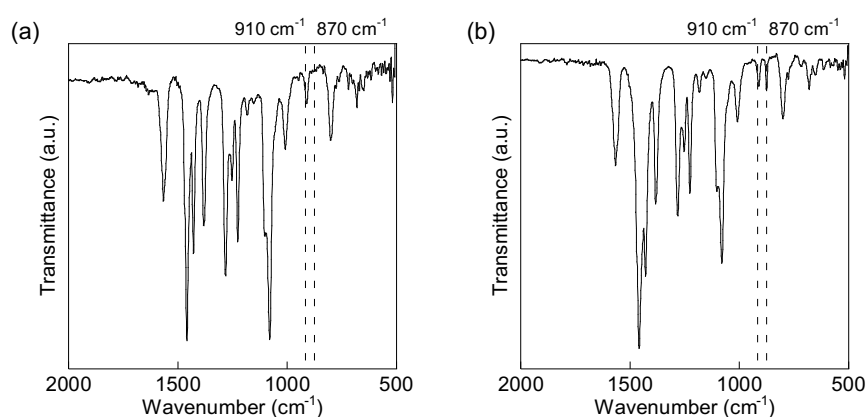


Figure 3.18. Cyclic voltammograms of the DPS monomers for the 10 mM solution in dichloromethane with 0.1 M TBABF₄ (Scanning rate: 10 mV s⁻¹): (a) **DOMEPS** and (b) bis(2-methoxyphenyl) disulfide (**OMeDPS**).

Table 3.4 Oxidative polymerization of **OMeDPS**^{a)}

Run	[DOMeDPS] (M)	[Acid] (M)	Yield (%)	M_n^b ($\times 10^3$)	M_w^b ($\times 10^3$)	M_w/M_n^b (-)
1	1	1	- ^{c)}	-	-	-
2	0.3	1	- ^{c)}	-	-	-
3	0.1	1	21	3.3	3.6	1.1
4	0.5	0.25	68	- ^{d)}	- ^{d)}	- ^{d)}
5	0.5	0.1	72	3.3	3.6	1.1

^{a)}Temp. = r.t., reaction time = 20 h. ^{b)}Determined by SEC (DMF containing 0.1 M LiCl). ^{c)}The reaction system was solidified and the product was unable to be collected. ^{d)}Sample was insoluble in DMF.

**Figure 3.19.** IR spectra of **DOMePPS**: (a) Run 4 and (b) Run 5 in **Table 3.4**.

The polymerization conditions, including monomer and acid concentrations on the oxidative polymerization, were optimized (Table 3.4). The product was successfully obtained with high yield and high solubility especially in the low monomer and acid concentration (run 5), whereas either large monomer or acid concentration afforded an insoluble product (runs 1, 2, and 4). **Figure 3.18** shows the IR spectra of **DOMePPS**. In the condition with low acid concentration (run 5), two absorption bands for C-H out-of-plane vibrations were observed at 910 and 870 cm^{-1} , which were ascribed to the isolated and adjacent aromatic protons, respectively, whereas only the former band was observed at the high acid concentration (run 4). Such selectivity was based on the substituent effect of two *o*-dimethoxy groups of **DOMeDPS**, which highly activated the electrophilic substitution reactions as well as the disulfide oxidation owing to the strong electron-donating features of methoxy groups. Accelerated oxidation and *m*-substitution complementarily produced branching structures under high concentration and finally produced excess 1,3,5-trisubstituted phenylene structures. Therefore, the molecular weight of **DOMePPS** while representing efficient solubility was limited in the low values (up to $M_w = 3.6 \times 10^3$ (runs 3 and 5)).

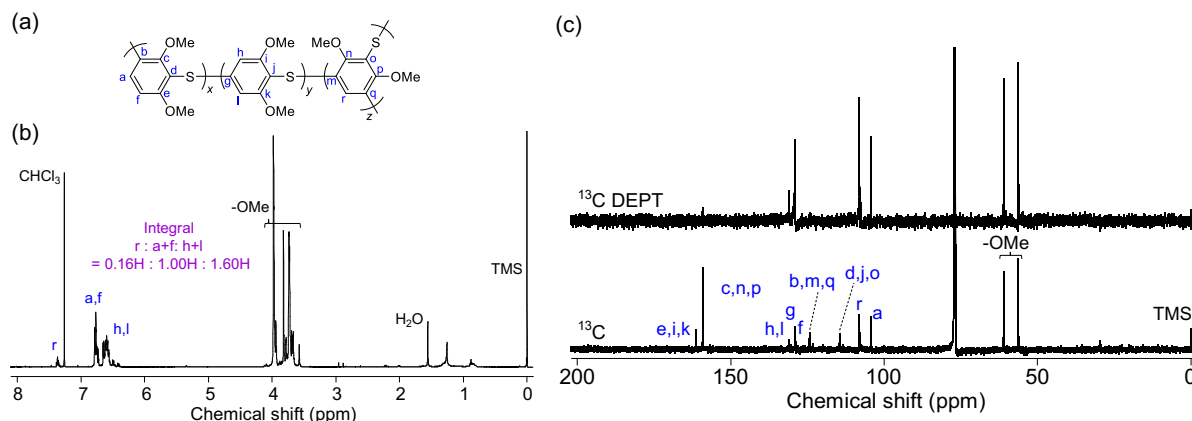


Figure 3.20. Spectroscopic analysis for **DOMEPPS** (run 5 in Table 3.4): (a) Structure of **DOMEPPS**. (b) ^1H NMR spectrum in chloroform-*d*. (c) ^{13}C and ^{13}C DEPT (135°) spectra in chloroform-*d*.

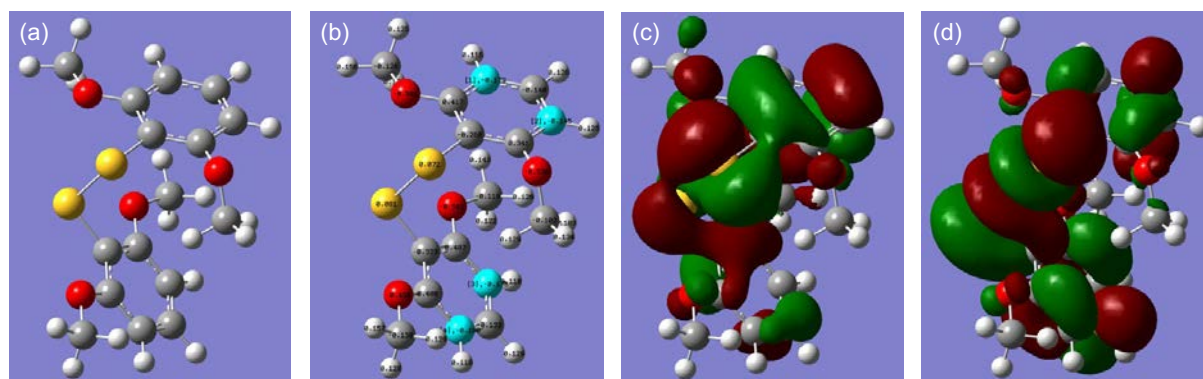


Figure 3.21. Structure optimization results of the DFT calculation for **DOMEPPS** at $\omega\text{B97XD}/6\text{-}31\text{G}(\text{d},\text{p})$ level of theory). (a) 3D optimized structure. (b) 3D Mulliken charge distributions, whose values (distribution ratio) were shown on each atom. The highlighted atoms, the aromatic carbons at the *m*-positions, showed the first and second largest negative values. (c) 3D shape of HOMO (isovalue = 0.02). (d) 3D shape of LUMO (isovalue = 0.02).

For the soluble samples, their structure analysis were further conducted (**Figure 3.20**). **Figure 3.20b** showed the ^1H NMR spectrum of run 5, and were observed the signals of four aromatic protons that can be assigned as the *m*-, *p*-, and 1,3,5-substituted phenylene structures. The composition ratio was determined as $x: y: z = 0.34:0.55:0.11$, suggesting less amount of the branched structures can maintain the solubility of the products. The ^{13}C NMR including DEPT spectra also confirmed the four C-H aromatic carbons with other aromatic and methoxy carbons, which were all constituent with the predicted structure from other spectroscopic analyses (**Figure 3.20c**). The density functional theory (DFT) calculations showed larger electron distribution at the *m*-position to disulfide than at the *p*-position according to the calculated Mulliken charge values, which also suggested high electrophilic substitution selectivity at the *m*-position (**Figure 3.21**).

3.4.2 Synthesis of dihydroxy-substituted PPS

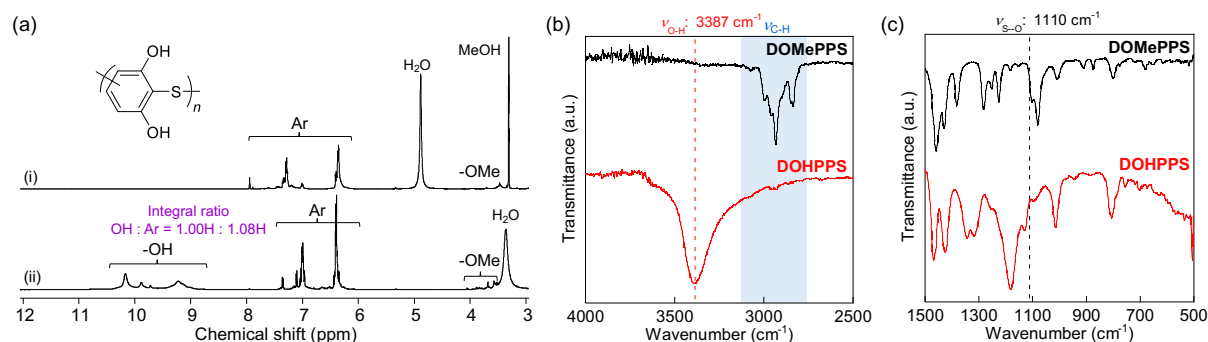


Figure 3.22. Structural analysis upon demethylation. (a) ¹H NMR spectra of **DOHPPS** in (i) methanol-*d*₄ and (ii) DMSO-*d*₆. Degree of demethylation was determined as 94% by comparing the integrals for the signals of aromatic and hydroxy groups. (b, c) IR spectra of **DOMEPPS** (black) and **DOHPPS** (red) in the range of (b) 4000-2500 cm⁻¹ and (b) 1500-500 cm⁻¹.

Following the similar route as the **OHPPS** synthesis, **DOHPPS** was synthesized by demethylating the side methoxy groups of **DOMEPPS** (see the second step of Scheme 3.3). Figure 3.22a showed the ¹H NMR spectrum of **DOHPPS**, resulting in high hydroxy content (94%) as well as the declined methoxy signals. The conversion did not reach 100% owing to the precipitation of the products corresponding to the low solubility in dichloromethane upon the demethylation. From the IR spectra in Figure 3.22b, remarkable decline in C-H vibration was observed while bands for the H-bonding hydroxy groups were simultaneously observed at 3387 cm⁻¹ that supported the ¹H NMR results. Absence of the bands for S-O bonds (ν_{S-O}: 1110 cm⁻¹) was confirmed after the demethylation in spite of the presence of the reactive interchain disulfide for **DOMEPPS** (Figure 3.22c). Such trend was different from the results for **OHPPS**, described in the section 3.2. 2,6-Dimethoxy or 2,6-dihydroxy substituents were steric enough to protect the disulfide bonds of **DOMEPPS** from the other side reactions involving BBr₃, and therefore methoxy groups and BBr₃ were selectively reacted to yield structurally defined **DOHPPS**.

3.5 Refractive Index Properties for Dihydroxy-containing Poly(phenylene sulfide)s

3.5.1 Thermal and Optical Properties

Despite the disubstituted hydroxy groups that can efficiently form H-bonding networks, **DOHPPS** exhibited anomalous bulk properties, which were described as follows. The XRD profiles in Figure 3.23a showed only broad halos without any crystalline diffraction peaks. Such peculiar broad peaks around the range of 2θ ~ 10-30 degrees were corresponded to the random π-π stacking between the aromatics, suggesting the disordered **DOHPPS** polymer chains based on the substituted PPS backbones with steric effect as well as the partial branching effect, in spite of the H-bond rich polymer skeleton. The DSC thermograms revealed the increased thermostability with the *T*_g shift from 116 °C to 140 °C, without any other thermal transition (Figure 3.23b). The synergistic effect of main-chain π-π

interactions and side-chain H-bonds resulted in a supramolecular amorphous networks in which the polymer chains were connected with strong intermolecular interactions.

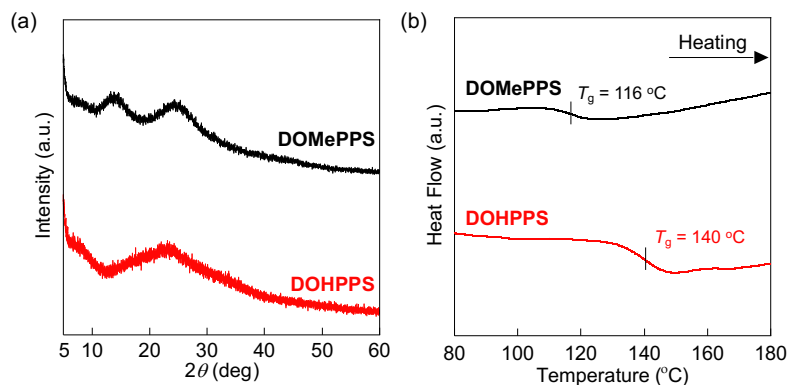


Figure 3.23. (a) XRD profiles of **DOMePPS** and **DOHPPS**. (b) DSC thermograms of **DOMePPS** (black) and **DOHPPS** (red).

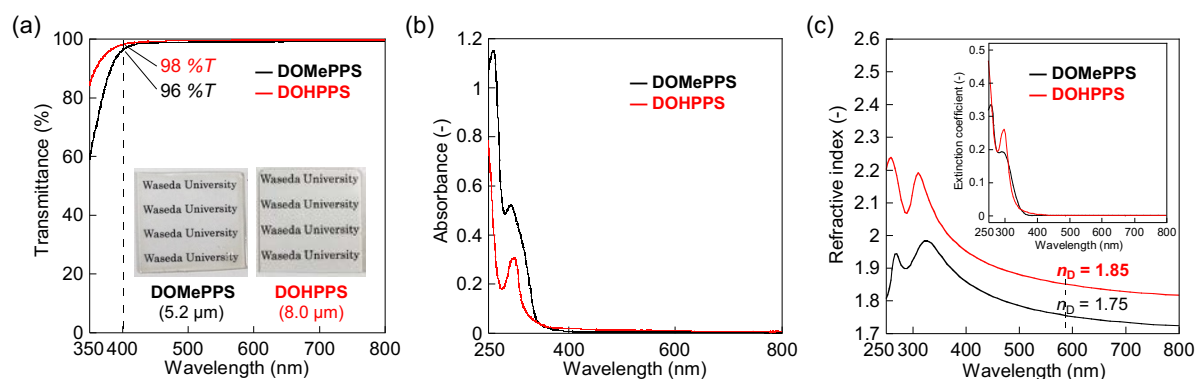


Figure 3.24. (a) Normalized UV-vis spectra of **DOMePPS** and **DOHPPS** (thin films with thickness of 1 μm) (inset: photographs of the polymer thin films on glass substrates). (b) UV-vis spectra in the solution (chloroform, 0.1 mM) (c) RI in the near-UV-visible region (inset: extinction coefficient of the polymers).

Thin film fabrication of **DOMePPS** and **DOHPPS** were successful in both dropcasting and spincoating techniques. As the resulting polymers were low molecular weight below 10^4 , fabrication of their free-standing films were unsuccessful, but they would be applied as thin-layer coatings on the conventional light-emitting materials because of its well film-formability on various substrates. The **DOHPPS** thin film on a glass substrate was transparent in the visible light region with a normalized transmittance of $> 98\%T$ for 1 μm thickness, which was higher than the **DOMePPS** film ($> 96\%T$) (**Figure 3.24a**). Although the cutoff wavelength (i.e., edge for the absorption) was blue-shifted in the UV-vis spectrum for the films upon demethylation, **DOHPPS** solution represented higher near-UV-visible transparency than **DOMePPS** whereas slight absorption was observed in the range of approx. 400-500 nm (**Figure 3.24b**). By spectroscopic ellipsometry, RI of **DOMePPS** and **DOHPPS** were determined as $n_D = 1.75$ and $n_D = 1.85$, respectively (**Figure 3.24c**), the latter of which was especially

higher than the estimated value ($n_{D, \text{estimated}} = 1.67$) using the empirical packing coefficient for amorphous polymers (0.681).^[36] The Abbe numbers were increased from $\nu_D = 15$ to 17, which were relatively in higher region compared to those properties of the previous HRIPs with ultrahigh RI over 1.8 (Table 3.5). Regarding the extinction coefficient (k), corresponding to the absorption of the thin films, k increased slightly from around 500 nm for **DOHPPS**, although did not increase in the case of **DOMePPS** (Figure 3.24c inset). Such behavior was in concordance with those absorption behaviors in the solution spectra, which included the gradual absorption only in the case of **DOHPPS** in the similar region, and the slight oxidized state of **DOHPPS** would induce such absorption bands.

Table 3.5. Comparison of optical properties of the ultrahigh-RI polymers^{a)}

Polymer	RI (wavelength)	Wavelength region intended for use	ν_D (-)	Absorptivity at 400 nm ($\times 10^2 \text{ cm}^{-1}$)	Ref.
DOMePPS	1.75 (D line)	Visible	15	1.7	This section
DOHPPS	1.85 (D line)	Visible	17	0.8	This section
OMePPS	1.73 (D line)	Visible	22	1.7	Chapter 2
OHPPS	1.80 (D line)	Visible	20	1.1	Section 3.3
Thianthrene- based PPS	1.8020 (633 nm)	Visible-NIR	- ^{b)}	7.6 ^{c)d)}	[37]
Poly(S-<i>r</i>-DIB) (20wt% DIB)	1.865 (633 nm)	NIR-IR	- ^{b)}	Yellow-red	[21]
Poly(S-<i>r</i>-TIB) (30wt% TIB)	1.836 (633 nm)	NIR-IR	- ^{b)}	Yellow-red	[22]
SCPs from sCVD	1.926 (D line)	Visible	14.698	3.2 ^{c)e)}	[38]

^{a)}Except for the polymers in this work, the values were taken from the previous report noted in the Ref. column. ^{b)}Not reported. ^{c)}Absorptivity at 400 nm was manually determined according to the reported UV-vis transmittance spectrum (or the reported value of transmittance at 400 nm) and the reported value of film thickness. The calculation process for absorptivity was based on our previous report (Ref. ^[19]). ^{d)}Calculated in Ref. ^[19]. ^{e)}The Value was determined using the values in Ref. ^[38] (Value of transmittance was read manually as 87.7 %T at 400 nm with a thickness of 1800 nm).

Density of the polymer was increased dramatically upon demethylation, from 1.416 for **DOMePPS** to 1.867 for **DOHPPS**. The ATR-IR spectra of **DOHPPS** revealed higher H-bonding density from the red-shifted H-bonding O-H vibration modes (3384 cm^{-1} for the powder state, 3329 cm^{-1} for the film state) (Figure 3.25). Therefore, several intermolecular interactions (mainly H-bond)

detected from the spectroscopic or X-ray analysis contributed to enhancing density of the polymer. In contrast to the previous section 3.3 (**OMePPS** and **OHPPS**), **DOHPPS** represented the same H-bonding effect while constructing more robust H-bond networks, which finally resulted in the enhanced RI and transparency.

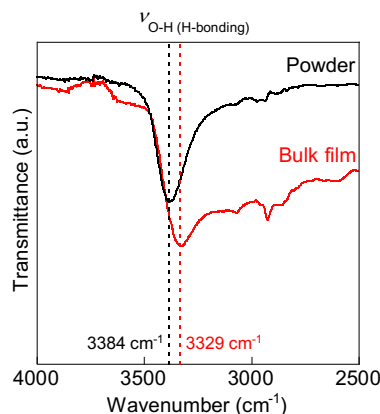


Figure 3.25. ATR-IR spectra of **DOHPPS** (hydroxy content: 84%) in the range of 4000-2500 nm, measured in the powder and the bulk film states (the bulk film was fabricated on the glass substrate). Note that the **DOHPPS** sample for this figure was different from the sample for other figures and tables.

In the latter sections (3.4 and 3.5), 2,6-dihydroxy PPS (**DOHPPS**) was synthesized for the first time and its properties as an optical material were investigated. Especially, disubstituted hydroxy groups, which can multiply form H-bonds between other chains, gave dense supramolecular networks with an ultrahigh RI of $n_D = 1.85$ as well as high visible transparency, which were further excellent properties compared to the single H-bonded **OHPPS**. In other words, more H-bonding scaffolds in the bulk polymeric system allows further RI enhancement in concordance with larger density (i.e. denser packing and declining free volume). However, the author should note that the resulting OH-containing polymers were low molecular weight (M_w ca. $3\text{-}4 \times 10^3$), the branching/bent structures of **DOHPPS** might differently affect the RI properties in the high-molecular-weight OH-containing systems (i.e., density/RI increment of **DOHPPS** and M_w might be in trade-off). Overall, this systematic study has demonstrated the concept, which explains that RI of a polymer is enhanced with the maintained amorphous nature through the synergistic combination of various interactions, such as steric effects, aromatic interactions, and intermolecular H-bonds. This concept provides new insights regarding intermolecular interaction effect on RI properties, which stands in a different role from the common RI-enhancing approach involving only high-[R] groups.

3.6 Experimental Section

3.6.1 Materials and Procedures for Sections 3.2-3.3

Reagents. Sodium borohydride, tetrahydrofuran (THF), dichloromethane, methanol, 1,1,2,2-tetrachloroethane, N,N-dimethylformamide (DMF), chloroform and hydrochloric acid were purchased

from Kanto Chemical Co. Iodomethane, boron tribromide (1 M solution in dichloromethane), diphenyl disulfide (DPS), Vanadyl acetylacetonate (VO(acac)₂), 2,3,-dichloro-5,6-dicyano-1,4-benzoquinone (DDQ), trifluoroacetic acid (TFA), trifluoroacetic anhydride (TFA anhydride), trifluoromethanesulfonic acid (TfOH) and N,N-dimethylacetamide (DMAc) were purchased by Tokyo Chemical Industry Co. Ethanol was purchased by Junsei Chemical Co. All reagents were used as received without further purification. The precursor polymer, poly(2-methoxy-1,4-phenylenesulfide) (**OMePPS**), was prepared via the oxidative polymerization of bis(2-methoxyphenyl) disulfide (**OMeDPS**) according to the previous report.^[41]

Synthesis of Methyl-End Functionalized Methoxy-substituted PPS. End-functionalization of **OMePPS** with methyl group was synthesized via one-pot reaction of disulfide reduction^[37] and nucleophilic reaction with thiolate and iodomethane.^[38] To a 50 mL two necked flask, **OMePPS** (M_n (GPC) = 2.5×10^3 , 0.6 g, 0.24 mmol of disulfide) was dissolved in THF (8.1 mL), and was added iodomethane (299 mL, 4.8 mmol) and stirred until the solution became homogeneous. The solution was then cooled to 0 °C, and was added dropwise sodium borohydride (182 mg, 4.8 mmol) dissolved in water (0.9 mL) to initiate the reduction of disulfide with the production of H₂ gas and stirred for 30 minutes at 0 °C, 2.5 hours at room temperature. After the reaction, the solution was precipitated in methanol (300 mL) and the precipitate was collected after filtration and drying in vacuo at room temperature and 80 °C to give Methyl-end functionalized **OMePPS** (**Me-OMePPS**) as a white powder (0.47 g, 79 % yield). The obtained polymer was soluble in DMF, THF, chloroform and dichloromethane, partially soluble in toluene and insoluble in acetone, methanol and water. GPC (eluent: THF, polystyrene standard): $M_n = 2.1 \times 10^3$, PDI = 1.8. End functionality f was estimated by comparing the M_n value of **Me-OMePPS** obtained from ¹H NMR ($M_{n, \text{NMR}}$) and the value obtained by GPC ($M_{n, \text{GPC}}$) as follows: $f = M_{n, \text{NMR}} / M_{n, \text{GPC}} = 0.94$.

Synthesis of Hydroxy-substituted PPS. Procedures for demethylation of methoxy group described below was referred to the previous report.^[39] To a 100 mL flask, **Me-OMePPS** (M_n (NMR) = 2.1×10^3 , 0.3 g, 2.17 mmol of methoxy group) was dissolved in dichloromethane (9.1 mL) under argon atmosphere, and was cooled to 0 °C and 1 M boron tribromide solution in dichloromethane (5.42 mL, 5.42 mmol) was added dropwise via a syringe with stirring and mixed for 30 minutes. The solution was then stirred at room temperature for 20 hours, yielding white precipitate. The mixture was then quenched by adding water (12 mL) dropwise, then solvents were removed via rotary evaporation, the residue was redissolved in DMF (10 mL) and was precipitated into 1 M hydrochloric acid aqueous to obtain the product. The precipitate was collected and reprecipitated by acetone/1 M hydrochloric acid aqueous (= 1/10 (v/v)), collected and dried under vacuo to give **OHPPS** as a white powder (0.21 g, 79 % yield). The obtained polymer was soluble in DMF, THF and acetone and insoluble in methanol, chloroform and water. M_n (¹H NMR) = 2.0×10^3 .

Oxidative Stability Test of OHPPS. To a 50 mL flask, **OHPPS** (M_n (NMR) = 2.1×10^3 , 150 mg) was dissolved in DMF (15 mL), was heated and refluxed at 80 °C under O₂ bubbling (flow rate: 5 mL min⁻¹) for 72 hours. The solution was precipitated in 1 M hydrochloric acid aqueous (300 mL), and the precipitate was collected, washed with water and dried under vacuo to give the product as a white powder (138.8 mg, 93 % yield, M_n (NMR) = 2.1×10^3). The ¹H NMR, IR and UV-vis spectra of **OHPPS** showed the same features as those of **OHPPS** before the bubbling (Figure S3-S5), indicating no structural change was occurred during the O₂ exposure.

Demethylation of Methoxy-Substituted PPS without End-Functionalization. Demethylation of **OMePPS** was also conducted as a controlled experiment to confirm the effect of remained disulfide bond. To a 30 mL flask, **OMePPS** (150 mg, 1.09 mmol of methoxy group) was dissolved in dichloromethane (4.52 mL) under argon atmosphere, and was cooled to 0 °C and 1 M boron tribromide solution in dichloromethane (2.71 mL, 2.71 mmol) was added dropwise via a syringe with stirring, and was mixed for 30 minutes and at room temperature for 20 hours. The mixture was then quenched by adding water (20 mL) dropwise, and then solvents were removed to give orange solid. The residue was redissolved in DMF (25 mL) and was precipitated into 1 M hydrochloric acid aqueous (500 mL) to obtain the product. The precipitate was collected and reprecipitated by DMF/water (= 3/50 (v/v)), again collected and dried under vacuo to give the product as a whitish orange powder (69.0 mg, 50 % yield). The obtained polymer was soluble in DMF, partially soluble in acetone and THF and insoluble in methanol, chloroform and water.

Synthesis of Copolymer-1. Here synthetic procedure of **Copolymer-1** with $x = 0.55$ was explained as an example. To a 100 mL flask, 2,3-dichloro-5,6-dicyano-1,4-benzoquinone (DDQ) (6.81 g, 30 mmol) was dispersed in chloroform (10 mL), was added trifluoroacetic acid (TFA) (765 mL, 10 mmol) and powder mixture of monomers (bis(2-methoxyphenyl) disulfide (**OMeDPS**) (4.18 g, 15 mmol) and diphenyl disulfide (DPS) (3.27 g, 15 mmol)) was quickly added with vigorous stirring, and mixed at room temperature for 40 hours. The solution was diluted with chloroform (15 mL), and the precipitate was filtrated to be removed. The filtrate was precipitated in ethanol with 5 vol% hydrochloric acid mixture (800 mL), collected and washed with ethanol, methanol, 3 wt% potassium hydroxide aqueous and water, respectively. The product was dissolved into chloroform again and reprecipitated in 20-fold excess methanol with 5 vol% hydrochloric acid mixture. The reprecipitated product was collected, washed (methanol, 3 wt% potassium hydroxide aqueous and water) and dried in vacuo at room temperature and 80 °C respectively to give Copolymer-1 as a white solid (5.74 g, 77 % yield). The obtained polymer was soluble in DMF, THF, chloroform and dichloromethane, partially soluble in toluene and insoluble in acetone, methanol and water, same as **OMePPS**. Introduction ratio: $x = 0.55$ (Determined by ¹H NMR). GPC (eluent: THF, polystyrene standard): $M_w = 4.2 \times 10^3$, PDI = 2.0. Further

end-capping of **Copolymer-1** by iodomethane was conducted in a similar manner as the abovementioned procedure for **Me-OMePPS**.

Synthesis of Hydroxyl-Substituted Copolymer (Copolymer-2). To a 100 mL flask, **Me-Copolymer-1** ($x = 0.61$, 0.5 g, 2.59 mmol of methoxy group) was dissolved in dichloromethane (21.7 mL) under argon atmosphere, and was cooled to 0 °C and 1 M boron tribromide solution in dichloromethane (6.48 mL, 6.48 mmol) was added dropwise via a syringe with stirring and mixed for 30 minutes at 0 °C and 20 hours at room temperature. The mixture was then quenched by adding water (20 mL) dropwise, then solvents were removed via rotary evaporation. The residue was redissolved in acetone (30 mL) and was precipitated into 1 M hydrochloric acid aqueous (500 mL) to obtain the product. The precipitate was collected and reprecipitated by acetone/1M hydrochloric acid aqueous (1/20) twice, subsequently collected and dried under vacuo to give **OHPPS** as a white powder (0.44 g, 94 % yield). The obtained polymer was soluble in DMF and THF, insoluble in methanol and water. Introduction ratio: $x = 0.58$ (Determined by $^1\text{H NMR}$). $M_n (^1\text{H NMR}) = 1.7 \times 10^3$.

Preparation of End-Functionalized Polymer Films (Me-OMePPS and Me-Copolymer-1). End-Functionalized Polymer (30 mg) was dissolved into DMAc (2 mL) and filtrated by 0.2 mm PTFE filter to obtain the polymer solution (concentration: 15 mg mL⁻¹). The solution (400 mL) was casted onto the glass substrate (25 mm × 25 mm) and was kept in vacuo at 50 °C for 12 hours and at room temperature overnight to give a transparent, visually colorless thin film. On preparing the sample for the haze measurement, the quartz substrate (25 mm × 25 mm) was used instead.

Preparation of Hydroxy-containing Polymer Films (OHPPS and Copolymer-2). **OHPPS** (30 mg) was dissolved into DMF (2 mL) and filtrated by 0.2 mm PTFE filter to obtain the polymer solution (concentration: 15 mg mL⁻¹). The solution (400 mL (Entries 1-4 in Table S4) or 300 mL (Entry 5 in Table S4)) was casted onto the 25 mm × 25 mm glass substrate (25 mm × 18.75 mm only in the case of Entry 5) and was kept in vacuo (-0.1 MPa) at 50 °C for 12 hours and at room temperature for 2 days to give a transparent, visually colorless thin film with a thickness of 7.9 nm. Thin film of **Copolymer-2** was prepared in the same procedure as above. On preparing the sample for the haze measurement, the quartz substrate (25 mm × 25 mm) was used instead.

Preparations of the Ellipsometry Samples of the End-Functionalized Polymers. End-functionalized polymer (30 mg) was dissolved into 1,1,2,2-tetrachloroethane (1 mL) and filtrated by 0.2 mm PTFE filter to obtain the polymer solution (concentration: 30 mg mL⁻¹). The solution was spin-coated onto the Si wafer at 500 rpm for 45 sec and at 1500 rpm for 50 sec, kept in vacuo (-0.1 MPa) at 50 °C for 12 hours and at room temperature overnight to give a homogeneous thin film.

Preparations of the Ellipsometry Samples of the Hydroxy-containing Polymer Samples.

OHPPS (60 mg) was dissolved into DMF (1 mL) and filtrated by 0.2 mm PTFE filter to obtain the polymer solution (concentration: 60 mg mL⁻¹). The solution was spin-coated onto the Si wafer at 2000 rpm for 30 sec, and was kept in vacuo (-0.1 MPa) at 50 °C for 12 hours and at room temperature for 2 days. Samples of **Copolymer-2** were prepared in the same procedure as above.

Humidity test. **OHPPS** (M_n (NMR) = 2.1×10^3 , M_n (GPC) = 2.5×10^3) was dissolved in DMF and its sample was prepared through spincoating the solution on a Si wafer with the same procedure described in section 2.3. After the spectroscopic ellipsometry measurement, the sample was placed in the sealed plastic box, in which humidity was set to 85 ± 3 %RH. The sample was kept at room temperature overnight, was then taken out from the box, and its spectroscopic ellipsometry was immediately conducted.

Determination of birefringence. Birefringence of polymers were determined from the spectroscopic ellipsometry results by adopting the anisotropic uniaxial layer fitting model. In case of a polymer thin film with aromatic rings fabricated on a substrate, in-plane RI (n_{TE}) is generally higher than out-of-plane RI (n_{TM}) due to the orientation of the polymer chain in the direction parallel to the substrate.^[4] Therefore, the fitting model was constructed assuming that the polymer had a retardation between the in-plane and out-of-plane axis (i.e., $n_x = n_y \neq n_z$), and ordinary and extraordinary RI corresponded to n_{TE} ($= n_x = n_y$) and n_{TM} ($= n_z$), respectively. Birefringence (Δn) of the polymer thin film was estimated according to the following equation:^[4]

$$\Delta n = n_{TE} - n_{TM}$$

In the present study, Δn values were determined from the n_{TE} and n_{TM} values measured at 633 nm.

Measurements. ¹H NMR spectra (500 MHz) were measured by JEOL ECX-500 or ECZ-500 spectrometer. ¹H DOSY-NMR spectra (600 MHz) were measured by Bruker AVANCE III 600 spectrometer (pulse sequence: ledbpgp2s). For the preparation of NMR samples, tetramethylsilane was used as an internal standard. Gel permeation chromatography (GPC) measurements were conducted by TOSOH HLC 8220, using tetrahydrofuran (THF), chloroform, or DMF (containing 0.1 M LiCl) as an eluent. Fourier-transformed infrared spectra were measured by Jasco FT/IR 6100 spectrometer, using KBr pellets (for powder samples). On measuring Attenuated total refraction-IR (ATR-IR) spectrum of the bulk film, ATR PRO ONE was attached to the spectrometer. UV-vis spectra of the thin films or diluted solution of polymers were measured by JASCO-V-550. Haze of the thin films were measured by Perkin Elmer LAMBDA 650, to which the integral sphere was attached. Haze values of the films were determined according to the Japanese Industrial standard (JIS K7136), by comparing diffusion transmittance and total light transmittance. Wide-angle X-ray powder diffraction (XRD) profiles were obtained by Rigaku RINT-Ultima III, using Cu (CuK α : $\lambda = 1.54$ Å) as an X-ray source. Differential

scanning calorimetry (DSC) measurements were conducted by TA Instruments Q200 by scanning with a heating/cooling rate of $20\text{ }^{\circ}\text{C min}^{-1}$. Thermogravimetric analyses (TGA) were conducted by Rigaku TG8120 under nitrogen flow with a heating rate of $10\text{ }^{\circ}\text{C min}^{-1}$, using α -alumina as a standard sample. Refractive indices and birefringence of polymers were measured by Horiba UVISEL ERAGMS iHR320. The Abbe numbers were calculated from the n_D , n_F , and n_C values obtained from the spectroscopic ellipsometry, according to Eq. (2) in the main text. Thickness of films were measured by stylus profiler, KLA Tencor P-6. Density of polymers were measured by SHIMADZU AccuPycII 1340.

3.6.2 Materials and procedures for sections 3.4-3.5

Reagents. 2-bromo-1,3-dimethoxybenzene, 1,2-dibromoethane, iodine, 2,3-dichloro-5,6-dicyano-1,4-benzoquinone (DDQ), tetrabutylammonium tetrafluoroborate (TBABF₄) were purchased from Tokyo Chemical Industry Co. Tetrahydrofuran (THF, dehydrated), sulfur, hydrochloric acid, chloroform, sodium thiosulfate, 1,2-dichloroethane (dehydrated), dichloromethane (dehydrated), N,N-dimethylformamide (DMF, dehydrated), 1,1,2,2-tetrachloroethane, sodium hydroxide, sodium chloride, and sodium sulfate were purchased from Kanto Chemical Co. Methanol and hexane were purchased from Kokusan Chemical Co. Magnesium turnings, trifluoroacetic acid (TFA), and boron tribromide (1 M solution in dichloromethane) were purchased from Fujifilm Wako Chemical Co. All reagents were used as received without further purification. Bis(2-methoxyphenyl) disulfide (**OMeDPS**) in the CV measurement was prepared following the procedure in the chapter 2.

Synthesis of bis(2,6-dimethoxyphenyl) disulfide. Bis(2,6-dimethoxyphenyl) disulfide (**DOMeDPS**) was prepared via Grignard reaction using the aromatic bromide as a starting material and subsequent oxidation of thiol by arranging several literatures.^[42,43] To a 100 mL two necked flask, Mg turnings (1.16 g, 48 mmol) was dispersed in THF (20 mL) and was purged with nitrogen after the addition of two drops of 1,2-dibromoethane. Then the solution of 2-bromo-1,3-dimethoxybenzene (8.68 g, 40 mmol) dissolved in THF (10 mL) was added dropwise and refluxed for 2 hours at room temperature. The solution was cooled to $0\text{ }^{\circ}\text{C}$, was added sulfur (0.70 g, 22 mmol), and was stirred at room temperature for another 3 hours. The reaction was quenched with 10vol% hydrochloric acid (50 mL) and was extracted with chloroform (150 mL). The solvent was then removed by rotary evaporator to give a crude product for 2,6-dimethoxybenzenethiol. Without further purification, the crude was dissolved in chloroform (100 mL), was added 0.5 mM iodine solution in methanol (15 mL) dropwise, and was stirred for 1 hour. The reaction was quenched with 15wt% sodium thiosulfate aqueous (added until the brownish color of unreacted iodine faded) and the solvent was removed by rotary evaporator. The product was extracted with chloroform and was purified by recrystallization with chloroform/methanol (= 1/10 (v/v)) to give **DOMeDPS** as a pale-yellow solid (4.30 g, 63 % yield). ¹H NMR (chloroform-*d*, 500 MHz, ppm, TMS): δ 7.23 (t, $J = 7.9, 8.5\text{ Hz}$, 2H), 6.51 (d, $J = 8.5\text{ Hz}$, 4H), 3.69 (s, 12H, -OCH₃). ¹³C NMR (chloroform-*d*, 125 MHz, ppm, TMS): δ 161.2, 130.9, 114.0, 103.8,

56.0. FAB-MS (m/z): M^+ (calcd for $C_{16}H_{18}O_4S_2$), 338.1; found, 338.1.

Synthesis of DOMEPPS. A typical procedure has been follows (run 5 in **Table 3.4**): To a 10 mL flask, **DOMeDPS** (0.17 g, 0.5 mmol) was added and dissolved in 1,2-dichloroethane (1 mL). The polymerization was initiated by adding trifluoroacetic acid (TFA) (7.5 μ L, 0.1 mmol) and DDQ (0.11 g, 0.5 mmol) and the solution was stirred for 20 hours at room temperature. The solution was then diluted with additional 1,2-dichloroethane (2 mL) for dispersing the precipitated impurities (by-produced hydroquinone) which was removed by subsequent filtration. The filtrate was precipitated in ethanol containing 5 vol% hydrochloric acid (300 mL in total), and the precipitate was collected through filtration, was washed with ethanol, 5 wt% potassium hydroxide aqueous, water, and methanol, and was dried in vacuo to obtain **DOMePPS** as white powder (0.12 g, 72 % yield). **DOMePPS** was soluble in chloroform and dichloromethane, partially soluble in DMF, DMSO, and DMAc, and insoluble in THF, methanol, water, acetone, and hexane.

Demethylataion of DOMEPPS. To a 50 mL flask, **DOMePPS** (0.2 g, 2.4 mmol of methoxy groups) was added and dissolved in dichloromethane (10 mL) under argon atmosphere. The solution was cooled to 0 °C, was added 1 M BBr_3 solution in dichloromethane (6 mL, 6 mmol), and was stirred at 0 °C for 30 minutes and at room temperature for 20 hours. The reaction was quenched with water and the solvent was removed by rotary evaporator. The crude product was dissolved in methanol (10 mL) and was precipitated in water (300 mL). The precipitate was collected through filtration, washed with water, and was dried in vacuo to obtain **DOHPPS** as white powder (0.16 g, 77 % yield). **DOHPPS** was soluble in DMF, DMSO, DMAc, THF, methanol, and acetone, partially soluble in chloroform, and insoluble in dichloromethane, water, and hexane.

Polymer film preparation on glass. A typical preparation procedure has been described as follows: A polymer was dissolved in solvent (1,1,2,2-tetrachloroethane for **DOMePPS**, DMF for **DOHPPS**) with a concentration of 30 mg mL⁻¹ and was filtrated with a 0.2 mm PTFE filter. The filtrate (400 mL) was poured carefully on a glass substrate (2.5 cm \times 2.5 cm) and was placed at 40 °C in vacuo to obtain a thin film.

Polymer film preparation on Si wafer. A polymer was dissolved in 1,1,2,2-tetrachloroethane with a concentration of 30 mg mL⁻¹ and was filtrated through a 0.2 mm PTFE filter. The filtrate was poured carefully on a Si wafer and spin-coated through the following procedure: slope, 3 sec \rightarrow 500 rpm, 45 sec \rightarrow slope, 3 sec \rightarrow 2000 rpm, 40 sec \rightarrow slope, 3 sec. The polymer-coated substrate was dried in vacuo for an overnight and was used for spectroscopic ellipsometry (thickness: ca. 40-70 nm).

DFT calculations. Density Functional Theory (DFT) calculations were performed by

Gaussian 16 software. The calculation procedure was designed by arranging the previous report:^[44] First the geometry of **DOMeDPS** was optimized by PM6 calculation, and its structure optimization was subsequently carried out through DFT calculation at ω B97XD/6-31G(d,p) level of theory.

References

- [1] T. Higashihara, M. Ueda, *Macromolecules* **2015**, *48*, 1915.
- [2] T. S. Kleine, R. S. Glass, D. L. Lichtenberger, M. E. Mackay, K. Char, R. A. Norwood, J. Pyun, *ACS Macro Lett.* **2020**, *9*, 245.
- [3] J. G. Liu, M. Ueda, *J. Mater. Chem.* **2009**, *19*, 8907.
- [4] Y. Terui, S. Ando, *J. Polym. Sci. B Polym. Phys.* **2004**, *42*, 2354.
- [5] E. K. Macdonald, M. P. Shaver, *Polym. Int.* **2015**, *64*, 6.
- [6] L. Fang, J. Sun, X. Chen, Y. Tao, J. Zhou, C. Wang, Q. Fang, *Macromolecules* **2020**, *53*, 125.
- [7] L. Fang, C. Wang, M. Dai, G. Huang, J. Sun, Q. Fang, *Mater. Chem. Front.* **2021**, *5*, 5826.
- [8] H. Mutlu, E. B. Ceper, X. Li, J. Yang, W. Dong, M. M. Ozmen, P. Theato, *Macromol. Rapid Commun.* **2019**, *40*, e1800650.
- [9] Y. Zhou, Z. Zhu, K. Zhang, B. Yang, *Macromol. Rapid Commun.* **2023**, e2300411.
- [10] J.-G. Liu, Y. Nakamura, Y. Suzuki, Y. Shibasaki, S. Ando, M. Ueda, *Macromolecules* **2007**, *40*, 7902.
- [11] N. Fukuzaki, T. Higashihara, S. Ando, M. Ueda, *Macromolecules* **2010**, *43*, 1836.
- [12] H. Okuda, R. Seto, Y. Koyama, T. Takata, *J. Polym. Sci. A Polym. Chem.* **2010**, *48*, 4192.
- [13] S. Iino, S. Sobu, K. Nakabayashi, S. Samitsu, H. Mori, *Polymer* **2021**, *224*, 123725.
- [14] N.-H. You, T. Higashihara, Y. Oishi, S. Ando, M. Ueda, *Macromolecules* **2010**, *43*, 4613.
- [15] M.-C. Fu, Y. Murakami, M. Ueda, S. Ando, T. Higashihara, *J. Polym. Sci. A Polym. Chem.* **2018**, *56*, 724.
- [16] M. Jikei, J. Katoh, N. Sato, K. Yamamoto, H. Nishide, E. Tsuchida, *Bull. Chem. Soc. Jpn.* **1992**, *65*, 2029.
- [17] K. Yamamoto, M. Jikei, J. Katoh, H. Nishide, E. Tsuchida, *Macromolecules* **1992**, *25*, 2698.
- [18] F. Aida, Y. Takatori, D. Kiyokawa, K. Nagamatsu, K. Oyaizu, H. Nishide, *Polym. Chem.* **2016**, *7*, 2087.
- [19] S. Watanabe, K. Oyaizu, *Bull. Chem. Soc. Jpn.* **2020**, *93*, 1287.
- [20] S. Watanabe, K. Oyaizu, *ACS Appl. Polym. Mater.* **2021**, *3*, 4495.
- [21] J. J. Griebel, S. Namnabat, E. T. Kim, R. Himmelhuber, D. H. Moronta, W. J. Chung, A. G. Simmonds, K.-J. Kim, J. van der Laan, N. A. Nguyen, E. L. Dereniak, M. E. Mackay, K. Char, R. S. Glass, R. A. Norwood, J. Pyun, *Adv. Mater.* **2014**, *26*, 3014.
- [22] T. S. Kleine, N. A. Nguyen, L. E. Anderson, S. Namnabat, E. A. LaVilla, S. A. Showghi, P. T. Dirlam, C. B. Arrington, M. S. Manchester, J. Schwiegerling, R. S. Glass, K. Char, R. A. Norwood, M. E. Mackay, J. Pyun, *ACS Macro Lett.* **2016**, *5*, 1152.

- [23] L. E. Anderson, T. S. Kleine, Y. Zhang, D. D. Phan, S. Namnabat, E. A. LaVilla, K. M. Konopka, L. Ruiz Diaz, M. S. Manchester, J. Schwiegerling, R. S. Glass, M. E. Mackay, K. Char, R. A. Norwood, J. Pyun, *ACS Macro Lett.* **2017**, *6*, 500.
- [24] Q. Li, K. L. Ng, X. Pan, J. Zhu, *Polym. Chem.* **2019**, *10*, 4279.
- [25] T. S. Kleine, T. Lee, K. J. Carothers, M. O. Hamilton, L. E. Anderson, L. Ruiz Diaz, N. P. Lyons, K. R. Coasey, W. O. Parker, L. Borghi, M. E. Mackay, K. Char, R. S. Glass, D. L. Lichtenberger, R. A. Norwood, J. Pyun, *Angew. Chem. Int. Ed.* **2019**, *58*, 17656.
- [26] C.-L. Tsai, G.-S. Liou, *Chem. Commun.* **2015**, *51*, 13523.
- [27] M.-C. Fu, M. Ueda, S. Ando, T. Higashihara, *ACS Omega* **2020**, *5*, 5134.
- [28] F. Aida, Y. Takatori, D. Kiyokawa, K. Nagamatsu, H. Nishide, K. Oyaizu, *Chem. Lett.* **2015**, *44*, 767.
- [29] M. C. Haibach, N. Lease, A. S. Goldman, *Angew. Chem. Int. Ed.* **2014**, *53*, 10160.
- [30] E. Tsuchida, K. Yamamoto, H. Nishide, S. Yoshida, M. Jikei, *Macromolecules* **1990**, *23*, 2101.
- [31] Y. Nakagawa, Y. Suzuki, T. Higashihara, S. Ando, M. Ueda, *Polym. Chem.* **2012**, *3*, 2531.
- [32] C. S. Ha, M. C. Choi, J. Wakita, S. Ando, *Macromolecules* **2009**, *42*, 5112.
- [33] A. Javadi, Z. Najjar, S. Bahadori, V. Vatanpour, A. Malek, E. Abouzari-Lotf, A. Shockravi, *RSC Adv.* **2015**, *5*, 91670.
- [34] K. Yamamoto, N. Iwasaki, H. Nishide, E. Tsuchida, *Eur. Polym. J.* **1992**, *28*, 341.
- [35] K. Yamamoto, E. Tsuchida, H. Nishide, M. Jikei, K. Oyaizu, *Macromolecules* **1993**, *26*, 3432.
- [36] G. L. Slonimskii, A. A. Askadskii, A. I. Kitaigorodskii, *Polymer Science U.S.S.R.* **1970**, *12*, 556.
- [37] Y. Suzuki, K. Murakami, S. Ando, T. Higashihara, M. Ueda, *J. Mater. Chem.* **2011**, *21*, 15727.
- [38] D. H. Kim, W. Jang, K. Choi, J. S. Choi, J. Pyun, J. Lim, K. Char, S. G. Im, *Sci Adv* **2020**, *6*, eabb5320.
- [39] A. Ookawa, S. Yokoyama, K. Soai, *Synth. Commun.* **1986**, *16*, 819.
- [40] T. Eom, A. Khan, *Chem. Commun.* **2020**, *56*, 7419.
- [41] K. Nishimori, M. Tenjimbayashi, M. Naito, M. Ouchi, *ACS Appl. Polym. Mater.* **2020**, *2*, 4604.
- [42] S. Watanabe, T. Takayama, K. Oyaizu, *ACS Polym Au* **2022**, *2*, 458.
- [43] T. Yanagi, K. Nogi, H. Yorimitsu, *Chem. Eur. J.* **2020**, *26*, 758.
- [44] K. Hatakeyama - Sato, C. Go, T. Akahane, T. Kaseyama, T. Yoshimoto, K. Oyaizu, *Batteries & Supercaps* **2022**, *5*, 4.

Figures, tables, and texts are partially adapted with permission from S. Watanabe, K. Oyaizu, *Macromolecules* **2022**, *55*, 2252-2259 (Copyright © 2022 American Chemical Society); S. Watanabe, K. Oyaizu, *ACS Appl. Polym. Mater.* **2023**, *5*, 2307-2311 (Copyright © 2023 American Chemical Society)

Chapter 4:

Refractive Index Enhancement of Poly(phenylene sulfide)s by Dual Control of Polarizability and Density

Contents

- 4.1 Introduction
 - 4.2 Synthesis of Sulfur-rich Aromatic Polymers via Oxidative Polymerization
 - 4.3 Copolymers with Hydroxy- and Methylthio-substituted Poly(phenylene sulfide)s
 - 4.4 Systematic Control of Optical Properties via Hydrogen Bonding and Polarizability
 - 4.5 Experimental Section
- References

4.1 Introduction

Enhancing refractive index (RI) of a polymer while representing high visible transparency is a critical issue not only in polymer chemistry but also in the field of materials science.^[1] Especially, the criteria for the refractive index (RI, n) values have been increased in accordance with the development of optoelectronics. Especially in the field of light-emitting materials, transparent materials with ultrahigh RI (over 1.8) are required for the usage as the encapsulants for organic light-emitting diodes that can increase the light extraction efficiency compared to the previous device structures.^[2] However, few reports of high-refractive-index polymers (HRIPs) that achieve ultrahigh RI as well as visible transparency and amorphous properties have been reported before.

In response to such request, introducing large amount of sulfur is one of the promising solutions that improve RI of a polymer.^[3] The representative example is inverse vulcanization of the multi-functionalized vinyl monomers with elemental sulfur, although these polymers resulted in strong absorption in the near-UV and visible regions that showed coloration and low Abbe numbers that have limited their application range.^[4,5] Recently, sulfur chemical vapor deposition (sCVD) technique to yield transparent sulfur-containing polymers have been established.^[6-8] These sCVD polymers exhibited were less colored in the thin-film states and much higher RI (up to $n_D = 1.982$)^[9] compared with the inverse vulcanized polymers. Large numbers of short polysulfide chains prepared from elemental sulfur and multi-vinyl comonomers are the keys for overcoming the trade-off between RI and transparency,^[6,9] although this sCVD process is applicable for only the vapor-phase reactions (i.e., unable to expand for solution-processing). Further versatile methods toward ultrahigh RI, adequate Abbe numbers, and film formability have been extensively desired. On the other hand, the author demonstrated the hydrogen bonding (H-bonding)-driven RI enhancement strategy using poly(phenylene sulfide) (PPS) derivatives with a moderately high- $[R]$ backbone, based on the reduction of the free volume via intermolecular interactions.^[10] As a proof of concept, monohydroxy- or dihydroxy-containing PPS represented ultrahigh RI over 1.8 as well as high Abbe numbers (~ 20).^[10,11] The RI and transparency of the hydroxy-substituted PPS increased according to the amount and density of the polymer, and such unprecedented properties were ascribed to the synergistic contribution of sulfur-based main chain and H-bonds in the side chains.

In this chapter, the author further expanded this proof-of-concept results toward the general strategy of ultrahigh-RI polymer designing. The designed polymer is methylthio-substituted PPS (**SMePPS**), representing ultrahigh RI ($n_D = 1.81$) based on its high sulfur content (42 wt%). By copolymerizing **SMePPS** with H-bonding **OHPPS** moieties, the RI reached up to $n_D = 1.85$ while remaining high Abbe number of $v_D = 20$. To the best of my knowledge, this is the first example that achieved the balanced optical properties with ultrahigh RI, adequate Abbe number, and visible transparency that were beyond the empirical n_D - v_D trade-off. The systematic relationship between multi-scale structures and optical properties were also investigated, which also supported that introduction of sulfur and H-bonds cooperatively contributes to the realization of such outstanding optical properties.

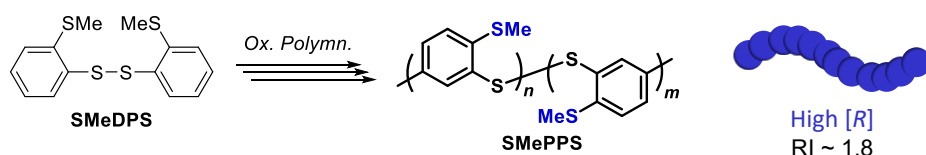
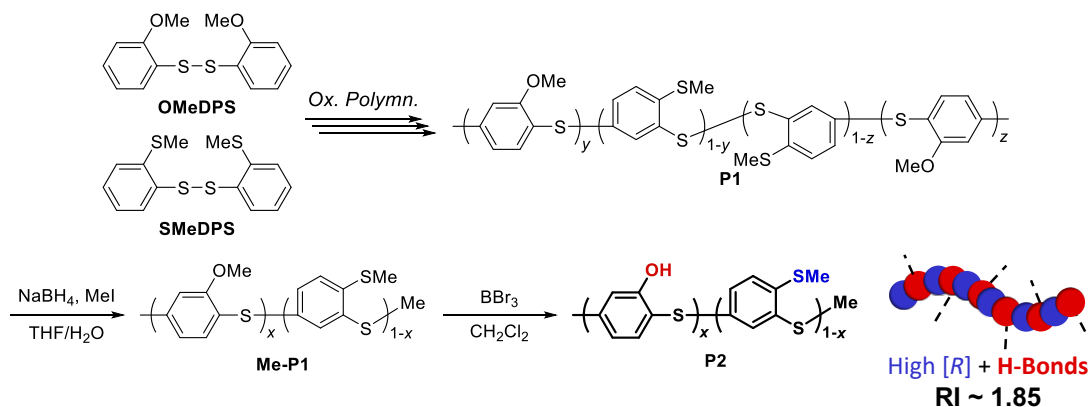
a) PPS with High Sulfur Content**b) Further Incorporation of "H-Bonding Scaffolds"**

Figure 4.1. Outline of the synthesis in this chapter. (a) Oxidative polymerization of bis(2-methylthiophenyl) disulfide to yield **SMePPS**. (b) Synthesis of **SMePPS-OHPPS** Copolymers with higher density, which were designed based on the further incorporation of the H-bonding scaffolds in the **SMePPS** units.

4.2 Synthesis of Poly(2-methoxy-1,4-phenylenesulfide)

4.2.1 Oxidative Polymerization

First, methylthio-substituted PPS (**SMePPS**) was synthesized through the oxidative polymerization of bis(2-methylthiophenyl) disulfide (**SMeDPS**) and its structure including the polymerization mechanism was investigated. The monomer **SMeDPS** was prepared via Grignard reaction of 1-bromo-2-thioanisole and subsequent oxidation of the thiol, affording yellow needle-like crystals. The structure was characterized by ^1H , ^{13}C NMR, and FAB-MS. From the cyclic voltammetry, **DOMeDPS** represented high oxidation potential (1.56 V vs. Ag/AgCl) enough to proceed the polymerization (See Chapter 4.5). The oxidative polymerization of **SMeDPS** proceeded in both the oxygen oxidation with the $\text{VO}(\text{acac})_2\text{-H}^+$ system^[12] or using 2,3-dichloro-5,6-dicyano-1,4-benzoquinone (**DDQ**)^[13] in the acidic condition.

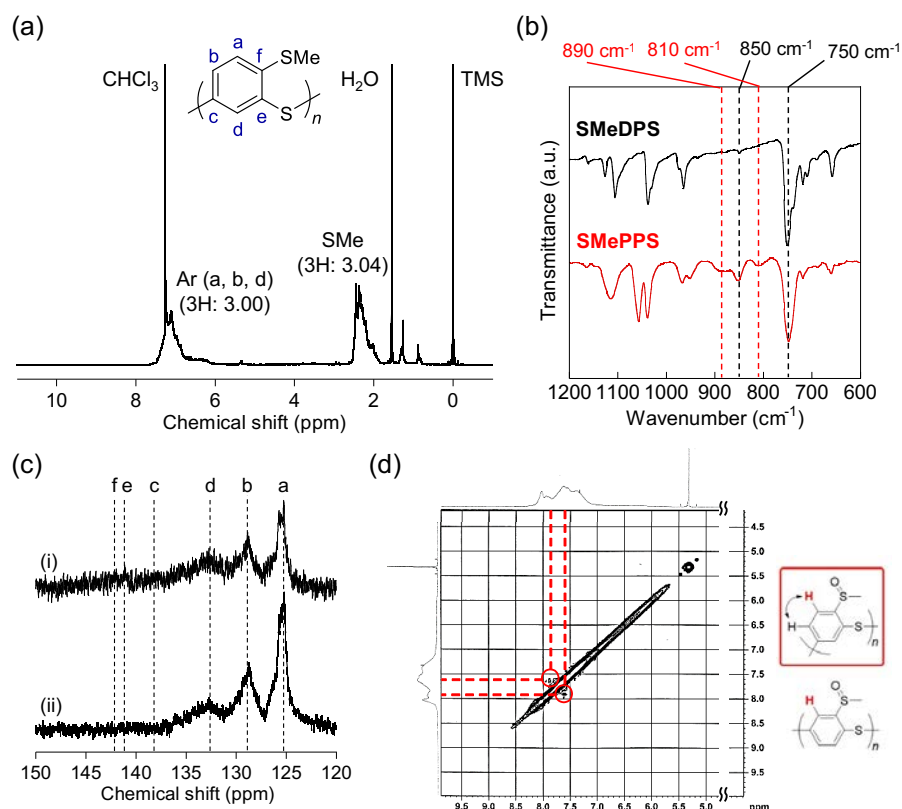


Figure 4.2. Spectroscopic analysis of **SMePPS**. (a) ^1H NMR spectrum in chloroform-*d*. (b) IR spectra of **SMeDPS** and **SMePPS** ($1200\text{--}600\text{ cm}^{-1}$). (c) (i) ^{13}C and (ii) ^{13}C DEPT NMR spectra in chloroform-*d*. (d) ^1H - ^1H COSY spectrum of the sulfoxide-containing **SMePPS** (**SOMePPS**). 2-Methylthio-1,5-thiophenylene repeating structure (structure circled by red square) was revealed according to the correlation signals of the aromatic protons.

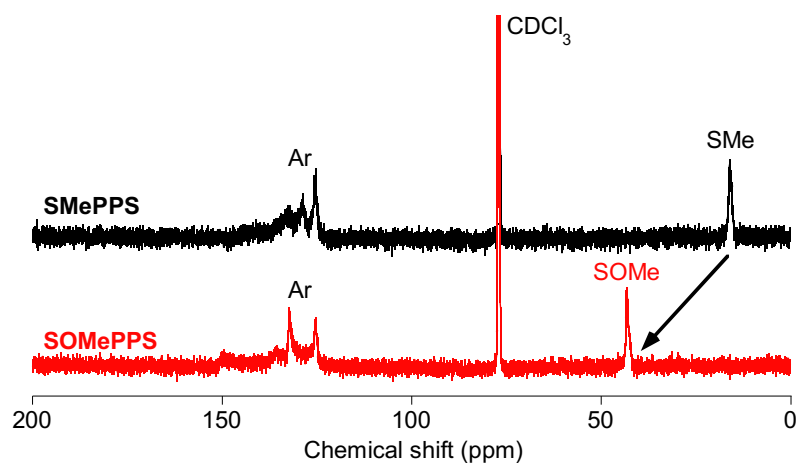


Figure 4.3. ^{13}C NMR spectra of **SMePPS** and **SOMePPS** in chloroform-*d*.

Structure of **SMePPS** including the polymerization behavior was analyzed with spectroscopic analyses. **Figure 4.2a** showed the ^1H NMR spectrum of **SMePPS**, representing the linear structure of **SMePPS** (i.e., two C-S linkages per repeating unit) according to the signals of aromatic and methylthio

protons with the similar integrals. From the IR spectrum (**Figure 4.2b**), the 1,2,4-substituted phenylene of **SMePPS** was detected from not only the absorption bands at 750 and 850 cm^{-1} (terminal *o*-substituted phenylene) but also new bands at 810 and 890 cm^{-1} (characterized as 1,2,4-phenylene). These results indicated the oxidative polymerization of **SMeDPS** proceeded via 4- or 5-phenylene selective electrophilic substitution reactions. The ^{13}C NMR spectra of **SMePPS** represented six signals of aromatic carbons, three of which were also observed in the DEPT spectra (i.e., aromatic C–H carbons), and the obtained polymer was characterized as a single trisubstituted aromatic structure (**Figure 4.2c**).

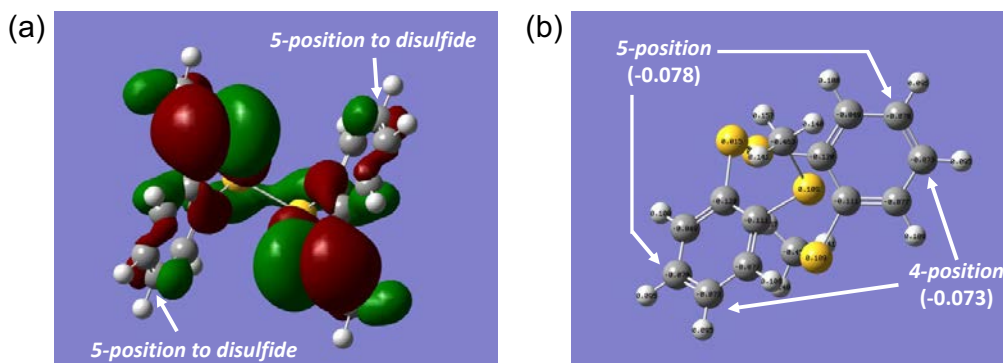


Figure 4.4. Structural Optimization of **SMeDPS** with the DFT calculations (at $\omega\text{B97XD}/6\text{-}31\text{G(d,p)}$ level of theory). (a) the shape of HOMO. (b) Mulliken charge distribution. The Mulliken charge values were directly shown on each atom.

However, the abovementioned results cannot conclude whether **SMePPS** had 1,2,4- or 1,2,5-trisubstituted phenylene structure. For the precise determination of the substitution position, the methylthio group was further selectively derived to the sulfoxide unit via the *m*CPBA oxidation in order to separate these two peaks. After the oxidation, the ^1H – ^1H COSY spectrum of the sulfoxide-labeled polymer revealed a ^1H – ^1H correlation observed between the signals at 7.9 and 7.6 ppm, supporting the 1,2,5-substructures with the downfield adjacent aromatic protons just next to the labeled sulfoxide (**Figure 4.2d**), and therefore the structure of **SMePPS** was finally determined as that of poly(2-methylthio-1,5-phenylenesulfide). ^{13}C NMR also monitored the sulfide of **SMePPS** selectively converted only to the sulfoxides and no signals for sulfone was detected (**Figure 4.3**). The density functional theory (DFT) calculation also held the higher reactivity of aromatic carbons at the 5-position compared to the 4-position, which was confirmed by the larger HOMO distribution and negatively larger Mulliken charge of the 5-position of the carbon (**Figure 4.4**).

Table 4.1. Oxidative polymerization of **SMeDPS**^{a)}

Run	Solvent (DN ^{b)})	Oxidant	[SMeDPS] (M)	Yield (%)	$M_n^c)$ ($\times 10^3$)	$M_w^c)$ ($\times 10^3$)	$M_w/M_n^c)$ (-)	$T_g^d)$ ($^{\circ}\text{C}$)
1	Nitrobenzene (4.4)	DDQ	1	80	0.9	1.8	2.0	84
2	Chloroform (4)	DDQ	1	70	0.9	1.8	2.1	93
3	Dichloromethane (1)	DDQ	1	82	0.9	1.8	2.1	96
4	1,2-Dichloroethane (0)	DDQ	1	85	1.3	2.3	1.8	103
5	1,2-Dichloroethane (0)	DDQ	2	77	1.0	1.9	1.9	97
6	1,2-Dichloroethane (0)	DDQ	3	79	0.9	2.0	2.1	92
7	1,2-Dichloroethane (0)	DDQ	0.5	75	1.0	1.9	1.9	102
8	1,2-Dichloroethane (0)	O ₂ with VO(acac) ₂	1	31	0.6	0.9	1.5	76

^{a)}Temp. = r.t., reaction time = 20 h, [TFA] = 1 M. ^{b)}Donor number of a solvent noted in the previous reports.^{[14-}

^{16]} ^{c)}Determined by SEC (eluent: chloroform). ^{d)}Determined by DSC (Scan rate: 20 $^{\circ}\text{C min}^{-1}$).

The reaction conditions were optimized with various solvents and monomer concentrations, but the molecular weight of **SMePPS** resulted in relatively low values ($M_w = 2.3 \times 10^3$ in maximum) according to size exclusion chromatography (SEC) (Table 4.1). Considering that **SMeDPS** represented low oxidation potential, oxidation of **SMeDPS** was instantly proceeded at the beginning of the polymerization and the subsequent electrophilic substitution reaction would be the rate-determining step in this system. Better progress of the polymerization for the conditions with a low-donor-number solvent and low concentration also held this trend. Therefore, such small M_w values were ascribed to the low Friedel-Crafts reactivity of **SMeDPS** compared with other DPS derivatives,^[14,15] owing to the 5-phenylene selective substitution that occurs high steric hindrance during the polymerization.

4.2.2 Thermal Properties

The differential scanning calorimetry (DSC) thermogram of **SMePPS** (Run 4 in Table 4.1) showed a single baseline shift derived in concordance with the glass transition temperature of $T_g = 103$ $^{\circ}\text{C}$ (Figure 4.5a inset). The XRD profile without no crystalline diffraction peaks like the case for pristine PPS also supported the amorphous nature of **SMePPS**, which was ascribed to the steric effect of the side methylthio group, which were in a larger molecular size than a methoxy group (Figure 4.5a). From the thermogravimetric analysis (TGA), thermal degradation temperature of **SMePPS** was

determined as $T_{d5} = 319\text{ }^{\circ}\text{C}$, similar values to other PPS derivatives (Figure 4.5b).^[14,17]

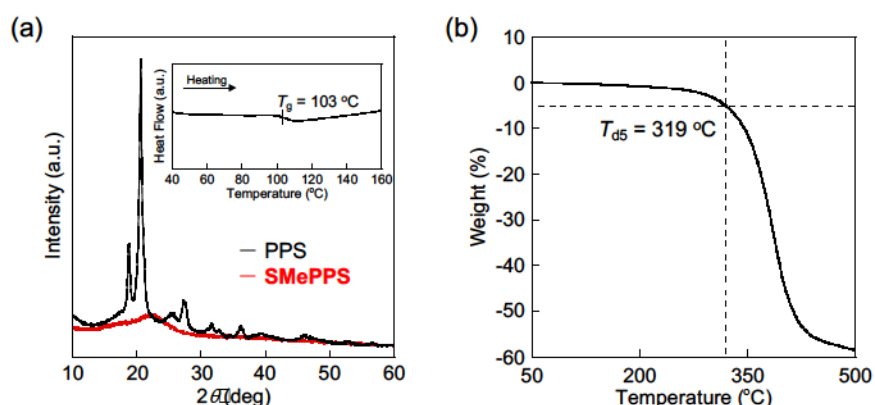


Figure 4.5. Thermal properties of SMePPS. (a) XRD profiles of SMePPS (red) and PPS (black) (Inset: DSC thermogram of SMePPS (run 4 in Table 4.1) with a scan rate: $20\text{ }^{\circ}\text{C min}^{-1}$). (b) TGA trace under nitrogen (heating rate: $10\text{ }^{\circ}\text{C min}^{-1}$).

4.2.3 Optical Properties

Thin films of SMePPS were successfully prepared on either a glass and a Si substrate. SMePPS showed visible transparency in the film state with a normalized transmittance of $> 94\%T$ for $1\text{ }\mu\text{m}$ thickness ($> 74\%T$ for the film with a thickness of $5.4\text{ }\mu\text{m}$) (Figure 4.6a). Sulfur-rich skeleton led to lower transparency compared with the previous OHPPS with similar RI ($n_D = 1.80$)^[10] but remained in high values. The spectroscopic ellipsometry revealed the ultrahigh RI of SMePPS ($n_D = 1.81$) with an Abbe number of $\nu_D = 19$, which were more balanced optical properties among the ultrahigh RI polymers (Figure 4.6b). Extinction coefficient of SMePPS and other PPS derivatives suggested the trend for the film transparency (Figure 4.6c). As sulfur can enhance the polarizability as well as steric hindrance, the resulting sulfur-rich SMePPS represented ultrahigh RI and adequate Abbe number simultaneously.

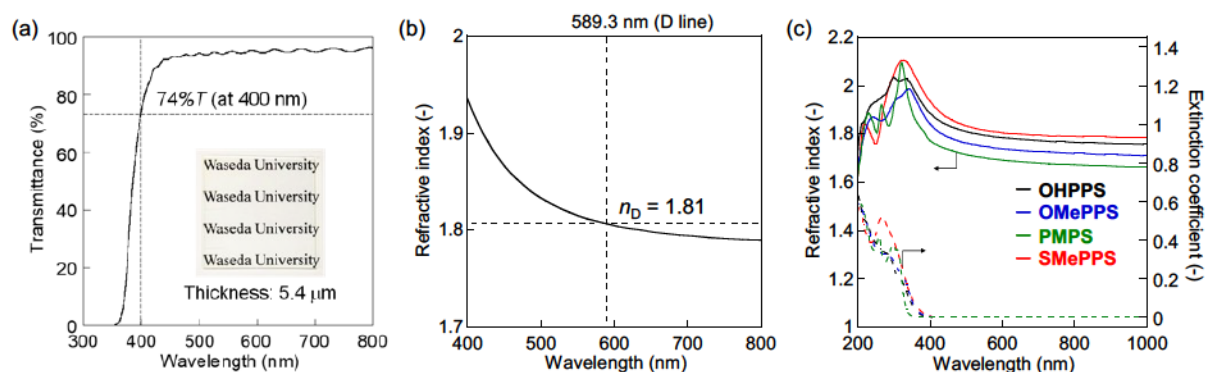


Figure 4.6. Optical properties. (a) UV-vis spectrum of the SMePPS thin film (thickness: $5.4\text{ }\mu\text{m}$) (inset: photograph of the SMePPS film on a glass). (b) RI of SMePPS. (c) RI (solid lines) and extinction coefficient (broken lines) of SMePPS and other PPS derivatives.

4.3 Copolymers with Hydroxy- and Methylthio-substituted Poly(phenylene sulfide)s

4.3.1 Synthesis of Copolymers

The author subsequently investigated the copolymers of **SMePPS** and **OHPPS**, because **OHPPS** unit can serve as a H-bonding trigger in the bulk PPS networks and can contribute to higher $[R]/V$ values.^[14] Such **SMePPS-OHPPS** copolymers (**P2**) were synthesized in three steps: preparation of copolymers with **SMePPS** and **OMePPS** (**P1**), capping of the end disulfide, and demethylation of the end-functionalized **P1** (**Figure 4.1b**).

Table 4.2 Synthesis of **P1**

Run	Feed ratio [OMeDPS]/[SMeDPS] (-)	Yield (%)	Composition ratio x^a (-)	M_n^b ($\times 10^3$)	M_w^b ($\times 10^3$)	M_w/M_n^b (-)	T_g^c ($^\circ\text{C}$)
1	0.25/0.75	70	0.29	1.2	2.5	2.2	97
2	0.50/0.50	77	0.53	1.5	3.2	2.2	105
3	0.75/0.25	81	0.77	2.4	5.5	2.2	114

^{a)}Determined by $^1\text{H NMR}$. ^{b)}Determined by SEC (eluent: chloroform). ^{c)}Determined by DSC (Scan rate: $20\text{ }^\circ\text{C min}^{-1}$).

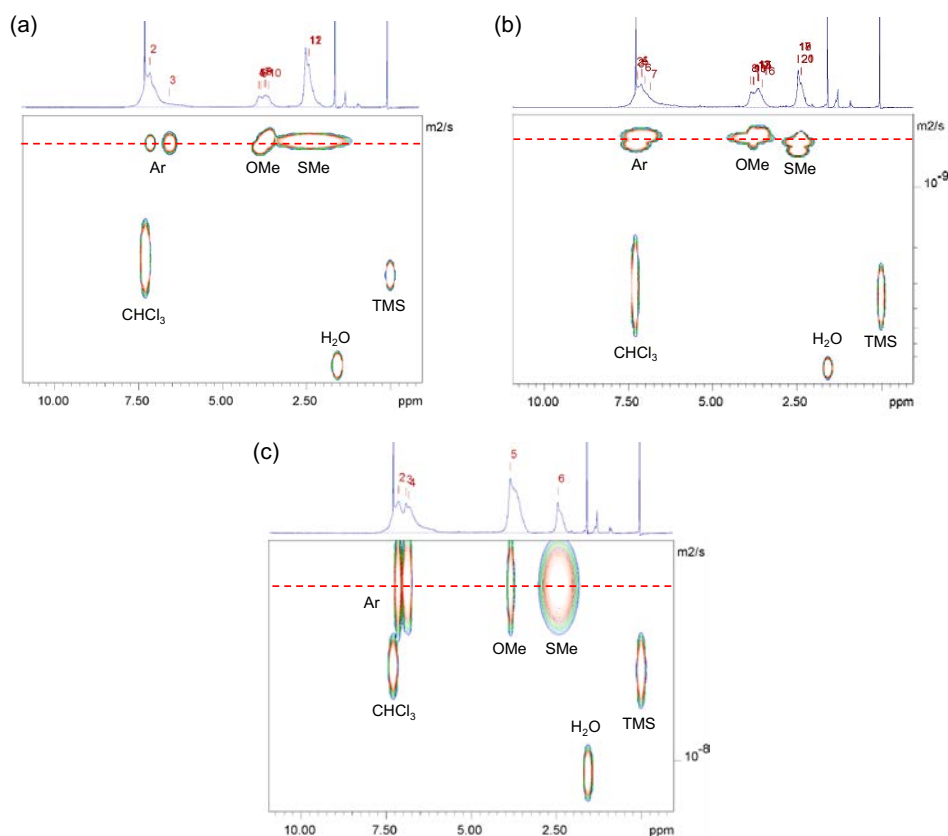


Figure 4.7. DOSY-NMR spectra of **P1** in chloroform-*d*: (a) run 1, (b) run 2, and (c) run 3.

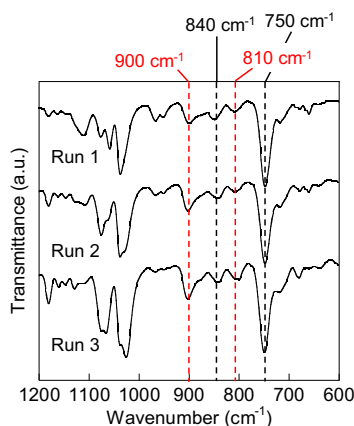


Figure 4.8. IR spectra of **P1**.

In the first step, copolymers of **SMePPS** and **OMePPS** units (**P1**) were synthesized with three different unit ratio via the oxidative polymerization of **SMeDPS** and **OMeDPS** as precursors. The composition ratio for **P1** was determined by ^1H NMR with the values similar to the feed ratio, indicating equal contribution of each monomer unit in the copolymerization system (**Table 4.2**, the spectra were displayed in **Fig. 4.10**). The progress of the copolymerization was checked from the DOSY-NMR spectra of **P1** shown in **Figure 4.7**, with the same diffusion coefficient for all signals for the main and side chain groups. The IR spectra revealed the absorptions characterized as the 1,2,4-substituted ($\delta_{\text{C-H}}$: 810 and 900 cm^{-1}) and terminal 1,2-substituted benzene rings ($\delta_{\text{C-H}}$: 750 and 840 cm^{-1}), which were consistent with the repeating structure corresponding to the introduced monomers (**Figure 4.8**).

The copolymerization kinetics were monitored for precisely understand the further structure-property relationships (**Figure 4.9**). On the copolymerization of **OMePPS/SMePPS** = 1/1 (mol/mol), molecular weight has increased in the early stage of the polymerization (within the first hour) (**Figure 4.9a** and **4.9b**). Such polymerization time-course suggested the step-growth mechanism of the copolymerization system in the beginning, meanwhile disulfide exchange or oligomer-oligomer coupling were the plausible major reactions in the middle-latter polymerization stage. Taking account of the order of the oxidation potentials for **SMeDPS** and **OMeDPS**: 1.56 V (see section 4.2) and 1.58 V, ^[16–18] respectively, these monomers were consumed in similar rate and composition ratio x were similar in any reaction time as approx. 0.5, close value to the case for theoretical monomer consumption (red dots for **Figure 4.9e**). Therefore, **P1** can be obtained as random-like copolymers close to the ideal distribution, which was in different sequence from that of **OMePPS-PPS** copolymers having the gradient distribution with the PPS-rich composition (black dots for **Figure 4.9e**). Although the molecular weight of **P1** were still in the small values with $M_w \sim 10^3$, the incorporation of **OMePPS** unit increased molecular weight up to $M_w = 5.5 \times 10^3$ (run 3 in **Table 4.2**), based on the higher reactivity of **OMeDPS** with the *p*-linkage and slightly high Friedel-Crafts reactivity in comparison to the **SMeDPS** with a *m*-linked feature.

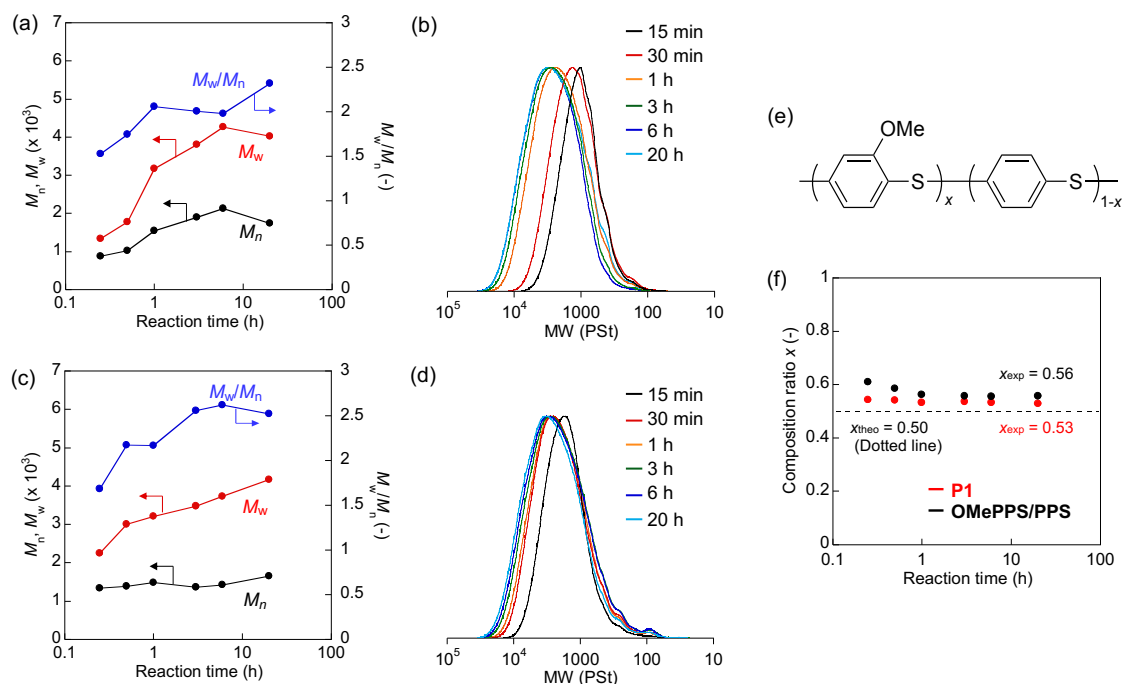


Figure 4.9. Time-course for the copolymerization. (a) M_n , M_w , and M_w/M_n (Fed: [OMeDPS]/[SMedPS] = 1/1). (b) SEC traces for the **P1** fractions (eluent: chloroform, UV detector (254 nm)). (c) M_n , M_w , and M_w/M_n (Fed: [OMeDPS]/[DPS] = 1/1). (d) SEC traces for the **OMePPS-PPS** fractions. (e) Chemical structure of **OMePPS/PPS**. (f) Composition ratio for the fractionated **P1** and **OMePPS/PPS**.

4.3.2 Post-polymerization Modification of Copolymers

Table 4.3 Synthesis of **Me-P1**

Run	Polymer	Yield (%)	x^a (-)	End functionality a) ^b (%)	M_n^a ($\times 10^3$)	M_n^b ($\times 10^3$)	M_w^b ($\times 10^3$)	M_w/M_n^b (-)	T_g^c ($^{\circ}\text{C}$)	d) at 400	n_D^e (-)	ν_D^e (-)	%T
													nm
1	P1	-	0.29	-	-	1.2	2.5	2.2	97	85	1.79	19	
1'	Me-P1	57 ^{f)}	0.29	88	0.9	0.8	1.2	1.5	92	98	1.78	20	
2	P1	-	0.53	-	-	1.5	3.2	2.2	105	93	1.77	18	
2'	Me-P1	73 ^{g)}	0.53	91	1.3	1.2	1.9	1.6	101	98	1.77	21	
3	P1	-	0.77	-	-	2.4	5.5	2.2	114	95	1.75	19	
3'	Me-P1	80 ^{h)}	0.77	100	1.6	1.6	2.9	1.8	108	99	1.75	19	

Determined by ^{a)}¹H NMR (solvent: chloroform-*d*), ^{b)}SEC (chloroform), ^{c)}DSC (scan rate: 20 $^{\circ}\text{C min}^{-1}$), ^{d)}UV-vis (normalized thickness of 1 μm), and ^{e)}spectroscopic ellipsometry. Yield for ^{f)}Run 1, ^{g)}Run 2, and ^{h)}Run 3.

Next, a series of **P2** were prepared via the post-polymerization modification of **P1** with the same route as described in the section 3.2. The disulfide bonds in the **P1** were converted to prepare methyl-terminated **P1** (**Me-P1**) prior to the demethylation (**Table 4.3**).

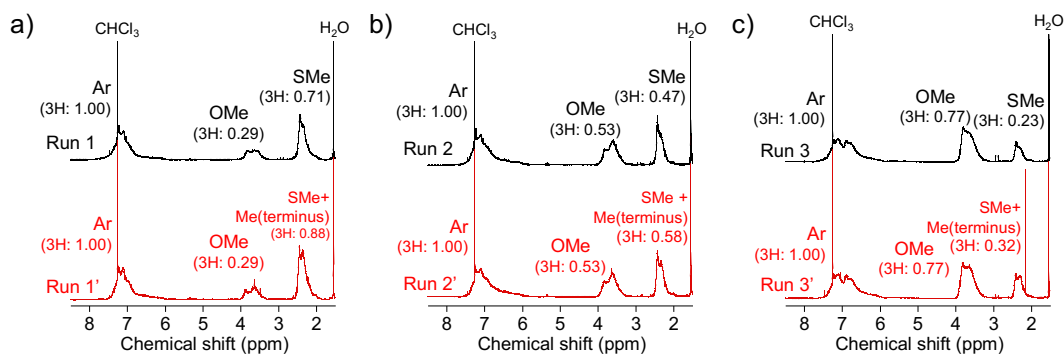


Figure 4.10. ^1H NMR spectra before and after the end-termination (chloroform-*d*) (a: runs 1 and 1', b: runs 2 and 2', c: runs 3 and 3'). The run numbers were corresponded to those in **Table 4.3**.

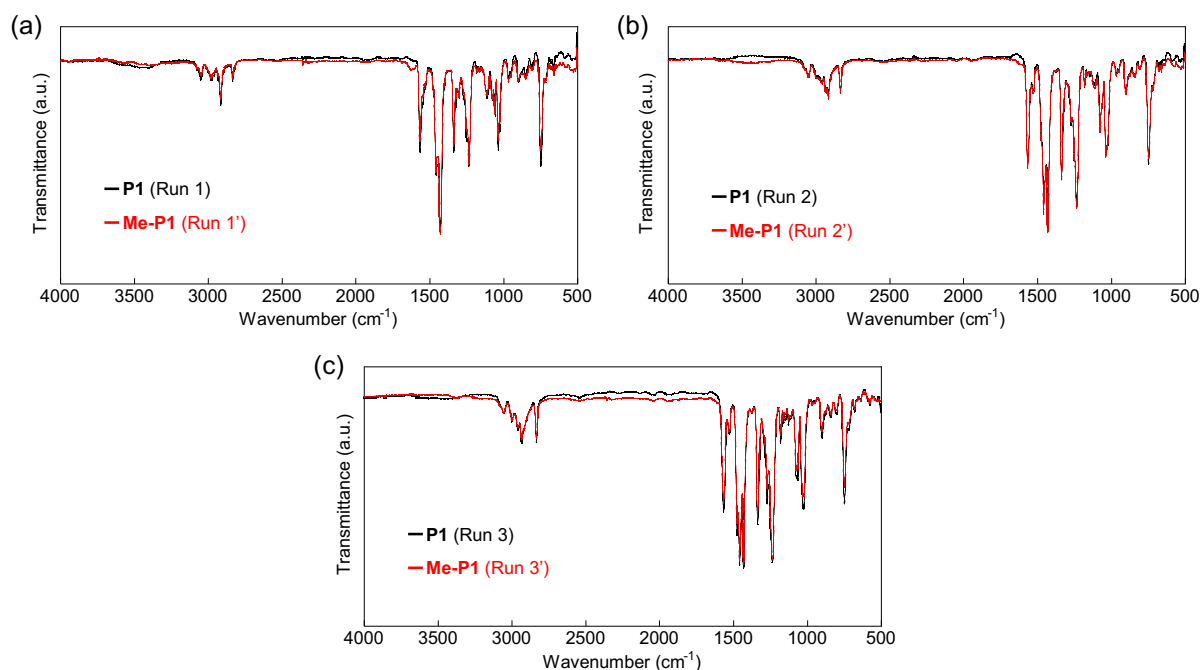


Figure 4.11. IR spectra of **P1** and **Me-P1** (a: runs 1 and 1', b: runs 2 and 2', c: runs 3 and 3').

According to the ^1H NMR spectra of **Me-P1** (**Figure 4.10**), the signals for the methyl terminus were observed in the similar chemical shift regions as of the methylthio groups and were not detected independently. Therefore, the end-functionalization progress was confirmed by comparing the integrals for aromatic region and the summation of methylthio and terminal groups (around 2.4 ppm) in the spectra of **Me-P1** with respect to that of **P1** (**Figure 4.10**). The IR spectra of **Me-P1** were almost identical to the spectra of the corresponding **P1**, suggesting no structural defects (**Figure 4.11**). The degree of end-

functionalization was determined as greater than 88 %, by comparing the M_n values determined by the ^1H NMR and the SEC results. The lower molecular weight of **Me-P1** than **P1** also supported the reduction of the disulfide bonds located in both at the terminus and at the interchain.

Table 4.4. Demethylation of **Me-P1**

Run	Polymer	x^a (-)	Yield (%)	Conversion ^a (%)	M_n^a ($\times 10^3$)	T_{d5}^b ($^{\circ}\text{C}$)	T_g^c ($^{\circ}\text{C}$)
1'	Me-P1	0.29	-	-	0.8	307	92
1''	P2	0.27	91 ^d	93	0.7	290	88
2'	Me-P1	0.53	-	-	1.2	310	101
2''	P2	0.53	82 ^e	100	1.1	260	98
3'	Me-P1	0.77	-	-	1.6	318	108
3''	P2	0.77	88 ^f	100	1.4	284	100

^a)Determined by ^1H NMR (solvent: $\text{DMSO-}d_6$). ^b)Determined by TGA. ^c)Determined by DSC. ^d)Yield for Run 1'. ^e)Yield for Run 2'. ^f)Yield for Run 3'.

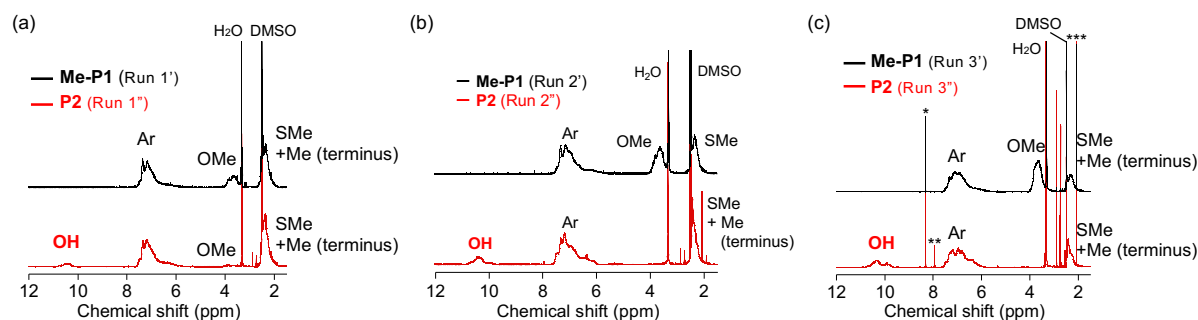


Figure 4.12. ^1H NMR spectra of **Me-P1** and **P2** in $\text{DMSO-}d_6$: (a) runs 1' and 1'', (b) runs 2' and 2'', runs 3' and 3'' (The signals with asterisks were the residues: *: chloroform, **: DMF, and ***: acetone).

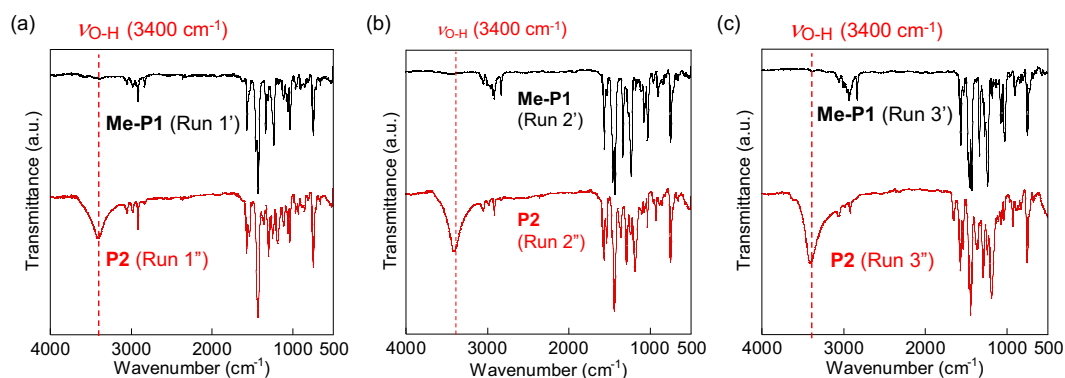


Figure 4.13. IR spectra of **Me-P1** and **P2** in $\text{DMSO-}d_6$: (a) runs 1' and 1'', (b) runs 2' and 2'', runs 3' and 3''.

The demethylation of **Me-P1** also proceeded with high OH introduction ratio (more than 93%), confirmed by the signal changes in the ^1H NMR and IR spectra corresponding to the unit structure (**Figure 4.12** and **4.13**). **P2** was finally obtained without any degradation, as confirmed by the similar M_n values before and after the demethylation (**Table 4.4**). However, further molecular weight should be required for the usage in the bulk states, especially for the free-standing or flexible device applications. Such attempt would be accomplished by utilizing the reactions involving the interchain disulfide bond of the PPS derivatives using multi-arm modification agents, disulfide metathesis reactions, or other click reactions toward the chain-extension.^[18–20]

4.4 Systematic Control of Optical Properties via Hydrogen Bonding and Polarizability

4.4.1 Structure-property Relationships

Me-P1 and **P2** were amorphous according to the XRD profiles representing only halos, regardless of the composition including H-bonding hydroxy groups (**Figure 4.14**). Such disordered polymer network of **P2** were based on the dual contribution of the random sequence of each copolymer unit and the effects of several intermolecular interactions (e.g., H-bonds, S- π interactions, and π - π interactions). Additionally, the bulkiness of the 1,5-substituted phenylene units compared with 1,4-substituted units presumably assisted with the amorphous structures of **Me-P1** and **P2**.

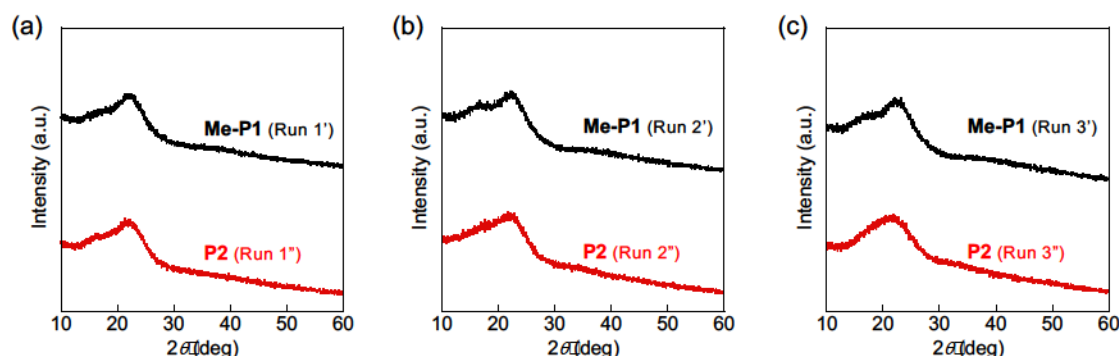


Figure 4.14. XRD patterns of **Me-P1** and **P2**: (a) runs 1' and 1'', (b) runs 2' and 2'', (c) runs 3' and 3'''.

The DSC thermograms showed only the glass transition for **P1**, **Me-P1**, and **P2**, which were the specific features for the amorphous polymers with high homogeneity. The T_g values of **P1** increased according to larger x (i.e. **OMePPS**-richer structures) based on the higher T_g of **OMePPS** ($T_g = 105$ - 132 °C)^[10] than the **SMePPS** counterpart. End-functionalized **Me-P1** were also in the same correlations (**Figure 4.15a**). The T_g of **P2** slightly decreased upon the demethylation of corresponding **Me-P1**, which was in the different trend in the case for homopolymers (**Me-OMePPS** and **OHPPS**) but similar to the case for **OMePPS-PPS** and **OHPPS-PPS** copolymers.^[10] The author think the randomized H-bonds of **P2** decreased T_g based on the lower rotational barrier compared with **Me-P1**, which was finally more contributing to the T_g shift than the polymer binding effect with H-bonds. Demethylation of **Me-P1**

decreased the degradation temperature (T_{d5}) owing to the presence of reactive hydroxy groups of **P2**, but remained in high values of more than 260 °C according to the TGA traces (**Table 4.4** and **Figure 4.15b**).

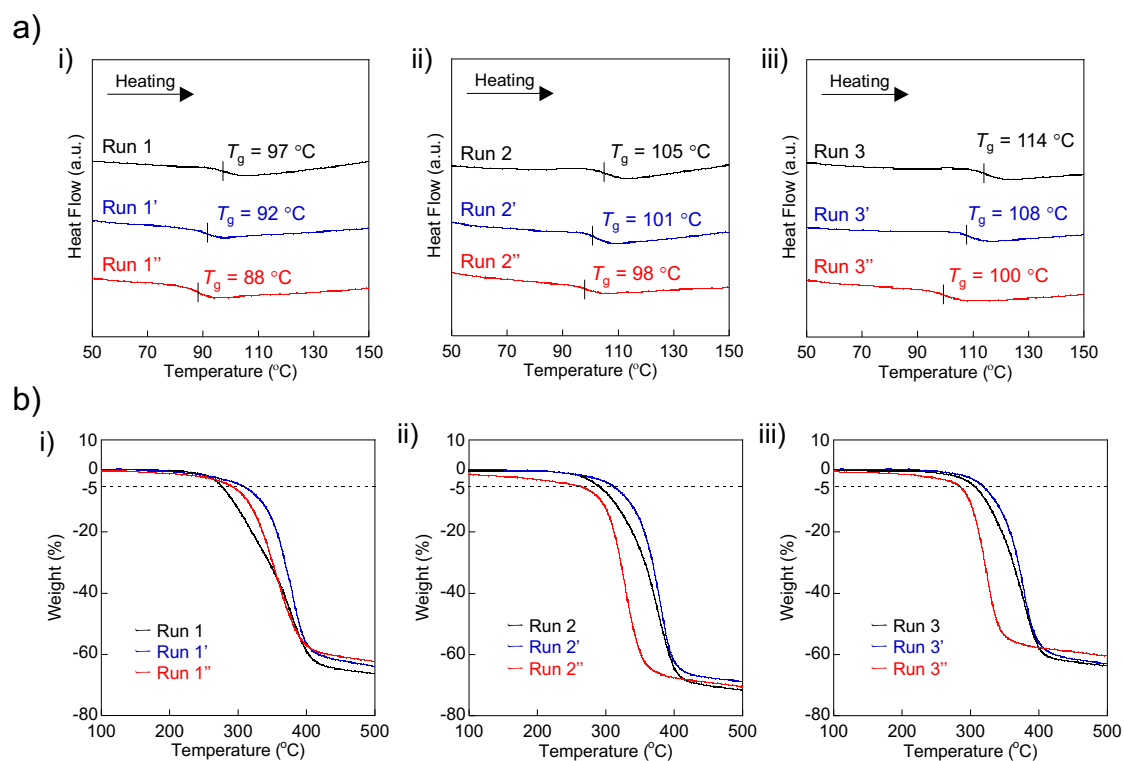


Figure 4.15. Thermal properties of copolymers. (a) DSC thermograms (scan rate: 20 °C min⁻¹) and (b) TGA traces (heating rate: 10 °C min⁻¹) of **P1**, **Me-P1**, and **P2**: (i) runs 1, 1', and 1'', (ii) runs 2, 2', and 2'', and (iii) runs 3, 3', and 3''.

4.4.2 Optical Properties

The effect of the sulfur and hydroxy contents in the **Me-P1** and **P2** systems on the optical properties was comprehensively investigated to reveal the structure-property relationships for the H-bonded highly polarizable HRIPs.

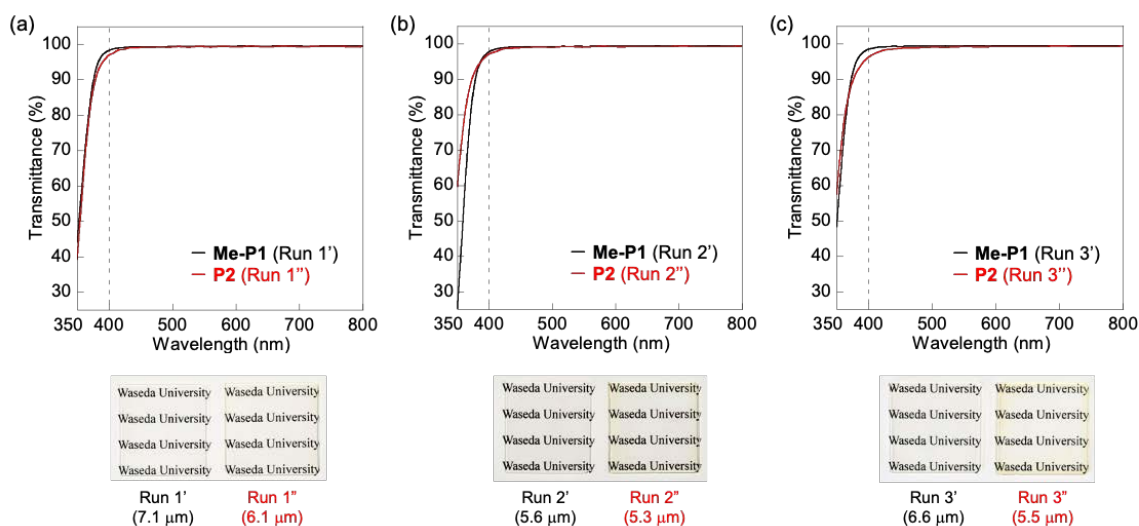


Figure 4.16. UV-vis spectra (thickness was normalized in 1 μm) and photographs of **Me-P1** and **P2** thin films on glass substrates: (a) runs 1' and 1'', (b) runs 2' and 2'', and (c) runs 3' and 3''.

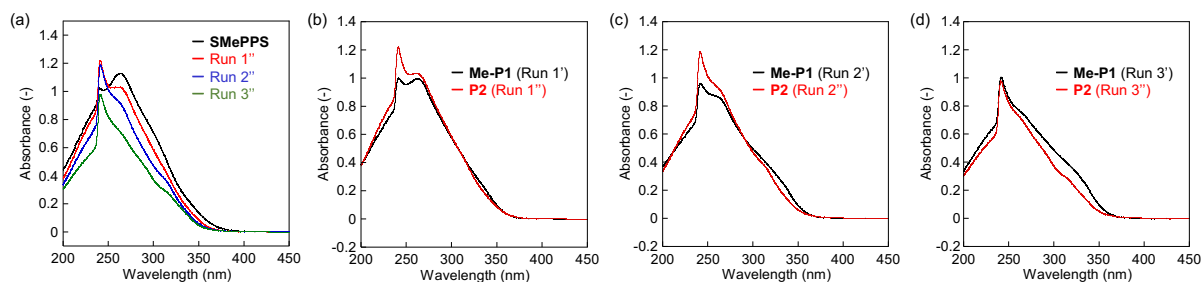


Figure 4.17. UV-vis spectra before and after the demethylation of the copolymers (0.1 mM solution in chloroform, cell length: 1 cm): (a) comparison with **P2** and **SMePPS**, (b) runs 1' and 1'', (c) runs 2' and 2'', and (d) runs 3' and 3''.

Owing to the less sulfur content of **Me-P1** and **P2** than **SMePPS**, the copolymers were more visible-transparent ($\geq 96\%T$ for 1 μm thickness) (**Figure 4.16**). Furthermore, **P2** were more transparent than **OHPPS-PPS** copolymers,^[15] which also suggested more homogeneous bulk structure with less scattering of **P2**, compared to the non-substituted PPS containing **OHPPS-PPS** structure that were easier to be aggregated. The UV-vis absorbance spectra of **P2** also showed higher near UV-visible transparency than **SMePPS**, which were consistent with the content of lone pairs and polarizable sulfur adjacent to the phenylene (**Figure 4.17a**).^[17] Comparing with the transparency in the solution and the bulk states, **P2** were slightly less transparent in the bulk state but more transparent in the solution (**Figure 4.16**, **4.17b-d**), and this was a different changing behavior from the case of **Me-OMePPS** and **OHPPS**.^[10] Such results were based on the presence of the methylthio groups as acceptors, which might induce plausible intermolecular interactions such as H-bonds and S- π interactions, which were especially obvious in the bulk states leading to lower film transparency.

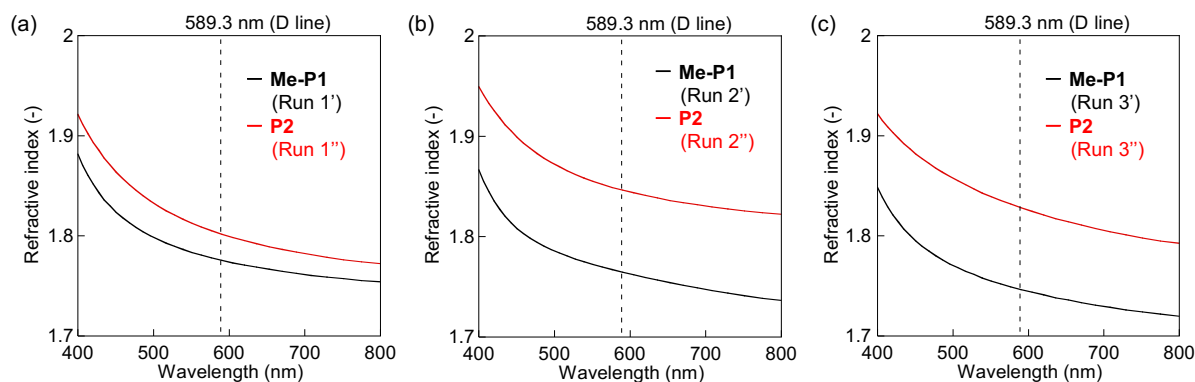


Figure 4.18. Refractive indices of **Me-P1** and **P2**: (a) runs 1' and 1'', (b) runs 2' and 2'', and (c) runs 3' and 3''.

Table 4.5 Optical properties and density of **P2**

Run	Polymer	x^a (-)	%T ^b at 400 nm	n_D^c (-)	ν_D^e (-)	Density ^d (g cm ⁻³)
-	SMePPS	0	94	1.81	19	1.39
1''	P2	0.27	97	1.80	16	1.39
2''	P2	0.53	97	1.85	20	1.48
3''	P2	0.77	96	1.83	17	1.47
-	OHPPS	1.00	97 ^e	1.80 ^e	20 ^e	1.50 ^e

^a)Determined by ¹H NMR. ^b)Determined by UV–vis spectroscopy (normalized values for a thickness of 1 μm). ^c)Determined by spectroscopic ellipsometry. ^d)Determined by a pycnometer (powder samples). ^e) Values from ref. [14].

Figure 4.18 shows RI spectra of **Me-P1** and **P2**. Upon the demethylation, RI was further enhanced regardless of the unit composition, which corresponded to the presence of intermolecularly interacted hydroxy groups resulting in more compact skeleton. Furthermore, the differences in n_D were smaller (ca. 0.02) in the low- x region (run 1'') but larger (ca. 0.08) in the large- x regions (runs 2'' and 3''), whereas the Abbe numbers (ν_D) were in the almost similar values (approx. 20) regardless of the composition (x values) (**Table 4.5**).

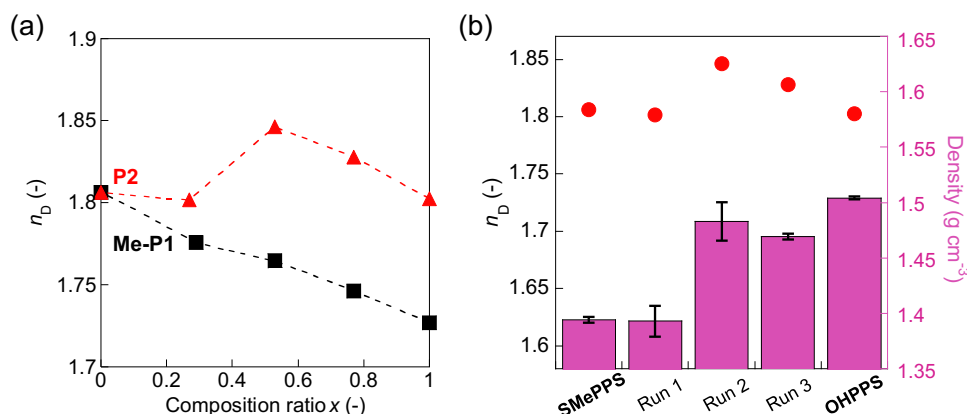


Figure 4.19. (a) Correlations between the composition (x) and n_D for **Me-P1** (black), **P2** (red), and homopolymers. Values for **OMePPS** (**Me-P1** with $x = 1.00$) and **OHPPS** (**P2** with $x = 1.00$) were referred from the previous reports (refs. ^[10] and ^[19], respectively). (b) n_D (red plots) and density (purple bars) of **P2**. The error bars showed the standard deviation (density was measured five times for each).

For further understanding of these RI changing behaviors, the n_D values of **Me-P1** and **P2** were plotted against the composition (x) (**Figure 4.19a**). For **Me-P1**, RI decreased upon the introduction of methoxy-containing units corresponding to the decreased molar refraction of the repeating unit (black plots in **Figure 4.19a**). After the demethylation, **P2** displayed larger RI values than the corresponding **Me-P1** based on the introduction of H-bonds (red plots in **Figure 4.19a**), which effectively lowered the free volume in the bulk state, as described before. However, n_D of **P2** anomalously changed with an unproportional change according to x and was in maximum value (n_D of 1.85) at the intermediate composition ($x = 0.53$, run 2''). In the case of general amorphous polymers, the RI of binary copolymers monotonically change according to the additivity rules derived from the Lorentz-Lorenz equation and decrease as the overall $[R]$ decreases like as the previous report,^[21] which was in the similar trend as for **Me-P1**. On the other hand, this empirical trend was unapplicable for the **P2** system due to the presence of H-bonds for **OHPPS** unit that might induce the unusual bulk structures.

For elucidating the key factors for such anomalous relationship, density, which directly reflect the bulk structures of **P2** including their intermolecular interactions and free volume, were further measured (**Figure 4.19b**). In contrast to the similar density of **P2** with a small x value (run 1'', $x = 0.27$) as **SMePPS**, **P2** with large x (run 2'', $x = 0.53$ and run 3'', $x = 0.77$) represented much higher densities similar to the case of **OHPPS** (1.50 g cm^{-3}).^[1,20] Such increment for the **P2** density corresponded to the sharp enhancement of RI from run 1'' to run 2''. From these results, decline of the free volume from **Me-P1** to **P2** was observed with middle-to-high hydroxy content that are enough to induce the H-bonding effect markedly lowered the free volume, which were also consistent with their RI changing trend.

4.4.3 Understanding Refractive Index Changing Mechanism by the Lorentz-Lorenz Equation

For precisely elucidating the mechanism of the anomalous RI change of **P2**, the RI values were calculated from the experimental densities, according to the Lorentz-Lorenz equation.

(1) Calculation of molar refraction

Prior to estimating RI, the calculated values for molar refraction ($[R]_{\text{unit}}$) are necessary according to each copolymerization ratio. Considering that the additive rule is adoptable for molar refraction (or polarizability), $[R]_{\text{unit}}$ for a repeating unit is determined as the sum of atomic refraction (defined $[R]$ of the j th atom as $[R_{A_j}]$) for all components, described as eq.(4.1):

$$[R]_{\text{unit}} = \sum_j [R_{A_j}] \quad \dots (4.1)$$

Table 4.6 shows the calculated $[R]_{\text{unit}}$ and molar mass $M_{0,\text{unit}}$ for **OHPPS**, **SMePPS**, and **OMePPS**. The values of $[R_A]$ for each atom/group were adopted from references.^[1,22].

Table 4.6 $[R]_{\text{unit}}$ and molar mass of homopolymers

Polymer	$[R]_{\text{unit}}$ ($\text{cm}^3 \text{mol}^{-1}$)	$M_{0,\text{unit}}$ (g mol^{-1})
OHPPS	33.43	124.2
SMePPS	45.39	154.3
OMePPS	38.32	138.2

For a series of copolymers, their molar refraction $[R]$ and molecular volume V were determined as average values according to the composition ratio. $[R]$ and M_0 of **P2** can be determined as equations (4.2) and (4.3), where $[R]_{\text{unit}}$ of **OHPPS**, **SMePPS**, and **OMePPS** are $[R]_{\text{OHPPS}}$, $[R]_{\text{SMePPS}}$, $[R]_{\text{OMePPS}}$, the composition ratio of **OHPPS**, **SMePPS**, and **OMePPS** are x , y , and z , and $M_{0,\text{unit}}$ of **OHPPS**, **SMePPS**, and **OMePPS** are $M_{0,\text{OHPPS}}$, $M_{0,\text{SMePPS}}$, and $M_{0,\text{OMePPS}}$, respectively:

$$[R] = x[R]_{\text{OHPPS}} + y[R]_{\text{SMePPS}} + z[R]_{\text{OMePPS}} \quad \dots (4.2)$$

$$M_0 = xM_{0,\text{OHPPS}} + yM_{0,\text{SMePPS}} + zM_{0,\text{OMePPS}} \quad \dots (4.3)$$

(2) Calculation of RI by the Lorentz-Lorenz equation

V was determined from the density as follows (ρ : density):

$$V = \frac{M_0}{\rho} \quad \dots (4.4)$$

By adopting the calculated $[R]$ and V values from eq. (4.2) and (4.4), the calculated RI of the copolymer (n_{calc}) were determined according to the Lorentz-Lorenz equation as follows:

$$n_{\text{calc}} = \sqrt{\frac{1 + 2[R]/V}{1 - [R]/V}} \quad \dots (4.5)$$

Table 4.7 showed the calculated parameters for the estimation of n_D values.

Table 4.7. Calculated $[R]/V$ and RI values of **P2** and the corresponding homopolymers

Sample	$[R]$ ($\text{cm}^3 \text{mol}^{-1}$)	M_0 (g mol^{-1})	$\rho^{\text{a)}$ (g cm^{-3})	V ($\text{cm}^3 \text{mol}^{-1}$)	$[R]/V$ (-)	n_{calc} (-)	$n_{\text{D, exp}}^{\text{b)c)}$ (-)
SMePPS	45.39	154.25	1.39	110.64	0.410	1.76	1.81
Run 1'' in Table 4.5	42.25	146.39	1.39	105.11	0.402	1.74	1.80
Run 2'' in Table 4.5	39.05	138.30	1.48	93.27	0.419	1.78	1.85
Run 3'' in Table 4.5	36.18	131.08	1.47	89.21	0.406	1.75	1.83
OHPPS	33.43	124.16	1.50 ^{d)}	82.54	0.405	1.74	1.80 ^{d)}

^{a)}Determined by dry densimeter (experimental values of the powder samples). ^{b)}Determined by spectroscopic ellipsometry. ^{c)}Experimental n_{D} values. ^{d)}Values from ref.^[21].

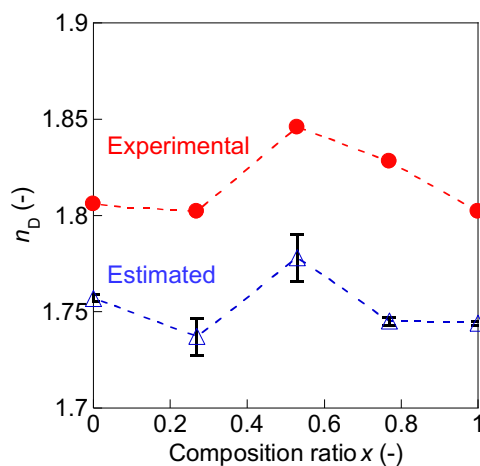


Figure 4.20. Estimated (blue) and experimental (red) n_{D} values for **SMePPS**, **OHPPS**, and **P2** (runs 1-3 in **Table 4.5**). The error bars showed the standard deviation.

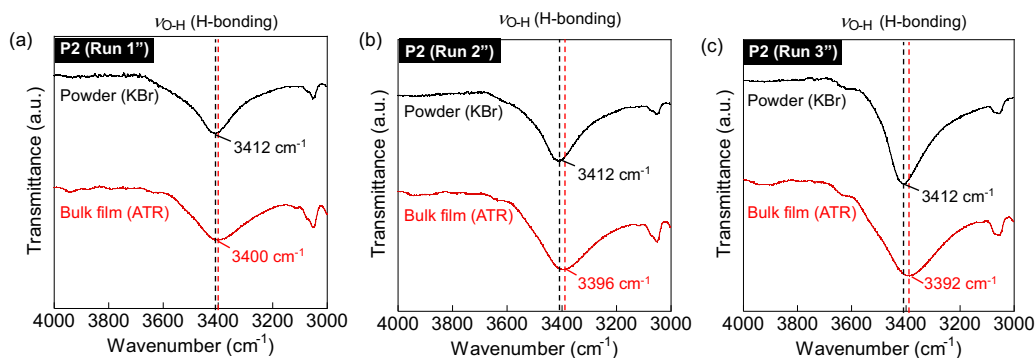


Figure 4.21. IR spectra of **P2** in the powder states (black, with KBr pellets) and the film states (red, with the ATR-IR measurements): (a) run 1'', (b) run 2'', (c) run 3'', which verified the enhancement of H-bonds upon the film formation.

Figure 4.20 showed the experimental and estimated n_{D} values with several compositions. The

changing trend of the calculated n_D (blue plots) was similar to the experimental n_D (red plots), suggesting that the measured RI followed the Lorentz-Lorenz equation (i.e., RI was changed according to the $[R]/V$ values). The deviations between the estimated and experimental RI values were because the author adopted the measured density for the powder samples in this study (for the difficulties in preparing the self-standing films of **P2**). Upon the film formation, the H-bonding networks would become stronger and more widespread compared with the bulk structure in the powder states, and therefore higher density would be expected. Also, larger number of voids and boundaries in the powder states than the films would be another reason for such deviations.^[23] The IR spectra of **P2** before and after the film fabrication represented the redshift of the absorption for the O-H stretching (**Figure 4.21**), indicating that H-bond networks became more dense and more homogeneous.

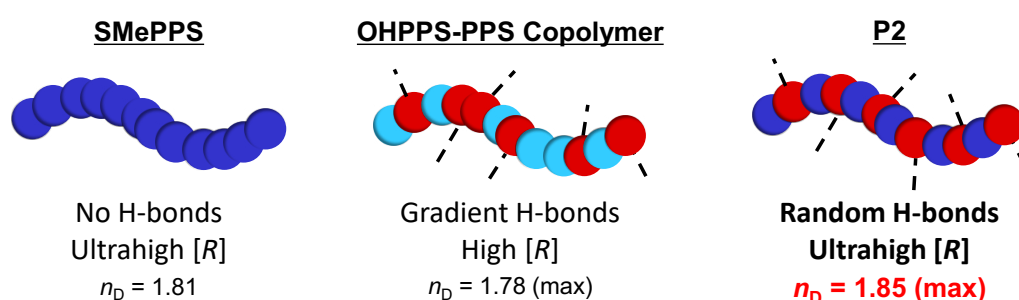


Figure 4.22. The schematic diagram representing the sequential features of **SMePPS**, **OHPPS–PPS** copolymer,^[13] and **P2**. The blue and red circles represent high- $[R]$ and H-bonding monomeric units, respectively, and the dotted lines describe intermolecular H-bonds between hydroxy groups. The color depth of the blue circles corresponds to the magnitude for $[R]$ values.

In chapter 3, the **OHPPS-PPS** copolymer system showed lower RI values than **OHPPS**, but in the **P2** system with the **SMePPS** unit resulted in higher RI than the homopolymers even though the polarizability of the copolymerization counterpart was higher than **OHPPS**. This difference indicated that the RI of OH-containing PPS copolymers are strongly dependent on the sequence, $[R]$ of each unit, and the composition of hydroxy-containing groups (**Figure 4.22**). Owing to the gradient sequence of **OHPPS–PPS** copolymers, the hydroxy groups were randomly and sparsely incorporated into the PPS chain in contrast to **P2** with a random sequence with homogeneously distributed hydroxy groups. Especially, the sequence was the most randomized in the polymerization condition with $x \sim 0.5$ based on the approximately equivalent incorporation of the comonomers. The above difference in the unit distribution were ascribed to the reactivity of the monomers regarding the oxidation of disulfide and subsequent Friedel-Crafts reaction, which are elementary reactions of the oxidative polymerization.^[10,14,22] Introducing electron-donating groups to a DPS monomer is an effective way for simultaneously lowering the oxidation potential (E_{ox}) and enhancing the electrophilic substitution reactions, and therefore selecting the oxidative copolymerization counterpart for **OMeDPS** with a

similar E_{ox} is appropriate for obtaining nearly random copolymers. Furthermore, the higher $[R]$ of **SMePPS** compared with the non-substituted PPS is also contributable to realize the anomalous RI changing trend. Summarizing above, the synergistic effect of increasing $[R]$ and decreasing free volume via H-bonds, which is the simplest requirement according to the Lorentz-Lorenz equation, was demonstrated for the first time with the **P2** system. Such anomalously high RI values of the copolymer were higher than the homopolymers including **OHPPS**, if the counterpart satisfies the following conditions: (1) a higher $[R]$ than **OHPPS** (the key for higher unit refractivity) and (2) similar E_{ox} to that of **OMeDPS** (the key for random sequences). Further precise control of the unit sequences through realizing more controlled oxidative polymerization system would be important for preparing various sequential copolymers as well as higher RI beyond the limit.

4.5 Experimental Section

Reagents. 2-bromothioanisole, 1,2-dibromoethane, iodine, bis(2,4-pentanedionato)vanadium(IV) Oxide (VO(acac)₂), trifluoroacetic acid (TFA), trifluoromethanesulfonic acid (TfOH), trifluoroacetic anhydride, 2,3-Dichloro-5,6-dicyano-1,4-benzoquinone (DDQ), and iodomethane were purchased from Tokyo Chemical Industry Co. Mg turnings and boron tribromide (1 M solution in dichloromethane) were purchased from Fujifilm Wako Chemical Co. Sulfur, sodium sulfate, *m*-chloroperbenzoic acid (*m*CPBA, > 65.0 % containing water), 1,2-dichloroethane, tetrahydrofuran (THF), chloroform, 1,1,2,2-tetrachloroethane, hydrochloric acid, sodium borohydride, dimethylformamide, and acetone were purchased from Kanto Chemical Co. Methanol and ethanol were purchased from Kokusan Chemical Co. and Junsei Chemical Co., respectively. Bis(2-methoxyphenyl) disulfide (**OMeDPS**) was prepared following the procedure described in chapter 2. Reference PPS was purchased from Sigma-Aldrich co. LLC (Product No. 182354). Poly(2-hydroxy-1,4-phenylenesulfide) (**OHPPS**) (M_n (NMR) = 2.0×10^3), poly(2-methoxy-1,4-phenylenesulfide) (**OMePPS**) (M_w (SEC) = 7.0×10^3), and poly(2,6-dimethyl-1,4-phenylenesulfide) (**PMPS**) (M_w (SEC) = 1.7×10^4) on **Figure 4.6c** were prepared following the previous reports.^[10,14,16]

Synthesis of bis(2-methylthiophenyl) disulfide. Bis(2-methylthiophenyl) disulfide (**SMeDPS**) monomer was prepared by Grignard reaction of aromatic bromides and subsequent oxidation of the thiols, referring and arranging the previous reports.^[14,24] To a 100 mL two-necked flask, Mg turnings (1.17 g, 1.2 eq) were added, dispersed in THF (20 mL) with two drops of 1,2-dibromoethane, and was purged with nitrogen gas for 15 min. Then, 2-bromothioanisole (8.12 g, 1 eq) with additional THF (10 mL) was subsequently added to the flask through cannulation and stirred for 2 hours at room temperature. The solution was cooled at 0 °C, was exposed in air, was added sulfur (0.71 g, 0.55 eq), and was further stirred for another 3 hours. The reaction was quenched with of 10 vol% hydrochloric acid aqueous (50 mL, added dropwise). The solution was extracted with chloroform, concentrated through removal of the solvent, and the yellow liquid was obtained as a crude product. Without any purification, the crude was

dissolved in chloroform (40 mL), was added 0.5 M iodine solution in methanol (40 mL), and was stirred at room temperature for 1 hour. The reaction was quenched with 15wt% sodium thiosulfate aqueous (added dropwise) until the brownish color was completely disappeared. The solvent was removed by rotary evaporator, and the residue was dissolved in chloroform and extracted with hydrochloric acid, NaOHaq, and brine. The obtained solid was recrystallized with chloroform/methanol to afford **SMeDPS** as yellow needle-like crystals (2.80 g, Yield: 45%). See Figure S1 for the detailed NMR spectra. ¹H NMR (chloroform-*d*, 500 MHz, ppm, TMS): δ 7.53 (dd, $J = 7.7, 1.7$ Hz, 2H, d), 7.29 (dd, $J = 7.7, 1.7$ Hz, 2H, a), 7.20 (td, $J = 7.7, 1.7$ Hz, 2H, b), 7.13 (td, $J = 7.7, 1.7$ Hz, 2H, c), 2.51 (s, 6H, Me). ¹³C NMR (chloroform-*d*, 125 MHz, ppm, TMS): δ 137.4, 136.4, 128.6, 128.1, 127.7, 126.6, 17.3. FAB-MS (m/z): M^+ (calcd for C₁₄H₁₄S₄), 310.0; found, 309.7.

Oxidative polymerization of SMeDPS with DDQ. A typical polymerization procedure has been described as shown below (Run 4 in **Table 4.1**). To a 10 mL flask, DDQ (0.80 g, 3.5 mmol, 1 eq) was dispersed in 1,2-dichloromethane (DCE) (3.5 mL) with trifluoroacetic acid (TFA) (268 μ L, 1 eq) and was stirred for preparing the homogeneous solution. Then **SMeDPS** (1.09 g, 1 eq) was added immediately and stirred for 20 hours at room temperature. After the stirring, the reaction was diluted with DCE (10 mL) and was precipitated in methanol containing 5 vol% hydrochloric acid (300 mL in total). The precipitate was collected, was washed with methanol, 3 wt% potassium hydroxide aqueous, and water, and was dried in vacuo to obtain **SMePPS** as a white powder (Yield: 85 %).

Oxidative polymerization of SMeDPS with oxygen and VO(acac)₂-H⁺ catalyst A typical polymerization procedure has been described as shown below (Run 8 in **Table 4.1**). To a 100 mL flask, **SMeDPS** (0.25 g, 0.8 mmol, 1 eq) was dissolved in DCE (3.5 mL) and was added VO(acac)₂ (10.6 mg, 0.05 eq), TfOH (7.1 μ L, 0.1 eq), and TFA anhydride (222 μ L, 2 eq). The reaction system was purged with oxygen, was sealed, and was stirred at room temperature for 20 hours. The solution was precipitated in methanol containing 5 vol% hydrochloric acid (100 mL in total). The precipitate was collected through filtration, washed with methanol and water, and dried in vacuo to obtain **SMePPS** as a white powder (Yield: 31%).

Synthesis of sulfoxide-labeled SMePPS (SOMePPS). To a 30 mL flask, **SMePPS** (0.12 g) was dissolved in chloroform (5 mL) with a concentration of 0.1 M, was cooled to 0 °C, was added *m*-chloroperbenzoic acid (*m*CPBA) (> 65.0%, 0.21 g, 1 eq for methylthio groups) solution in chloroform (3 mL) dropwise, and was stirred at 0 °C for 2 hours and at room temperature for 3 hours. The solution was then precipitated in diethyl ether (200 mL). The precipitate was collected, was washed with ether, and dried under vacuo to yield sulfoxide-labeled **SMePPS (SOMePPS)** as a white powder (weight yield: 89 % for fed **SMePPS**).

Synthesis of methoxy- and methylthio-substituted copolymers (P1). Precursor with the methoxy- and methylthio-substituted PPS units (**P1**) were synthesized through oxidative polymerization of **OMeDPS** and **SMeDPS** with DDQ. Herein, a typical polymerization procedure has been described. To a 10 mL flask, DDQ (0.68 g, 3 mmol, 1 eq) was dispersed in DCE (1 mL) with TFA (77 μ L, 1 eq) and stirred until the solution became homogeneous. The mixture of **OMeDPS** and **SMeDPS** (3 mmol in total, 3 eq) was added immediately to the solution and was stirred at room temperature for 20 hours. The solution was diluted with DCE (10 mL) and filtered for removing the by-produced 2,3-dichloro-5,6-dicyano-1,4-dihydroxybenzene (DDH). The filtrate was precipitated in methanol containing 5 vol% hydrochloric acid (200 mL in total). The precipitate was collected, washed with methanol, 3 wt% potassium hydroxide aqueous, and water, and dried in vacuo. The crude product was dissolved in chloroform and was reprecipitated in ethanol containing 5 vol% hydrochloric acid (300 mL in total). The precipitate was collected through filtration, washing with methanol, 3 wt% potassium hydroxide aqueous, and water, and dried under vacuo to obtain **P1** as a white powder.

Copolymerization kinetics studies for OMeDPS and SMeDPS. To a 10 mL flask, DDQ (0.34 g, 1.5 mmol) was dispersed in DCE (0.5 mL) with TFA (38 μ L, 0.5 mmol) and the mixture of **OMeDPS** (0.21 g, 0.75 mmol) and **SMeDPS** (0.23 g, 0.75 mmol) was added immediately. The solution was stirred and each fraction (50 μ L) was collected after 15 min, 30 min, 1 h, 3 h, 6 h, and 20 h during the polymerization. The fractionated solution was diluted with chloroform and precipitated in methanol containing 5 vol% hydrochloric acid (10 mL in total). The precipitate was collected by the centrifugation, was washed with methanol, and was dried in vacuo to obtain the product. The polymerization kinetics were monitored by the ^1H NMR spectra and SEC chromatograms (in chloroform) for determining the composition ratio and the molecular weight, respectively.

Copolymerization kinetics studies for OMeDPS and DPS. To a 10 mL flask, DDQ (0.68 g, 3 mmol) was dispersed in DCE (1 mL) with TFA (77 μ L, 1 mmol) and the mixture of **OMeDPS** (0.42 g, 1.5 mmol) and **DPS** (0.33 g, 1.5 mmol) was added immediately. The solution was stirred and each fraction (100 μ L) was collected 15 min, 30 min, 1 h, 3 h, 6 h, and 20 h after the reaction was started. The fractionated solution was diluted with DCE and precipitated in methanol containing 5 vol% hydrochloric acid (50 mL in total). The precipitate was collected through centrifugation, was washed with methanol, and was dried in vacuo to obtain the product. The monitoring experiments for the fractionated products were the same as the case of the kinetics studies for the **OMeDPS-SMeDPS** copolymerization.

End functionalization of P1. The following procedure was based on the experimental section in chapter 3. A typical procedure has been described as shown below (Run 1'). To a 50 mL two-necked flask was dissolved **P1** (0.45 g, 0.39 mmol of S-S (estimated by the SEC results)) in THF (7.0 mL), was

added iodomethane (483 μL , 8 mmol), and was cooled to 0 $^{\circ}\text{C}$ prior to the reaction. The reaction started by adding dropwise NaBH_4 (0.29 g, 7.75 mmol, 20 eq for disulfide) solution in water (0.78 mL), and was stirred at 0 $^{\circ}\text{C}$ for 30 min and at room temperature for 20 hours. The solution was precipitated in methanol (200 mL). The precipitate was collected, was washed with methanol and water, and was dried in vacuo to obtain **Me-P1** as a whitish powder (0.26 g, Yield: 57 %).

Demethylation of Me-P1. The following procedures were based on that in chapter 3.

For Run 1'': To a 30 mL flask was dissolved **Me-P1** (Run 1' in Table S6, 0.18 g, 1.2 mmol unit, 0.34 mmol of methoxy groups) in dichloromethane (6.0 mL) under argon atmosphere in the glove box. The solution was cooled to 0 $^{\circ}\text{C}$, was added 1 M BBr_3 dichloromethane solution (0.85 mL, 0.85 mmol, 2.5 eq for OMe) via a syringe, and was stirred at 0 $^{\circ}\text{C}$ for 30 minutes and at room temperature for 20 hours. The reaction was terminated by adding water (3 mL) in air and the solvent was removed by rotary evaporator. The crude product was redissolved in DMF (5 mL) and the solution was precipitated in 1 M hydrochloric acid (100 mL). The precipitate was collected, was washed with water, and was dried in vacuo. After the adequate drying, the crude product was redissolved in DMF and reprecipitated in 1 M hydrochloric acid twice, and a white powder (**P2**) was finally obtained (Yield: 91%).

For Run 2'' and 3'': A typical procedure has been described as follows (Run 2''). To a 30 mL flask was dissolved **Me-P1** (Run 2' in Table S6, 0.22 g, 1.5 mmol unit, 0.80 mmol of methoxy groups) in dichloromethane (7.5 mL) under argon atmosphere in the glove box. The solution was cooled to 0 $^{\circ}\text{C}$, was added 1 M BBr_3 solution in dichloromethane (2.0 mL, 2.0 mmol, 2.5 eq for OMe) via syringe, and was stirred at 0 $^{\circ}\text{C}$ for 30 minutes and at room temperature for 20 hours. The reaction was terminated by adding water (5 mL) and the solvent was removed by rotary evaporator. The crude product was redissolved in DMF (6 mL) and was precipitated in 1 M hydrochloric acid (120 mL). The precipitate was collected, was washed with water, and was dried in vacuo. After the adequate drying, the product was redissolved in acetone and was reprecipitated in 1 M hydrochloric acid twice, and a white powder (**P2**) was finally obtained (Yield: 82 %).

Film preparation on a glass. A typical preparation procedure has been described as follows. Polymer solution in tetrachloroethane (concentration: 10 mg mL^{-1}) was filtrated through a 0.2 μm PTFE filter. The solution (400 μL) was dropped on glass substrate (2.5 cm \times 2.5 cm) and was placed at 60 $^{\circ}\text{C}$ in vacuo to yield a transparent thin film.

Film preparation on a Si wafer. A typical procedure has been described. Polymer was dissolved in 1,1,2,2-tetrachloroethane (concentration: 30 mg mL^{-1}) and the solution was filtrated through a 0.2 μm PTFE filter. The solution was then spin-coated on a Si wafer with the following program: slope, 3 sec; 800 rpm, 10 sec; slope, 3 sec; 2000 rpm, 30 sec; slope, 3 sec. The substrate was then dried in vacuo to obtain a sample.

DFT calculations. Density Functional Theory (DFT) calculations were performed using Gaussian 16. Structure optimization of **SMeDPS** (including its orbital and charge distributions) were optimized at the ω B97XD/6-31G(d,p) level of theory.

References

- [1] T. Higashihara, M. Ueda, *Macromolecules* **2015**, *48*, 1915.
- [2] J. G. Liu, M. Ueda, *J. Mater. Chem.* **2009**, *19*, 8907.
- [3] Y. Zhou, Z. Zhu, K. Zhang, B. Yang, *Macromol. Rapid Commun.* **2023**, e2300411.
- [4] J. J. Griebel, S. Namnabat, E. T. Kim, R. Himmelhuber, D. H. Moronta, W. J. Chung, A. G. Simmonds, K.-J. Kim, J. van der Laan, N. A. Nguyen, E. L. Dereniak, M. E. Mackay, K. Char, R. S. Glass, R. A. Norwood, J. Pyun, *Adv. Mater.* **2014**, *26*, 3014.
- [5] T. S. Kleine, R. S. Glass, D. L. Lichtenberger, M. E. Mackay, K. Char, R. A. Norwood, J. Pyun, *ACS Macro Lett.* **2020**, *9*, 245.
- [6] D. H. Kim, W. Jang, K. Choi, J. S. Choi, J. Pyun, J. Lim, K. Char, S. G. Im, *Sci Adv* **2020**, *6*, eabb5320.
- [7] K. Choi, W. Jang, W. Lee, J. S. Choi, M. Kang, J. Kim, K. Char, J. Lim, S. G. Im, *Macromolecules* **2022**, *55*, 7222.
- [8] W. Jang, K. Choi, M. Kang, S. Park, D. H. Kim, J. Ahn, H. Lim, K. Char, J. Lim, S. G. Im, *Chem. Mater.* **2023**, *35*, 8181.
- [9] W. Jang, K. Choi, J. S. Choi, D. H. Kim, K. Char, J. Lim, S. G. Im, *ACS Appl. Mater. Interfaces* **2021**, *13*, 61629.
- [10] S. Watanabe, K. Oyaizu, *Macromolecules* **2022**, *55*, 2252.
- [11] S. Watanabe, H. Nishio, T. Takayama, K. Oyaizu, *ACS Appl. Polym. Mater.* **2023**, *5*, 2307.
- [12] K. Yamamoto, E. Tsuchida, H. Nishide, M. Jikei, K. Oyaizu, *Macromolecules* **1993**, *26*, 3432.
- [13] K. Yamamoto, M. Jikei, J. Katoh, H. Nishide, E. Tsuchida, *Macromolecules* **1992**, *25*, 2698.
- [14] S. Watanabe, K. Oyaizu, *Bull. Chem. Soc. Jpn.* **2020**, *93*, 1287.
- [15] F. Cataldo, *Eur. Chem. Bull* **2015**, *4*, 92.
- [16] M. Jikei, J. Katoh, N. Sato, K. Yamamoto, H. Nishide, E. Tsuchida, *Bull. Chem. Soc. Jpn.* **1992**, *65*, 2029.
- [17] S. Watanabe, T. Takayama, H. Nishio, K. Matsushima, Y. Tanaka, S. Saito, Y. Sun, K. Oyaizu, *Polym. Chem.* **2022**, *13*, 1705.
- [18] H. Otsuka, S. Nagano, Y. Kobashi, T. Maeda, A. Takahara, *Chem. Commun.* **2010**, *46*, 1150.
- [19] Y. Nakai, A. Takahashi, R. Goseki, H. Otsuka, *Polym. Chem.* **2016**, *7*, 4661.
- [20] S. Watanabe, K. Oyaizu, *ACS Appl. Polym. Mater.* **2021**, *3*, 4495.
- [21] Y. Sato, S. Sobu, K. Nakabayashi, S. Samitsu, H. Mori, *ACS Appl. Polym. Mater.* **2020**, *2*, 3205.
- [22] N. Tanio, Y. Momono, K. Hosoi, M. Okura, J. Matuhara, *Kobunshi Ronbunshu* **2009**, *66*, 24.

- [23] Y. Nambu, Y. Yoshitake, S. Yanagi, K. Mineyama, K. Tsurui, S. Kuwata, T. Takata, T. Nishikubo, K. Ishikawa, *J. Mater. Chem. C* **2022**, *10*, 726.
- [24] T. Yanagi, K. Nogi, H. Yorimitsu, *Chem. Eur. J* **2020**, *26*, 758.

Figures, tables, and texts are partially adapted from S. Watanabe, T. Takayama, K. Oyaizu, *ACS Polym. Au* **2022**, *2*, 458-466 (Copyright © 2022 The Authors).

Chapter 5:

Multi-functional Aromatic Poly(thiourea)s with Ultrahigh Refractive Index and Degradability Based on Polarizable Hydrogen Bonds

Contents

- 5.1 Introduction
- 5.2 Synthesis and Optical Properties of Aromatic Poly(thiourea)s
- 5.3 Hydrogen Bonding Features in the Bulk States
- 5.4 Demonstration of Poly(thiourea) thin film as an Amplifying Layer for Light-emitting Electrochemical Cells
- 5.5 Degradation Studies of Poly(thiourea)s via Dynamic Covalent Chemistry
- 5.6 Experimental Section

References

5.1 Introduction

The molecular design of high refractive index polymers (HRIPs) ranges from introducing highly polarizable groups to the bulk structure control while maintaining amorphous states, based on the Lorentz-Lorenz equation.^[1-6] Especially, introducing such HRIP thin film layers into optoelectronic devices including organic light-emitting diodes (OLEDs) is effective for further high light-extraction efficiency.^[7-9] Considering the implementation of such polymers for optoelectronic devices, not only ultrahigh RI but also colorless film transparency, high glass transition temperature (T_g), and flexibility should be simultaneously required.

To date, many attempts have been conducted for enhancing RI, and the representative examples with especially ultrahigh RI (~ 1.8) are sulfur-containing polymers,^[10-12] inverse-vulcanized polymers,^[13,14] and heavy-chalcogenide polymers.^[15,16] In contrast, the authors have reported the systematical RI enhancing investigation through reducing free volume by means of non-covalent interactions. For example, monohydroxy-substituted poly(phenylene sulfide) (PPS) represented ultrahigh RI (above 1.80) and amorphous properties based on the intermolecular H-bonds within the steric restraints of rigid PPS backbones (chapter 3). Upon incorporating sulfur-rich skeleton^[17] or expanding to the dihydroxy-PPS,^[18] RI finally reached in $n_D = 1.85$ owing to the increment of molar refraction or decline in free volume (chapters 3 and 4).

Among various H-bonding moieties, multiple H-bond shows promising features that enable higher supramolecular-crosslinking density. Although such properties are preferential for responsive materials including self-assembled systems that require strong interactions,^[19,20] excessive introduction of such multiple H-bonds is inappropriate for transparent optical materials due to the crystallization or macrophase-separation.^[21,22] For the H-bonding induced RI and transparency enhancement of the polymers, the balanced contribution of moderately high polarizability, intermolecular interactions, and randomized polymer chain bulk structures is important. Among such multiple H-bond skeletons, thiourea is an exceptional structure that can construct disordered H-bonds due to the high polarizability ascribed to the large electron distribution around sulfur.^[23] Thiourea-containing polymers are usually in densely packed amorphous network structures,^[24,25] which exhibits attractive bulk properties such as self-healability in a glassy state,^[25,26] Li^+ conduction,^[27] metal absorption,^[28] covalent adaptable networks,^[29,30] and high dielectric constants.^[31-33] Although RI of a few poly(thiourea)s were reported as a guideline for dielectric constants,^[34] detailed investigations on optical properties, including HRIP applications, have not been reported to date.

In this chapter, the author describes the properties of aromatic poly(thiourea)s (**PTU**) as a category of ultrahigh RI polymers. Though the combination of polarizable thiourea with dense and amorphous H-bonds and aromatic spacers, they showed high RI (1.7-1.8) and visible transparency enough for optoelectronic applications. Such **PTUs** can be depolymerized to the low-molecular-weight compounds with excessive diamines, which were based on the bond exchange properties of thioureas. Such properties were valuable for realizing environmentally friendly lightning devices.

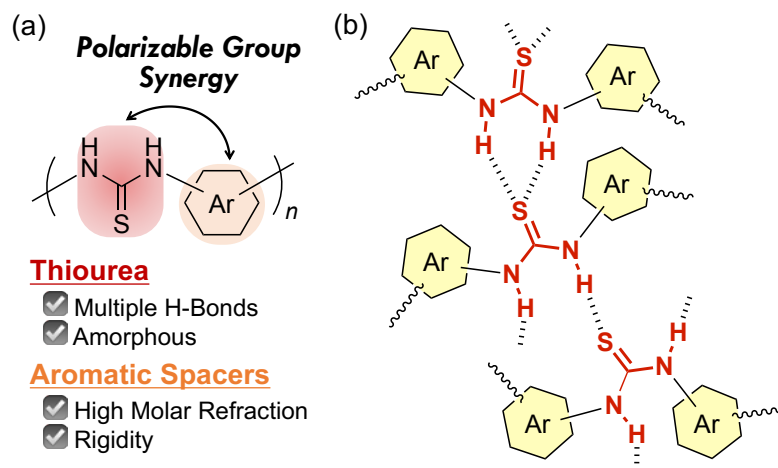


Figure 5.1. Concept of this chapter. (a) Molecular design of PTUs with “polarizable group synergy”. (b) Schematic representation of disordered H-bonding arrays between the PTU chains that enable polarizable supramolecular networks.

5.2 Synthesis and Optical Properties of Aromatic Poly(thiourea)s

5.2.1 Synthesis of poly(thiourea)s

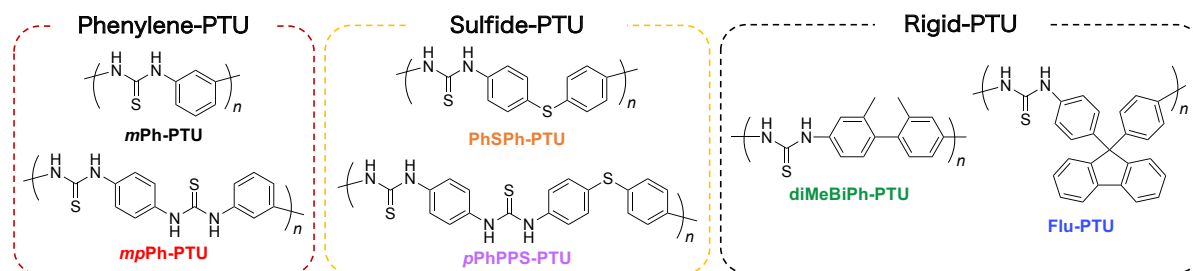


Figure 5.2. Structure of poly(thiourea)s synthesized in this study.

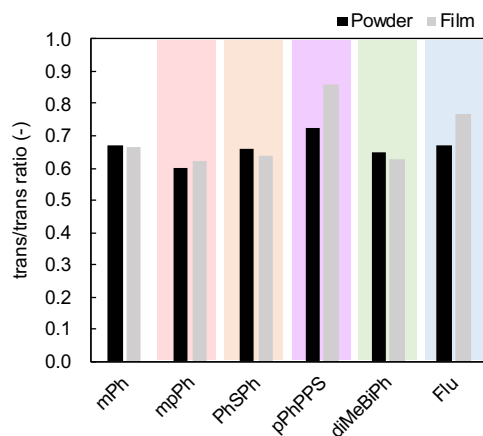


Figure 5.3. Conformational ratio of H-bonding thioureas for PTUs in the powder and the film states, determined by the IR spectra.

The target poly(thiourea)s were synthesized by either polyaddition of the corresponding

diamines and diisothiocyanates or polycondensation of the diamines with 1,1'-thiocarbonyldiimidazole as C=S source, by referring the previous reports.^[25,32] For pursuing polymers with excellent optical properties, we designed six aromatic-based PTUs and categorized with three groups: **Phenylene-PTUs** with maximized thiourea content (*mPh-PTU*, *mpPh-PTU*), **Sulfide-PTUs** with high-[*R*] (**PhSPh-PTU**, *pPhPPS-PTU*), **Rigid-PTUs** with a biphenyl (**diMeBiPh-PTU**) and a cardo-based fluorene skeleton (**Flu-PTU**) (**Figure 5.2**). The resulting polymers were high molecular weight (M_w over 10^4) and soluble only in polar amide solvents such as DMF, DMSO, and NMP ascribed to the H-bond rich structures. Their structures were characterized by ^1H , ^{13}C NMR, and IR spectroscopy (see the section 5.5). All the ^1H NMR spectra showed the signals consistent with the corresponding repeating structures, especially at near 10 ppm were observed the N-H signals for thiourea units. The IR spectra revealed two vibration modes for H-bonding N-H groups (linear H-bonding N-H stretching and nonlinear H-bonding N-H deformation vibrations)^[25] (The spectra have been displayed in **Figure 5.7d**). The conformational ratio of trans/trans H-bonds ranged from 0.60 to 0.72, suggesting that the H-bonding array of thiourea slightly favors a linear conformation rather than the zig-zag cis/trans structure (**Figure 5.3**).

5.2.2 Crystalline and Thermal Properties of poly(thiourea)s

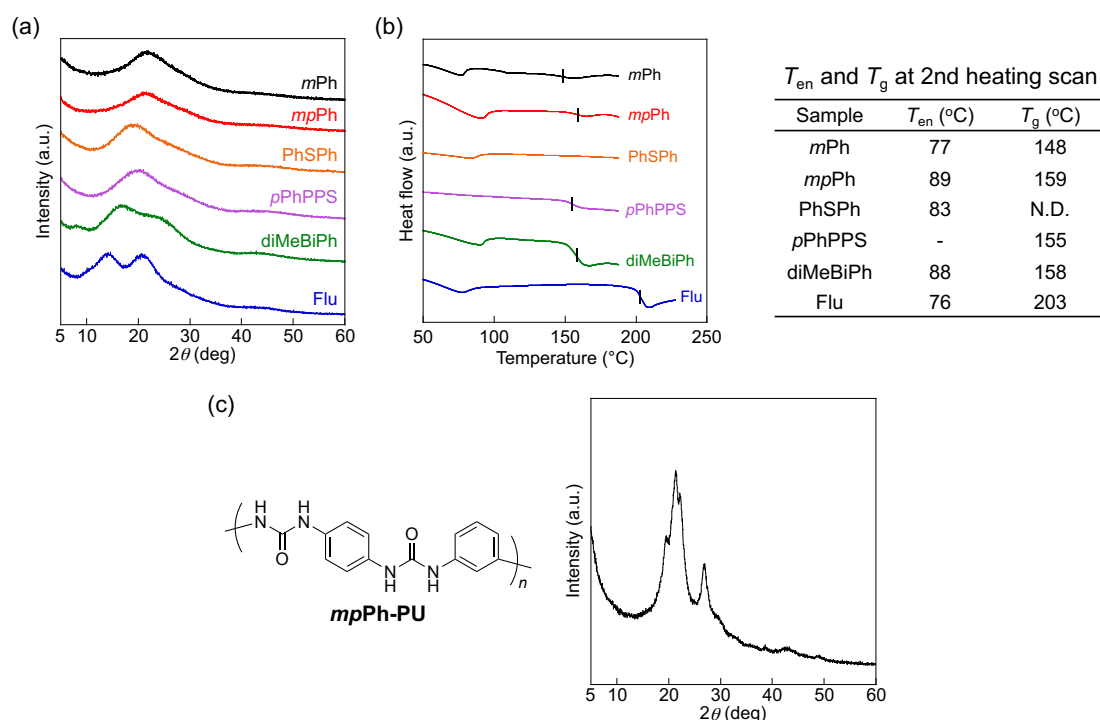


Figure 5.4. Crystalline and thermal properties of PTUs. (a) XRD profiles. (b) DSC thermograms including the glass transition temperature (T_{g}) (measured on 2nd heating, scan rate: $20\text{ }^{\circ}\text{C min}^{-1}$). T_{en} denotes the peaktop temperature for the exothermic peak below T_{g} (near $80\text{ }^{\circ}\text{C}$). (c) Structures and XRD profile of *mpPh-PU*.

Next, crystalline and thermal properties were revealed. From the XRD profiles, no diffraction

peaks were observed for all **PTU** even in the presence of hydrogen bonding networks owing to their random conformations (**Figure 5.4a**). The microstructures were further evaluated by differential scanning calorimetry (DSC), whose thermograms showed a slight exothermic peak ranging in 76-89 °C (except for *pPhPPS-PTU*) and a baseline shift ranging in 148-203 °C (except for **PhSPH-PTU**) for each **PTU** (**Figure 5.4b**). These thermal transitions were ascribed as a micro-Brownian motion of flexible thiourea arrays and glass transition of rigid aromatic backbones, respectively. Therefore, **PTUs** in this study were amorphous in a broader sense, where small nano-sized crystals that were undetectable from the XRD profiles remained as thiourea segments in the solid state. Considering that *mpPh-PU*, a polyurea analog of *mpPh-PTU*, showed strong diffraction peaks in the XRD profile (**Figure 5.4c**), thiourea moieties disorganized the H-bonding-derived crystalline region that were contributable to preventing macroscopic agglomeration of the polymer chains based on its two H-bonding array conformations proven by the IR spectra (vide supra).

5.2.3 Optical Properties of poly(thiourea)s

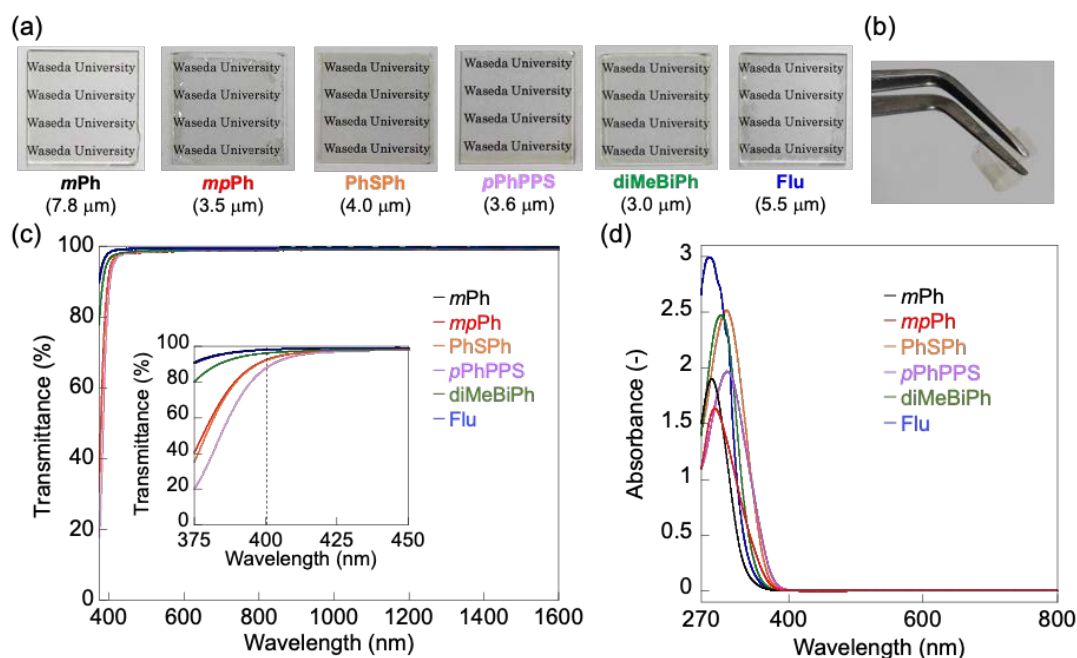


Figure 5.5. Optical properties of **PTUs** in the film states: (a) Photographs and thickness (Parentheses) for the **PTU** thin films on glass substrates. (b) Flexible free-standing *mpPh-PTU* thin film upon bending with a tweezer. (c) Normalized UV-vis transmittance spectra for the **PTU** films with thickness of 1 μm (inset: expanded spectra in the region of 375-450 nm). (d) UV-vis absorbance spectra of 0.1 mM **PTU** solutions in DMF.

Optical properties for **PTUs** were also investigated in the film and the solution states. Transparent thin films of **PTU** were prepared via wet-processing of their DMF or DMF/DMSO solutions

(Figure 5.5a). Especially the *mpPh*-PTU film can be peeled off from the substrate and was not fractured upon bending (Figure 5.5b), which were contradictory to the brittle features of previous aromatic-based ultrahigh-RI polymers (e.g., PPS derivatives).^[5,17,18] Such flexibility was ascribed to the dense and disordered H-bonds of thiourea units that were especially strengthened in the case of the *mpPh*-PTU with the most robust and dense H-bonding (detailed discussions were mentioned later, in the section 5.3).

Table 5.1 Optical properties and density of PTUs

Polymer	ε ^{a) b)} at 400 nm (M ⁻¹ cm ⁻¹)	Absorptivity ^{a) c)} at 400 nm ($\times 10^2$ cm ⁻¹)	% <i>T</i> ^{a) c) d)} at 400 nm	n_D ^{e)} (-)	ν_D ^{e)} (-)	Density ^{f)} (g cm ⁻³)
<i>mPh</i> -PTU	8.9	0.8	98	1.79	11	1.41
<i>mpPh</i> -PTU	10.4	3.4	92	1.81	11	1.50
<i>PhSPh</i> -PTU	37.6	3.5	92	1.83	15	1.34
<i>pPhPPS</i> -PTU	64.4	5.6	88	1.81	15	1.40
<i>diMeBiPh</i> -PTU	8.8	1.6	96	1.75	12	1.23
<i>Flu</i> -PTU	20.4	0.8	98	1.72	18	1.23

^{a)} Determined by UV-vis spectroscopy. ^{b)} Values for a polymer solution in DMF. ^{c)} Values for a polymer thin film. ^{d)} Normalized value with 1 μm thickness. ^{e)} Determined by spectroscopic ellipsometry.

^{f)} Determined by pycnometer (average values for 5 experiments).

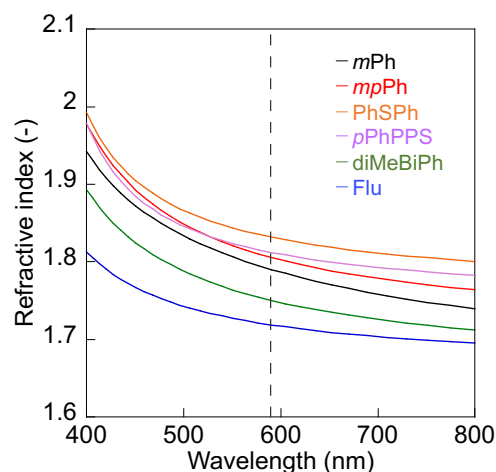


Figure 5.6. Refractive indices of PTUs.

The UV-vis spectroscopy showed high transparency of PTU films of over 88%*T* (with 1 μm thickness) in the visible-near infrared (NIR) region (Figure 5.5c). While highly polarizable Sulfide-PTUs (*PhSPh*-PTU and *pPhPPS*-PTU) showed low transparency, the PTU containing *p*-phenylene (*mpPh*-PTU) represented higher transparency of 92 %*T* at 400 nm whereas *m*-phenylene (*mPh*-PTU)

or **Rigid-PTUs** (**diMeBiPh-PTU** and **Flu-PTU**) resulted in even higher transparency (95-98 %*T* at 400 nm) based on less polarizable spacers than for **Sulfide-PTUs**. This trend in the film states was consistent with the absorption features in the solution states (**Figure 5.5d**), and considering that there was no decline in transparency in the visible region at large wavelength (ca. 500-800 nm), transparency was correlated with the polarizability and no scattering was observed in the **PTU** thin films.

RI of **PTUs** resulted n_D (RI at 589 nm) over 1.7 with Abbe numbers of $\nu_D = 11-18$ (**Table 5.1**, **Figure 5.6**). The detailed RI for each **PTU** also depends on the spacer structure, which was in the contrary relationship to the trend for UV-vis absorption. In contrast to **Rigid-PTUs** (**diMeBiPh-PTU** and **Flu-PTU**) with n_D below 1.75, **Phenylene-PTUs** and **Sulfide-PTUs** resulted in higher RI based on their high thiourea and sulfur content. Among ultrahigh RI **PTUs** with n_D over 1.8, **mpPh-PTU** especially possessed higher molecular weight and higher T_g while representing similar film absorptivity compared to the previous ultrahigh RI polymers (**Table 5.2**). Such superior properties of **mpPh-PTU**, including its flexibility shown in **Figure 5.5b**, are favorable features for visible-transparent optical thin-film applications (e.g., encapsulants for flexible OLEDs).

Table 5.2 Comparison of optical properties for **PTUs** and other ultrahigh RI polymers^{a)}

Polymer	RI (wavelength)	Region intended for use	n_D (-)	Absorptivity at 400 nm ($\times 10^2 \text{ cm}^{-1}$)	Molecular weight	Solubility	Ref.
mpPh-PTU	1.81 (D line)	Visible-NIR	11	3.4	1.4×10^5 (M_w)	○	This work
PhSPh-PTU	1.83 (D line)	Visible-NIR	15	3.5	5.0×10^4 (M_w)	○	
pPhPPS-PTU	1.81 (D line)	Visible-NIR	15	5.6	6.2×10^4 (M_w)	○	
DOHPPS	1.85 (D line)	Visible	17	0.8	3.6×10^3 (M_n , precursor)	○	[18]
OHPPS	1.80 (D line)	Visible	20	1.1	2.0×10^3 (M_n)	○	[5]
Thianthrene-based PPS	1.8020 (633 nm)	Visible-NIR	- ^{b)}	7.6	5.0×10^3 (M_n)	○	[35]
Poly(S-r-DIB) (20wt% DIB)	1.865 (633 nm)	NIR-IR	- ^{b)}	Yellow-red	N.D. (Network)	×	[13]
Poly(S-r-TIB) (30wt% TIB)	1.836 (633 nm)	NIR-IR	- ^{b)}	Yellow-red	N.D. (Network)	×	[36]
SCPs from sCVD	1.926 (D line)	Visible	14.698	3.2	N.D. (Network)	×	[37]

^{a)}Partially adopted with permission from ref. [18] (Copyright © 2023 American Chemical Society). ^{b)}Not reported.

5.3 Hydrogen Bonding Features in the Bulk States

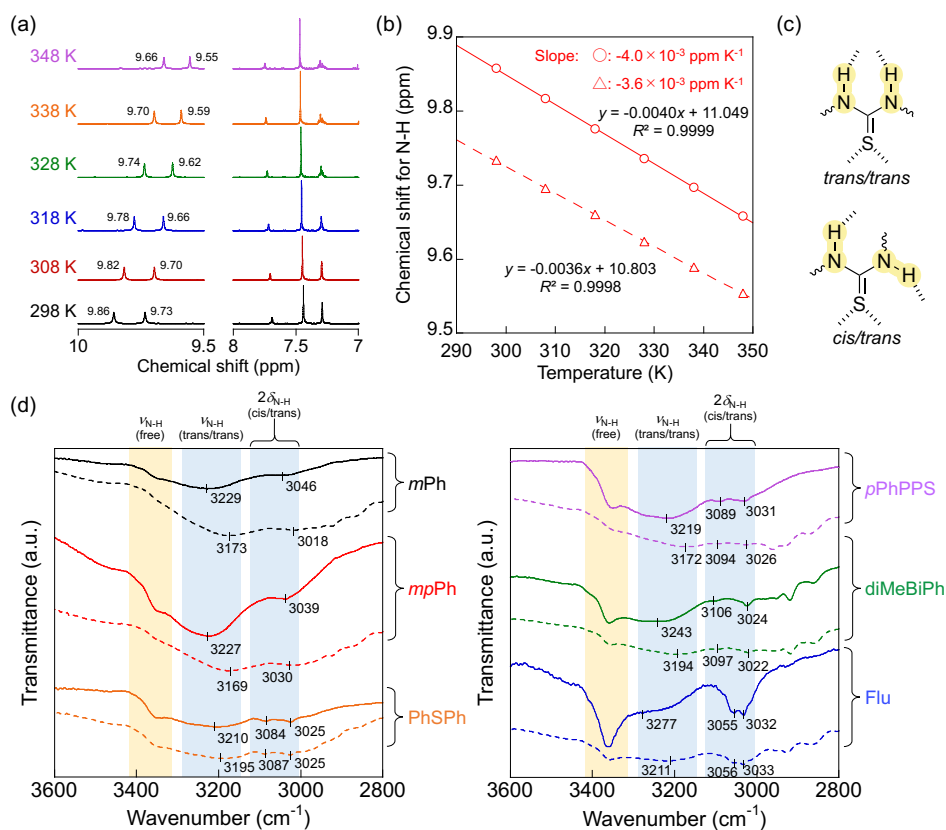


Figure 5.7. Investigating H-bonds of PTUs in the solution and the bulk states. (a) Expanded ^1H VT-NMR spectra for *mpPh*-PTU in $\text{DMSO-}d_6$ at 298, 308, 318, 328, 338, 348 K. Two signals for N-H groups were observed due to the conformational change of *cis/trans* and *trans/trans* conformations during the NMR measurements.^[38] (b) Correlation between temperature and chemical shift for N-H (thiourea) signals in the VT-NMR spectra for *mpPh*-PTU. Only the signals for N-H bonds were shifted in accordance with the temperature change. (c) two conformational states of the multiple H-bonds for thiourea. (d) IR spectra of the PTUs in the powder (solid lines) and the bulk (dotted lines) states. Yellow and blue brackets corresponded to the absorption bands for free and H-bonded N-H vibration modes, respectively.

Table 5.3 Peak shifting rates for the N-H proton signals in the ^1H VT-NMR spectra for PTUs

Polymer	Rate ^{a)} ($\times 10^3 \text{ ppm K}^{-1}$)
<i>mPh</i> -PTU	-3.8
<i>mpPh</i> -PTU	-4.0, -3.6
<i>PhSPh</i> -PTU	-4.1
<i>pPhPPS</i> -PTU	-4.0
<i>diMeBiPh</i> -PTU	-4.1
<i>Flu</i> -PTU	-3.9

^{a)} Determined from VT-NMR.

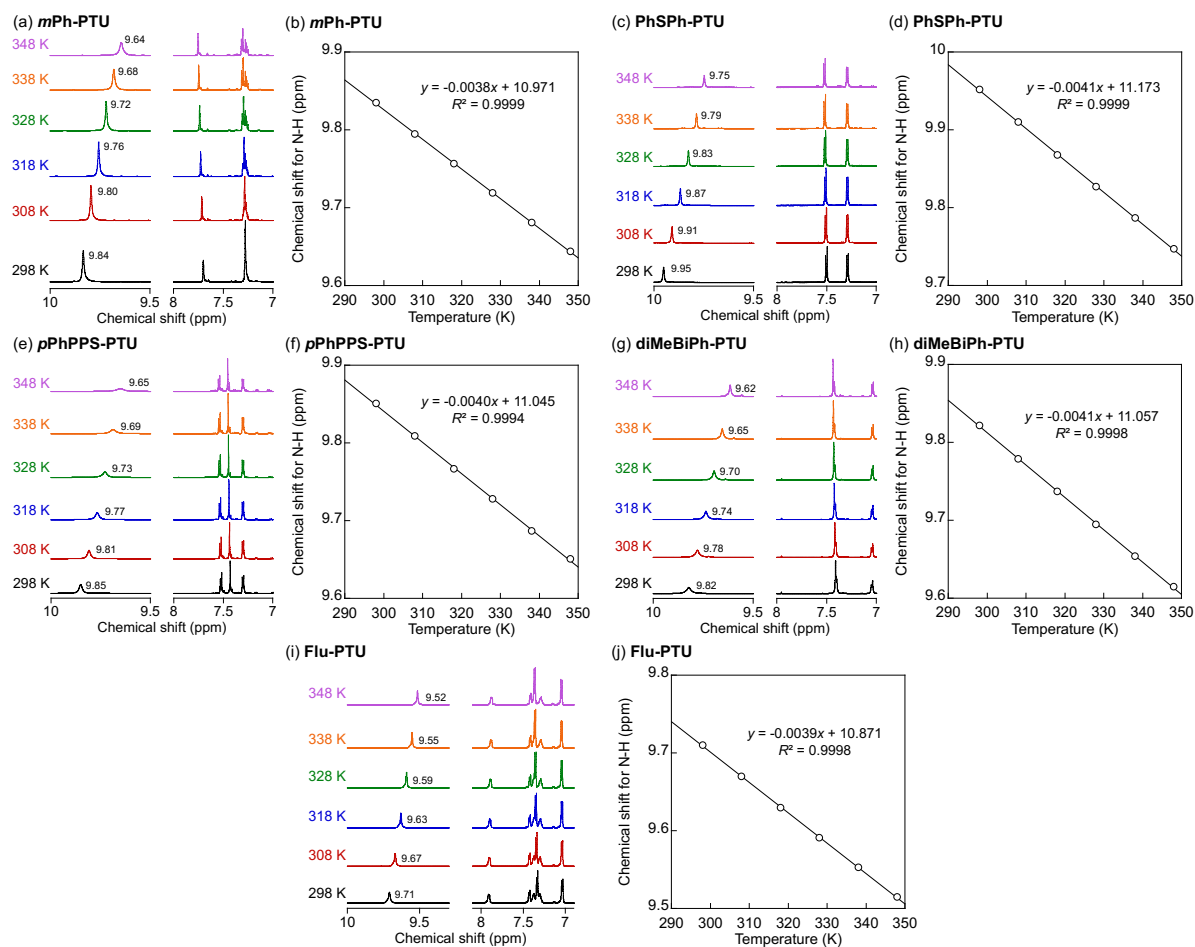


Figure 5.8. ^1H NMR (in the expanded region for thiourea and aromatic groups) in $\text{DMSO-}d_6$ at 298, 308, 318, 328, 338, 348 K (600 MHz) and correlation between temperature and chemical shift for N-H (thiourea) signals for *mPh*-PTU (a, b), *PhSPh*-PTU (c, d), *pPhPPS*-PTU (e, f), *diMeBiPh*-PTU (g, h), and *Flu*-PTU (i, j).

For elucidating the mechanism for the structure-property relationships of PTUs, the conformational information of the H-bonds of thiourea were examined in the solution/bulk states. First, the author conducted ^1H variable temperature (VT)-NMR measurements, in which only the N-H signals of thiourea showed upfield shift for all PTUs with increasing temperature. The shifting rate were determined as approx. -4×10^{-3} ppm K^{-1} regardless of the spacer structure, which were in the range of intermolecular H-bonds (Figure 5.7a, 5.7b, 5.8, and Table 5.3).^[39] Only for *mpPh*-PTU were confirmed two N-H signals of thiourea, which were observed when the conformational change between trans/trans and cis/trans is slower than the timescale of ^1H NMR,^[38] representing its more robust H-bonding features in contrast to the other PTUs. Subsequently, we examined the H-bonds in the solid states from the IR spectra. In the bulk (film) states, the signals for the trans/trans type H-bonding N-H stretching were drastically red-shifted than in the case for powder states, whereas the signal for free N-H bonds was

simultaneously decreased (**Figure 5.7c, 5.7d**). On the other hand, the *cis/trans* type H-bonding N-H deformation vibration, which were characteristic bands of not urea but thiourea groups,^[25] were detected with red-shifting in the film state for **Phenylene-PTUs**, whereas no significant shift were found for the other **PTUs**. Such spectral change describes the uniform and more widespread H-bonding network of **PTUs** upon the film formation, whose effect is especially remarkable for the case with the compact spacers. Regardless of the film/powder states and the spacer structures, both conformations existed with the ratio for *trans/trans* type H-bonds of approx. 0.6-0.8 (**Figure 5.3**). The *cis/trans* type H-bonds disrupted the ordered H-bond networks to avoid microphase-separated domains despite of the preferential *trans/trans* type H-bonds, resulting in high transparency of **PTUs**.

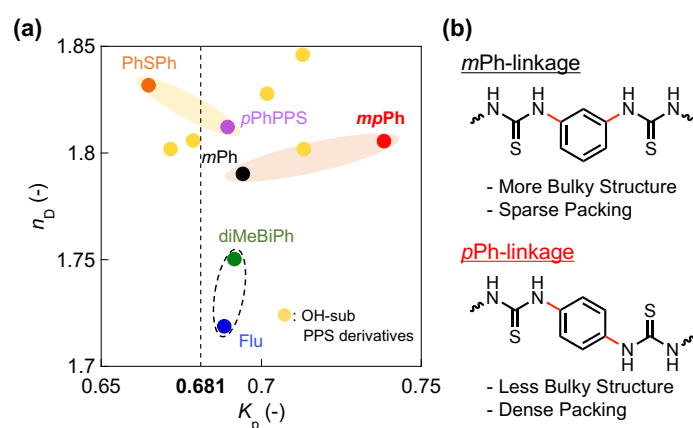


Figure 5.9. Packing features of **PTUs**. (a) Correlation between n_D vs K_p for **PTUs** and ultrahigh RI polymers with single H-bonds (hydroxy-containing PPS derivatives)^[17]. Orange, yellow, and black brackets categorize **Sulfide-PTU**, **Phenylene-PTU**, and **Rigid-PTU**, respectively. (b) Schematic representation of *m*-Ph and *p*-Ph linkages including their packing features.

The packing features for **PTUs** in the solid states were further investigated via density measurements, in which the packing constants (K_p) were evaluated (**Figure 5.9**). Except for **PhSPh-PTU**, the **PTU** chains were densely packed with K_p over 0.681, which was the empirical value for general amorphous polymers.^[40] The multiple H-bond networks between thiourea units enhanced chain packing regardless of the spacer structures. Among the **PTUs** reaching or coming close to the ultrahigh RI (~ 1.8), **Phenylene-PTUs** (red bracket in **Figure 5.9a**) represented the highest K_p than **Sulfide-PTUs** (orange bracket), which showed that the dominant factor of achieving ultrahigh RI was high sulfur content for the **Sulfide-PTUs** and high K_p for the **Phenylene-PTUs**, respectively. On comparing **Phenylene-PTUs**, *mpPh-PTU* with the alternating *m*- and *p*-phenylene linkage led to much higher K_p (0.738) than *mPh-PTU* as well as the other **PTUs**. As *p*-phenylene spacer connected straightly to the adjacent thioureas, more densely H-bonded thiourea arrays were constructed in the bulk states compared with the case for only the *m*-phenylene group with a bent linkage (**Figure 5.9b**). Based on the above structure-property relationships for **PTUs**, we conclude that the **Sulfide-PTU** skeleton resulted in high

RI but poor visible transparency for its excessively high polarizability, while the **Phenylene-PTU** skeleton with linearly connected adjacent thioureas resulted in high RI as well as the maintained high transparency based on its enhanced H-bonding density. Additionally, **mpPh-PTU** exhibited higher K_p than the previous OH-containing PPS derivatives with single H-bonding moiety (yellow plots in **Figure 5.9a**), representing the synergistic effect of compact spacers and multiple H-bonded thioureas for achieving denser H-bond networks. Therefore, the present **PTU**-based system represented stronger chain packing compared with the **OHPPS**-based systems (chaps 3 and 4), only when the spacer satisfied the compact and linear-like skeleton that efficiently contact neighboring thiourea moieties.

5.4 Demonstration of Poly(thiourea) thin film as an Amplifying Layer for Light-emitting Electrochemical Cells

For evaluating the light extraction efficiency upon loading in light-emitting devices, **PTU** thin layers were fabricated as a light-amplifying layer for light-emitting electrochemical cells (LEC) and their lighting efficiency were investigated.

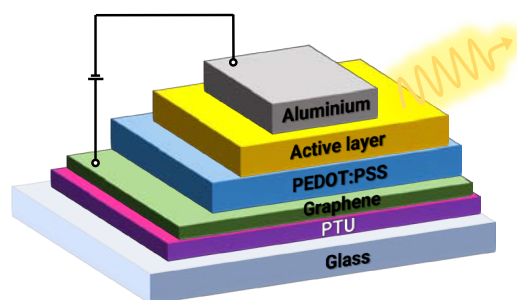


Figure 5.10. Configuration of the investigated LEC devices (*mpPh-PTU* thickness: 0, 28, and 75 nm).

In this study, the author fabricated the polymer layer at the bottom of the devices for compensating the RI mismatching between the glass (RI: ca. 1.5) and the graphene electrode (RI: 2.69 at 590 nm)^[41] (**Figure 5.10**),^[42] based on the previous report for the OLED configuration.^[43] Also, **mpPh-PTU** was selected as a target polymer because of its ultrahigh RI ($n_D = 1.81$), high visible transparency, and well flexibility in the film states that surely led to the further improvement of light-outcoupling efficiency in a practical level. The **mpPh-PTU** thin film layer was fabricated on a glass substrate by spin-coating, in which the solvent transfer deposition of a graphene electrode (thickness: 1 nm) was subsequently conducted to prepare the anode. Then, the PEDOT:PSS layer was spray-coated onto the graphene and the emitter ($[\text{Ir}(\text{dtbbpy})(\text{ppy})_2]\text{PF}_6$)^[44] was further spin-coated (thickness: 90 nm). Finally, the cathode was fabricated through physical vapor deposition of Al (thickness: 100 nm). From the RI-matching aspects, the RI between transparent electrode (i.e., graphene) and **mpPh-PTU** were almost similar and the remained RI-mismatching layer is the polymer-glass interface.^[43]

Prior to the device fabrication, the optical simulation (Setfos 5.3) was conducted for estimating

the change of light-outcoupling efficiency upon the **mpPh-PTU** loading.^[45,46] The simulation was based on the dipole emission model and the transfer matrix method. The simulated outcoupling efficiency (η_{OC}) with various thickness of PEDOT:PSS and **mpPh-PTU** layers is shown in **Figure 5.11a** (Note that other layers were set in the constant thickness (vide supra). In the conditions of 120-130 nm of PEDOT:PSS, η_{OC} reached the highest upon loading a 25 nm thickness of **mpPh-PTU** layers and the corresponding increase of external quantum efficiency (EQE) was $\sim 5\%$.

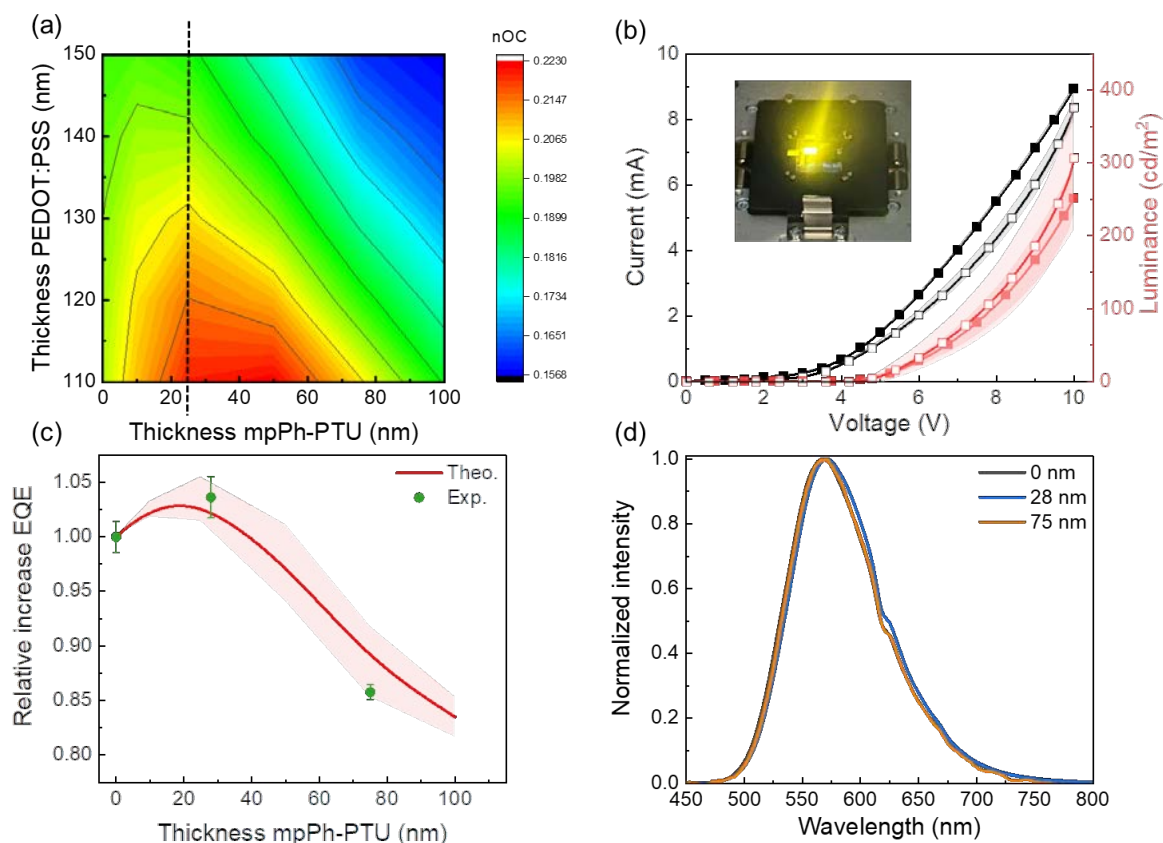


Figure 5.11. Simulation and experimental results of the LEC device performance. (a) Simulated values of light-outcoupling efficiency for several thicknesses of PEDOT:PSS and **mpPh-PTU** layers. The dashed line corresponds to 25 nm thickness. (b) L-I-V characteristics of LECs fabricated without **mpPh-PTU** (full symbols) and with **mpPh-PTU** film of 28 nm (open symbols). The inset shows a picture of a device in operando. (c) Comparison of calculated and experimental values of EQE vs. **mpPh-PTU** thickness showing outcoupling enhancement at *ca.* 25 nm. Enhancement ratios are based on theoretical results obtained from the Setfos simulation software. (d) Electroluminescence spectra recorded at peak luminance.

To confirm the actual light-outcoupling behaviors of the **mpPh-PTU**-loaded devices, the potential devices were experimentally prepared and their luminance-current-voltage (LIV) measurements were conducted in the conditions with or without loading **mpPh-PTU** layers (thickness:

0, 28, and 75 nm) (**Figure 5.11b**). The average maximum value was improved from 252 cd m^{-2} (without *mpPh-PTU* layer) to 310 cd m^{-2} (with a 28 nm *mpPh-PTU* layer), which can be converted to the 5% increase of total EQE (**Figure 5.11c**). Furthermore, their electroluminescence features were almost identical with a broad, structureless, and yellow emission peak at 560 nm, indicating that the loaded *mpPh-PTU* did not affect the overall emission performance of the fabricated devices (**Figure 5.11d**). The stability of the devices was finally measured with the pulse current scheme for evaluating the operational behavior (50 mA cm^{-2} , see the detailed experimental conditions in the legend of **Figure 5.12**). The time-course operational features were resulted as follows: (1) an initial voltage of ca. 5.0 V following the exponential attenuation to reach a plateau. (2) the enhanced luminance from ca. 50 cd m^{-2} to ca. 250, 350, 300 cd m^{-2} for the conditions with the stack of 0, 28, and 75 nm of *mpPh-PTU* layer, respectively. The quick decline of the average voltage corresponded to the effect of electric double layer formation between the electrodes, suggesting the proper electrochemical doping upon the initial voltage bias. Finally, the device measurement was finally ended up after ca. 20 h accompanied with a luminance drop recording the halftime (i.e., time reaching the half of the maximum luminance value) of $t_{1/2} > 120 \text{ h}$ for each measurement. These superior performance of the *mpPh-PTU*-loaded devices were comparable to the values for other reported LECs using the graphene-based electrodes.^[44,47,48]

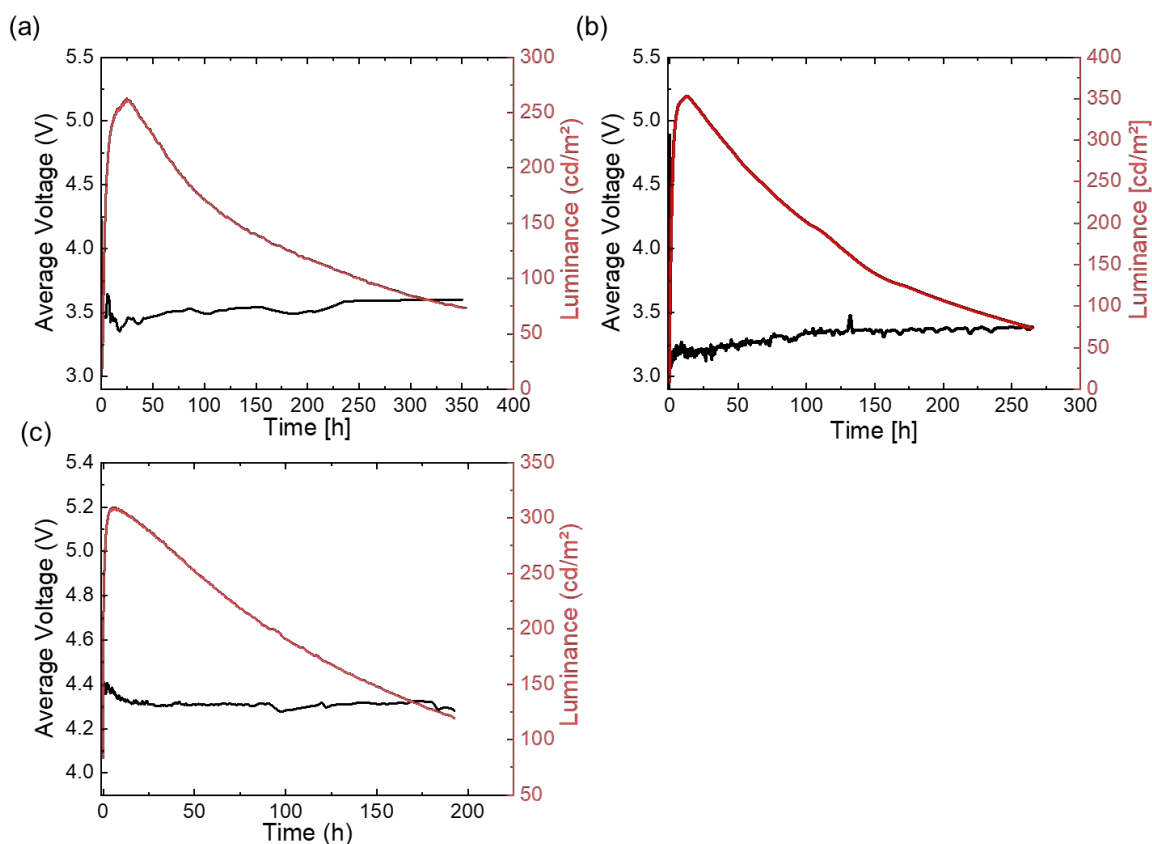


Figure 5.12. Luminance (red) and average voltage (black) for LECs devices with *mpPh-PTU* layers of

(a) 0 nm, (b) 28 nm, and (c) 75 nm (pulsed current density: 50 mA cm⁻², block wave: 1 kHz, duty cycle: 50 %).

5.5 Degradation Studies of Poly(thiourea)s via Dynamic Covalent Chemistry

5.5.1 Degradation Tests for Poly(thiourea)s

Finally, degradability of PTUs were also investigated. Due to recent environmental issues caused by the plastic wastes, degradation of polymers to monomers becomes one of the essential functionalities leading to the sustainable recycling. To the best of our knowledge, the only attempt to impart degradability to HRIPs is the recyclable poly(trithiocarbonate)s by Ren *et al.*^[49] Also, systematic design for degradable HRIPs has not been proposed before in spite of such global request. For affording degradability to polymers, molecular design that enables chain cleavage under the presence of external trigger is necessary.^[50–55] As thiourea is a dynamic covalent bond that reversibly dissociate to the corresponding amines and isothiocyanates especially under the base-catalyzed heating conditions,^[29,30,56,57] we anticipated that PTU can be degraded to low-molecular-weight compounds using the excessive diamines (**Figure 5.13a**). Here, the excessive diamine behaves as both the catalyst and the end-capping agent of isothiocyanate groups for cleaving the polymer chains.

mpPh- and *pPhPPS*-PTU were selected for the degradation tests because these polymers showed the most efficient potentials with ultrahigh RI as well as high molecular weight and high solubility in DMF. Each PTU was stirred with or without excess *m*-phenylenediamine (*mPDA*) in DMF at room temperature or under heating (at 50 °C) and molecular weights were monitored by SEC (**Figure 5.13c, 5.13d, 5.15b, 5.15c**). On the degradation of *mpPh*-PTU ($M_n = 2.7 \times 10^4$), both the addition of *mPDA* and heating accelerated the degradation reaction owing to the accelerated bond exchange reactions. For the entry 1 in **Figure 5.13b** (diamine addition and heating), *mpPh*-PTU was depolymerized rapidly and finally reached to the lowest M_n of 1.8×10^3 (**Figure 5.13e**) with the highest degradation efficiency (i.e., conversion of thiourea) of 91% after 72 hours (**Figure 5.14**). According to the ¹H NMR spectra of the degraded fraction, new signals for thiourea, phenyl, and amino groups were confirmed in conjunction with the degradation (**Figure 5.13g**). After the molecular weight was saturated, most of these signals can be characterized as the protons of the terminal structures that can only be observed after the end-capping by *mPDA*. These SEC and NMR results supported the main-chain degradation mechanism, in which the additive diamines were selectively inserted to the isothiocyanate terminal of the degraded PTU fragment during the bond exchange reaction (**Figure 5.17a**, black and red brackets). Such selectivity was observed presumably because the terminal amine of PTU had less nucleophilicity than of aromatic diamine, being attributed to the electron-withdrawing effect of the thiourea moiety adjacent to the end aminophenyl unit of the PTU chain.

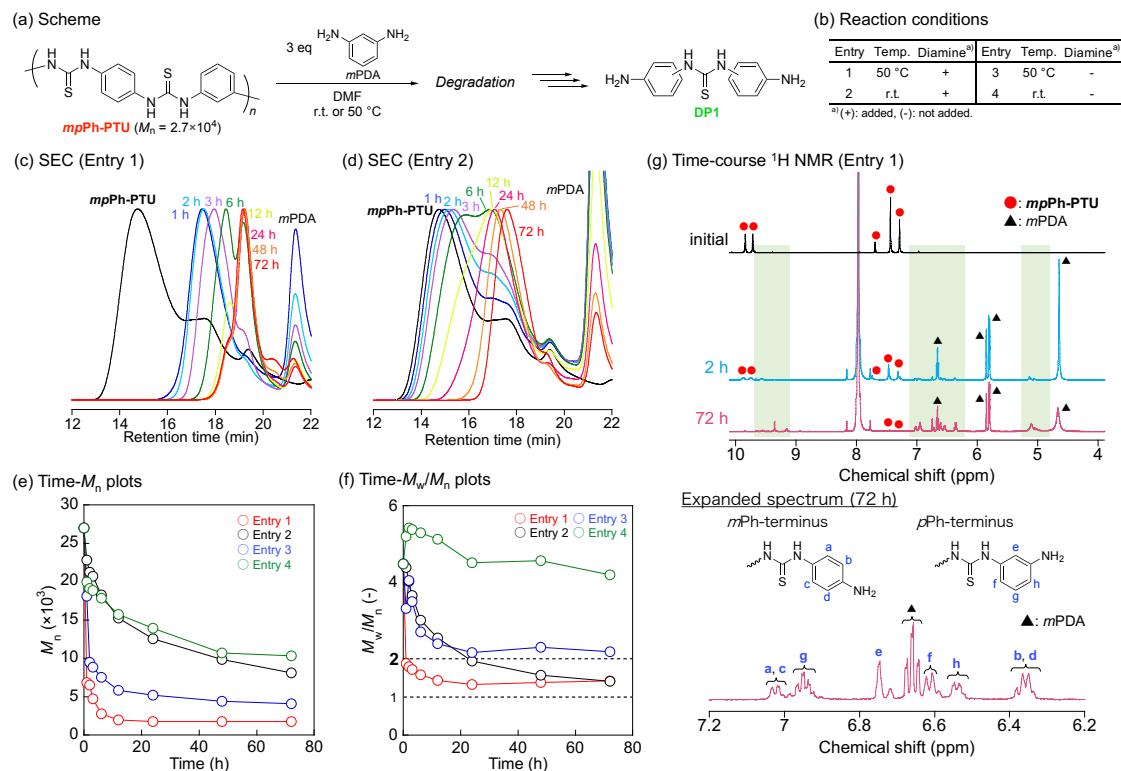


Figure 5.13. Time-course for the degradation of *mpPh-PTU*: (a) Degradation scheme of *mpPh-PTU*. (b) Reaction conditions. (c) SEC chromatograms of the fractionated products for entry 1 (at 50 °C, with diamine) in DMF (with 10 mM LiCl). (d) SEC chromatograms for entry 2 (at room temperature, with diamine). (e) Time- M_n plots. (f) Time- M_w/M_n plots. (g) Time-course selected ^1H NMR spectra (initial, 2 h, and 72 h) including the expanded spectrum (72 h) for entry 1.

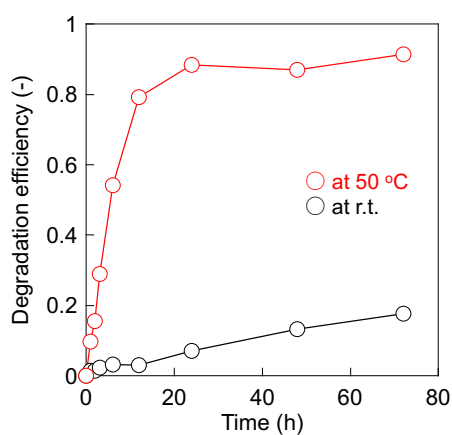


Figure 5.14. Degradation efficiency of *mpPh-PTU* for entries 1 (at 50 °C) and 2 (at r.t.). Entry numbers were corresponded to those in **Figure 5.13b**.

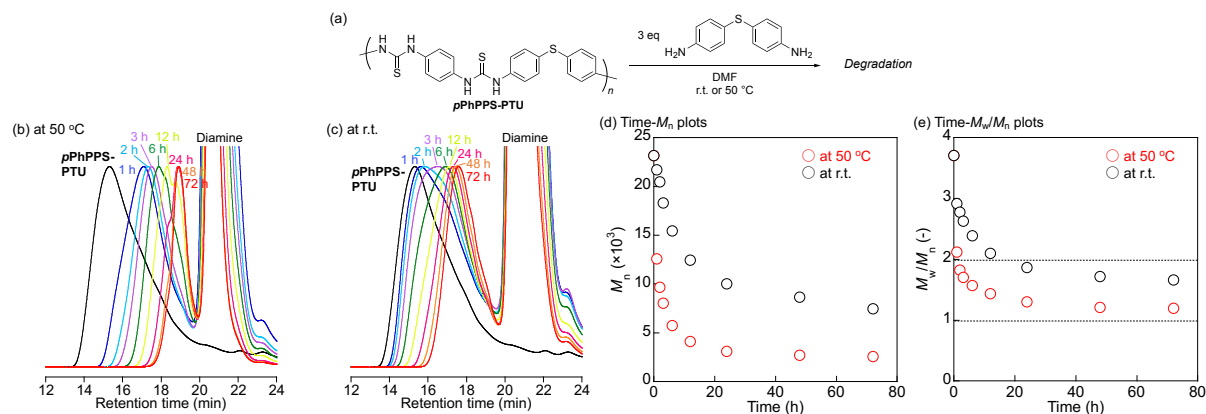


Figure 5.15. Time-course for the degradation of *pPhPPS-PTU* with diamine: (a) Scheme. (b) SEC chromatograms of the fractionated products degraded at room temperature (eluent: DMF containing 10 mM LiCl) (c) SEC chromatograms (eluent: DMF containing 10 mM LiCl) of the fractionated products at 50 °C, with diamine. (d) SEC chromatograms at room temperature with diamine. (e) Correlation between reaction time and M_n . (f) Correlation between reaction time and M_w/M_n . The two dotted lines indicate $M_w/M_n = 2$ (ideal value for step-growth polymerization) and 1 (ideal value for complete degradation).

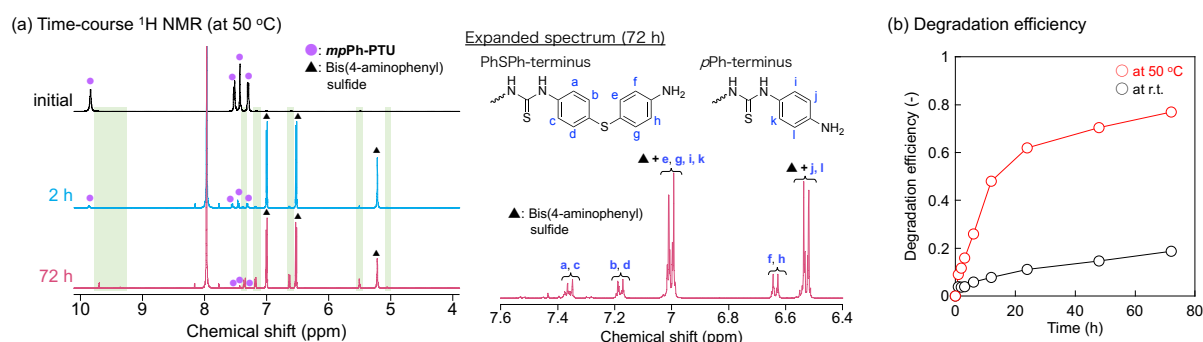


Figure 5.16. Degradation of *pPhPPS-PTU*. (a) Time-course of the selected ^1H NMR spectra (initial, 2 h, and 72 h) of the fractionated products including the expanded spectrum (72 h) for the degradation at 50 °C. (b) Degradation efficiency (at 50 °C and at r.t.).

5.5.2 Evaluation of Dynamic Covalent Properties of Poly(thiourea)s

For further revealing the precise mechanism of the degradation properties, the dynamic covalent nature of poly(thiourea)s including the molecular weight distribution has been investigated without the non-diamine conditions. Upon stirring *mpPh-PTU* without diamine (entries 3 and 4 for **Figure 5.13b**), the molecular weight of *PTU* also decreased although the degradation was suppressed compared with the corresponding entries 1 and 2. Especially for the heating condition (entry 3), the molecular weight reduced significantly and was finally saturated with the higher value than entry 1 ($M_n = 4.1 \times 10^3$) (**Figure 5.13e**, blue line). The molecular weight distribution (M_w/M_n) also decreased in concordance with the degradation progress, and especially for entry 3, M_w/M_n was saturated at approx.

2 (Figure 5.13f, blue line), corresponding to the ideal distribution for step-growth polymerization.^[58] Such time-course behavior was similar to the case of dynamic covalent polymers,^[59] in which the polymer chains were reconfigured to the most randomized distribution via the repetition of bond exchange reactions. In the case of entries 3 and 4, only bond exchange reaction was occurred under heating without diamines and therefore M_n values were not drastically changed upon stirring. The degradation/redistribution of *pPhPPS-PTU* were also resulted in the same trend (Figure 5.15 and 5.16). Summarizing the above degradation/redistribution features, heating PTU solutions without additives reached the bond exchange to the equilibrium yielding middle-MW products with $M_w/M_n \sim 2$ (Figure 5.17b (i)), whereas heating with diamines gave low-MW products with low molecular weight dispersion ($M_w/M_n \sim 1-1.5$) (Figure 5.17b (ii)).

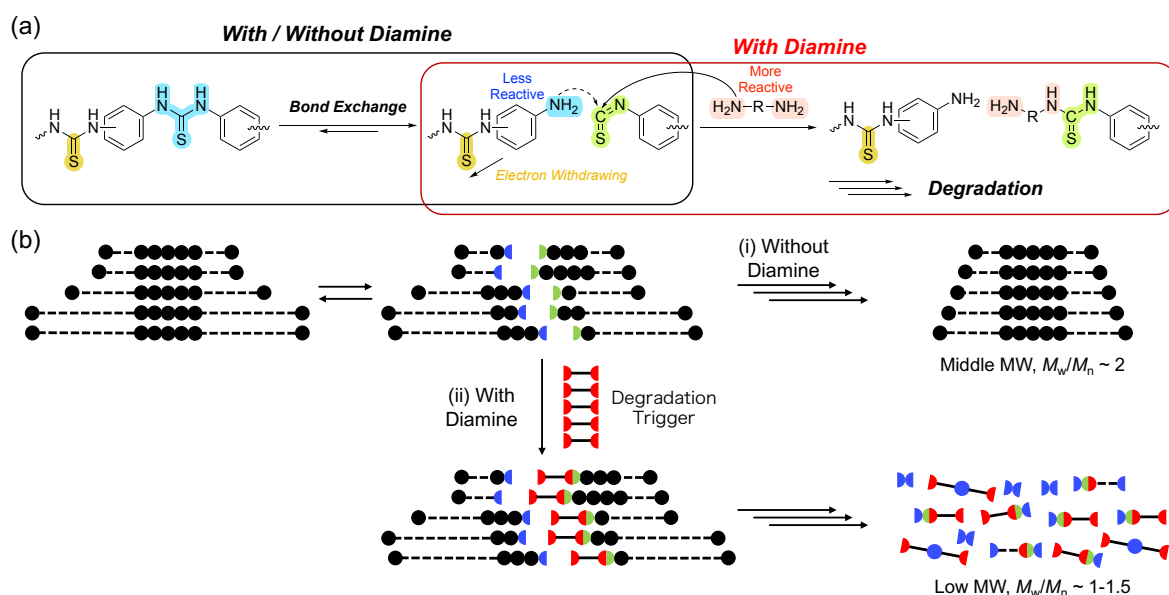


Figure 5.17. Degradation/redistribution reaction of PTU. (a) Plausible mechanism for the degradation of *mpPh-PTU* via dynamic covalent chemistry. (b) Schematic representation for the length distribution of the polymer chains under the degradation/redistribution reaction with or without diamine.

The switchable degradation system of PTUs via dynamic covalent chemistry has been demonstrated. Still, the reaction preciseness should be improved because the redistribution reaction of PTUs were occurred even in the conditions without diamines. As a solution, enhancing bond-dissociation energy of C-N bonds for thiourea, which is a driving force of bond exchanging reaction, would be precisely optimized by introducing additional side groups or heteroaromatic spacers into the PTU skeletons.

In summary, six aromatic poly(thiourea)s (PTUs) have been synthesized and their properties including their thermal, crystal, and optical properties and degradation functionalities toward multifunctional optoelectronic materials were investigated. PTUs were synthesized from conventional

diamines under mild conditions and exhibited high molecular weight, well solution-processability, and thermal properties. Notably, the compact phenylene-containing **PTU** achieved the highest density and packing constant (1.50 g cm^{-3} , $K_p = 0.738$), high visible transparency (over 92 % T at 1 μm), and an ultrahigh RI ($n_D = 1.81$). These fascinating properties were attributed to the “polarizable group synergy”, whereby multiple H-bonding thioureas and phenylene spacers have contributed cooperatively to achieving amorphous, dense and high-RI polymer networks based on their high polarizability. Practically, **PTUs** represented efficient mechanical properties with enough flexibility and film-formability, which can easily be adopted to the wet-processing optoelectronic device fabrication process as demonstrated with light-emitting electrochemical cells. Furthermore, **PTUs** were dynamic covalent polymers which also can be degraded to the low molecular weight components by just adding diamine to the solution upon heating.

For overcoming the empirical RI-transparency dichotomy, this chapter represents new important concept that the introduction of polarizable and multiple H-bonds can contribute to realize transparent polymers with exceptional RI. Together with the degradable features of various sulfur-containing substructures,^[60] this is a first step toward the comprehensive design of next-generation optoelectronic polymers achieving high light-extraction efficiency and environmental friendliness. As a future work, the author aims to further configurate the **PTU** microstructures as well as their polarizability and H-bonding array conformations achieving further high densities, which will be accomplished through various annealing process under heating or external electric field.^[61]

5.6 Experimental Section

Materials. 1,3-phenylenediamine (*m*PDA), 1,4-phenylene diisothiocyanate, bis(4-aminophenyl sulfide), *m*-tolidine, 9,9'-bis(4-aminophenyl) fluorene were purchased from Tokyo Chemical Industry Co. Dimethyl sulfoxide (DMSO), N-methyl-2-pyrrolidone (NMP), N,N-dimethylformamide (DMF) were purchased from Kanto Chemical Co. 1,1'-thiocarbonyl diimidazole was purchased from Sigma-Aldrich Co. Methanol was purchased from Kokusan Chemical Co. All reagents were used as purchased without further purification.

Synthesis of Poly(1,3-phenylene thiourea) (*m*Ph-PTU). Poly(thiourea)s were synthesized via either polycondensation of diamine with 1,1-thiocarbonyl diimidazole or polyaddition of diamine with diisothiocyanate, by arranging procedures in the previous reports.^[25,32] To a 5 mL flask was added 1,3-phenylenediamine (324 mg, 3 mmol) and was dissolved in DMF (3 mL). Subsequently, 1,1'-thiocarbonyl diimidazole (594 mg, 3 mmol) was added and was stirred at room temperature for 24 hours. After the polymerization, the solution was diluted with DMF (4 mL) and was precipitated in methanol (500 mL). The precipitate was collected through filtration, was washed with methanol, and was dried in vacuo (at room temperature and 85 °C) to obtain *m*Ph-PTU as a whitish powder (0.38 g, 84% yield). SEC (DMF with 10 mM LiCl): $M_w = 1.2 \times 10^4$, $M_w/M_n = 3.0$.

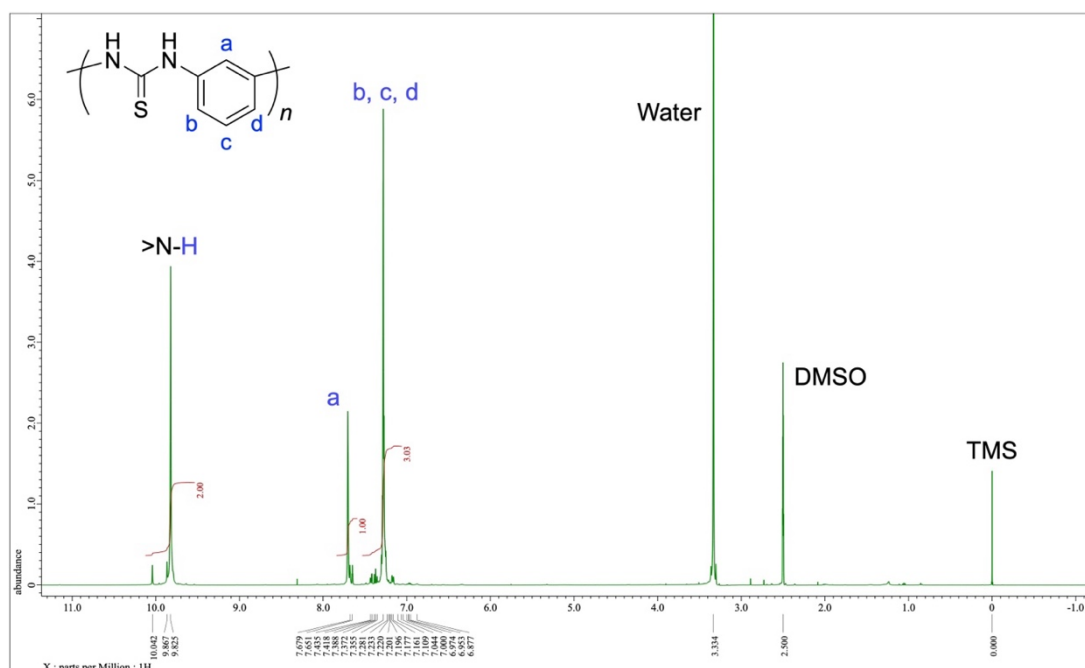


Figure 5.18. ^1H NMR spectrum of *mPh*-PTU in $\text{DMSO-}d_6$.

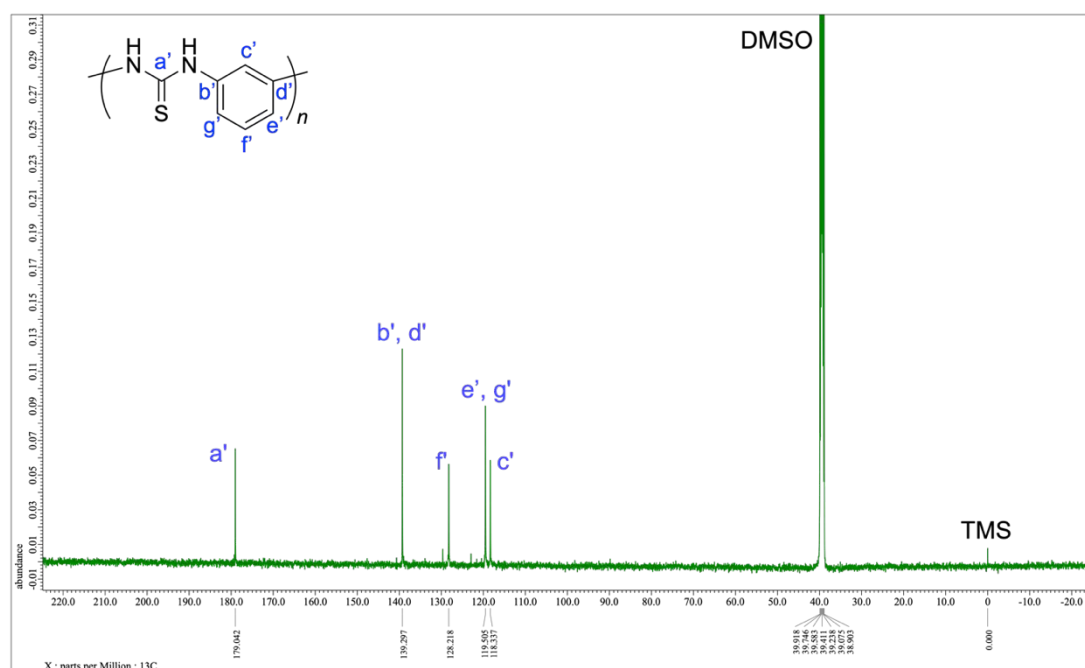


Figure 5.19. ^{13}C NMR spectrum of *mPh*-PTU in $\text{DMSO-}d_6$.

Synthesis of Poly(1,3-phenylene thiourea)-alt-poly(1,4-phenylene thiourea) (*mpPh*-PTU). To a 30 mL flask were added 1,4-phenylene diisothiocyanate (640 mg, 3.32 mmol) and 1,3-phenylenediamine (360 mg, 3.32 mmol), were dissolved in DMSO (11.1 mL), and were stirred at room temperature for 24 hours. After the polymerization, the solution was diluted with DMF (14 mL) and was precipitated in

methanol (800 mL). The precipitate was collected through filtration, was washed with methanol, and was dried in vacuo (at room temperature and at 70 °C) to obtain **mpPh-PTU** as a whitish powder (0.94 g, 94% yield). SEC (DMF with 10 mM LiCl): $M_w = 1.4 \times 10^5$, $M_w/M_n = 4.8$.

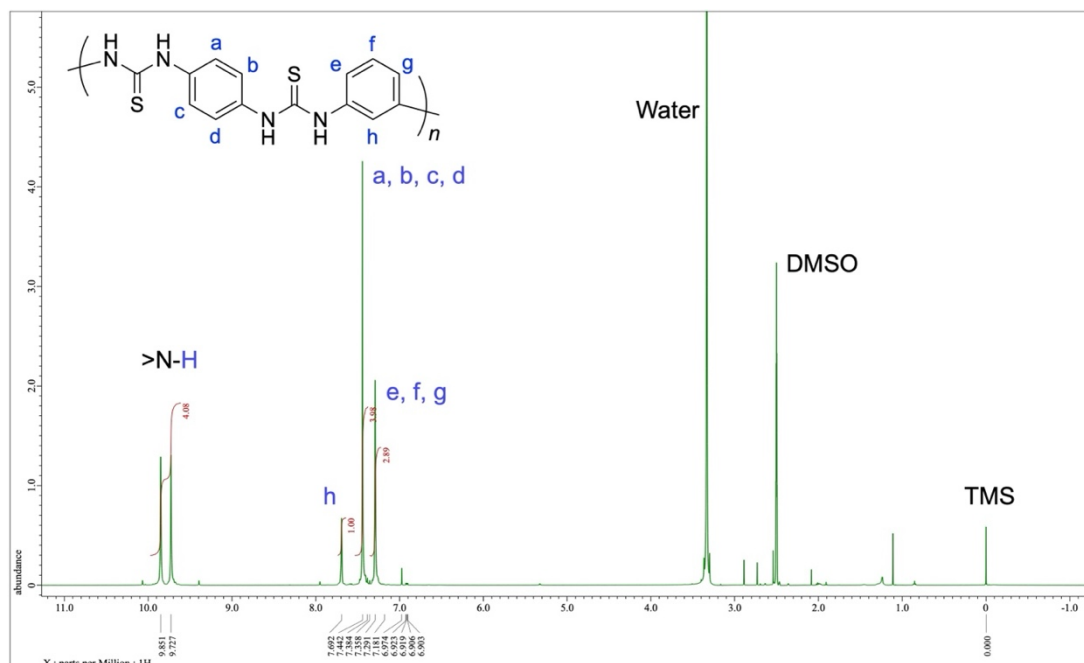


Figure 5.20. ^1H NMR spectrum of **mpPh-PTU** in $\text{DMSO-}d_6$.

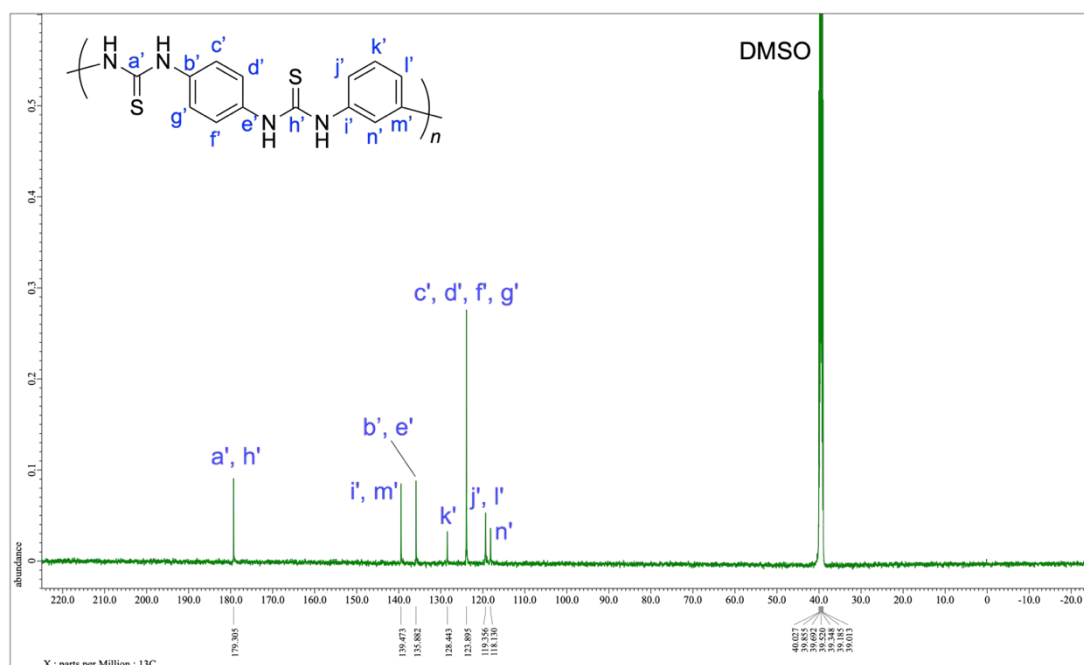


Figure 5.21. ^{13}C NMR spectrum of **mpPh-PTU** in $\text{DMSO-}d_6$.

Synthesis of Poly(4,4'-phenylsulfide thiourea) (PhSPh-PTU). To a 30 mL flask were added bis(4-aminophenyl sulfide) (1.50 g, 6.93 mmol) and 1,1'-thiocarbonyl diimidazole (1.30 g, 7.30 mmol), were dissolved in NMP (13.9 mL), and were stirred for 24 hours at room temperature. After the

polymerization, the reaction solution was diluted with NMP (35 mL) and was precipitated in methanol (1000 mL). The precipitate was collected through filtration, was washed with methanol, and was dried in vacuo. The collected product was reprecipitated with NMP (50 mL)/methanol (1000 mL) for further purification. The precipitate was collected after filtration, was washed (methanol), and was dried in vacuo (at room temperature and at 85 °C) to obtain **PhSPh-PTU** as a whitish powder (1.65 g, 92% yield). SEC (DMF with 10 mM LiCl): $M_w = 5.0 \times 10^4$, $M_w/M_n = 3.7$.

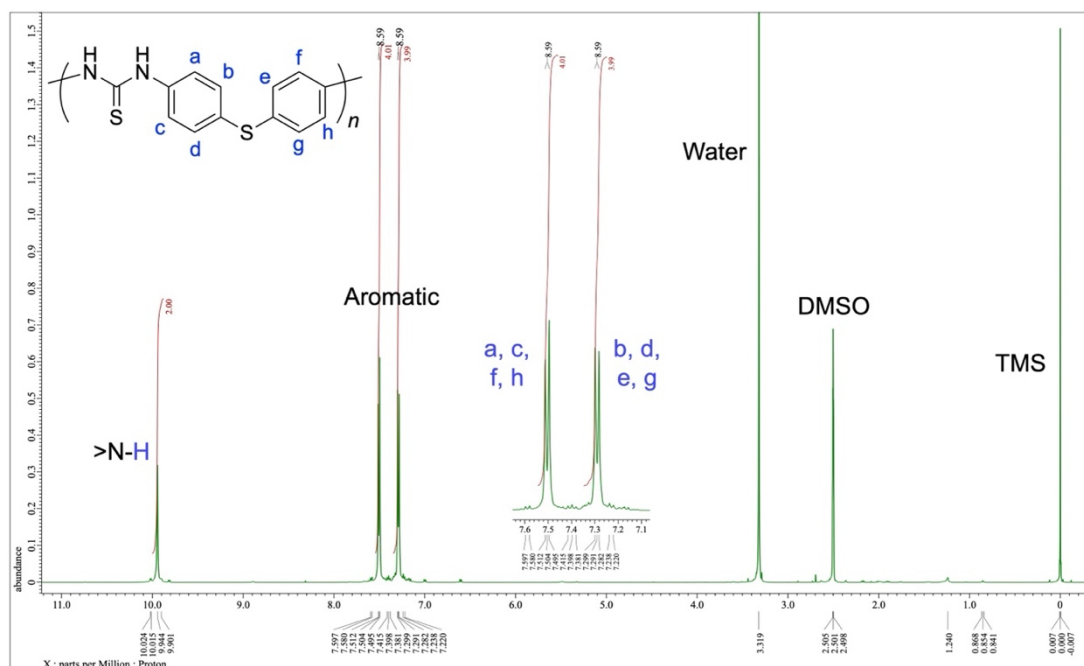


Figure 5.22. ^1H NMR spectrum of PhSPh-PTU in $\text{DMSO-}d_6$ (inset: expanded spectrum).

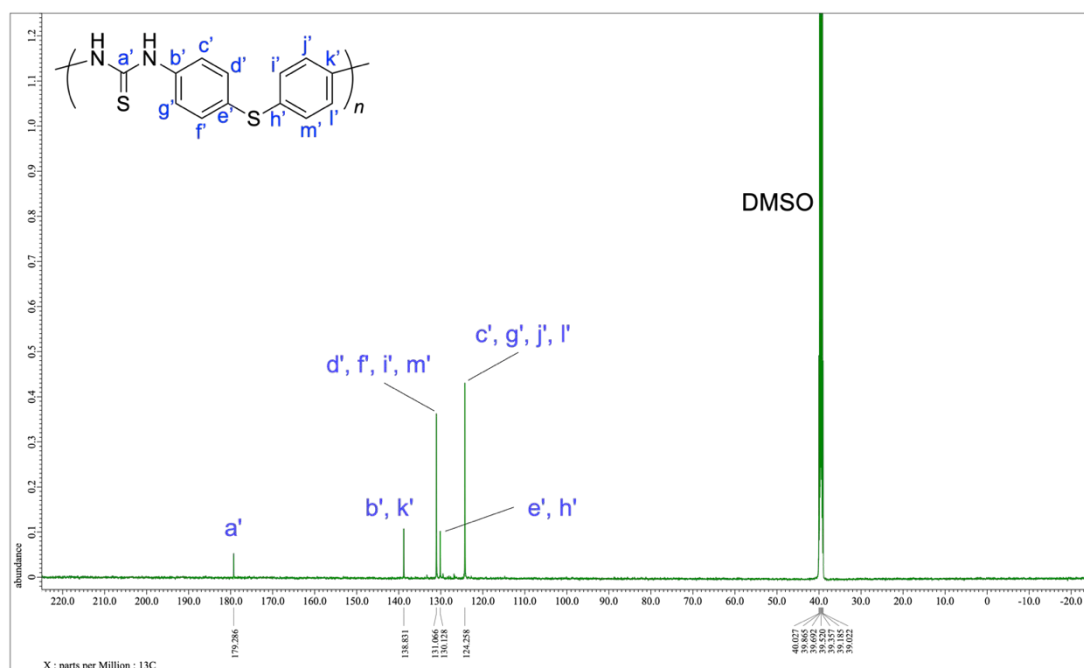
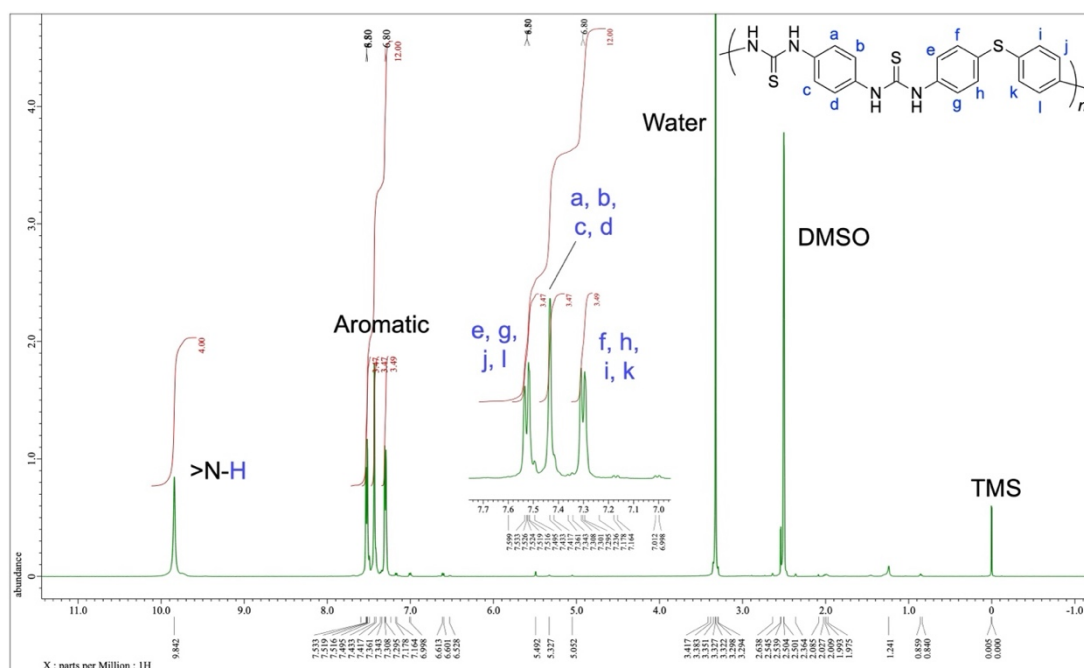


Figure 5.23. ^{13}C NMR spectrum of PhSPh-PTU in $\text{DMSO-}d_6$.**Synthesis of Poly(1,4-phenylene thiourea)-*alt*-poly(4,4'-phenylsulfide thiourea) (*p*PhPPS-PTU).**

To a 100 mL flask were added 1,4-phenylene diisothiocyanate (577 mg, 3.0 mmol) and bis(4-aminophenyl) sulfide (649 mg, 3.0 mmol), were purged with nitrogen for 10 minutes, was added DMSO (18 mL), and was stirred for 24 hours at 30 °C. The solution was then diluted with DMSO (20 mL) and was precipitated in methanol (900 mL). The precipitate was collected through filtration, was washed with methanol, and was dried in vacuo (at room temperature, at 80 °C, and at 85 °C) to obtain *p*PhPPS-PTU as a whitish powder (1.11 g, 90% yield). SEC (DMF with 10 mM LiCl): $M_w = 6.2 \times 10^4$, $M_w/M_n = 3.2$.

**Figure 5.24.** ^1H NMR spectrum of *p*PhPPS-PTU in $\text{DMSO-}d_6$ (inset: expanded spectrum).

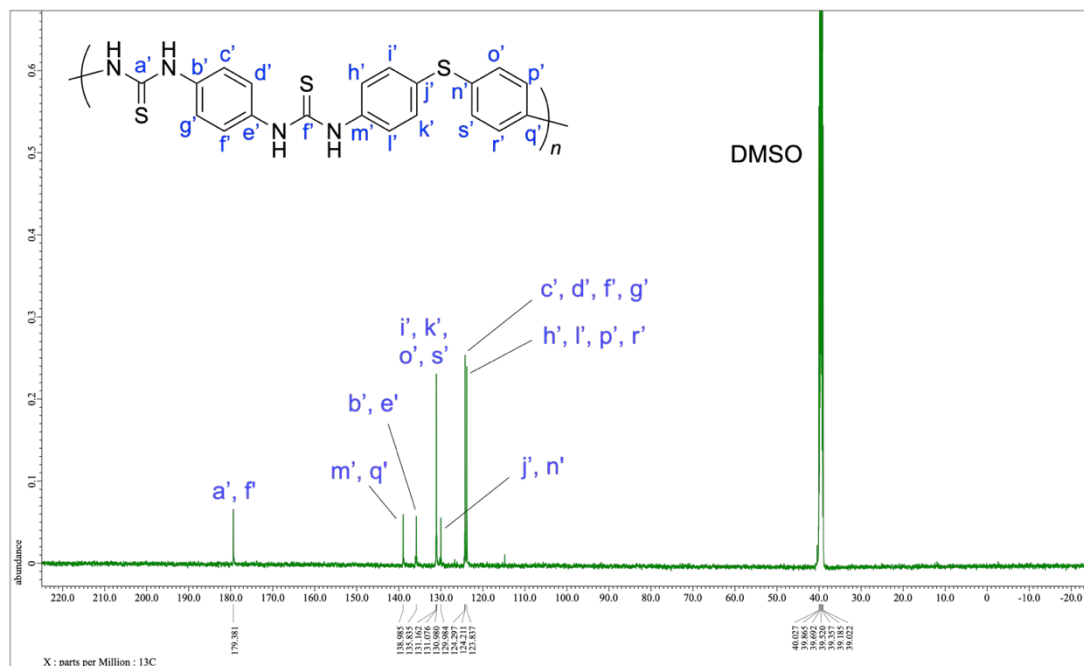


Figure 5.25. ^{13}C NMR spectrum of *p*PhPPS-PTU in $\text{DMSO-}d_6$.

Synthesis of Poly(2,2'-dimethyl-4,4'-biphenylene thiourea) (diMeBiPh-PTU). To a 30 mL flask were added *m*-tolidine (835 mg, 3.93 mmol) and 1,1'-thiocarbonyl diimidazole (736 mg, 4.13 mmol), were dissolved in DMF (8.06 mL), and were stirred at room temperature for 24 hours. The solution was then diluted with DMF (40 mL) and was precipitated in methanol (800 mL). The precipitate was collected through filtration, was washed with methanol, and was dried in vacuo (at room temperature). The solid was then reprecipitated with DMF (40 mL) / methanol (700 mL) and the purified precipitate was collected through filtration, was washed with methanol, and was dried in vacuo (at room temperature and at 70 °C) to obtain **diMeBiPh-PTU** as a whitish powder (1.00 g, 100% yield). SEC (DMF with 10 mM LiCl): $M_w = 3.9 \times 10^5$, $M_w/M_n = 2.1$.

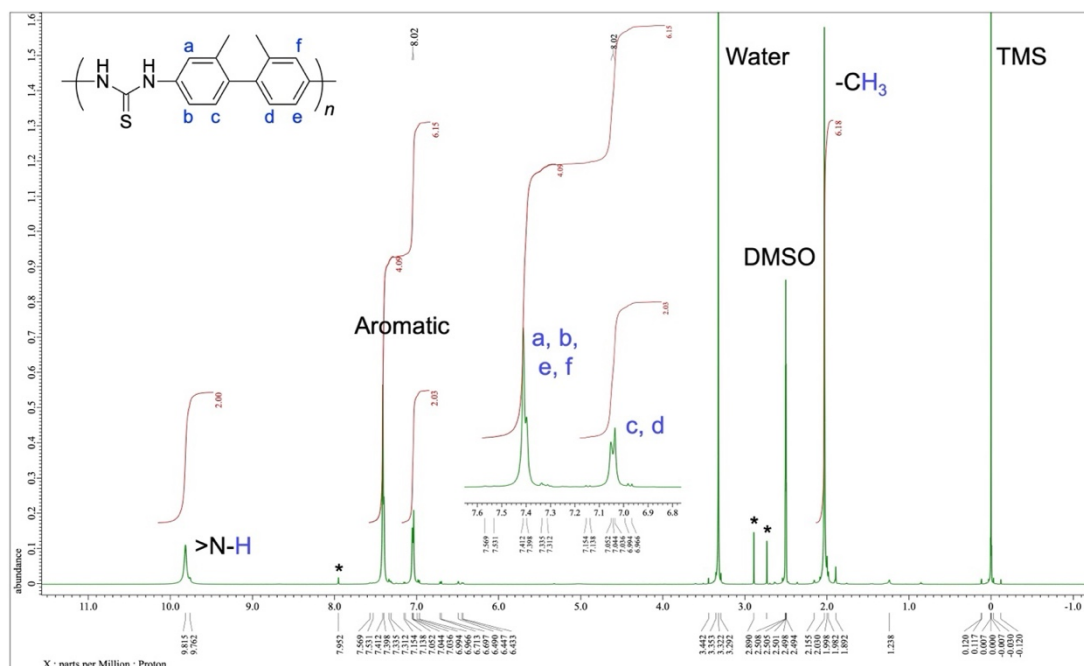


Figure 5.26. ^1H NMR spectrum of diMeBiPh-PTU in $\text{DMSO-}d_6$ (inset: expanded spectrum, *: signals for residual DMF).

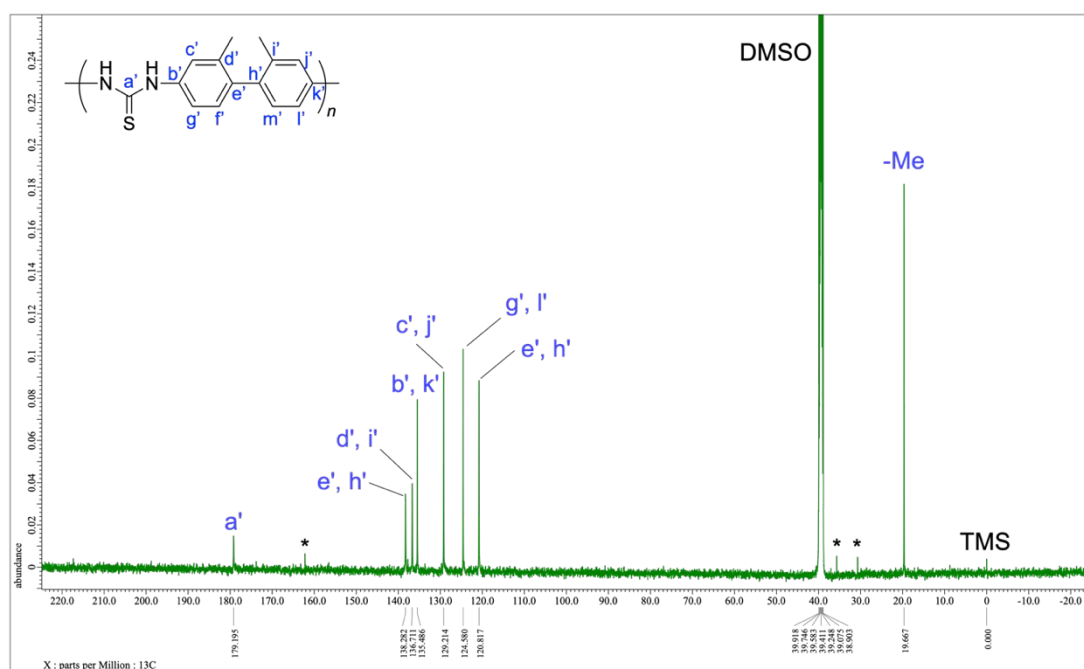


Figure 5.27. ^{13}C NMR spectrum of diMeBiPh-PTU in $\text{DMSO-}d_6$ (*: signals for residual DMF).

Synthesis of Poly(4,4'-(9-fluorenylidene)diphenylene thiourea) (Flu-PTU). To a 10 mL flask, 9,9'-bis(4-aminophenyl) fluorene (523 mg, 1.5 mmol) was dissolved in DMF (5 mL), was added 1,1'-thiocarbonyl diimidazole (297 mg, 1.67 mmol), and was stirred at room temperature for 24 hours. The solution was then diluted with DMF (5 mL) and was precipitated in methanol (300 mL). The precipitate was collected by filtration, was washed with methanol, and was dried in vacuo. The obtained solid was

redissolved in DMF (8 mL) and was reprecipitated with methanol (300 mL). The product was collected by filtration, was washed with methanol, and was dried in vacuo to obtain **Flu-PTU** as a white powder (0.50 g, 85% yield). SEC (DMF with 10 mM LiCl): $M_w = 4.7 \times 10^4$, $M_w/M_n = 1.8$.

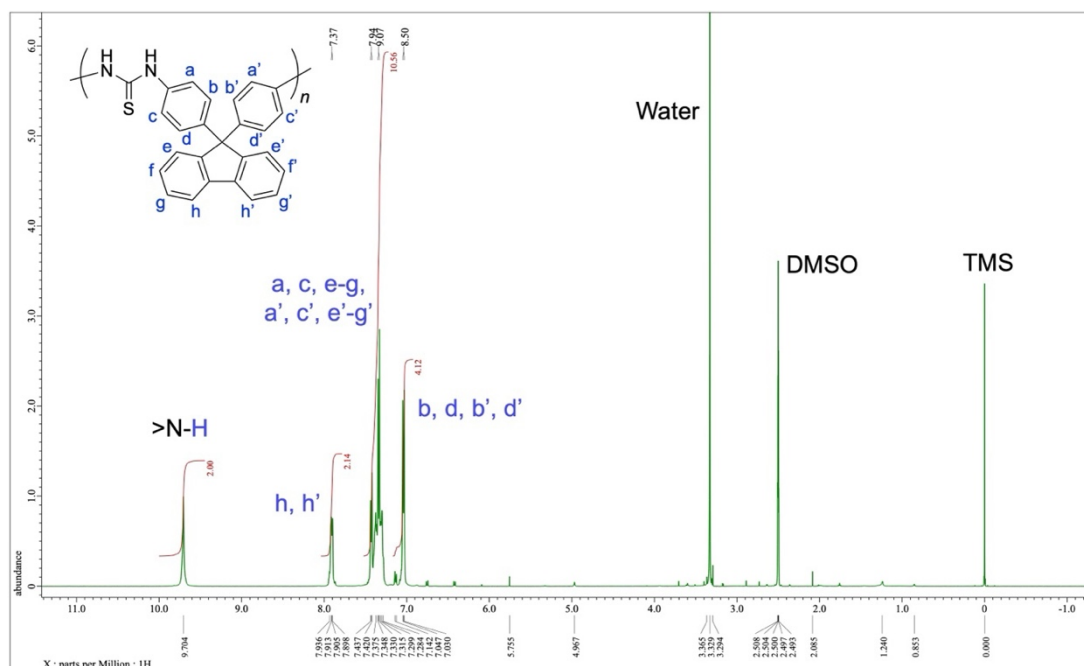


Figure 5.28. ^1H NMR spectrum of **Flu-PTU** in $\text{DMSO-}d_6$.

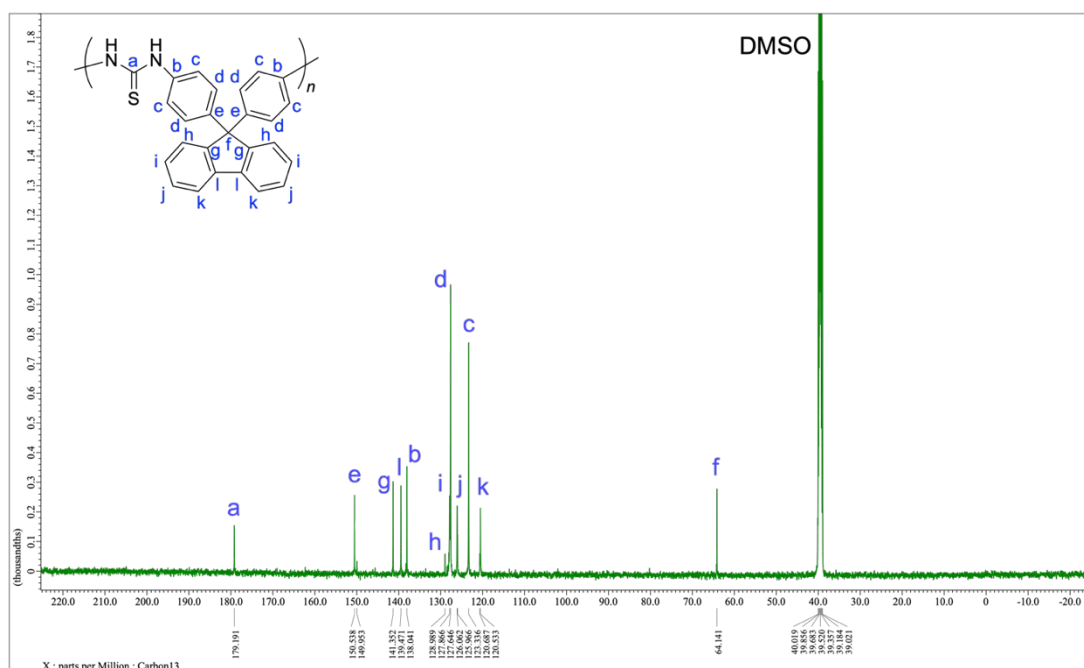


Figure 5.29. ^{13}C NMR spectrum of **Flu-PTU** in $\text{DMSO-}d_6$.

Synthesis of Poly(1,3-phenylene urea)-*alt*-poly(1,4-phenylene urea) (*mpPh*-PU). To a 10 mL flask were added 1,4-phenylene diisocyanate (240 mg, 1.5 mmol) and 1,3-phenylenediamine (162 mg, 1.5

mmol) in DMF (5 mL), and was stirred at room temperature. The products were soon precipitated and reaction was terminated by adding DMF (10 mL) after 3 minutes. The solution was immediately precipitated in methanol (300 mL) and the precipitate was collected through filtration, was washed with methanol, and was dried in vacuo to obtain **mpPh-PU** as a whitish powder (0.40 g, 99% yield). **mpPh-PU** was insoluble in any organic solvents (such as DMF and DMSO).

Film fabrication on glass substrates. For UV-vis measurements, thin films of **PTUs** were prepared on glass substrates via drop-casting. Herein the typical procedure has been described. Glass substrates were pre-cleaned by ultrasonication in 2-propanol, chloroform, methanol, and acetone before the film preparation. Except in the case of **PhSPh-PTU**, a polymer solution in DMF (concentration: 15 mg mL⁻¹, filtrated with a $\phi = 0.2$ mm PTFE filter) (0.4 mL) was dropped onto a glass substrate. The film was prepared through heating in vacuo at 50 °C for 14 hours, at 70 °C for 7 hours, and at 90 °C for 21 hours. On preparing the **PhSPh-PTU** film, DMF/DMSO = 1/1 (v/v) mixture was used as a solvent owing to the solubility of the polymer. The other conditions and procedures were the same as in the case of the other polymers.

Film fabrication on Si wafers. For spectroscopic ellipsometry, thin films of **PTUs** were prepared on glass substrates via spin-coating. Si wafers were pre-cleaned by ultrasonication with the same procedure as the case of 1.3.1. A typical procedure is as follows: A polymer solution in DMF, DMSO or NMP (solvent was selected depends on the solubility of a polymer) (concentration: 60 mg mL⁻¹, filtrated with a $\phi = 0.2$ mm PTFE filter) was poured on a Si wafer and the substrate was rotated according to the following procedure: slope 3 sec, 2000 rpm 20 sec, slope 3 sec, 3000 rpm 30 sec, slope 3 sec. The spin-coated films were dried in vacuo at 90 °C (at 100 °C for only **PhSPh-PTU**) for two overnights.

Determination of H-bond conformations of PTUs. The ratio of trans/trans or cis/trans conformations for thiourea was determined from the IR spectra. The procedure was based on the previous report^[32] with some modifications. After the baseline calibration, each IR spectrum was peak-separated in the range of 3600-2800 cm⁻¹. Conformation ratio was determined by comparing integrals of the H-bonding N-H stretching peaks for trans/trans and cis/trans conformations.

Degradation of PTUs with diamine. To a 50 mL flask, **mpPh-PTU** (150 mg, 1.0 mmol of thiourea unit) and *m*-phenylenediamine (324 mg, 3.0 mmol) was added, was dissolved in DMF (10 mL), and was stirred at room temperature or at 50 °C. The reaction solution (0.6 mL) was fractionated after 1, 2, 3, 6, 12, 24, 48, 72 hours. The fractionated solution was immediately analyzed by SEC chromatograms and ¹H NMR.

PTU degradation without diamine upon heating (entry 3 for Figure 5.11b): To a 50 mL flask,

mpPh-PTU (150 mg, 1.0 mmol of thiourea unit) was dissolved in DMF (10 mL) and was stirred at room temperature or at 50 °C. The procedures for the fractionation and the ¹H NMR and SEC measurements were the same as the case of the degradation with diamine.

PTU degradation without diamine at room temperature (entry 4 for Figure 5.11b): To a 50 mL flask, **mpPh-PTU** (75 mg, 0.5 mmol of thiourea unit) was dissolved in DMF (5 mL) and was stirred at room temperature or at 50 °C. The procedures for the fractionation and the ¹H NMR and SEC measurements were the same as the case of the degradation with diamine, except that 0.4 mL of the reaction solution was fractionated for each time conditions.

Determination of degradation efficiency. The degradation progress of **PTU** was monitored by determining degradation efficiency, which indicates the ratio of thiourea groups adjacent to the arylamino terminus to all thiourea groups. Here, degradation efficiency can be described as follows:

$$(\text{Degradation efficiency}) = \frac{A_{\text{amino}}}{2A_{\text{thiourea}}}$$

where A_{thiourea} and A_{amino} denote ¹H NMR integrals of the signals for all thiourea N-H groups (approx. 9-10.5 ppm) and terminal NH₂ groups (note that NH₂ groups of the diamines were excluded). (Note: For example, in the case that all adjacent moieties of thiourea groups in the **PTU** chains were fully converted to the arylamino groups, E_{deg} was calculated as 1.00.)

Measurements. ¹H (500 MHz) and ¹³C (125 MHz) NMR spectra were recorded by JEOL JNM-ECX500 or ECZ500. Fourier-transform infrared (IR) spectra were recorded by JASCO FT/IR-6100 with KBr pellets or with attenuated total reflection (ATR) method (attached kit: JASCO ATR PRO ONE). Variable temperature NMR (VT-NMR) measurements (600 MHz) were conducted by Bruker AVANCE 600 NEO. Size exclusion chromatography (SEC) was conducted with SHIMADZU LC-20AD/CBM-20A using TOSOH TSK-GEL column with SHIMADZU SPD-M20A UV detector (wavelength: 275 nm) (eluent: DMF with 10 mM LiCl, flow rate: 0.3 mL min⁻¹, molecular weights were calibrated by polystyrene standards). Differential scanning calorimetry (DSC) were conducted with TA Instruments Q200. UV-vis spectra were recorded by Jasco V-670 spectrometer. For the UV-vis measurement of polymer solutions, a quartz cell with 1 cm length was used. Spectroscopic ellipsometry were conducted by HORIBA UVISEL ER AGMS iHR320. Density of the polymer samples were measured by AccuPycII 1340 (the average values for five experiments were adopted).

References

- [1] T. Higashihara, M. Ueda, *Macromolecules* **2015**, *48*, 1915.
- [2] J.-G. Liu, M. Ueda, *J. Mater. Chem.* **2009**, *19*, 8907.

- [3] H. Ma, A. K.-Y. Jen, L. R. Dalton, *Adv. Mater.* **2002**, *14*, 1339.
- [4] T. S. Kleine, R. S. Glass, D. L. Lichtenberger, M. E. Mackay, K. Char, R. A. Norwood, J. Pyun, *ACS Macro Lett.* **2020**, *9*, 245.
- [5] S. Watanabe, K. Oyaizu, *Macromolecules* **2022**, *55*, 2252.
- [6] S. Watanabe, K. Oyaizu, *Bull. Chem. Soc. Jpn.* **2023**, *96*, 1108.
- [7] E. Kim, H. Cho, K. Kim, T.-W. Koh, J. Chung, J. Lee, Y. Park, S. Yoo, *Adv. Mater.* **2015**, *27*, 1624.
- [8] Q. Wei, R. Pöttsch, X. Liu, H. Komber, A. Kiriya, B. Voit, P.-A. Will, S. Lenk, S. Reineke, *Adv. Funct. Mater.* **2016**, *26*, 2545.
- [9] J.-H. Kim, N. X. V. Lan, U. Kulkarni, C. Kim, S. M. Cho, P. J. Yoo, D. Kim, M. Schroeder, G.-R. Yi, *Adv. Mater. Interfaces* **2020**, *7*, 2001422.
- [10] Z. Sun, H. Huang, L. Li, L. Liu, Y. Chen, *Macromolecules* **2017**, *50*, 8505.
- [11] Y. Hu, L. Zhang, Z. Wang, R. Hu, B. Z. Tang, *Polym. Chem.* **2023**, *14*, 2617.
- [12] Y. Zhou, Z. Zhu, K. Zhang, B. Yang, *Macromol. Rapid Commun.* **2023**, e2300411.
- [13] J. J. Griebel, S. Namnabat, E. T. Kim, R. Himmelhuber, D. H. Moronta, W. J. Chung, A. G. Simmonds, K.-J. Kim, J. van der Laan, N. A. Nguyen, E. L. Dereniak, M. E. Mackay, K. Char, R. S. Glass, R. A. Norwood, J. Pyun, *Adv. Mater.* **2014**, *26*, 3014.
- [14] M. Lee, Y. Oh, J. Yu, S. G. Jang, H. Yeo, J.-J. Park, N.-H. You, *Nat. Commun.* **2023**, *14*, 2866.
- [15] Q. Li, K. L. Ng, X. Pan, J. Zhu, *Polym. Chem.* **2019**, *10*, 4279.
- [16] X. Wu, J. He, R. Hu, B. Z. Tang, *J. Am. Chem. Soc.* **2021**, *143*, 15723.
- [17] S. Watanabe, T. Takayama, K. Oyaizu, *ACS Polym Au* **2022**, *2*, 458.
- [18] S. Watanabe, H. Nishio, T. Takayama, K. Oyaizu, *ACS Appl. Polym. Mater.* **2023**, *5*, 2307.
- [19] C. Kim, S. Nakagawa, M. Seshimo, H. Ejima, H. Houjou, N. Yoshie, *Macromolecules* **2020**, *53*, 4121.
- [20] S. Mondal, J. J. Lessard, C. L. Meena, G. J. Sanjayan, B. S. Sumerlin, *J. Am. Chem. Soc.* **2022**, *144*, 845.
- [21] S. Chen, W. H. Binder, *Acc. Chem. Res.* **2016**, *49*, 1409.
- [22] W.-X. Liu, Z. Yang, Z. Qiao, L. Zhang, N. Zhao, S. Luo, J. Xu, *Nat. Commun.* **2019**, *10*, 4753.
- [23] R. Custelcean, N. L. Engle, P. V. Bonnesen, *CrystEngComm* **2007**, *9*, 452.
- [24] R. Custelcean, *Chem. Commun.* **2008**, 295.
- [25] Y. Yanagisawa, Y. Nan, K. Okuro, T. Aida, *Science* **2018**, *359*, 72.
- [26] Y. Fujisawa, A. Asano, Y. Itoh, T. Aida, *J. Am. Chem. Soc.* **2021**, *143*, 15279.
- [27] S. Dai, J. He, X. Chen, J. Cui, H. Zhao, R. Zhang, H. Lei, J. Yin, L. Cai, F. Ye, X. Kong, R. Hu, M. Huang, *Macromolecules* **2023**, *56*, 3660.
- [28] S. Wu, M. Luo, D. J. Darensbourg, X. Zuo, *Macromolecules* **2019**, *52*, 8596.
- [29] D. S. Lee, Y.-S. Choi, J. H. Hwang, J.-H. Lee, W. Lee, S.-K. Ahn, S. Park, J.-H. Lee, Y. S. Kim, D.-G. Kim, *ACS Appl. Polym. Mater.* **2021**, *3*, 3714.
- [30] Y. M. Li, Z. P. Zhang, M. Z. Rong, M. Q. Zhang, *Nat. Commun.* **2022**, *13*, 2633.

- [31] S. Wu, W. Li, M. Lin, Q. Burlingame, Q. Chen, A. Payzant, K. Xiao, Q. M. Zhang, *Adv. Mater.* **2013**, *25*, 1734.
- [32] Y. Feng, Y. Hasegawa, T. Suga, H. Nishide, L. Yang, G. Chen, S. Li, *Macromolecules* **2019**, *52*, 8781.
- [33] Y. Feng, L. Jiang, A. Yang, X. Liu, L. Yang, G. Lu, S. Li, *Macromol. Rapid Commun.* **2022**, *43*, e2100700.
- [34] R. Ma, V. Sharma, A. F. Baldwin, M. Tefferi, I. Offenbach, M. Cakmak, R. Weiss, Y. Cao, R. Ramprasad, G. A. Sotzing, *J. Mater. Chem. A* **2015**, *3*, 14845.
- [35] Y. Suzuki, K. Murakami, S. Ando, T. Higashihara, M. Ueda, *Journal of Materials Chemistry* **2011**, *21*, 15727.
- [36] T. S. Kleine, N. A. Nguyen, L. E. Anderson, S. Namnabat, E. A. LaVilla, S. A. Showghi, P. T. Dirlam, C. B. Arrington, M. S. Manchester, J. Schwiegerling, R. S. Glass, K. Char, R. A. Norwood, M. E. Mackay, J. Pyun, *ACS Macro Lett.* **2016**, *5*, 1152.
- [37] D. H. Kim, W. Jang, K. Choi, J. S. Choi, J. Pyun, J. Lim, K. Char, S. G. Im, *Sci Adv* **2020**, *6*, eabb5320.
- [38] Y. Feng, M. Li, K. Shang, H. Niu, G. Qu, G. Lu, S. Li, *Appl. Phys. Lett.* **2023**, *122*, 123902.
- [39] T. Chen, X. He, Q. Lu, *ACS Appl. Polym. Mater.* **2023**, *5*, 5436.
- [40] G. L. Slonimskii, A. A. Askadskii, A. I. Kitaigorodskii, *Polymer Science U.S.S.R.* **1970**, *12*, 556.
- [41] S.-Y. Kim, J.-H. Lee, H.-S. Shim, J.-J. Kim, *Org. Electron.* **2013**, *14*, 1496.
- [42] E. Fresta, R. D. Costa, *Adv. Funct. Mater.* **2020**, *30*, 1908176.
- [43] M. C. Gather, S. Reineke, *J. Photonics Energy* **2015**, *5*, 057607.
- [44] E. Fresta, R. D. Costa, in *Springer Handbook of Inorganic Photochemistry* (Eds.: D. Bahnemann, A. O. T. Patrocínio), Springer International Publishing, Cham, **2022**, pp. 1849–1877.
- [45] H. Benisty, R. Stanley, M. Mayer, *J. Opt. Soc. Am. A* **1998**, *15*, 1192.
- [46] M. Furno, R. Meerheim, S. Hofmann, B. Lüssem, K. Leo, *Phys. Rev. B* **2012**, *85*, 115205.
- [47] L. M. Cavinato, K. Yamaoka, S. Lipinski, V. Calvi, D. Wehenkel, R. van Rijn, K. Albrecht, R. D. Costa, *Adv. Funct. Mater.* **2023**, *33*, 2302483.
- [48] S. van Reenen, R. A. J. Janssen, M. Kemerink, *Adv. Funct. Mater.* **2012**, *22*, 4547.
- [49] J.-Z. Zhao, T.-J. Yue, B.-H. Ren, Y. Liu, W.-M. Ren, X.-B. Lu, *Macromolecules* **2022**, *55*, 8651.
- [50] T. Kimura, K. Kuroda, H. Kubota, M. Ouchi, *ACS Macro Lett.* **2021**, *10*, 1535.
- [51] H. S. Wang, N. P. Truong, Z. Pei, M. L. Coote, A. Anastasaki, *J. Am. Chem. Soc.* **2022**, *144*, 4678.
- [52] Z. Huang, M. Shanmugam, Z. Liu, A. Brookfield, E. L. Bennett, R. Guan, D. E. Vega Herrera, J. A. Lopez-Sanchez, A. G. Slater, E. J. L. McInnes, X. Qi, J. Xiao, *J. Am. Chem. Soc.* **2022**, *144*, 6532.
- [53] A. Kazama, Y. Kohsaka, *Polym. Chem.* **2022**, *13*, 6484.
- [54] B.-S. Wang, Q. Zhang, Z.-Q. Wang, C.-Y. Shi, X.-Q. Gong, H. Tian, D.-H. Qu, *Angew. Chem. Int.*

Ed Engl. **2023**, *62*, e202215329.

- [55] Y. Minami, N. Matsuyama, Y. Takeichi, R. Watanabe, S. Mathew, Y. Nakajima, *Commun Chem* **2023**, *6*, 14.
- [56] M. Vlatković, B. L. Feringa, *Tetrahedron* **2019**, *75*, 2188.
- [57] H. Feng, N. Zheng, W. Peng, C. Ni, H. Song, Q. Zhao, T. Xie, *Nat. Commun.* **2022**, *13*, 397.
- [58] H. Otsuka, *Polym. J.* **2013**, *45*, 879.
- [59] H. Otsuka, K. Aotani, Y. Higaki, Y. Amamoto, A. Takahara, *Macromolecules* **2007**, *40*, 1429.
- [60] T.-J. Yue, L.-Y. Wang, W.-M. Ren, *Polym. Chem.* **2021**, *12*, 6650.
- [61] Y. Feng, L. Yang, G. Qu, T. Suga, H. Nishide, G. Chen, S. Li, *Macromol. Rapid Commun.* **2020**, *41*, e2000167.

Chapter 6:

Synthesis of Telechelic Poly(phenylene sulfide) Derivatives via the Aromatic Electrophilic Substitution with Electron-deficient Electrophiles

Contents

- 6.1 Introduction
 - 6.2 One-pot Synthesis of End-functionalized Poly(phenylene sulfide)s
 - 6.3 Telechelic Poly(phenylene sulfide) Synthesis via Post Polymerization Modification
 - 6.4 Cross-coupling Synthesis of Vinyl-terminated Poly(phenylene sulfide)s
 - 6.5 Experimental Section
- References

6.1 Introduction

In the field of polymer chemistry, precise control of multi-scale polymer structures, varying from the first- to the higher-order, is an important technique for realizing functional polymers with desirable properties. Such attempts have been reported by means of controlled (and sterically confined) polymerization^[1-4] and post-polymerization modification.^[5,6] Especially, end-functionalization is also an important technique for polymers because such reactive polymers are useful for connecting multiple polymer segments or hybridizing other materials for such as bioconjugation^[7,8] and surface modification of particles.^[9,10] Telechelic polymers, which are difunctionalized end-functionalized linear polymers, are also important precursors for further post-polymerization modification or chain extension in order to prepare triblock copolymers^[11-14] and cyclic polymers.^[15-17] The typical telechelic polymers were synthesized by the living polymerization techniques (e.g., atom transfer radical polymerization (ATRP), reversible addition-fragmentation polymerization (RAFT), and chain-growth polycondensation, and post-polymerization modification) that always give reactive groups at the termini.^[18,19] Topology transformation between cyclic and linear polymers based on the dynamic covalent chemistry^[20,21] is another route for obtaining telechelic polymers. As these routes are applicable for the limited polymers, which always have reactive end groups or reactive repeating units. Although there are some post-polymerization modification routes for unreactive polymers,^[22,23] to the best of our knowledge, no examples that apply such reaction systems to the telechelic polymer synthesis have not been reported.

Poly(phenylene sulfide) (PPS) is an unreactive and insoluble polymer that is difficult to be end-functionalized, although the functionalization of PPS is extensively desired for the realization of compatible polymer blends or hybrid materials.^[24,25] Oyaizu *et al.* have reported the synthesis and properties of PPS derivatives, which were synthesized via the oxidative polymerization of aromatic disulfides.^[26,27] Focusing on their soluble and reactive interchain disulfide bonds, α -end-functionalized PPS derivatives^[25,28] and diblock copolymers of PPS and other vinyl polymers^[29] were synthesized. However, the application range of such end-functionalization was limited to the mono end-functionalized derivatives because the reactive end groups has been lacked. Oyaizu *et al.* solved this issue by using three-centered sulfonium cations with electron-withdrawing substituents at the *p*-positions^[30] as Friedel–Crafts electrophiles for aromatic rings. In the presence of such reactive species in the oxidative polymerization of diphenyl disulfide, the corresponding α,ω -dihalogenated oligo(phenylene sulfide)s were obtained^[31] although resulting in poor solubility, low molecular weight (in a oligomeric level), low end-functionalization degree (60-90%), and low yield (32-52%).

In this chapter, a facile synthesis of side-functionalized telechelic PPS with high conversion and high yield has been developed, by using a highly soluble as well as structurally confined poly(2,6-dimethyl-1,4-phenylenesulfide) (**PMPS**) and optimizing the reaction procedures including the use of post-polymerization modification. Specifically, the in situ generated sulfonium cation bis(4-halothiophenyl) phenylsulfonium cation (**X-DPS⁺**) (**Figure 6.1a**) was unpolymerized but reacted with another electron-rich aromatics in a Friedel-Crafts reaction-like fashion, and therefore both termini of

the PPS derivatives were selectively functionalized (**Figure 6.1b**). This study also expanded such α,ω -dihalogenated PPS derivatives as a reagent for end-vinylated PPS derivatives via several cross-coupling reactions.

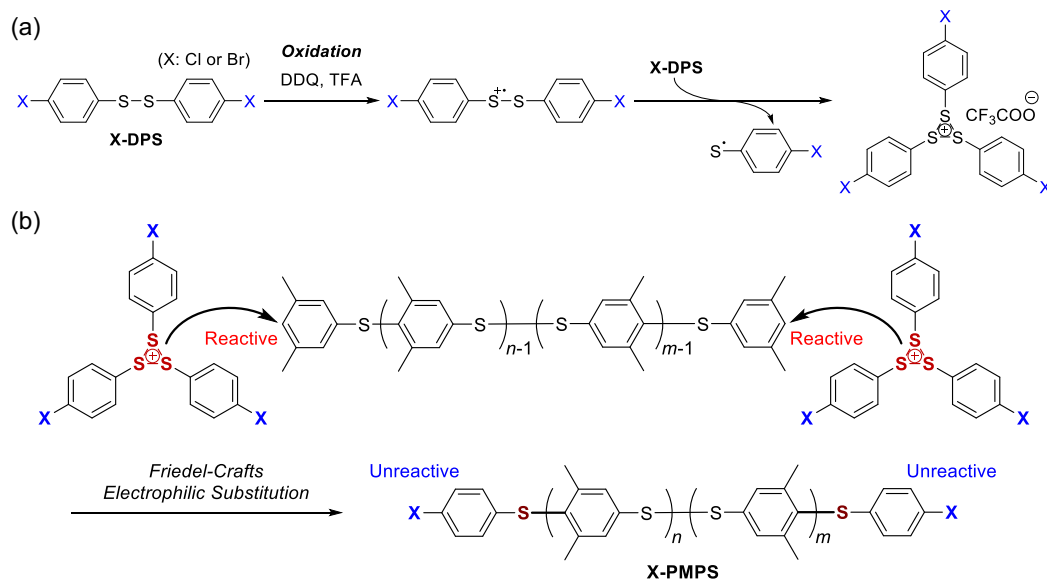
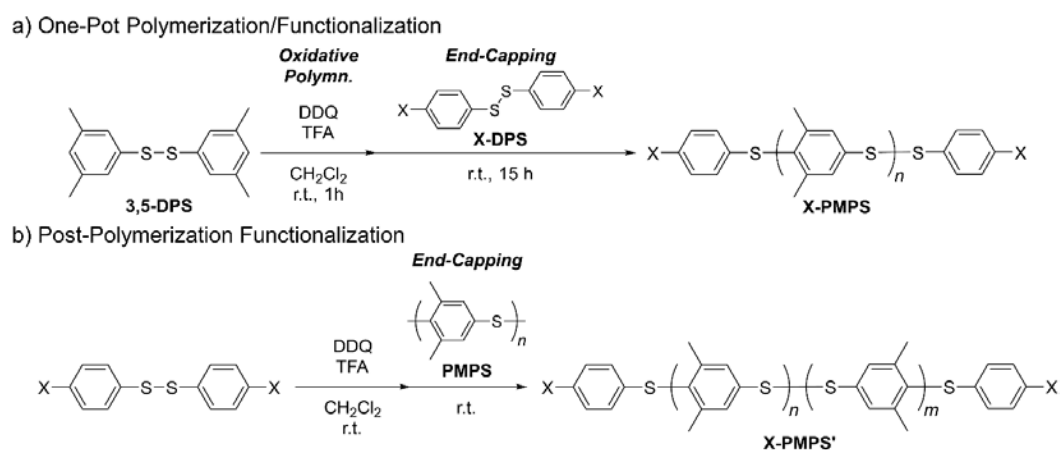


Figure 6.1. End-functionalization of PMPS by 4,4'-halogenated diphenyl disulfide (X-DPS): (a) Oxidation of X-DPS to synthesize the sulfonium cation (X-DPS⁺). (b) End-capping of reactive PMPS with X-DPS⁺ to afford end-dihalogenated PMPS (X-PMPS').

6.2 One-pot Synthesis of End-functionalized Poly(phenylene sulfide)s



Scheme 6.1. Synthesis of dihalogenated telechelic PMPS (X: Cl or Br): (a) One-pot synthesis and (b) Post-polymerization modification.

First, the one-pot synthesis of α,ω -dichlorinated PMPS (Cl-PMPS), by combining oxidative polymerization of 3,5-DPS and electrophilic addition reaction with 4,4'-dichlorophenyl disulfide (Cl-

DPS) to proceed the end capping (Scheme 6.1a, X = Cl). **Figure 6.2** showed the ^1H NMR spectra of **Cl-PMPS** and **PMPS**, indicating new doublet aromatic ^1H signals, which were not identical to the signals for **PMPS** and **Cl-DPS** (Note: Detailed characterization of the terminal groups was described in Fig. 3). High degree of end-functionalization with 100% also indicated the efficient progress of one-pot end-capping reaction. From the IR spectrum of **Cl-PMPS**, the absorption peaks of the 1,4-phenylene ($\delta_{\text{C-H}}$: 820 cm^{-1}) and chlorine ($\nu_{\text{C-Cl}}$: 740 cm^{-1}) were observed (**Figure 6.3**). The DOSY NMR spectrum of **Cl-PMPS** revealed the successful end-capping system confirmed by the same diffusion coefficient for all aromatic peaks (**Figure 6.4**). Considering the reaction of **Cl-DPS** with the oxidant and trifluoroacetic acid (TFA) did not undergo (see section 6.5 for the details), **Cl-DPS**⁺ selectively reacted with the dimethyl-substituted aromatic rings and end-capping was completed. However, as end-capping reaction in the early stage of the polymerization was also occurred in this case, this one-pot functionalization system resulted in the low yield (33%) and low molecular weight ($M_n = 4.5 \times 10^3$) presumably owing to large amount of the unreacted **3,5-DPS** and the oligomers with low molecular weight.

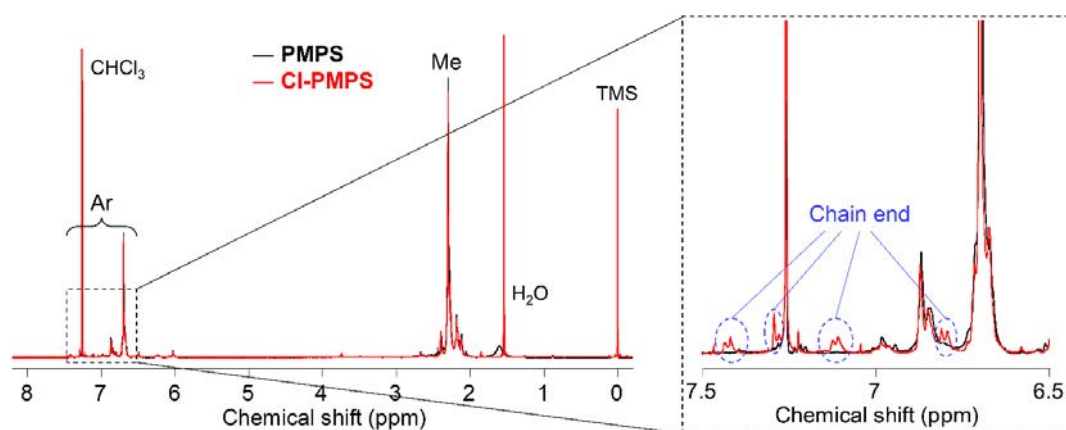


Figure 6.2 Overall (left) and expanded (right) ^1H NMR spectra of **PMPS** (same as the sample in Fig. S3) and Cl-terminated **PMPS** (**Cl-PMPS**) in chloroform-*d*.

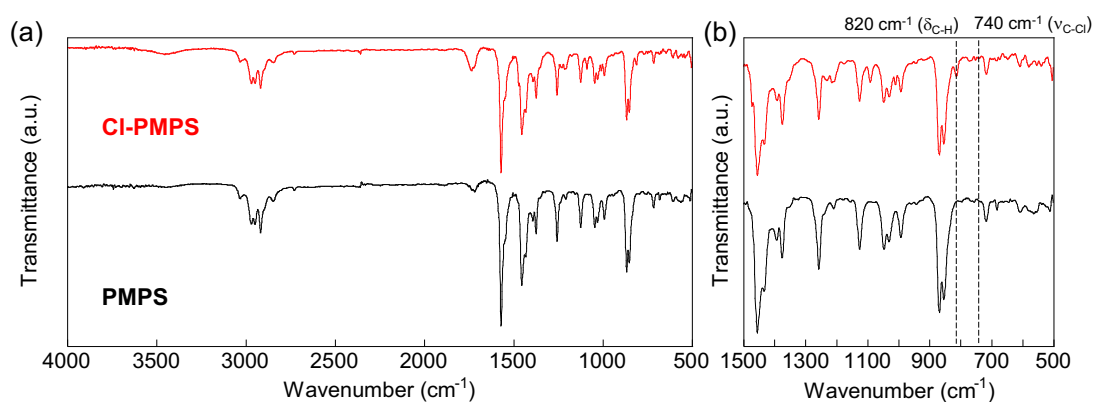


Figure 6.3. IR spectra of **Cl-PMPS** and **PMPS**: (a) Overall ($4000\text{--}500\text{ cm}^{-1}$) and (b) expanded ($1500\text{--}500\text{ cm}^{-1}$) spectra.

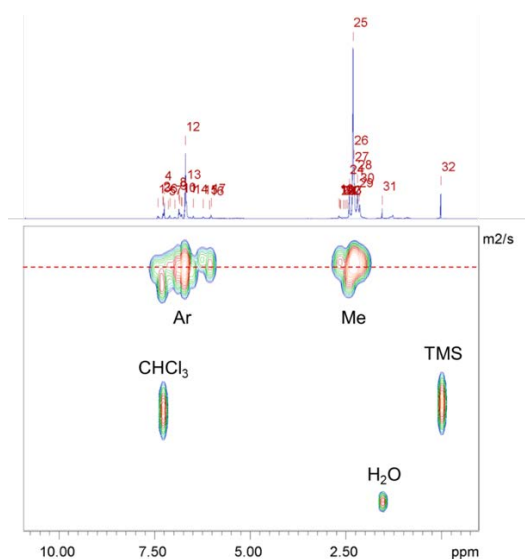


Figure 6.4. DOSY-NMR spectrum of Cl-PMPS in chloroform-*d*.

6.3 Telechelic Poly(phenylene sulfide) Synthesis via Post Polymerization Modification

6.3.1 Synthesis of Cl-Terminated Telechelic PMPS via Post-polymerization Modification

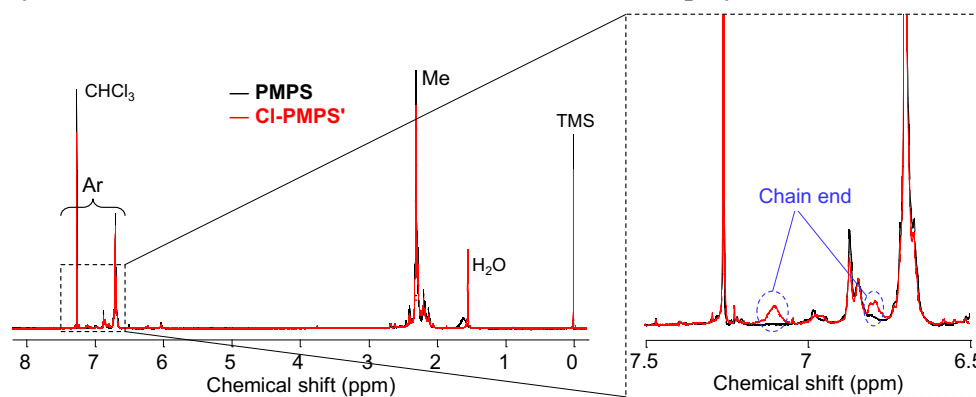


Figure 6.5 ^1H NMR spectra of PMPS and Cl-PMPS' in chloroform-*d*.

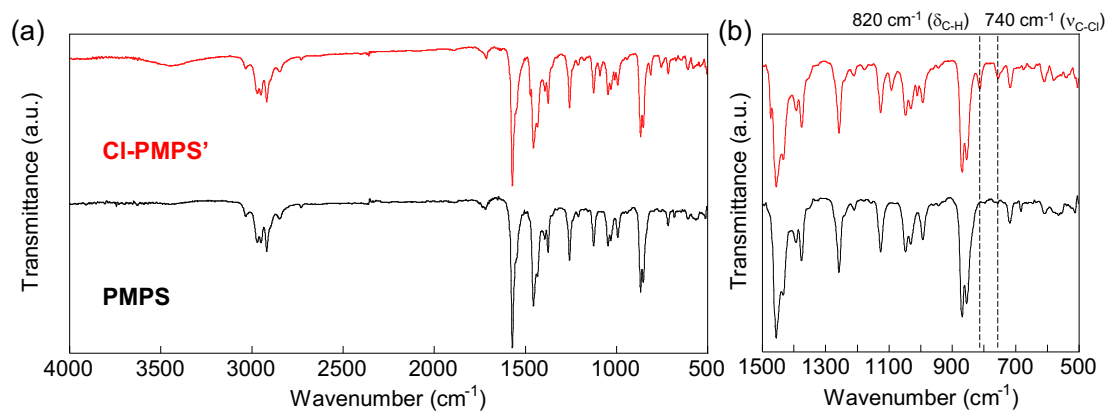


Figure 6.6. IR spectra of PMPS and Cl-PMPS'.

In order to increase both yield and end-functionalization efficiency, the amount of low-molecular-weight **PMPS** should be decreased in order to avoid their end-capping reaction. Therefore, the author anticipated that post-polymerization modification of **PMPS** and **CI-DPS** would overcome this issue owing to the selective end-capping reaction between **CI-DPS**⁺ and **PMPS**, obtaining chlorine-terminated **PMPS** (**CI-PMPS'**) with high yield, higher molecular weight, and high end-functionalization degree simultaneously. A **CI-DPS**⁺ solution was prepared by mixing **CI-DPS**, 2,3-dichloro-5,6-dicyano-1,4-benzoquinone (DDQ), and TFA in dichloromethane. Compared with the reactive and unstable phenylbis(thiophenyl)sulfonium cation,^[32] which was essential to proceed the oxidative polymerization, **CI-DPS**⁺ was unreactive only by itself and did not self-polymerize owing to the electron-withdrawing chlorine atoms at the *p*-positions.

The chlorinated phenylene termini of **CI-PMPS'** were detected from the ¹H NMR spectrum (**Figure 6.5**), in which the signals for the end aromatics were almost identical with the signals of **CI-PMPS** (the details were discussed in **Figure 6.7**). **Figure 6.6** showed the IR spectra exhibiting the bands for chlorinated terminal groups. The yield and degree of end-functionalization of **CI-PMPS'** were in the highest value (75 % and 99 %, respectively) in the condition with low **PMPS** and high TFA concentration (Run 1 in **Table S1**). Therefore, excessive amount of the electrophile relative to the terminal phenylene of **PMPS** can proceed the end-capping reaction more efficiently.

Table 6.1 Optimization of the reaction condition for the **CI-PMPS'** synthesis

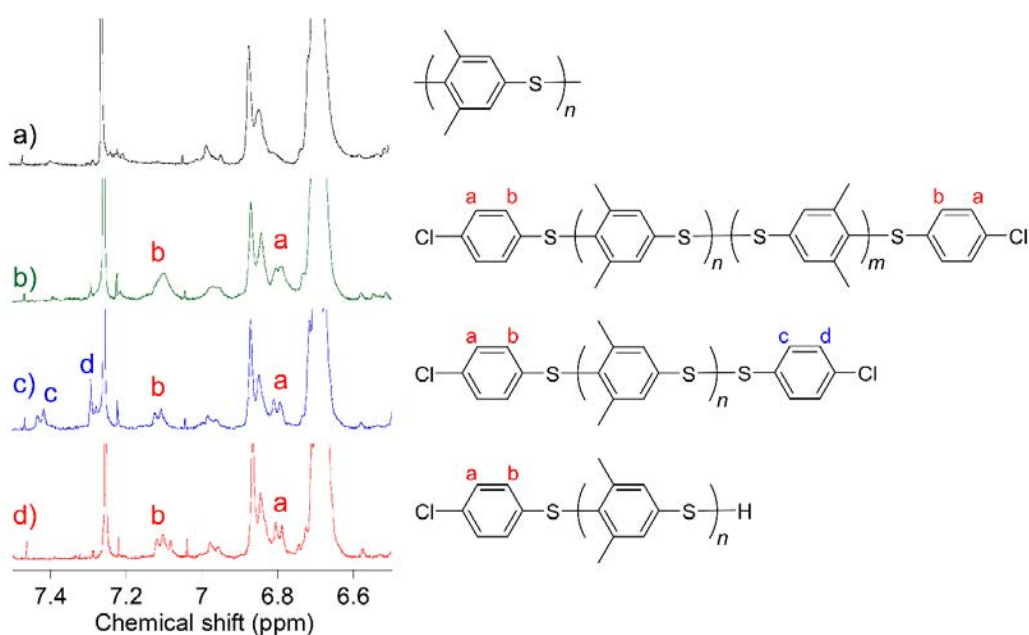
R u n	[CI-DPS] (M)	[PMPS] (M)	[TFA] (M)	Yield (%)	M_n^a ($\times 10^3$)	M_n^b ($\times 10^3$)	M_w^b ($\times 10^3$)	M_w/M_n^b (-)	M_n of precursor PMPS ^{b)} ($\times 10^3$)	Degree of end- functionalization (%)
1	0.1	0.1	0.5	75	8.7	8.6	17.0	2.0	6.8	99
2	0.05	0.2	0.25	44	11.1	4.9	6.6	1.3	4.6	44
3	0.1	0.2	1.0	51	N.D. ^{c)}	2.3	4.4	1.9	4.6	N.D. ^{c)}

^{a)}Determined by ¹H NMR spectroscopy. ^{b)}Determined by SEC in chloroform. ^{c)}Not determined because of the main-chain degradation (side reaction).

6.3.2. End Structure Characterization of CI-Terminated Telechelic PMPS

For further investigation of the end-capping reaction mechanism, we precisely characterized the ¹H NMR spectra especially focusing on the terminal groups. In order to distinguish the phenylene signals at the disulfide terminus and the sulfide terminus, the interchain disulfide bond of **CI-PMPS** was subjected to be reduced to prepare thiol-end **PMPS** (**Red-CI-PMPS**) (**Scheme 6.2**). The terminal structure was finalized by comparing its spectrum and other related **PMPS** derivatives (**Figure 6.7**). Two downfield signals (7.43 and 7.29 ppm for protons c and d, respectively) for the spectrum of **CI-PMPS** (**Figure 6.7b**) were absent after the reduction (**Figure 6.7c**). On the other hand, the spectra of

Red-Cl-PMPS and **Cl-PMPS'** were mostly identical. These results indicated that **Cl-PMPS'** had an interchain disulfide in the middle of the chain whereas **Cl-PMPS** has a disulfide bond at the terminus (i.e. adjacent to the chlorinated thiophenylene). Such a trend was presumably based on the predominantly occurred exchange reaction between the terminal disulfide of the oligomer and **Cl-DPS⁺** in the one-pot system.^[31]



6.3.3 Synthesis of Br-Terminated Telechelic PMPS

This post-polymerization end-functionalization was expanded to the synthesis of bromo-end **PMPS (Br-PMPS)**. Termination by bromine is more effective than by chlorine owing to its high reactivity as a leaving group, which is an advantage for realizing further post-polymerization modification such as cross-coupling reactions.

Table 6.2 Synthesis of **Br-PMPS** via post-polymerization modification^{a)}

R	[Br-DPS] (M)	[PMPS] (M)	Reaction time (h)	Yield (%)	M_n^b ($\times 10^3$)	M_n^c ($\times 10^3$)	M_w^c ($\times 10^3$)	M_w/M_n^c (-)	M_n precursor PMPS ^{c)} ($\times 10^3$)	Degree of End- functionaliz- ation (%)
1	0.1	0.1	20	45	7.1	4.9	6.4	1.3	4.6	70
2	0.1	0.2	20	58	9.4	4.0	6.0	1.5	4.6	53
3	0.1	0.1	40	71	8.1	7.3	12.9	1.8	7.1	91
4	0.2	0.2	40	91	6.3	6.3	13.1	2.1	7.1	99

^{a)}Temp.= r.t., [TFA] = 0.5 M. ^{b)}Determined by ¹H NMR spectroscopy. ^{c)}Determined by SEC in chloroform.

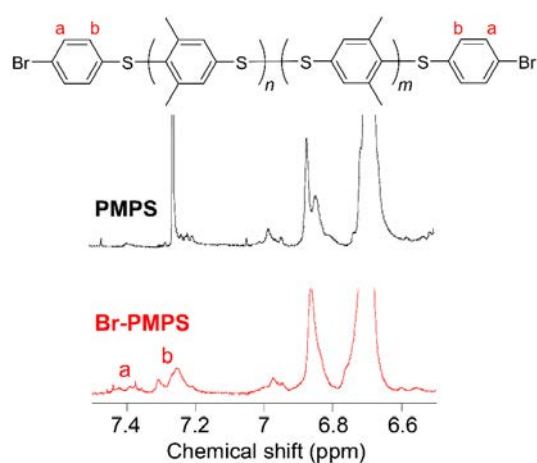


Figure 6.8 Expanded ¹H NMR spectra of **PMPS** (chloroform-*d*) and **Br-PMPS** (Run 4) (dichloromethane-*d*₂).

Br-PMPS was synthesized by the post-polymerization modification method in dichloromethane and the reaction conditions were optimized (**Table 6.2**). According to the ¹H NMR spectra of **Br-PMPS** (**Figure 6.8**), signals a and b (for terminal phenylene rings) were observed in a more downfield chemical shifts (7.42–7.26 ppm) compared to **Cl-PMPS**. Such peak shifting of the end groups supported the same end-capping mechanism as proposed in the **Cl-PMPS** synthesis, in which the halogenated terminal groups without adjacent disulfides were obtained (see section 6.3.2). While the optimized end-capping conditions for the **Cl-PMPS** synthesis was less effective for the **Br-PMPS** synthesis (70 %, Run 1 for **Table 6.2**), highly concentrated conditions with longer time (Run 4 for **Table 6.2**) led to the highest degree of functionalization (99 %) and highest yield (91 %) of **Br-PMPS**. As **Cl-DPS** showed slightly higher oxidation potential compared with **Br-DPS** according to the cyclic voltammograms (i.e., a similar reactivity for producing **X-DPS**⁺) (**Figure 6.9**), harsh reaction conditions were needed for **Br-PMPS** owing to the steric effect derived from **X-DPS**⁺ upon the Friedel-Crafts substitution. The IR spectrum of **Br-PMPS** also detected the absorption ascribed to the terminal 1,4-phenylene (δ_{C-H} : 820 cm⁻¹)

(Figure 6.10). The DOSY NMR spectrum revealed the presence of the end-functionalized product according to the same diffusion coefficient for all signals (Figure 6.11).

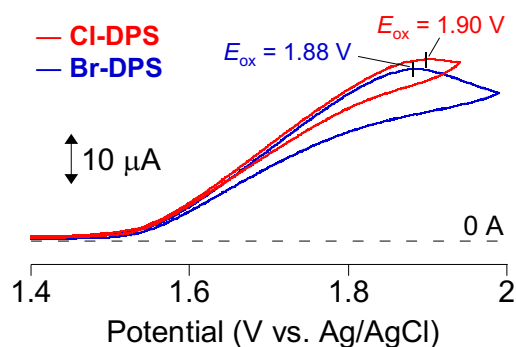


Figure 6.9. Cyclic voltammograms of Cl-DPS and Br-DPS in 0.1 M TBABF₄ dichloromethane solution (monomer concn.: 10 mM, scan rate: 10 mV s⁻¹).

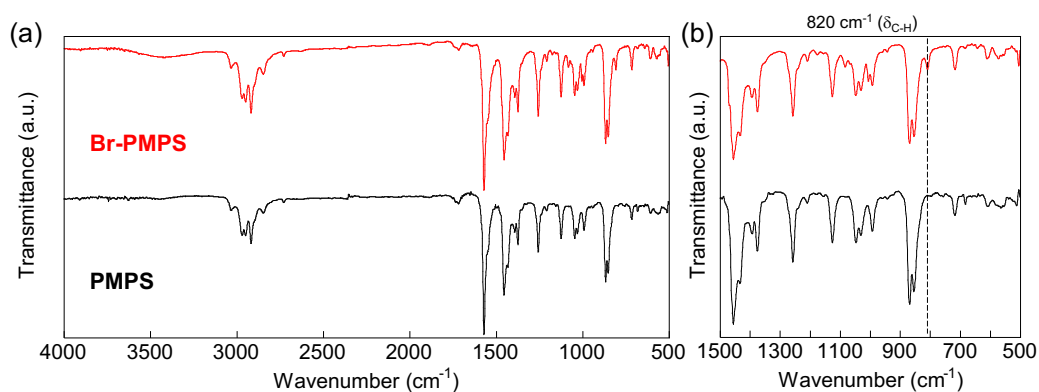


Figure 6.10. IR spectra of PMPS and Br-PMPS: (a) Overall (4000-500 cm⁻¹) and (b) expanded (1500-500 cm⁻¹) spectra.

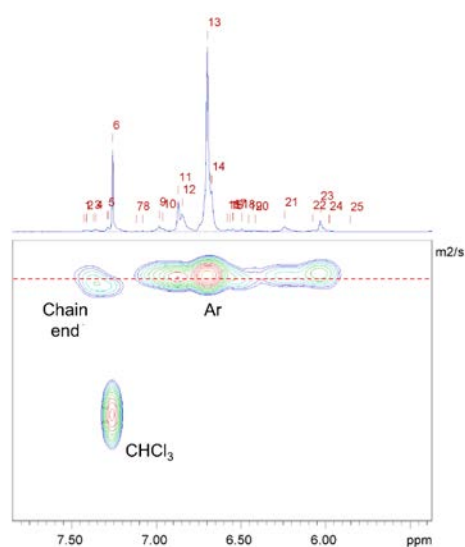
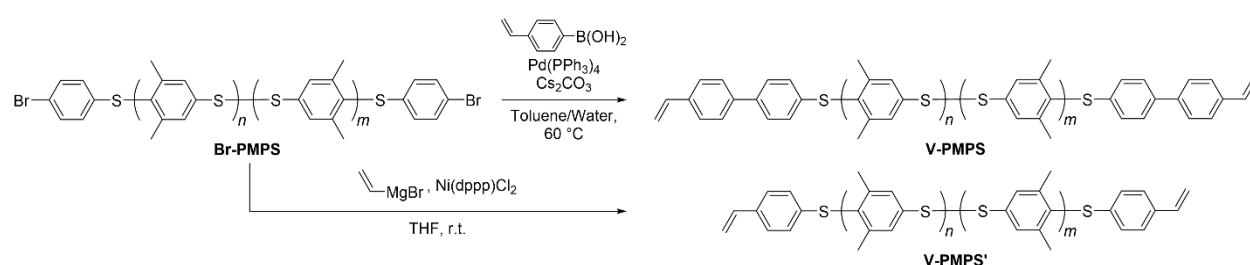


Figure 6.11. DOSY NMR spectrum of Br-PMPS in chloroform-*d*.

6.4 Cross-coupling Synthesis of Vinyl-terminated Poly(phenylene sulfide)s

6.4.1 Suzuki-Miyaura Cross-coupling Modification

Using the reactivity of **Br-PMPS**, the author firstly conducted the Suzuki-Miyaura cross-coupling modification of **Br-PMPS** and 4-vinylphenylboronic acid using a Pd catalyst for synthesizing the vinyl-functional derivative (**V-PMPS**) (**Scheme 6.3** upper part). While the ^1H NMR spectrum of **V-PMPS** showed larger integrals for the signals of aromatic protons including the end groups, the signals for the terminal vinyl groups were undetectable (**Figure 6.12**). The IR spectrum of **Br-PMPS** also resulted in a same trend with no absorptions related to the vinyl groups (**Figure 6.13**). Such results were owing to the poor end-functionalization efficiency of this system derived from the strong Pd-sulfur interactions^[33,34] upon the cross-coupling, yielding a brownish product with few vinyl termini.



Scheme 6.3. End-functionalization of **Br-PMPS** with vinyl groups via Suzuki-Miyaura cross-coupling (**V-PMPS**) and Kumada-Tamao cross-coupling (**V-PMPS'**).

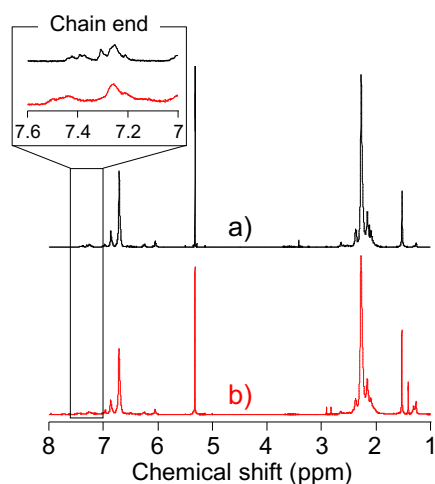


Figure 6.12 ^1H NMR spectra of (a) **Br-PMPS** (Run 3 in **Table 6.2**) and (b) **V-PMPS** in dichloromethane- d_2 .

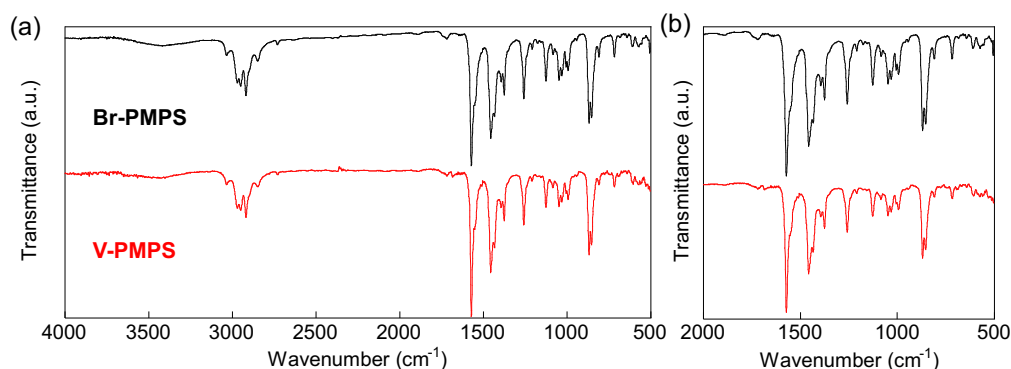


Figure 6.13. IR spectra of **Br-PMPS** (Run 3 in Table 6.2) and **V-PMPS**: (a) 4000-500 cm^{-1} . (b) 2000-500 cm^{-1} .

6.4.2 Kumada-Tamao Cross-coupling Modification

In order to improve the efficiency for the end cross-coupling modification, we changed the synthetic route to the Kumada–Tamao cross-coupling using a Ni catalyst, owing to the feasibility of the Ni-based reaction that undergoes even under the presence of thioethers.^[35] The cross-coupling was conducted with **Br-PMPS**, vinyl magnesium bromide, and Ni(dppp)Cl₂ to obtain the whitish powder-like product. The ¹H NMR spectrum showed the signals ascribed to the terminal 4-vinylphenyl protons (7.14 and 7.03 ppm) (**Figure 6.14a**). Two signals of the end vinyl groups (5.34 and 5.12 ppm) were also observed with a end-functionalization degree of of 38 % (**Figure 6.14b**). Despite the absence of the signals of the bromophenyl terminal groups after the cross-coupling, the degree of functionalization from bromine to vinyl groups was low. This was presumably because of the exchange reaction between the macro-Grignard reagent from **Br-PMPS** end and the excess amount of vinyl magnesium bromide that quenched the Grignard reagents to eliminate bromine and give phenylene terminus.^[36] The IR spectrum of **V-PMPS'** also supported the reaction progress according to the bands for the vinylated C-H groups (**Figure 6.15**).

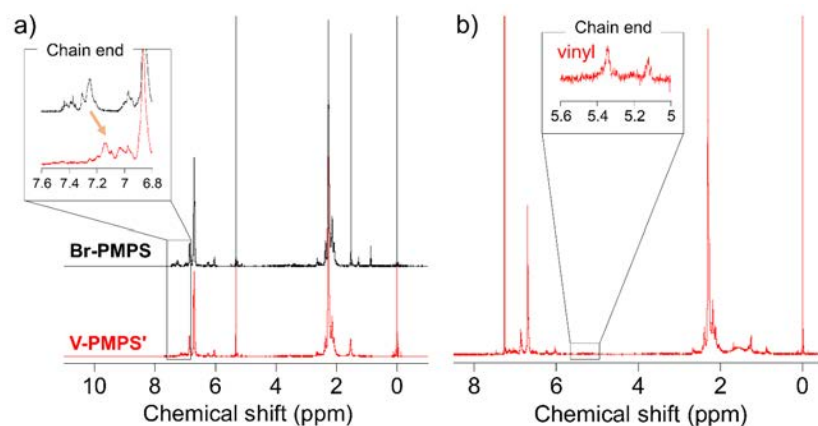


Figure 6.14 ¹H NMR spectra of (a) **Br-PMPS** (Run 4 in Table 6.2) and **V-PMPS'** in dichloromethane-*d*₂ and (b) **V-PMPS'** in chloroform-*d*.

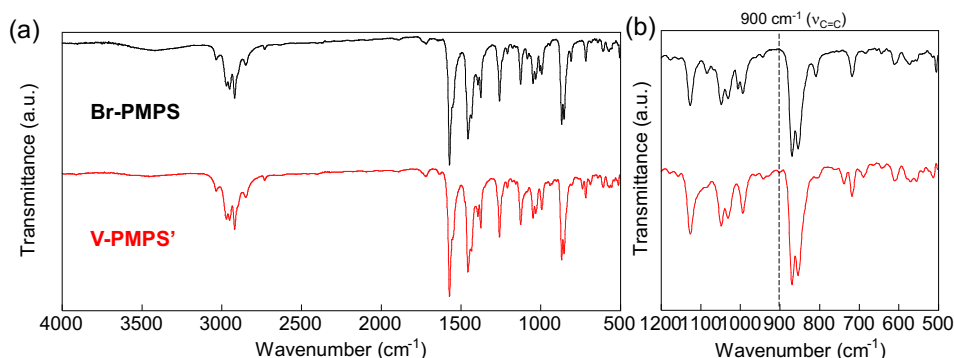


Figure 6.15 IR spectra of **Br-PMPS** (Run 4 in Table 2) and **V-PMPS'**: (a) Overall (4000-500 cm⁻¹) and (b) expanded (1200-500 cm⁻¹) spectra.

Finally, dynamic scanning calorimetry (DSC) thermograms were measured in order to detect the thermal reactions involving the end vinyl groups (**Figure 6.16**). For **V-PMPS'**, glass transition and the exothermic peak with an enthalpy change $\Delta H = 5.5 \text{ J g}^{-1}$ were observed in the first heating scan, which were ascribed to the thermosetting reaction of the vinyl terminus. In the second heating, only glass transition ($T_g = 176 \text{ }^\circ\text{C}$) was observed due to the consumption of the reactive vinyl groups in the first heating (Fig. 6a). Although such exothermic peak was observed in the case of **V-PMPS**, but the enthalpy change was smaller ($\Delta H = 2.2 \text{ J g}^{-1}$) based on its smaller efficiency for the vinyl end-functionalization.

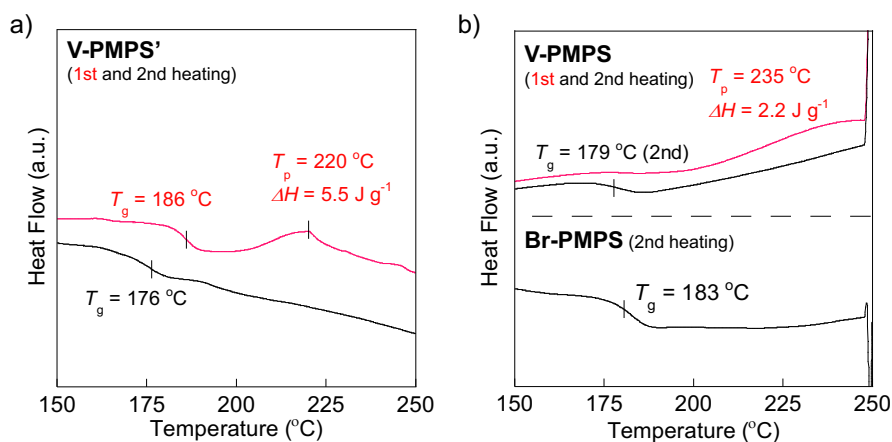


Figure 6.16 DSC thermograms before and after the cross-coupling end-functionalization: (a) **V-PMPS'** (1st and 2nd heating). (b) **V-PMPS** (1st and 2nd heating) and **Br-PMPS** (Run 3 in Table 2) (2nd heating).

In summary, the facile end-functionalization of PPS derivatives for obtaining telechelic polymers, using the *p*-dihalogenated DPS-derived sulfonium cation as the end-capping agent, was developed. End-capping of **PMPS** proceeded in both the one-pot system and post-polymerization

modification, especially the latter resulted in higher yield, higher end-functionality, and higher molecular weight. Telechelic **PMPS** with bromine end groups were end-functionalized to obtain end-vinylated **PMPS** via the Kumada–Tamao cross-coupling reaction. This method would be applicable for various aromatic polymers to functionalize the polymer termini including side-chain transformation.

6.5 Experimental Section

Reagents. 2,3-Dichloro-5,6-dicyano-1,4-benzoquinone (DDQ), dichloromethane, 4,4'-dichlorodiphenyl disulfide (**Cl-DPS**), bis(4-bromophenyl) disulfide (**Br-DPS**), tetrabutylammonium tetrafluoroborate (TBABF₄), tetrakis(triphenylphosphine)palladium(0) (Pd(PPh₃)₄), cesium carbonate, 4-vinylphenylboronic acid, [1,3-bis(diphenylphosphino)propane]nickel(II) dichloride (Ni(dppp)Cl₂), and vinylmagnesium bromide (ca. 1M solution in THF) were purchased from Tokyo Chemical Industry Co. (TCI). Methanol was purchased from Kokusan Chemical Co. or TCI. Hydrochloric acid, potassium hydroxide, tetrahydrofuran (THF), hexane, sodium borohydride, and toluene were purchased from Kanto Chemical Co. Trifluoroacetic acid (TFA) was purchased FUJIFILM Wako Pure Chemical Co. Bis(3,5-dimethylphenyl) disulfide (**3,5-DPS**) was synthesized following the previous report.^[29]

Synthesis of Cl-terminated PMPS in a One-pot Manner. The procedure was arranged according to the previous report^[31] with several modifications. To a 20 mL flask, DDQ (1.18 g, 5.3 mmol) was dispersed in dichloromethane (3.5 mL) and TFA (133 μ L, 1.75 mmol) was added. Then, **3,5-DPS** (0.72 g, 2.63 mmol) was added and stirred at room temperature to proceed with the polymerization. After 1 hour, **Cl-DPS** (0.75 g, 2.63 mmol) was added and was further stirred for 15 hours at room temperature for the termination. The solution was diluted with dichloromethane (15 mL) and was precipitated in methanol containing 5 vol% hydrochloric acid (500 mL). The solid was collected by filtration after subsequent washing with methanol, potassium hydroxide aqueous, and water. The solid was redissolved in THF (20 mL) and was purified by reprecipitating in hexane (500 mL). The precipitate was collected by filtration, was washed with hexane, and was dried in vacuo to obtain **Cl-PMPS** as a whitish powder (0.24 g, Yield: 33 %, $M_n = 4.5 \times 10^3$ (NMR), $M_n = 4.5 \times 10^3$ (SEC), $M_w/M_n = 1.3$ (SEC), End-functionalization degree: 100 %).

Oxidation of Cl-DPS with DDQ and TFA. To a 10 mL flask were dissolved **Cl-DPS** (0.82 g, 2.9 mmol) in dichloromethane (6 mL) and were added DDQ (0.623 g, 2.7 mmol) and TFA (383 μ L, 5 mmol). The reaction solution turned as deep green after the reaction, indicating the charge-transfer complexation of **Cl-DPS** and DDQ, although no products were yielded 15 hours after the reaction.

Reduction of Cl-Terminated PMPS for end structure detection. Cl-terminated telechelic **PMPS** (**Red-Cl-PMPS**) without a disulfide bond was prepared, according to the previous report^[25] with

several modifications. To a two-necked 50 mL flask, was dissolved **Cl-PMPS** (0.16 g) in THF (5.4 mL), was added sodium borohydride (0.15 g) and methanol (0.6 mL), and was refluxed at 70 °C for 15 hours. The solution was precipitated in methanol with 5 vol% hydrochloric acid (200 mL). The precipitate was collected by filtration, was washed with methanol and water, and was dried in vacuo to obtain **Red-Cl-PMPS** (0.15 g, Yield: 92%).

Synthesis of Cl-terminated PMPS with Post-polymerization Modification. A typical procedure has been described as follows (Run 1, Table 1). To a 30 mL flask, **Cl-DPS** (0.57 g, 2 mmol) was dissolved in dichloromethane (20 mL) and TFA (765 μ L, 10 mmol) and DDQ (0.45 g, 2 mmol) were added and stirred at room temperature to prepare **Cl-DPS⁺** solution. Then, **PMPS** (0.26 g, 2 mmol of unit) was added and further stirred for 20 hours at room temperature. The solution was precipitated in methanol containing 5 vol% hydrochloric acid (500 mL) and the solid was collected by filtration and was washed with methanol, potassium hydroxide aqueous, and water. The solid was then reprecipitated with THF/hexane (15 mL/300 mL), and the filtrate was collected, was washed with hexane, and was dried in vacuo to obtain **Cl-PMPS'** as a whitish powder (0.20 g, Yield: 75 %).

Synthesis of Br-Terminated PMPS. A typical procedure has been described as follows (Run 4, Table 2). To a 50 mL flask, **Br-DPS** (1.88 g, 5 mmol) was dissolved in dichloromethane (25 mL), TFA (0.83 mL, 12.5 mmol), and DDQ (1.14 g, 5 mmol) were added and stirred at room temperature. **PMPS** (0.68 g, 5 mmol of unit) was further added and stirred at room temperature for 40 hours at room temperature. The solution was precipitated in methanol containing 5 vol% hydrochloric acid (1000 mL) and the solid was collected by filtration, was washed with methanol, potassium hydroxide aqueous, and water, and was dried in vacuo. The solid was reprecipitated with THF/hexane (20 mL/800 mL) and the precipitate was collected, was washed with hexane, and was dried in vacuo to obtain **Br-PMPS** (0.63 g, Yield: 91 %).

Suzuki-Miyaura Cross-coupling Post-functionalization of Br-PMPS. To a 30 mL flask were added **Br-PMPS** (Run 3, Table 6.2) (0.16 g, 40 μ mol Br), toluene (16 mL), Pd(PPh₃)₄ (46 mg, 40 μ mol), cesium carbonate (37 mg, 112 μ mol), 4-phenylboronic acid (15 mg, 100 μ mol), and water (0.16 mL) and were stirred at 60 °C for 24 hours. The solution was precipitated in methanol with 5 vol% hydrochloric acid (total 300 mL). The precipitate was collected via filtration, was washed with methanol and water, and was dried in vacuo to obtain **V-PMPS** as a brownish powder (69 mg, Yield: 42%, $M_n = 7.4 \times 10^3$, $M_w/M_n = 2.2$).

Kumada-Tamao Cross-coupling Post-functionalization of Br-PMPS. To a 30 mL flask, **Br-PMPS** (Run 4, Table 2) (96 mg, 10 μ mol Br) and Ni(dppp)Cl₂ (11 mg, 20 μ mol) was added and

dissolved in THF (7.6 mL) under argon atmosphere. 1 M vinylmagnesium bromide solution in THF (0.4 mL, 0.4 mmol) was further added and stirred for 24 hours at room temperature. The solution was precipitated in methanol containing 5vol% hydrochloric acid (300 mL). The precipitate was collected by filtration, was washed with methanol and water, and was dried in vacuo to obtain **V-PMPS'** as a whitish powder (28 mg, Yield: 29%, $M_n = 5.1 \times 10^3$, $M_w/M_n = 2.3$).

Measurements. ^1H NMR spectra (500 MHz) were recorded by JEOL JNM-ECX500 (internal standard for NMR measurements: tetramethylsilane (TMS)). Diffusion-ordered spectroscopy (DOSY) NMR spectra (600 MHz) were recorded by Bruker AVANCE 600 NEO (pulse sequence: ledbpgp2s). IR spectroscopy was conducted by JASCO FT/IR-6100. Size exclusion chromatography (SEC) was performed with SHIMADZU LC-20AD/CBM-20A using TOSOH TSKgel SuperHM-N column with SHIMADZU SPD-M20A UV detector (wavelength: 254 nm) (eluent: chloroform, flow rate: 0.3 mL min^{-1} , molecular weights were calibrated by polystyrene standards). Cyclic voltammetry (CV) was conducted by BAS ALS 660D with a Pt wire, a Pt electrode (ϕ : 1.6 mm), and an Ag/AgCl electrode as a counter, a working, and a reference electrode, respectively, whose potential was corrected by ferrocene/ferrocenium redox couple ($E_{1/2} = 0.45$ V vs Ag/AgCl). Differential scanning calorimetry (DSC) was performed using TA Instruments Q200 (Scanning rate: 20 $^\circ\text{C min}^{-1}$).

References

- [1] K. Satoh, M. Kamigaito, *Chem. Rev.* **2009**, *109*, 5120.
- [2] A. J. Teator, T. P. Varner, P. C. Knutson, C. C. Sorensen, F. A. Leibfarth, *ACS Macro Lett.* **2020**, *9*, 1638.
- [3] Y. Kametani, F. Tournilhac, M. Sawamoto, M. Ouchi, *Angew. Chem. Int. Ed.* **2020**, *59*, 5193.
- [4] N. Hosono, S. Mochizuki, Y. Hayashi, T. Uemura, *Nat. Commun.* **2020**, *11*, 3573.
- [5] M. A. Gauthier, M. I. Gibson, H.-A. Klok, *Angew. Chem. Int. Ed.* **2009**, *48*, 48.
- [6] A. S. Goldmann, M. Glassner, A. J. Inglis, C. Barner-Kowollik, *Macromol. Rapid Commun.* **2013**, *34*, 810.
- [7] L. Tao, J. Liu, J. Xu, T. P. Davis, *Chem. Commun.* **2009**, 6560.
- [8] S. M. Henry, A. J. Convertine, D. S. W. Benoit, A. S. Hoffman, P. S. Stayton, *Bioconjug. Chem.* **2009**, *20*, 1122.
- [9] A. S. Goldmann, A. Walther, L. Nebhani, R. Joso, D. Ernst, K. Loos, C. Barner-Kowollik, L. Barner, A. H. E. Müller, *Macromolecules* **2009**, *42*, 3707.
- [10] P. Tao, Y. Li, A. Rungta, A. Viswanath, J. Gao, B. C. Benicewicz, R. W. Siegel, L. S. Schadler, *J. Mater. Chem* **2011**, *21*, 18623.
- [11] M. R. Kember, J. Copley, A. Buchard, C. K. Williams, *Polym. Chem.* **2012**, *3*, 1196.

- [12] K. Dan, S. Ghosh, *Polym. Chem.* **2014**, *5*, 3901.
- [13] T. Yan, D. Guironnet, *Angew. Chem. Int. Ed* **2020**, *59*, 22983.
- [14] S. Inagaki, T. Higashihara, *Polym. Chem.* **2022**, *13*, 3613.
- [15] B. A. Laurent, S. M. Grayson, *J. Am. Chem. Soc* **2006**, *128*, 4238.
- [16] Q. Tang, Y. Wu, P. Sun, Y. Chen, K. Zhang, *Macromolecules* **2014**, *47*, 3775.
- [17] L. Zhang, Y. Wu, S. Li, Y. Zhang, K. Zhang, *Macromolecules* **2020**, *53*, 8621.
- [18] M. A. Tasdelen, M. U. Kahveci, Y. Yagci, *Prog. Polym. Sci.* **2011**, *36*, 455.
- [19] T. Yokozawa, Y. Ohta, *Chem. Rev.* **2016**, *116*, 1950.
- [20] H. Yokochi, R. Takashima, D. Aoki, H. Otsuka, *Polym. Chem.* **2020**, *11*, 3557.
- [21] T. Katoh, T. Suzuki, Y. Ohta, T. Yokozawa, *Polym. Chem.* **2022**, *13*, 794.
- [22] J. B. Williamson, S. E. Lewis, R. R. Johnson, I. M. Manning, F. A. Leibfarth, *Angew. Chem. Int. Ed.* **2019**, *58*, 8654.
- [23] E. R. King, S. B. Hunt, L. J. Hamernik, L. E. Gonce, J. S. Wiggins, J. D. Azoulay, *JACS Au* **2021**, *1*, 1342.
- [24] P. Zuo, A. Tcharkhtchi, M. Shirinbayan, J. Fitoussi, F. Bakir, *Macromol. Mater. Eng.* **2019**, *304*, 1800686.
- [25] S. Watanabe, K. Oyaizu, *ACS Appl. Polym. Mater.* **2021**, *3*, 4495.
- [26] S. Watanabe, T. Takayama, H. Nishio, K. Matsushima, Y. Tanaka, S. Saito, Y. Sun, K. Oyaizu, *Polym. Chem.* **2022**, *13*, 1705.
- [27] S. Watanabe, K. Oyaizu, *Bull. Chem. Soc. Jpn.* **2023**, *96*, 1108.
- [28] S. Watanabe, K. Oyaizu, *Macromolecules* **2022**, *55*, 2252.
- [29] M. Jikei, J. Katoh, N. Sato, K. Yamamoto, H. Nishide, E. Tsuchida, *Bull. Chem. Soc. Jpn.* **1992**, *65*, 2029.
- [30] F. Aida, K. Oyaizu, *Chem. Lett.* **2016**, *45*, 102.
- [31] E. Tsuchida, K. Yamamoto, K. Oyaizu, F. Suzuki, A. S. Hay, Z. Y. Wang, *Macromolecules* **1995**, *28*, 409.
- [32] E. Tsuchida, K. Yamamoto, H. Nishide, S. Yoshida, M. Jikei, *Macromolecules* **1990**, *23*, 2101.
- [33] S. Yun, S. Lee, S. Yook, H. A. Patel, C. T. Yavuz, M. Choi, *ACS Catal.* **2016**, *6*, 2435.
- [34] Z. Lian, B. N. Bhawal, P. Yu, B. Morandi, *Science* **2017**, *356*, 1059.
- [35] P.-S. Lin, Y. Shoji, S. N. Afraj, M. Ueda, C.-H. Lin, S. Inagaki, T. Endo, S.-H. Tung, M.-C. Chen, C.-L. Liu, T. Higashihara, *ACS Appl. Mater. Interfaces* **2021**, *13*, 31898.
- [36] A. Kiriy, V. Senkovskyy, M. Sommer, *Macromol. Rapid Commun.* **2011**, *32*, 1503.

Figures, tables, and texts are partially adapted from S. Watanabe, H. Nishio, K. Oyaizu, *RSC Adv.* **2023**, *13*, 32363-32370 (Copyright © 2023 The Authors).

Chapter 7:
Conclusion and Future Prospects

Contents

7.1 Conclusion

7.2 Future Prospects

References

7.1 Conclusion

In this dissertation, the molecular design of HRIPs based on various intermolecular interactions, including the nanohybrid transparent materials and sulfur-containing polymers with hydrogen bonding (H-bonding) moieties, has been demonstrated as a transparent and ultrahigh-refractive-index material that can overcome the empirical trade-off dichotomy between RI, Abbe number, and visible transparency. In this section, important progress of the present study has been summarized based on the structures and optical properties of HRIPs.

In Chapter 2, methoxy-substituted poly(phenylene sulfide) was synthesized as an inorganic-hybridizable polymers with a high sulfur content and refractivity. In contrast to the hydrophobic nature of poly(phenylene sulfide) derivatives, the introduction of hydrophilic methoxy groups greatly enhances the solubility and affinity of the inorganic metal oxide nanoparticles for preparing transparent and high-refractive-index ($n_D = 1.76$) hybrid materials with TiO_2 having a dispersed particle size of 20-100 nm. Furthermore, the terminal modification of methoxy-substituted poly(phenylene sulfide) by catechol groups further increased the dispersivity of the inorganic nanoparticles up to 30wt% $\text{TiO}_2/\text{ZrO}_2$ addition, enhancing their refractive indices to $n_D = 1.82$, and also achieving good transparency and high Abbe numbers.

In Chapter 3, a new RI enhancement concept for polymers that realizes ultrahigh RI and high visible transparency with H-bonds and sulfur-containing skeletons is discussed. Hydroxy-substituted poly(phenylene sulfide) forms widespread intermolecular H-bonds in the bulk states despite its amorphous structure. Compared to the methoxy-substituted derivative (the methylated precursor), the hydroxy-substituted poly(phenylene sulfide) showed a high glass transition temperature, higher visible transparency, and a higher RI of $n_D = 1.80$, based on the increased density. Dihydroxy-substituted poly(phenylene sulfide)s with a mixture of linear and branched phenylene linkage also represented amorphous properties and better thermostability ($T_g = 140\text{ }^\circ\text{C}$) with even higher RI, based on their high density derived from the denser H-bonding networks.

In Chapter 4, the dual-contribution HRIP skeleton (i.e., H-bonds and highly polarizable groups) was revealed to be an effective design for even higher-RI polymers. The copolymers of hydroxy- and methylthio-substituted poly(phenylene sulfide)s were synthesized from the corresponding methoxy-protected copolymers, and exhibited anomalous RI with unproportional changes accompanying the maximum RI value ($n_D = 1.85$) exceeding those of homopolymers at equal component contributions. The key to this mechanism was identified as the balanced contribution from the H-bond networks and the high sulfur content, with the greatest effectiveness observed in the randomized unit sequence.

In Chapter 5, aromatic poly(thiourea) was demonstrated to be a promising HRIP skeleton based on its highly polarizable unit that enabled zig-zag and randomized H-bonds with high molar refraction, achieving ultrahigh RI yet transparent polymers. A series of poly(thiourea)s were prepared under mild conditions with high-molecular-weight products ($M_w \sim 10^4$), representing thermostable (T_g over $140\text{ }^\circ\text{C}$), transparent, and high RI features. Spectroscopic analyses and density measurements

revealed the presence of reinforced H-bonds for poly(thiourea)s in the bulk state, especially for the compact *p*-phenylene containing skeletons.

Chapter 6 discusses the facile preparation of telechelic poly(phenylene sulfide) derivatives. The *p*-halogenated diaryl disulfides having electron-deficient moieties did not self-polymerize, whereas their corresponding sulfonium cations were selectively substituted with the electron-rich aromatic molecules. These features were adopted for the synthesis of end-dihalogenated poly(phenylene sulfide) derivatives, resulting in almost quantitative conversions and high yields. Notably, bromo-end substituted derivatives can be subjected to further Kumada-Tamao cross-coupling reactions to synthesize the divinyl-substituted poly(phenylene sulfide), which shows thermosetting properties that are useful for compatibility with other materials.

7.2 Future Prospects

In this dissertation, the author represents a new RI-enhancing strategy for polymeric materials while maintaining their transparency without serious colorations. Still, issues remain in balancing many requirements, including superior optical properties for implementation in optoelectronic devices. There remains a huge exploration space for the application of our strategy, especially from the perspective of intermolecular interactions. Moreover, such strategies to make polymers highly dense with amorphous properties might be desired in other functional polymer fields, which should be further explored in the near future. Especially, most multiple H-bonds are based on the bio-mimic system represented by the DNA crosslinks, which will be highly compatible with the protein/biological applications.^[1,2] The following section proposes the solutions and new molecular designs that can contribute to even high-performance HRIPs and optical devices.

7.2.1 Demonstration with Practical Optical Devices

Most of the polymer skeletons in this dissertation contains a large number of H-bonds. This feature is attractive for realizing dense bulk structures that contribute to visible transparency and high-RI bulk structures, although many H-bonds generally result in a hygroscopic nature.^[3,4] In terms of long-term stability, a large amount of swollen water in a polymer matrix leads to plasticization of the bulk materials, which seriously affects the mechanical properties and performance of optoelectronic devices. Considering the optical element usage, such water-induced plasticization negatively caused the RI to decline based on the sparser chain packing and less polarizability.

(1) Double-layer Configuration with Water-resistant Polymers

One solution is to combine a water-resistant polymer as an additional layer for the OLED encapsulants or antireflective functional coatings. For device applications, the HRIP is not used by itself, but with a multi-layer configuration to efficiently enhance the performance.^[5] For example, the OLED efficiency is generally increased by adopting a graded RI-encapsulating layer structure that can reduce the light reflection based on the RI-mismatching problems between the layers, which finally results in

higher optical transmittance (**Figure 7.1**).^[6] Representative water-tolerant polymers are thermosetting polymers including poly(benzoxazine)s,^[7] whose RI and transparency can be controlled by optimizing the spacer structures (**Figure 7.2**).

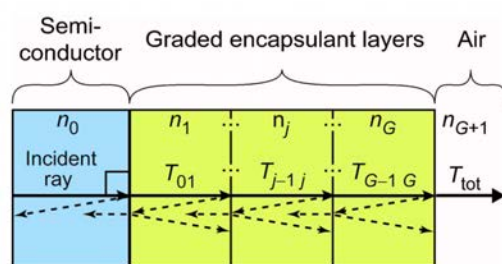


Figure 7.1. A schematic representation of graded-RI configuration for OLED. Reprinted from ref. ^[6] with the permission of AIP Publishing.

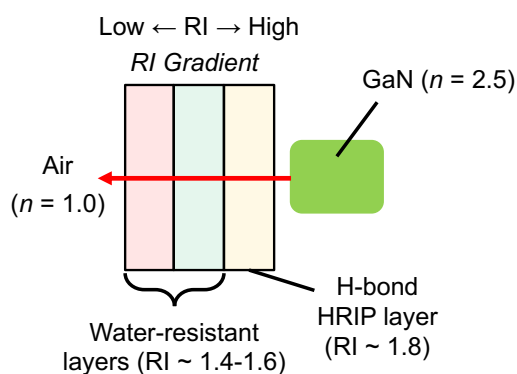


Figure 7.2. One example of a layer structure for LED coatings for realizing high long-term stability.

(2) Enhancing Humidity Tolerance

The second strategy involved the application of a humidity-tolerant spacer skeleton to the HRIP design. For example, Aida *et al.* reported a solution for preventing humidity-induced plasticization of self-healable thiourea polymers by incorporating noncovalently packed dicyclohexylmethane spacers.^[8] By incorporating a small amount (~20%) of highly packed skeletons with interactions other than H-bonds, the polymer properties were maintained under humid conditions. By adopting this strategy to the present HRIP design, the ultrahigh RI, transparency, mechanical strength, and humidity tolerance have been comprehensively improved by the precise optimization of the spacer structures (e.g., sulfur-containing highly packed spacers).

7.2.2 Halogen-bond Driven Ultrahigh-RI Polymers

The author presented an H-bond-induced RI enhancement strategy in this thesis, although numerous molecular designs with several molecular structures and various interactions has remained. In this strategy, utilizing as many UV-visible transparent H-bond skeletons as possible is the key to simultaneously achieving ultrahigh RI and colorless properties. One possible design is to utilize interactions involving polarizable skeletons such as chalcogen bonds^[9] or halogen bonds.^[10] In contrast

to the previous charge-transfer complexation strategy, which resulted in poor film stability triggered by iodine evaporation,^[11] this method can induce the packing between the macromolecules, thereby realizing chain-chain interactions with high thermostability. In the case of poly(thiourea)s, heavy halogen (Br, I)-containing spacers can interact with thiocarbonyl groups, which behave as halogen-bond acceptors (**Figure 7.3**). The plausible concerns for introducing such a design are as follows: (1) Decline in transparency accompanied by high polarizability of the halogen (or heavy chalcogen) atom itself, which can be overcome through the combination with highly transparent counterparts such as triazine or acrylic groups. (2) Weakening of the H-bonding effects by the introduced halogen groups (based on their large atomic radii), which can be solved by copolymerization with highly compact spacers (e.g., *p*-phenylene described in the Chapter 5).

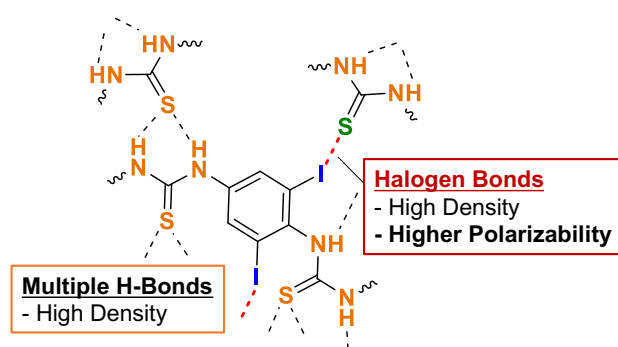


Figure 7.3. Molecular design concept of halogen bond-driven RI enhancement strategy.

References

- [1] S. Mondal, J. J. Lessard, C. L. Meena, G. J. Sanjayan, B. S. Sumerlin, *J. Am. Chem. Soc.* **2022**, *144*, 845.
- [2] S. Chen, W. H. Binder, *Acc. Chem. Res.* **2016**, *49*, 1409.
- [3] Y. Yanagisawa, Y. Nan, K. Okuro, T. Aida, *Science* **2018**, *359*, 72.
- [4] Y. Fujisawa, Y. Nan, A. Asano, Y. Yanagisawa, K. Yano, Y. Itoh, T. Aida, *Angew. Chem. Int. Ed Engl.* **2023**, *62*, e202214444.
- [5] T. Higashihara, M. Ueda, *Macromolecules* **2015**, *48*, 1915.
- [6] F. W. Mont, J. K. Kim, M. F. Schubert, E. F. Schubert, R. W. Siegel, *J. Appl. Phys.* **2008**, *103*, 083120.
- [7] H. Kimura, A. Matsumoto, H. Sugito, K. Hasegawa, K. Ohtsuka, A. Fukuda, *J. Appl. Polym. Sci.* **2001**, *79*, 555.
- [8] Y. Fujisawa, A. Asano, Y. Itoh, T. Aida, *J. Am. Chem. Soc.* **2021**, *143*, 15279.
- [9] R. Zeng, Z. Gong, L. Chen, Q. Yan, *ACS Macro Lett.* **2020**, *9*, 1102.
- [10] H. Guo, R. Puttreddy, T. Salminen, A. Lends, K. Jaudzems, H. Zeng, A. Priimagi, *Nat. Commun.* **2022**, *13*, 7436.
- [11] N. Huo, W. E. Tenhaeff, *Macromolecules* **2023**, *56*, 2113.

List of Publications

1. Seigo Watanabe, Hiromichi Nishio, Kenichi Oyaizu, “Facile Synthesis of Telechelic Poly(phenylene sulfide)s by Means of Electron-Deficient Aromatic Sulfonium Electrophiles”, *RSC Adv.* **2023**, *13*, 32363-32370.
2. Kan Hatakeyama-Sato, Seigo Watanabe, Naoki Yamane, Yasuhiko Igarashi, Kenichi Oyaizu, “Using GPT-4 in Parameter Selection of Polymer Informatics: Improving Predictive Accuracy Amidst Data Scarcity and 'Ugly Duckling' Dilemma”, *Digit. Discov.* **2023**, *2*, 1548-1557.
3. Seigo Watanabe, Kenichi Oyaizu, “Designing Strategy for High Refractive Index Polymers: From the Molecular Level to Bulk Structure Control”, *Bull. Chem. Soc. Jpn.* **2023**, *96*, 1108-1128. (Accounts)
4. Seigo Watanabe, Hiromichi Nishio, Teru Takayama, Kenichi Oyaizu, “Supramolecular Crosslinking of Thiophenylene Polymers via Multiple Hydrogen Bonds toward Ultrahigh Refractive Indices”, *ACS Appl. Polym. Mater.* **2023**, *5*, 2307-2311.
5. Seigo Watanabe, Teru Takayama, Kenichi Oyaizu, “Transcending the Trade-off in Refractive Index and Abbe Number for Highly Refractive Polymers: Synergistic Effect of Polarizable Skeletons and Robust Hydrogen Bonds”, *ACS Polym. Au* **2022**, *2*, 458-466.
6. Seigo Watanabe, Teru Takayama, Hiromichi Nishio, Kanta Matsushima, Yoko Tanaka, Seiya Saito, Yushun Sun, Kenichi Oyaizu, “Synthesis of colorless and high-refractive-index sulfoxide-containing polymers by the oxidation of poly(phenylene sulfide) derivatives”, *Polym. Chem.* **2022**, *13*, 1705-1711.
7. Seigo Watanabe, Kenichi Oyaizu, “Designing Ultrahigh-Refractive-Index Amorphous Poly(phenylene sulfide)s Based on Dense Intermolecular Hydrogen-Bond Networks”, *Macromolecules* **2022**, *55*, 2252-2259.
8. Seigo Watanabe, Seiya Saito, Motoyasu Hirai, Kenichi Oyaizu, “Synthesis of methylated phenylene sulfide polymers via bulk oxidative polymerization and their heat curing triggered by dynamic disulfide exchange”, *Polym. J.* **2022**, *54*, 1-10.
9. Seigo Watanabe, Kenichi Oyaizu, “Catechol End-Capped Poly(arylene sulfide) as a High-Refractive-Index “TiO₂/ZrO₂-Nanodispersible” Polymer”, *ACS Appl. Polym. Mater.* **2021**, *3*, 4495-4503.
10. Seigo Watanabe, Kenichi Oyaizu, “Methoxy-Substituted Phenylenesulfide Polymer with Excellent Dispersivity of TiO₂ Nanoparticles for Optical Application”, *Bull. Chem. Soc. Jpn.* **2020**, *93*, 1287-1292.

List of Presentations

1. Seigo Watanabe, Kenichi Oyaizu, “High Refractive Index Aromatic Poly(thiourea)s Bearing Polarizable Hydrogen Bonds”, *6th G'L'owing Polymer Symposium in KANTO*, Online, November 2023.
2. Seigo Watanabe, Kenichi Oyaizu, “Ultrahigh-Refractive-Index Poly(thiourea)s with Hydrogen-Bonding Networks and Polarizable Substituents”, *72nd symposium on Macromolecules*, Kagawa, September 2023.
3. Seigo Watanabe, Kenichi Oyaizu, “Thiourea-Based High Refractive Index Polymers with Efficient Degradability”, *12th Jilin-Korea-Waseda Alliance Annual Symposium*, Tokyo, August 2023.
4. Seigo Watanabe, Kenichi Oyaizu, “Ultrahighly Refractive and Degradable Thiourea Polymers with Dense and Multiple Intermolecular Hydrogen Bonds”, *The 103rd Chemical Society of Japan Annual Meeting*, Chiba, March 2023.
5. Seigo Watanabe, Kenichi Oyaizu, “Thiourea-Incorporated Ultrahigh-Refractive-Index Polymers Based on Random yet Dense Hydrogen Bonding Networks”, *The 17th Pacific Polymer Conference*, Australia, December 2022.
6. Seigo Watanabe, Kenichi Oyaizu, “Development of Thiourea-Containing Ultrahigh-refractive-index Polymers Bearing Dense Hydrogen Bonds”, *71st symposium on Macromolecules*, Hokkaido, September 2022.
7. Seigo Watanabe, Hiromichi Nishio, Kenichi Oyaizu, “Synthesis and Anomalous Refractive Index Properties of Poly(phenylene sulfide) Derivatives Bearing Sulfur-Containing Pendants and Hydroxy Groups”, *71st SPSJ Annual Meeting*, Online, May 2022.
8. Seigo Watanabe, Teru Takayama, Hiromichi Nishio, Kenichi Oyaizu, “Synthesis of Ultrahigh Refractive Index Poly(phenylene sulfide)s via the Dual Control of Polarizability and Intermolecular Interactions”, *Student Annual Meeting on Tokyo Young Polymer Scientists 2022*, Tokyo, March 2022.
9. Seigo Watanabe, Hiromichi Nishio, Kenichi Oyaizu, “Synthesis of Functionalized Poly(phenylene sulfide)s via Oxidative Polymerization and Their Ultrahigh Refractive Indices Driven by Hydrogen Bonds”, *The International Chemical Congress of Pacific Basin Societies 2021*, Online, December 2021.
10. Seigo Watanabe, Kenichi Oyaizu, “Refractive Index and Abbe Number Enhancement of Poly(phenylene sulfide)s by Phenolic Hydroxy Groups and Their Optical Functions”, *11th Chemical Society of Japan Chemistry Festa*, Online, October 2021.
11. Seigo Watanabe, Kenichi Oyaizu, “Hydroxy-Bearing Poly(phenylene sulfide): A Colorless and Transparent Polymer with Unprecedented Ultrahigh Refractive Index”, *10th Jilin-Korea-Waseda Alliance Annual Symposium*, Online, September 2021.
12. Seigo Watanabe, Hiromichi Nishio, Kenichi Oyaizu, “Synthesis and Optical Properties of Ultrahigh Refractive Index Poly(phenylene sulfide)s via Oxidative Polymerization”, *70th SPSJ Annual Meeting*, Online, May 2021.
13. Seigo Watanabe, Kenichi Oyaizu, “Synthesis and Properties of Ultrahigh Refractive Index and

- Amorphous Poly(phenylene sulfide)”, *Student Annual Meeting on Tokyo Young Polymer Scientists 2021*, Online, February 2021.
14. Seigo Watanabe, Teru Takayama, Kenichi Oyaizu, “High Refractive Index Poly(arylene sulfide)s with Functional Groups for Finely Compatibilized Hybrid Materials”, *3rd G'Lowing Polymer Symposium in KANTO*, Online, November 2020.
 15. Seigo Watanabe, Kenichi Oyaizu, “Synthesis of Poly(phenylene sulfide) Derivatives with High Dispersivity of TiO₂ Nanoparticles and Their Application to High Refractive Index Hybrid Materials”, *69th SPSJ Symposium on Macromolecules*, Online, September 2020.
 16. Seigo Watanabe, Motoyasu Hirai, Kenichi Oyaizu, “Synthesis of Methoxy-Substituted Poly(phenylene sulfide) through Oxidative Polymerization and Its Application to Organic-Inorganic Hybrid Material”, *9th Chemical Society of Japan Chemistry Festa*, Tokyo, October 2019.
 17. Seigo Watanabe, Motoyasu Hirai, Kenichi Oyaizu, “Synthesis and Properties of Methoxy-Substituted Poly(phenylene sulfide) through Oxidative Polymerization”, *68th SPSJ Symposium on Macromolecules*, Fukui, September 2019.

Award

Encouragement Prize

Morimura Houmeikai Foundation (2021.03)

CSJ Chemistry Festa Oral Presentation Award for Ph.D Students

CSJ Poster Presentation Award 2021 for Excellent Research

11th Chemical Society of Japan Chemistry Festa (2021.12)

Best Oral Presentation Award

Tokyo Young Polymer Scientists 2022 (2022.03)

Poster Award

71st Annual Meeting of The Society of Polymer Science (2022.06)

Encouragement Prize for Young Scientists

Waseda Research Institute for Science and Engineering, Early Bird (2023.03)

Best Presentation Award

6th G'Lowing Polymer Symposium in KANTO (2023.11)

Acknowledgements

This dissertation is the collections of the studies conducted under the supervision of Prof. Dr. Kenichi Oyaizu, Department of Applied Chemistry, Waseda University, in 2019-2023. The author expresses the greatest acknowledgment to Prof. Dr. Kenichi Oyaizu for his invaluable suggestions, fruitful discussions, and continuous encouragement for this work.

The author greatly expresses his acknowledgement to Assoc. Prof. Dr. Takeo Suga (Waseda Univ.) for his valuable discussions and kind support. The author also acknowledges him for the effort as a member of the jugging committee for this doctoral dissertation.

The author greatly wishes to acknowledge Prof. Dr. Yoshiyuki Sugahara (Waseda Univ.) for his valuable comments that greatly improved the doctoral dissertation, and his effort as a member of the jugging committee for this doctoral dissertation.

The author expresses the great acknowledgement to Prof. Dr. Hiroyuki Nishide (Waseda Univ.) for valuable comments, fruitful discussions, and very kind and consistent support.

The author is extremely grateful to Prof. Dr. Rubén D. Costa (Technical Univ. of Munich) for his invaluable comments and giving the opportunity to collaborate and conduct research activities in his laboratory. The author also greatly acknowledges Mr. Luca M. Cavinato (Technical Univ. of Munich) for his kind support during the visit and for the collaborative work.

The author is grateful to Dr. Kan Hatakeyama-Sato (Tokyo Tech), Dr. Yu Wang (Hitachi Co.), Dr. Koki Suwa (Sumitomo Chemicals Co.), Dr. Kouki Oka (Tohoku Univ.) for their invaluable comments and valuable discussions.

The author expresses great thanks to all active collaborators, Mr. Seiya Saito (Japan Tobacco Inc.), Mr. Yushun Sun (Denka Co.), Mr. Motoyasu Hirai (Japan Science and Technology Agency), Mr. Kanta Matsushima (Nihon M&A Center Inc.), Mr. Teru Takayama (Fujifilm Co.), Mr. Hiromichi Nishio (Asahikasei Co.), Mr. Tomohiro Miura (Resonac Co.), Ms. Yoshino Tsunekawa, Ms. Zekin An, Mr. Shuma Miura, Mr. Yuto Nakamura, Ms. Sumire Hariyama, Mr. Tomoya Yano, and Mr. Yuki Yoshida.

The author express acknowledges Mr. Yusuke Kaiwa for his kind support and assistance for pursuing Ph.D.

The author acknowledges Dr. Toshimichi Shibue, Dr. Natsuhiko Sugimura, and all other

members in Materials Characterization Central Laboratory (Waseda Univ.) for their valuable discussions and kind technical support for conducting the research. Also, the author expresses the acknowledgement to Mr. Yoshito Nozaki (Nanotechnology Research Center, Waseda Univ.) for his technical support for the ellipsometry measurements.

The author acknowledges the JSPS fellowship by MEXT, the early bird program by Waseda Research Institute for Science and Engineering, and Mizuho Foundation for the Promotion of Sciences for their funding support.

Special thanks to Toshiyuki Mizuno Scholarship, Satomi Scholarship, and Shozo Nakasone Scholarship for their financial support.

Finally, the author would like to express his deepest gratitude to his family, Mr. Katsuya Watanabe and Mrs. Takako Watanabe for their heartfelt and contentious support.

January, 2024
Seigo Watanabe